Higgs dynamics in the early universe

Vis, J.M. van de

Higgs dynamics in the early universe

Proefschrift

ter verkrijging van
de graad van Doctor aan de Universiteit Leiden,
op gezag van Rector Magnificus prof.mr. C.J.J.M. Stolker,
volgens het besluit van het College voor Promoties
te verdedigen op dinsdag 2 juli 2019
klokke 13.45 uur

door

Jorinde Marjolein van de Vis

geboren te Delft
in 1991

Promotor:	Prof. dr. J.W. van Holten
Copromotor:	Dr. M.E.J. Postma (Nikhef)

Promotiecommissie:	Dr. T. M. Konstandin (DESY, Hamburg, Duitsland)
	Prof. dr. D. Roest (Rijksuniversiteit Groningen)
	Prof. dr. A. Achúcarro
	Prof. dr. E. R. Eliel
	Prof. dr. K. E. Schalm

ISBN 978-90-8593-406-6
An electronic version of this thesis can be found at https://openaccess.leidenuniv.nl

This work is part of the research program 'Observing the Big Bang' with project number 160, which is financed by the Netherlands Organization for Scientific Research (NWO). This work was carried out at Nikhef.

The cover shows bubbles of broken electroweak symmetry in a first order phase transition.

Contents

Publications

This thesis is based on the following publications

[1] *Electroweak stability and non-minimal coupling*, M. Postma and J. van de Vis JCAP, **1705**, 004 (2017), hep-ph/1702.07636.

[2] *Preheating after Higgs Inflation: Self-Resonance and Gauge boson production*, E.I. Sfakianakis and J. van de Vis, Phys. Rev. **D99**, 083519 (2019), hep-ph/1810.01304.

[3] *Electroweak Baryogenesis and the Standard Model Effective Field Theory*, J. de Vries, M. Postma, J. van de Vis and G. White, JHEP **01**, 089 (2018), hep-ph/1710.04061.

[4] *The role of leptons in electroweak baryogenesis*, J. de Vries, M. Postma and J. van de Vis, JHEP **04**, 024 (2019), hep-ph/1811.11104.

Other publications

[5] *Spinning bodies in curved spacetime*, G. d'Ambrosi, S. Satish Kumar, J. van de Vis and J. W. van Holten, Phys. Rev. **D93**, 044051, (2016), gr-qc/1511.05454.

[6] *Ultrametricity increases the predictability of cultural dynamics*, A.I. Băbeanu, J. van de Vis and D. Garlaschelli, New J. Phys. **20**, 10 (2018), soc-ph/1712.05959.

Abbreviations

BAU	**B**aryon **A**symmetry of the **U**niverse
BBN	**B**ig **B**ang **N**ucleosynthesis
BD	**B**unch-**D**avies
BSM	**B**eyond the **S**tandard **M**odel
CMB	**C**osmic **M**icrowave **B**ackground
CP	**C**harge-**P**arity
CPV	**C**harge-**P**arity **V**iolating
CTP	**C**losed **T**ime **P**ath
DM	**D**ark **M**atter
EDM	**E**lecric **D**ipole **M**oment
EFT	**E**ffective **F**ield **T**heory
EOM	**E**quation **O**f **M**otion
EW	**E**lectro**W**eak
EWBG	**E**lectro**W**eak **B**aryo**G**enesis
EWPT	**E**lectro**W**eak **P**hase **T**ransition
FOPT	**F**irst **O**rder **P**hase **T**ransition
GUT	**G**rand **U**nified **T**heories
HBB	**H**ot **B**ig **B**ang
LHC	**L**arge **H**adron **C**ollider
MSSM	**M**inimal **S**upersymmetric **S**tandard **M**odel
RGE	**R**enormalization **G**roup **E**quation
RG	**R**enormalization **G**roup
SM	**S**tandard **M**odel
vev	**v**acuum **e**xpectation **v**alue
VIA	**V**ev **I**nsertion **A**pproximation

Notation and Conventions

We will work in units where

$$\hbar = c = k_B = 1\,,$$

where $\hbar$ is the reduced Planck constant, c the speed of light and k_B the Boltzmann constant. In this system

$$[\text{energy}] = [\text{mass}] = [\text{temperature}] = [\text{time}]^{-1} = [\text{length}]^{-1}\,.$$

The reduced Planck mass is defined by

$$m_{\text{pl}} = \frac{1}{\sqrt{8\pi G}}\,,$$

with G Newton's constant.

In chapters 1 through 4 we use a metric with signature $(-,+,+,+)$. In the remainder of the thesis we use a metric with signature $(+,-,-,-)$.

The sign convention of the antisymmetric tensor in two dimensions ϵ^{ab} is $\epsilon^{12} = 1$. Similarly, ϵ^{abc} with $\epsilon^{123} = 1$ is the antisymmetric tensor in three dimensions.

Chapter 1

Introduction

Cosmology is the study of the universe as a whole. It aims to understand the evolution from a state of very large energy density, 13.8 billion years ago, to the universe that we live in today, that is filled with radiation, dust and clusters of galaxies and the mysterious dark matter and dark energy. Cosmological structures and observations involve very large length scales. Particle physics, on the contrary, is about the very small (subatomic) scales. The Standard Model (SM) of particle physics describes the elementary particles and their interactions. This thesis describes research at the interface of particle physics and cosmology.

Even though the length scales of cosmological observations today are very large, the data contain traces of particle physics processes in the early universe. These processes happened at energy scales much larger than the scales accessible at particle accelerators on earth. Observations of the early universe are thus a unique probe of particle physics. Properties of elementary particles guide us in unravelling the history of the universe whilst cosmological observations also constrain models of Beyond the Standard Model (BSM) physics. We list some examples of this interplay.

- The particles that dominate the energy density of the universe determine its rate of expansion. Very early in the history of the universe, the energy density was dominated by relativistic particles. This epoch is referred to as radiation-dominated. At a later time, the main constituent became massive, non-relativistic particles. In the matter-dominated epoch the rate of expansion of the universe is different from the expansion rate in the radiation-dominated epoch.

- Measurements of e.g. rotation curves of galaxies [7–9], gravitational lensing [10] and oscillations in the power spectrum of the Cosmic Microwave Background [11] indicate that there is a large amount of 'dark matter' (DM) in the universe. This massive contribution to the energy budget

of the universe does not interact through the electromagnetic interaction and is therefore not visible. The observations above can be explained by DM with a particle nature, which is an indication of BSM physics. There are also searches for alternative descriptions of gravity [12, 13], but these alternatives have so far not managed to explain all observational indications for DM.

- The value of the neutrino masses affects the evolution of cosmological perturbations and structure formation. The sum of neutrino masses can be constrained by observations of the Cosmic Microwave Background and Large Scale Structure [14].

There are many more examples of the interplay between particle physics and cosmology but in this thesis we will focus on two: reheating after inflation and electroweak baryogenesis. Before diving into these two topics, we will give a brief introduction into the Standard Model of particle physics and cosmology.

1.1 The Standard Model of particle physics

It would be an impossible task to introduce the Standard Model of particle physics in its full glory in a short introductory section. We will therefore only focus on the aspects of the SM that are relevant for this work. More extensive introductions than the one presented here, can be found in Refs. [15–17].

The formulation of the SM was a formidable task that took several decades. A very important first step was the theory of Quantum Electrodynamics. This theory was formulated and proved to be renormalizable in the '40s, with major contributions from Bethe, Tomonaga, Schwinger and Feynman [18–24]. The full electroweak sector was written down by Glashow, Weinberg and Salam [25–27] and shown to be renormalizable by 't Hooft and Veltman [28].

Of all the particles of the SM, the Higgs particle plays the main role in this thesis. Since a Higgs field on its own does not lead to very interesting particle physics, we will first present the full particle content of the SM in section 1.1.1. We will then introduce the electroweak Lagrangian and its gauge invariance in section 1.1.2. In section 1.1.3 we show how the SM particles obtain their masses through spontaneous symmetry breaking.

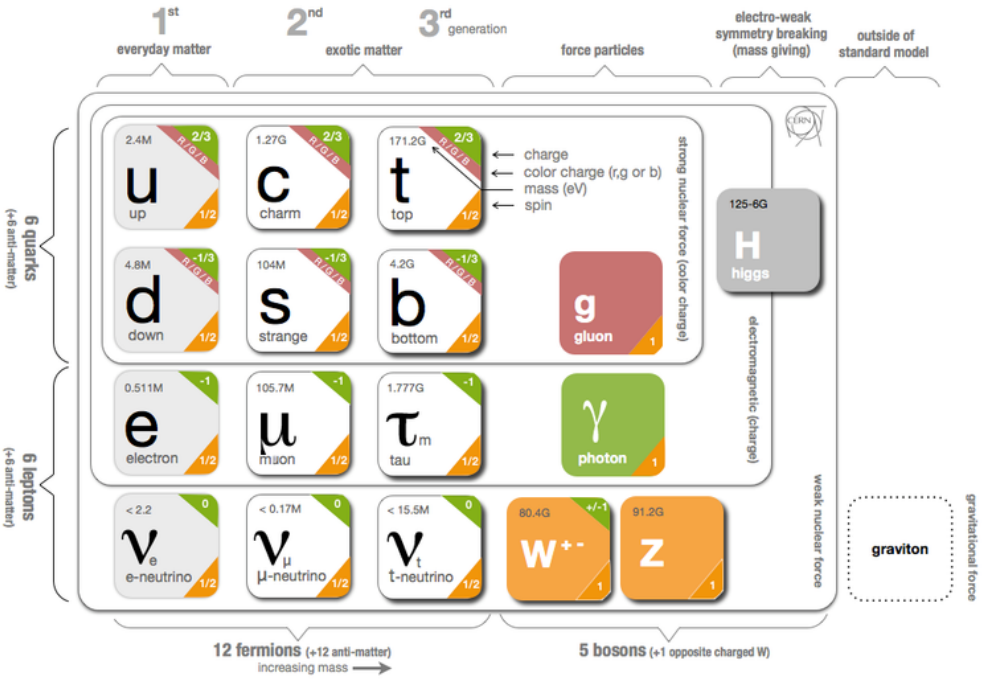

FIGURE 1.1: Particle content of the Standard Model (credit: CERN). Fermions are shown on the left, with quarks in the top two rows and leptons in the bottom two rows. On the right-hand side the bosons are shown.

1.1.1 Particle content

Figure 1.1 shows the particle content of the SM. The matter sector, consisting of fermions with spin 1/2, is shown on the left. There are three generations of quarks and three generations of leptons. Quarks participate in all three fundamental interactions described by the SM: the strong interaction, the weak interaction and the electromagnetic interaction. Leptons are not charged under the strong interaction, and therefore only interact via weak and electromagnetic interactions. The neutrinos have zero electromagnetic charge and consequently only interact through the weak interaction.

In the SM Lagrangian, fermions are represented by four-component spinors. An important property of these spinors is 'chirality' or 'handedness'. A right-handed spinor ψ_R is an eigenvector of the chirality matrix γ^5 with eigenvalue $+1$. A left-handed spinor ψ_L has eigenvalue -1,

$$\gamma^5 \psi_R = +\psi_R \,, \qquad \gamma^5 \psi_L = -\psi_L \,. \tag{1.1}$$

We will see below that the properties of right- and left-handed particles are not identical.

The gluon, photon and W- and Z-bosons are spin 1 particles. They are the gauge bosons of the strong, electromagnetic and weak interaction respectively. The gauge bosons are represented by

vector fields in the SM Lagrangian. The gluon and photon are massless, but the mediators of the weak interaction are massive.

The particle on the very right of figure 1.1 is the Higgs boson. It has spin 0 and is therefore represented by a scalar field in the SM Lagrangian.

1.1.2 Gauge symmetry

The SM is a gauge theory with gauge group $SU(3)_C \times SU(2)_L \times U(1)_Y$ (see Ref. [29] for an introduction into gauge theories in particle physics). $U(1)$ is an Abelian gauge group, but $SU(3)$ and $SU(2)$ are non-Abelian, which means that the elements of the group do not commute.

The spin 1 gauge fields correspond to the generators of the different gauge groups. The group $SU(3)_C$ is associated to the strong force. It has 8 generators, corresponding to 8 gluons. The weak and electromagnetic interaction are unified in the $SU(2)_L \times U(1)_Y$ electroweak (EW) interaction. We denote the three gauge bosons associated to $SU(2)_L$ by A^i_μ and the gauge boson corresponding to $U(1)_Y$ (hypercharge) by B_μ. We will see below that the photon and W- and Z-bosons are linear combinations of the fields A^i_μ and B_μ. The subscript L in $SU(2)_L$ indicates that the $SU(2)_L$-part only interacts with left-handed fermions. The left-handed fermions form $SU(2)_L$-doublets

$$Q_L = \begin{pmatrix} u_L \\ d_L \end{pmatrix} , \qquad L_L = \begin{pmatrix} \nu_L \\ e_L \end{pmatrix} , \tag{1.2}$$

where Q_L and L_L denote quark and lepton doublets respectively. u_L (d_L) is a left-handed up- (down-)type quark, and ν_L (e_L) is a left-handed neutrino- (electron-)type lepton. The corresponding right-handed fields

$$u_R\,, \qquad d_R\,, \qquad e_R\,, \tag{1.3}$$

are singlets under $SU(2)_L$. The SM does not include right-handed neutrino fields.

To see how the gauge symmetry works, we will write down the Lagrangian for the electroweak sector. For simplicity, we only consider a single generation of quarks and leptons.

$$\begin{aligned} \mathcal{L}_{EW} = &- \bar{Q}_L i\not{D}\, Q_L - \bar{u}_R i\not{D}\, u_R - \bar{d}_R i\not{D}\, d_R - \bar{L}_L i\not{D}\, L_L - \bar{e}_R i\not{D}\, e_R - (D_\mu\Phi)^\dagger D^\mu\Phi \\ &- \frac{1}{4}\left(A^i_{\mu\nu}A^{i\,\mu\nu} + B_{\mu\nu}B^{\mu\nu}\right) \\ &- \mu^2\Phi^\dagger\Phi - \lambda(\Phi^\dagger\Phi)^2 - \left(\bar{Q}_L Y_u \tilde{\Phi}\, u_R + \bar{Q}_L Y_d \Phi\, d_R + \bar{L}_L Y_e \Phi\, e_R + \text{h.c.}\right) . \end{aligned} \tag{1.4}$$

The first line is the kinetic term for the fermions and the Higgs field Φ. As usual, the 'barred' spinor $\bar{\psi}$ is defined as $\bar{\psi} = \psi^\dagger \gamma^0$. The derivatives D_μ are covariant derivatives instead of ordinary partial derivatives to make the Lagrangian gauge invariant. We have used the notation $\not{D} = \gamma^\mu D_\mu$, with

$$D_\mu = \partial_\mu - igA^i_\mu \frac{\tau^i}{2} - ig' \frac{Y}{2} B_\mu \,, \tag{1.5}$$

where g and g' are the coupling constants of $SU(2)_L$ and $U(1)_Y$ respectively and the $\tau^i/2$ are the generators of $SU(2)$, with the τ^i the Pauli matrices. A summation over the repeated index i is implied. Y denotes the hypercharge of the field that the covariant derivative is acting on.

The second line of the Lagrangian (1.4) contains the kinetic terms for the gauge fields. The third line describes the Higgs potential and the interactions between the Higgs and the fermions. $\tilde{\Phi}$ is defined as $\tilde{\Phi}^a = \epsilon^{ab} \Phi^{b*}$, where ϵ^{ab} is the antisymmetric tensor in two dimensions ($\epsilon^{12} = +1$).

Let's see what happens to the terms in the Lagrangian (1.4) under a $SU(2)_L \times U(1)_Y$ gauge transformation. The transformations are described by $3+1$ spacetime-dependent parameters $\{\vartheta^1(x), \vartheta^2(x), \vartheta^3(x), \xi(x)\}$. The unitary representations of the transformations are

$$U(\vec{\vartheta}) = \exp\left[\frac{i\vartheta^i \tau^i}{2}\right], \qquad U(\xi) = \exp\left[\frac{i\xi Y}{2}\right], \tag{1.6}$$

or, combined

$$U(\vec{\vartheta}, \xi) = \exp\left[\frac{i\vartheta^i \tau^i}{2} + \frac{i\xi Y}{2}\right]. \tag{1.7}$$

Under a $SU(2)_L \times U(1)_Y$-transformation, the left-handed quark and lepton doublets transform as

$$\begin{aligned} Q_L \to Q'_L &= U(\vec{\vartheta}, \xi) Q_L = \exp\left[\frac{i\vartheta^i \tau^i}{2} + \frac{i\xi}{6}\right] Q_L \,, \\ L_L \to L'_L &= U(\vec{\vartheta}, \xi) L_L = \exp\left[\frac{i\vartheta^i \tau^i}{2} - \frac{i\xi}{2}\right] L_L \,, \end{aligned} \tag{1.8}$$

where we used that quark doublets have hypercharge $Y = 1/3$ and lepton doublets $Y = -1$. Since the right-handed fields are singlets under $SU(2)_L$, they simply transform as

$$u_R \to u'_R = \exp\left[\frac{2}{3} i\xi\right] u_R \,, \qquad d_R \to d'_R = \exp\left[-\frac{1}{3} i\xi\right] d_R \,, \qquad e_R \to e'_R = \exp\left[-i\xi\right] e_R \,, \tag{1.9}$$

where we used that the hypercharges of u_R, d_R and e_R are $4/3$, $-2/3$ and -2 respectively. The Higgs field, which has hypercharge $+1$, transforms as

$$\Phi \to \Phi' = \exp\left[\frac{i\vartheta^i \cdot \tau^i}{2} + \frac{i\xi}{2}\right]\Phi\,. \tag{1.10}$$

Finally, we write down the transformation of the gauge fields themselves:

$$\begin{aligned} A^i_\mu \frac{\tau^i}{2} \to A'^i_\mu \frac{\tau^i}{2} &= U(\vec{\vartheta})\left[A^i_\mu \frac{\tau^i}{2} - \frac{i}{g}\partial_\mu\right] U^{-1}(\vec{\vartheta})\,, \\ B_\mu \frac{Y}{2} \to B'_\mu \frac{Y}{2} &= U(\xi)\left[B_\mu \frac{Y}{2} - \frac{i}{g'}\partial_\mu\right] U^{-1}(\xi)\,. \end{aligned} \tag{1.11}$$

Plugging in the transformation of the gauge fields into the covariant derivatives, we find that $D_\mu \to D'_\mu = U(\vartheta,\xi) D_\mu U^{-1}(\vartheta,\xi)$ and this implies that the kinetic terms are indeed invariant under gauge transformations.

Gauge invariance in the second line of the Lagrangian (1.4) is obtained for the following field strength tensors

$$\begin{aligned} A^i_{\mu\nu} &= \partial_\mu A^i_\nu - \partial_\nu A^i_\mu + g\epsilon^{ijk} A^j_\mu A^k_\nu\,, \\ B_{\mu\nu} &= \partial_\mu B_\nu - \partial_\nu B_\mu\,, \end{aligned} \tag{1.12}$$

with ϵ^{ijk} the structure constant of $SU(2)$. Since the $B_{\mu\nu}B^{\mu\nu}$ contains only terms that are quadratic in B_μ, this field does not have self-interactions. The last term in $A^i_{\mu\nu}$ *does* allow for self-interactions, which is a typical property of non-Abelian gauge groups.

1.1.3 Spontaneous symmetry breaking

It is known from experiments that the W- and Z-bosons, which mediate the weak interaction, are massive. This raises a problem for the theory as it was just described. For concreteness, consider the Abelian hypercharge field (the same problem arises for the non-Abelian gauge fields). The gauge transformation of eq. (1.11) can be written as:

$$B_\mu \to B'_\mu - \frac{1}{g'}\partial_\mu \xi\,. \tag{1.13}$$

If we added a mass term

$$\mathcal{L}_{\rm m} = -\frac{1}{2} m^2 B_\mu B^\mu\,, \tag{1.14}$$

this would clearly break gauge invariance.

The fermions have a related problem: the left-handed particles are part of $SU(2)_L$-doublets, but the right-handed particles are singlets under $SU(2)_L$. A fermion mass term would mix the left- and right-handed components, and would therefore violate $SU(2)_L$-gauge invariance.

A consistent solution of these problems is provided by spontaneous symmetry breaking using the Higgs mechanism[1] which generates masses for the Z- and W-bosons and fermions. This is achieved by introducing a doublet of scalar fields parameterized as

$$\Phi = \frac{1}{\sqrt{2}} \begin{pmatrix} \theta^1 + i\theta^2 \\ \phi + i\theta \end{pmatrix} . \tag{1.15}$$

It will be useful to split the component ϕ into a classical background value φ and an excitation h (the Higgs boson), $\phi(x,t) = \varphi + h(x,t)$ [2].

The Higgs field couples to the electroweak gauge bosons through its kinetic term and to the fermions through the Yukawa interactions. The potential can be read off from eq. (1.4)

$$V(\Phi, \Phi^\dagger) = \mu^2 \Phi^\dagger \Phi + \lambda (\Phi^\dagger \Phi)^2 , \tag{1.16}$$

where λ is assumed to be positive, such that the potential is bounded from below [3] and μ^2 is negative. The shape of this potential is often described as a Mexican hat. The potential is minimized for

$$\Phi^\dagger \Phi = \frac{v_0^2}{2} , \qquad \text{with } v_0 = \sqrt{-\frac{\mu^2}{\lambda}} , \tag{1.17}$$

which defines the vacuum state. v_0 is referred to as the 'vacuum expectation value' (vev). Combining eq. (1.17) with the requirement that electromagnetic gauge symmetry is unbroken, we obtain the expectation value of the Higgs field:

$$\langle \Phi \rangle = \frac{1}{\sqrt{2}} \begin{pmatrix} 0 \\ v_0 \end{pmatrix} , \tag{1.18}$$

[1] The terms 'Higgs field' and 'Higgs mechanism' do not do justice to all scientists that introduced these concepts. The often-used names 'Higgs field', 'Higgs boson' and 'Higgs mechanism' refer to Peter Higgs, who introduced this mechanism in Ref. [30]. He also pointed out the existence of a neutral spin 0 boson, that would eventually be detected at the LHC [31, 32]. The same mechanism that gives mass to the fermions and gauge bosons was introduced by Robert Brout and François Englert in Ref. [33], who however did not mention the existence of the corresponding boson. It could thus be argued that the name 'Higgs boson' is appropriate, but that the corresponding field and mechanism should be called 'BEH-field' and 'BEH-mechanism'. In order to avoid confusion, we will stick to the names that are most commonly used in literature, and thus refer to the 'Higgs field' and 'Higgs mechanism'.

[2] In cosmology, $\varphi(t)$ is time-dependent.

[3] The measured values of the Higgs and top quark mass indicate that λ could run negative at large energy scales $\gtrsim 10^{11}$ GeV. We study this possibility in chapter 3. If this is the case, the potential should be bounded from below by higher-dimensional operators.

where v_0 is the value of φ. The vev spontaneously breaks the $SU(2)_L \times U(1)_Y$-symmetry into a residual $U(1)_Q$-symmetry. The spontaneous symmetry breaking generates mass terms for the gauge bosons. To see this, we write Φ in unitary gauge:

$$\Phi = \frac{1}{\sqrt{2}} \begin{pmatrix} 0 \\ v_0 + h \end{pmatrix} , \tag{1.19}$$

and plug this into the Higgs Lagrangian $\mathcal{L}_{\text{Higgs}} = -(D_\mu \Phi)^\dagger D^\mu \Phi - V(\Phi, \Phi^\dagger)$:

$$\mathcal{L}_{\text{Higgs}} = -\frac{1}{2}\partial_\mu h \partial^\mu h - \frac{g^2}{4}(v_0 + h)^2 W_\mu^\dagger W^{\dagger\mu} - \frac{g^2}{8\cos^2\theta_W}(v_0 + h)^2 Z_\mu Z^\mu - \frac{\lambda}{4}(h^2 + 2v_0 h)^2 . \tag{1.20}$$

We can read off the Higgs boson mass

$$m_h = \sqrt{-2\mu^2} , \tag{1.21}$$

where we used eq. (1.17). The W- and Z-bosons are linear combinations of the A_μ^i and B^μ fields defined above

$$W_\mu = \frac{A_\mu^1 - iA_\mu^2}{\sqrt{2}} , \qquad Z_\mu = \cos\theta_W A_\mu^3 - \sin\theta_W B_\mu , \tag{1.22}$$

where θ_W is the Weinberg angle [26]. The masses of the gauge bosons are

$$m_W = \frac{g v_0}{2} , \qquad m_Z = \frac{g v_0}{2\cos\theta_W} . \tag{1.23}$$

Spontaneous symmetry breaking has thus resulted in mass terms for the gauge bosons without breaking gauge symmetry at the level of the Lagrangian. The photon, which is the combination of A_μ^3 and B_μ orthogonal to Z_μ, does not couple to the Higgs boson. It remains massless and mediates the electromagnetic force; it is associated with the residual $U(1)_Q$-symmetry, with Q standing for electric charge. Q is related to Y, hypercharge, and I_3, weak isospin, by

$$Q = I_3 + \frac{Y}{2} . \tag{1.24}$$

The value of I_3 is zero for $SU(2)_L$-singlets and $+1/2$ $(-1/2)$ for the upper (lower) components of $SU(2)_L$ doublets.

The Higgs field also gives masses to the fermions, for which gauge symmetry also forbids an explicit mass term in the Lagrangian. The Higgs field couples to fermions via so-called 'Yukawa' interactions, as written in the last line of eq. (1.4). After spontaneous symmetry breaking the mass of a fermion

f is

$$m_f = \frac{y_f v_0}{\sqrt{2}} \,. \tag{1.25}$$

Since the neutrinos do not have Yukawa interactions, they are massless in the SM. However, the observation of neutrino oscillations indicates that they must be massive. This mass is an indication of BSM physics.

In the upcoming chapters we will often encounter the situation where the Higgs field does not sit at its zero-temperature vev. Instead, its background value $\varphi(t)$, will be dynamical. In the adiabatic limit, the masses of the fermions and gauge bosons are obtained by replacing v_0 with φ in eqs. (1.23) and (1.25).

1.2 Cosmology

We will now give a very brief overview of what is currently known about the evolution of the universe. The estimated age of the universe is 13.8×10^9 years [34], but we will mostly focus on the first 380,000 years. The processes that are described in this thesis, reheating and baryogenesis, both take place before the universe was even a second old. We will nevertheless describe the further evolution of the universe, because observational constraints on the very early universe can be derived from processes that happened later.

The formation of light elements during Big Bang Nucleosynthesis (BBN) is the first process that can be probed by observations. Strictly speaking, any description of the universe before BBN is speculation. However, data from the Cosmic Microwave Background (CMB) and BBN and properties of elementary particles strongly restrict the history of the universe. In section 1.2.2 we will introduce the widely accepted Hot Big Bang (HBB) model, which gives accurate predictions for BBN and CMB observables. The inflationary phase, which is the topic of section 1.2.4, was introduced to solve some shortcomings of the HBB model that are explained in section 1.2.3. We will start with an important pillar of cosmology: the cosmological principe. Extensive introductions into the phenomenology of the early universe can be found for example in Refs. [35–38].

1.2.1 Cosmological principle

Modern cosmology is built on the so-called cosmological principle, which states that, on large scales, the universe is homogeneous and isotropic. The cosmological principle is not just some philosophical

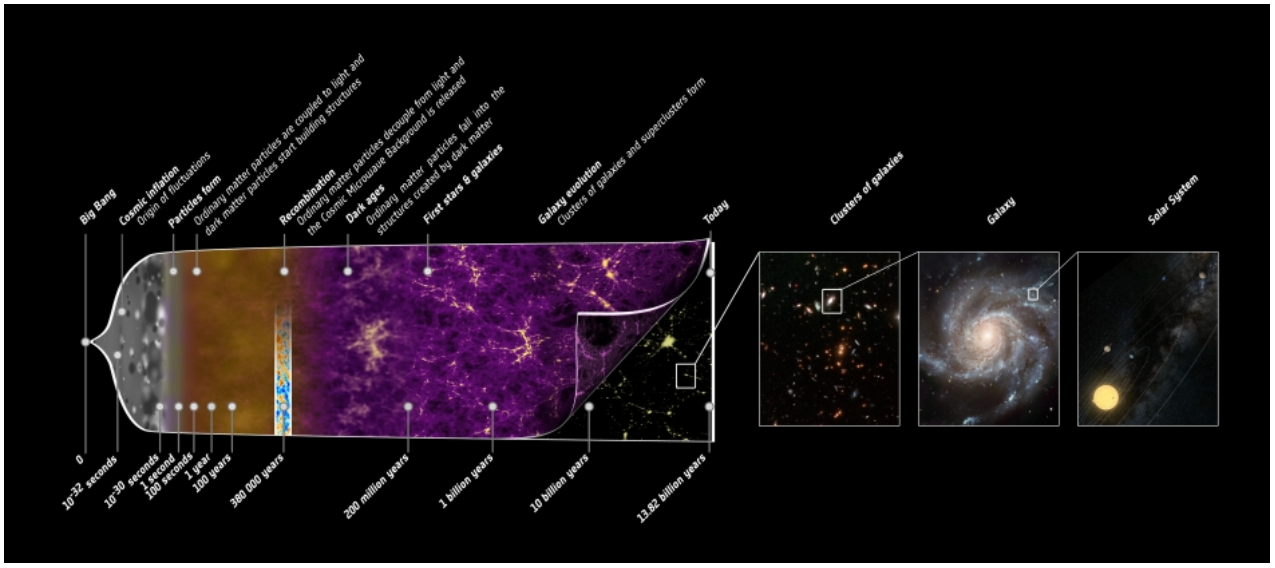

FIGURE 1.2: Sketch of the evolution of the universe (credit: NASA).

idea, but it is also confirmed by observations [39–41]. A homogeneous and isotropic universe is described by the Friedman-Lemaître-Robertson-Walker [42–45] solution of the Einstein equations [46], with line element in spherical coordinates:

$$ds^2 = -dt^2 + a^2(t)\left[\frac{dr^2}{1-kr^2} + r^2 d\Omega^2\right], \tag{1.26}$$

where t is cosmic time, r, θ, ϕ spherical polar coordinates and $d\Omega^2 = d\theta^2 + \sin^2\theta d\phi^2$. k is the curvature parameter, it has dimensions of length^{-2}. A positive k corresponds to a closed universe, $k = 0$ to a spatially flat universe and negative k to an open universe. $a(t)$ is the time-dependent scale factor. The metric can also be written in conformal form

$$ds^2 = a^2(\tau)\left[-d\tau^2 + \frac{dr^2}{1-kr^2} + r^2 d\Omega^2\right], \tag{1.27}$$

which defines conformal time as $d\tau = dt/a(t)$. The coordinates r, θ and ϕ are called comoving coordinates: particles that are at rest in these coordinates, will remain at rest. If we take two comoving particles, with comoving distance $d_{\rm com}$, the *physical* distance $d_{\rm phys}$ between these two particles is given by

$$d_{\rm phys}(t) = a(t) d_{\rm com}\,. \tag{1.28}$$

Since $d_{\rm com}$ remains constant, the physical distance between the two particles increases if the universe is expanding ($\dot{a}(t) > 0$):

$$\dot{d}_{\rm phys}(t) = \frac{\dot{a}(t)}{a(t)} d_{\rm phys}(t) \equiv H(t) d_{\rm phys}(t)\,. \tag{1.29}$$

This relation is known as the Hubble-Lemaître law [43, 47] and $H(t)$ as the Hubble parameter. The value of the Hubble parameter today is denoted as H_0. If we let d_{phys} denote the physical distance between two galaxies instead of two particles, we see that galaxies move away from each other with increasing velocity, which has also been confirmed by observations [47].

The evolution of the scale factor $a(t)$ depends on the energy content of the universe. We model the matter and energy in the universe as a perfect fluid with energy density ρ and pressure P. It will be convenient to define the equation of state parameter w

$$w \equiv \frac{P}{\rho} \,. \tag{1.30}$$

The equations of state for matter, radiation and vacuum energy (cosmological constant) are shown in table 1.1. Plugging the energy-momentum tensor of the perfect fluid into the Einstein equation, we obtain the two Friedmann equations

$$H^2 = \frac{\rho}{3m_{\text{pl}}^2} - \frac{k}{a^2} \,, \tag{1.31}$$

$$\frac{\ddot{a}}{a} = -\frac{1}{2m_{\text{pl}}^2}\left(\frac{\rho}{3} + P\right) \,. \tag{1.32}$$

From energy-momentum conservation, $\nabla_\nu T^{\mu\nu}$, we obtain a continuity equation

$$\dot{\rho} + 3H(\rho + p) = 0 \,, \tag{1.33}$$

which can be used instead of the second Friedmann equation. The continuity equation gives us a relation between the energy density and the scale factor

$$\rho \propto a^{-3(1+w)} \,, \tag{1.34}$$

which depends on the equation of state w. In reality, the universe consists of components with different equations of state and the total energy density is the sum of these components. The dominant contribution to the energy density then determines the dependence on the scale factor. Solving eq. (1.31) with $k = 0$ [4], for the dominant constituent gives the time-dependence of the scale factor

$$a(t) \propto \begin{cases} t^{2/3(1+w)} & w \neq -1 \,, \\ \exp Ht & w = -1 \,. \end{cases} \tag{1.35}$$

[4] Observations show that the energy density associated to curvature is small: $\Omega_k \equiv -\frac{k}{H^2a^2} = 0.001 \pm 0.002$ [34]. Setting $k = 0$ is thus a good approximation.

	w	$a(t)$	$\rho(a)$
Matter	0	$t^{2/3}$	a^{-3}
Radiation	$\frac{1}{3}$	$t^{1/2}$	a^{-4}
Vacuum energy	-1	$\exp Ht$	a^0

TABLE 1.1: Equation of state, time-dependence of the scale factor and scale-factor-dependence of the energy density for matter, radiation and vacuum energy.

Table 1.1 shows the dependence of the energy density on the scale factor and the time-dependence of the scale factor for matter, radiation and vacuum energy.

The very early universe has a temperature that is much larger than the masses of the SM particles[5]. As a consequence, all particles are relativistic and radiation is thus the main contribution to the energy density. The scale factor evolves as $a \propto t^{1/2}$. As table 1.1 shows, the energy density in radiation decreases faster with the expansion of the universe than the energy density in matter. When the universe is approximately 60,000 years old, at a temperature of $T = 0.75$ eV, the energy density in matter becomes equal to the energy density in radiation. The matter-dominated expansion $a \propto t^{2/3}$ persists until the energy density in matter has diluted to ρ_Λ, the energy density of dark energy. This happens when the universe is about 9×10^9 years old, at $T = 0.33$ meV. Since then, the universe has been in a phase of accelerated expansion.

1.2.2 Standard Hot Big Bang Cosmology

The original Hot Big Bang (HBB) model [48, 49] describes the evolution of a universe that started in a very hot and dense state. Even though the model was later complemented with a period of inflation that preceded Hot Big Bang evolution, this should not affect the predictions of HBB cosmology. We will thus start our description of the evolution of the universe in the HBB model and find out why the inflationary phase was introduced along the way.

We will focus on processes involving SM particles, but we stress that HBB evolution does not apply to SM physics only. There are strong indications (e.g. DM and neutrino oscillations) that the SM is not complete. Any BSM degrees of freedom can be incorporated into the HBB model, as long as the BSM physics does not spoil the successful predictions of HBB. The BBN and CMB data are thus useful tools to constrain BSM physics.

[5]Since we have set $k_B = c = 1$, we can express temperature and mass in units of energy. A temperature of 1 eV corresponds to $T = 1.16 \times 10^4$ K.

1.2.2.1 Plasma of relativistic particles

The HBB evolution starts at some high temperature T at which the Higgs potential is dominated by finite-temperature contributions, such that it only has a minimum at $\varphi = 0$ (more about this in section 5.2). All SM particles are thus massless and relativistic[6,7]. The universe is radiation-dominated, with energy density

$$\rho = \frac{\pi^2}{30} g^*(T) T^4 \,, \tag{1.36}$$

where g^* is the total number of relativistic degrees of freedom. The SM particles can exchange momentum and energy efficiently, since interaction rates Γ are large with respect to the Hubble parameter H. If $\Gamma \gg H$ holds for a certain reaction

$$A + B \leftrightarrow C + D \,, \tag{1.37}$$

the particles are said to be in chemical equilibrium, which sets a relation between the chemical potentials

$$\mu_A + \mu_B = \mu_C + \mu_D \,. \tag{1.38}$$

In the early universe, particles that have a large number density typically have very small chemical potentials that can be neglected [37, 38]. A relativistic particle i that is in chemical equilibrium has the following number density

$$n_i = \frac{\zeta(3)}{\pi^2} g_i T^3 \begin{cases} 1 & \text{bosons}\,, \\ \frac{3}{4} & \text{fermions}\,, \end{cases} \tag{1.39}$$

where g_i is the number of internal degrees of freedom of species i.

1.2.2.2 Electroweak phase transition and annihilation

Combining eq. (1.36) with the scale-factor dependence of the energy density in a radiation-dominated universe, we see that the temperature T decreases as $T \propto a(t)^{-1}$. When the temperature reaches $T \approx 100\,\text{GeV}$ the finite-temperature contributions to the Higgs potential become small enough such that the potential obtains the Mexican-hat shape described in section 1.1.3. The vev transitions

[6] The SM particles would also be relativistic if the Higgs field would have a nonzero vev, as long as $T > m$.

[7] Technically, the temperature at which HBB evolution starts is only constrained by Big Bang Nucleosynthesis (see section 1.2.2.3) to be above a few MeV. For this relatively low temperature, the Higgs is already in its broken phase and the SM particles are massive. However, most inflationary models end in a thermal state with a temperature many orders of magnitude above $\mathcal{O}(1\,\text{MeV})$. In our description we will assume that this is the case.

from $\varphi = 0$ to $\varphi \neq 0$ and the SM fermions and W- and Z-bosons become massive. This is referred to as the Electroweak Phase Transition (EWPT).

Once the particles become massive, the top quark becomes non-relativistic, since $T \lesssim m_t$. Its number density then gets Boltzmann-suppressed due to annihilations of top quarks and anti-top quarks. The equilibrium number density of a nonrelatvistic particle i is given by

$$n_i = g \left(\frac{m_i T}{2\pi} \right)^{3/2} \exp \left[\frac{\mu_i - m_i}{T} \right] . \tag{1.40}$$

Soon after top-antitop annihilation, the Higgs boson and the W- and Z-bosons become non-relativistic and annihilate as well, followed by the bottom and charm quarks and the tau lepton. The temperature lowers further to $T \approx 150\,\mathrm{MeV}$, the temperature of the QCD phase transition [50]. Below this scale, quarks and gluons are confined to baryons (consisting of three quarks) and mesons (consisting of a quark-antiquark pair). The baryons and mesons become immediately nonrelatvistic during the phase transition and thus get Boltzmann-suppressed, except for the light pions. At a slightly lower temperature, the pions and muons annihilate as well. At a temperature of a few MeV all SM particles are still in chemical equilibrium and most of them are Boltzmann suppressed. If this equilibrium would persist forever, all massive particles would eventually annihilate and the universe would be filled with photons only. Fortunately, chemical equilibrium is disturbed when the weak interaction freezes out and light nuclei are formed in Big Bang Nucleosynthesis.

1.2.2.3 Big Bang Nucleosynthesis

Big Bang Nucleosynthesis [49, 51] describes the formation of light elements in the early universe. Recent reviews of BBN can be found in Refs. [52–55].

At a temperature of a few MeV neutrons n and protons p are non-relativistic and their interactions with electrons and neutrinos

$$p + e \leftrightarrow n + \nu_e \,, \tag{1.41}$$

(and the interactions that are related by crossing symmetry) are in equilibrium. As the chemical potentials of electrons and neutrinos are negligible at this stage, chemical equilibrium implies $\mu_n = \mu_p$ and the neutron-to-proton ratio is given by

$$\frac{n_n}{n_p} = \left(\frac{m_n}{m_p} \right)^{3/2} \exp \left[-\frac{m_n - m_p}{T} \right] . \tag{1.42}$$

If equilibrium persisted forever, the number density of neutrons would drop to zero. This does not happen, since the weak interaction becomes too slow to compete with the expansion of the universe around $T \approx 1$ MeV (step 1 in figure 1.3). The neutron-to-proton ratio then remains constant up to neutron decay:

$$\frac{n_n}{n_p} = \left.\frac{n_n}{n_p}\right|_{\text{freeze out}} \exp\left[-t/\tau\right], \tag{1.43}$$

with $\tau = 886.7 \pm 0.8$ s the neutron lifetime and $\left.\frac{n_n}{n_p}\right|_{\text{freeze out}}$ the value of the neutron-to-proton ratio at the instant when the weak interactions freeze out. Figure 1.3 clearly shows that the neutron abundance (light blue line) decreases much more slowly than it would in the equilibrium situation (black line). But again, if nothing would change, all neutrons would decay into protons. Fortunately, the temperature has now dropped below the nuclear binding energy ($B_D = 2.2$ MeV) of deuteron D (an isotope of hydrogen consisting of a proton and a neutron), that is formed via the reaction

$$n + p \to \mathrm{D} + \gamma\,. \tag{1.44}$$

Deuteron formation actually only becomes efficient at $T \lesssim 100$ keV, because the number density of photons is much larger than the number densities of protons and neutrons. Even though the *average* photon energy at $T \lesssim 2.2$ MeV is too small to disassociate a deuterium nucleus, there are enough photons in the energetic tail of the spectrum to block production of significant amounts of deuteron before $T \lesssim 100$ keV. As soon as deuteron becomes available, it combines with protons to form ^{3}He and subsequently ^{3}He and D form ^{4}He (formation of ^{4}He can also proceed through combination of tritium and deuteron). Since the nuclear binding energy of ^{4}He is larger than the nuclear binding energy of deuteron and tritium, the abundance of ^{4}He is energetically favored. As a consequence, virtually all available neutrons combine into ^{4}He, which then makes up $\sim 25\%$ of the baryonic mass. Hydrogen nuclei make up $\sim 75\%$ and there are still some small traces of other light elements (D, ^{3}He and ^{7}Li). BBN completes at a temperature of ~ 10 keV.

The predictions of light element abundances from BBN match observations very well [53]. This is one of the main triumphs of the HBB model. The success of BBN tells us that, at a temperature of a few MeV, the universe needs to be radiation-dominated with SM particles in chemical equilibrium. This constrains BSM physics. Furthermore, the value of the helium-to-hydrogen ratio depends on the neutron-to-photon ratio at neutron freeze-out. The latter depends on the temperature at freeze-out and thus on the number of relativistic degrees of freedom, which puts another constraint on new physics. See Ref. [56] for other examples of BSM constraints from BBN.

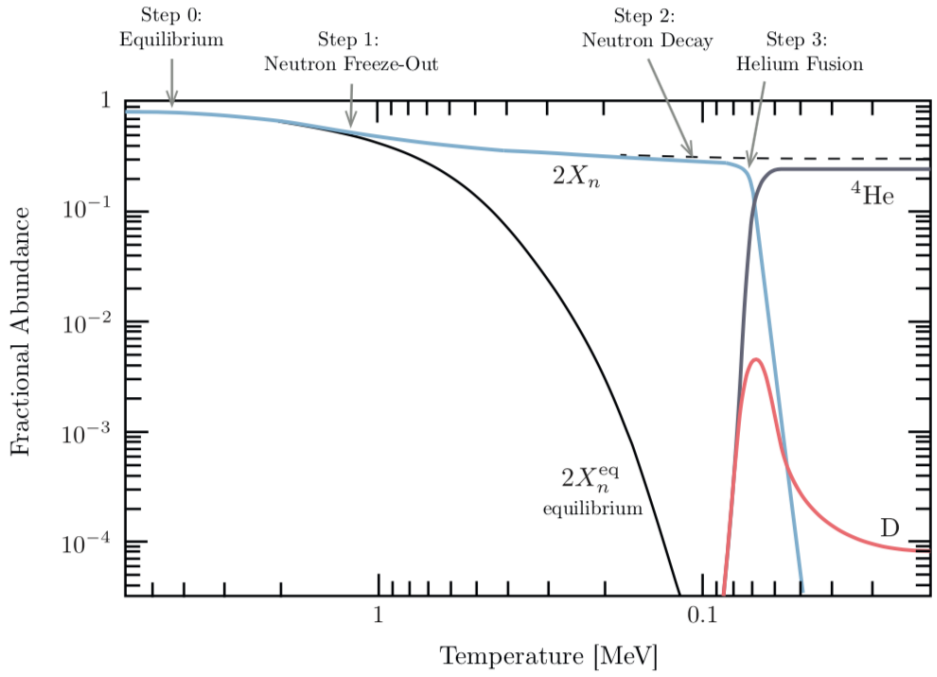

FIGURE 1.3: Numerical results for the evolution of neutron, deuteron and helium abundance. Figure copied from Ref. [38].

1.2.2.4 Recombination and photon decoupling

At a temperature of $T \approx 10$ keV, BBN has completed and the universe is filled with photons, relativistic electrons and positrons and baryons, mostly in the form of H and ^{4}He nuclei. When the temperature drops below the electron mass, electrons and positrons become non-relativistic and their density becomes Boltzmann-suppressed. Despite Boltzmann suppression, Thomson scattering between photons and electrons

$$e + \gamma \leftrightarrow e + \gamma \,, \tag{1.45}$$

is in equilibrium, such that the universe is still opaque. Neutral hydrogen and helium do not yet form, as the temperature is above the atomic binding energies. As the temperature drops, neutral helium forms first, as it has the larger atomic binding energy. The atomic binding energy of hydrogen is 13.6 eV, but as in the case of deuteron above, the formation of neutral hydrogen becomes efficient at a lower temperature $T \approx 0.3$ eV, because of the relatively large number density of photons. The formation of neutral atoms from free electrons and nuclei is called 'recombination'.

During recombination, the number density of free electrons drops dramatically. At $T \approx 0.27$ eV the number density of free electrons has become so small that the interaction rate for Thomson scattering drops below the expansion rate H. When this interaction freezes out, photons are no longer coupled to the primordial plasma. This implies that the universe becomes transparent to

photons and they start to stream freely. These photons, that last interacted with the primordial plasma when the universe was about 380,000 years old, are observed today as the Cosmic Microwave Background (CMB) radiation.

The existence of background radiation as a consequence of HBB evolution was first predicted by Alpher and Herman in 1948 [57]. It was discovered by Penzias and Wilson in 1964 [58] and has become a very important probe of the early universe. Over the past decades, it has been measured with ever increasing accuracy [34, 59, 60]. The background radiation has a blackbody spectrum with a very uniform temperature $T_{\mathrm{CMB}} = 0.23\,\mathrm{meV}$ (or $T_{\mathrm{CMB}} = 2.7\,\mathrm{K}$) . There are, however, small temperature fluctuations, that form the seeds of stars and galaxies that start to form later.

Even though the detection of the CMB corroborates the HBB model, the fact that it is so homogeneous also indicates that the HBB model is not complete, as we will see in section 1.2.3.

1.2.2.5 Intermezzo: asymmetry between baryons and antibaryons

In our description of BBN and recombination we tacitly assumed that our universe has a baryon asymmetry: it contains more baryons (matter) than antibaryons (antimatter). As a result, before the QCD phase transition, the number density of quarks is slightly larger than the number density of antiquarks. After the phase transition, the quarks and antiquarks combine into baryons and a slightly smaller amount of antibaryons. As the (anti)baryons become immediately non-relativistic, baryons and antibaryons start to annihilate. The slight excess of baryons prevents these annihilations to complete and some nonzero baryon number remains. These leftover baryons, which have a number density that is much smaller than the number density of photons, eventually end up in neutral hydrogen and helium.

BBN and CMB observations are two independent methods to determine the value of the baryon asymmetry [61]. The value of the baryon asymmetry determines T_{BBN}, the temperature at which the production of light elements starts. The final abundances depend on the initial neutron-to-proton ratio, which is determined by T_{BBN}. To determine the abundances of light elements for a given value of the baryon asymmetry one needs to solve a coupled set of Boltzmann equations. By comparing the predicted abundances to the observed values, the correct value of the baryon asymmetry can be determined. Alternatively, the value of the baryon asymmetry can be obtained from the angular power spectrum of the CMB [62].

The origin of the baryon asymmetry is unknown. Since the SM can not explain the value of the observed asymmetry, this is a strong hint for BSM physics. Part II of this thesis focuses on electroweak baryogenesis, a mechanism in which the baryon asymmetry is generated during the electroweak phase transition. For an introduction into the generation of the baryon asymmetry, with a focus on electroweak baryogenesis, see chapter 5.

1.2.2.6 Structure formation

The small temperature fluctuations observed in the CMB correspond to slightly overdense and underdense regions. Due to gravity, matter collapses onto the overdense regions, which then become even denser. The overdense regions form the seeds of stars and galaxies. The first stars formed when the universe was approximately 700 million years old [63]. An overview of galaxy formation can e.g. be found in Ref. [64].

1.2.3 Shortcomings of the HBB model

The predictions of the abundances of light elements were already a success of the Hot Big Bang model, but especially the confirmation of the existence of a CMB lead to the acceptance of the HBB model as the correct description of the history of the universe (during the '50s there was a fierce debate between supporters of the HBB model and supporters of the Steady State Theory [65, 66]).

The HBB seems a very good model for the description of the early universe, but it has two main issues: the horizon problem and the flatness problem.

1.2.3.1 Horizon problem

Let's ask the following question: how far could a light ray, emitted at t_i, the time of the beginning of Hot Big Bang evolution, have travelled at the time of photon decoupling, t_{CMB}? At t_{CMB}, this is the largest distance over which information could have been exchanged within the lifetime of the universe. This distance is called the 'particle horizon', R_p.

We take a light ray moving in the radial direction: $\theta = \phi = 0$. Light rays travel along null geodesics, so $dr = \pm\frac{1}{a(t)}dt$. The physical distance that the light ray could have travelled is thus

$$R_p = a(t_{\mathrm{CMB}}) \int_{t_i}^{t_{\mathrm{CMB}}} \frac{1}{a(t)} dt = a(t_{\mathrm{CMB}}) \int_{\ln a_i}^{\ln a_{\mathrm{CMB}}} \frac{d(\ln a)}{aH} \approx \frac{2}{1+3w} (H(t_{\mathrm{CMB}}))^{-1} \,. \tag{1.46}$$

We assumed the same equation of state throughout (this is not completely correct, as the universe becomes matter-dominated before recombination, but this is a small effect and it does not change the main point) and in the last step neglected the contribution from the lower bound on the integral. We can do this if $1 + 3w > 0$, which holds for all matter sources that we have so far encountered in HBB evolution. The length scale $(aH)^{-1}$ is called the 'comoving Hubble radius' (or comoving Hubble horizon). For standard HBB cosmology it is approximately equal to the (comoving) particle radius, but this is not true in general.

The horizon problem is the following [67]: comparing any two points on the CMB map, the differences in the temperature are as small as $\frac{\delta T}{T} = 10^{-5}$, suggesting that all regions had been in causal contact at the time of recombination. However, using eq. (1.46) to compute the particle horizon at that time, one finds that patches larger than 1 squared degree on the CMB map were not causally connected at the time of recombination! How did the temperature of the universe become so homogeneous?

1.2.3.2 Flatness problem

The first Friedmann equation (1.31) contains a contribution from the spatial curvature k. So far, we did not pay much attention to this contribution, since observations show that it is small: $\Omega_k \equiv -\frac{k}{a^2H^2} = 0.001 \pm 0.002$ [34].

For matter satisfying $1 + 3w > 0$, Ω_k *increases* as the universe expands. To get a small value of Ω_k today, the value of Ω_k in the early universe had to be extremely small. The value of Ω_k needs to be tuned by $\sim \mathcal{O}(10^{-60})$ (the exact amount of tuning depends on the initial temperature) [68]. The requirement of such a large amount of fine-tuning to explain the small value of the spatial curvature is called the flatness problem.

The horizon problem and the flatness problem both concern the initial conditions of the HBB evolution. In principle, the spatial curvature and fluctuations in the temperature could be tuned to match the values that are observed today. The enormous amount of fine-tuning would be a very unattractive feature of the HBB model. It turns out that a period of inflation prior to the HBB evolution can solve the flatness and horizon problems, without further modifications to the HBB model.

1.2.4 Inflation

Both the horizon and flatness problem could be solved if, before the standard HBB evolution starts, there is a phase in which the comoving Hubble horizon $(aH)^{-1}$ decreases. For such a phase, the *lower* bound in the integral of eq. (1.46) dominates and the particle horizon becomes much larger than the value from HBB. During this phase the value of Ω_k *decreases* such that the small value of Ω_k does no longer require fine-tuning. We call this phase *inflation* [69–71]. Readers that want to read more about inflation than this very brief introduction can for example consult Refs. [36, 38, 72, 73].

A phase of decreasing comoving Hubble horizon is equivalent to a phase of accelerated expansion

$$\frac{d}{dt}(aH)^{-1} < 0 \iff \ddot{a} > 0\,. \tag{1.47}$$

This also implies that the fractional change of H per e-fold N (an increase of the scale factor by a factor e) is small

$$\frac{d}{dt}(aH)^{-1} < 0 \iff \epsilon < 1\,, \qquad \text{where}\, \epsilon \equiv -\frac{\dot{H}}{H^2} = -\frac{d\ln H}{dN}\,. \tag{1.48}$$

Assuming that the energy scale of the universe at the end of inflation is $\sim 10^{15}$ GeV, it can be shown that inflation solves the hierarchy and flatness problems if the scale factor grows by at least a factor $\sim 10^{28}$ between the beginning I and end E of inflation [8]

$$\frac{a_I}{a_E} \gtrsim 10^{28} \rightarrow N = \ln\frac{a_I}{a_E} \gtrsim 64. \tag{1.49}$$

Note that this is only a lower bound on the duration of inflation.

We have seen above that matter with an equation of state satisfying $1 + 3w > 0$ will not lead to a decreasing comoving Hubble horizon. Instead we need some source of energy density with negative pressure

$$w = \frac{P}{\rho} < -\frac{1}{3}\,. \tag{1.50}$$

In eq. (1.35) and table 1.1 we have already seen an example of matter satisfying the condition $w < -1/3$: vacuum energy has an equation of state $w = -1$, leading to $a \propto \exp Ht$, a deSitter universe. The inflationary phase should however not be exactly deSitter, because inflation has to

[8] If inflation happens at a much lower scale, for example the electroweak scale, the required amount of e-folds of expansion is smaller.

end and allow for HBB evolution. Fortunately, there are other ways of to generate an inflationary phase. We will focus on the one that is most widely used.

1.2.4.1 Scalar field inflation

A phase of accelerated expansion occurs when the energy density is dominated by a homogeneous scalar field $\chi(t)$ moving in a flat potential $V(\chi)$. The energy density and pressure of the inflaton field χ are

$$\rho = \frac{1}{2}\dot{\chi}^2 + V(\chi)\,, \qquad P = \frac{1}{2}\dot{\chi}^2 - V(\chi)\,, \tag{1.51}$$

and the equation of motion

$$\ddot{\chi} + 3H\dot{\chi} + V_{,\chi} = 0\,, \tag{1.52}$$

with the subscript $_{,\chi}$ denoting a derivative with respect to the χ-field. By plugging the energy density and pressure of the inflaton into the Friedmann equations, we find that $\dot{H} = -\dot{\chi}^2/(2m_{\rm pl})^2$. Substituting into eq. (1.48) gives

$$\epsilon = \frac{\frac{1}{2}\dot{\chi}^2}{m_{\rm pl}^2 H^2}\,. \tag{1.53}$$

Remembering that $m_{\rm pl}^2 H^2 = \rho/3$, we find that the requirement $\epsilon < 1$ is satisfied if the kinetic energy is smaller than 1/3 of the full energy density, or

$$\dot{\chi}^2 < V(\chi)\,, \tag{1.54}$$

and this indeed leads to an equation of state $w < -1/3$.

Inflation ends when ϵ becomes larger than 1. In many models, and also the ones that we study in chapters 2, 3 and 4 the inflaton then starts to oscillate at the bottom of its potential. Since inflation was introduced to solve the problems of the initial conditions of the HBB model, but not to replace it, we should connect the end state of inflation to the beginning of HBB evolution. The energy density of the inflaton field has to be transferred to the particles of the SM that then thermalize. This process is called reheating and is the subject of the first part of this thesis. It will be introduced more extensively in chapter 2.

1.2.4.2 Fluctuations and CMB constraints

Besides solving the horizon and flatness problems, inflation can also explain the small fluctuations

that are observed in the CMB and that eventually formed stars and galaxies. The temperature fluctuations correspond to fluctuations in the energy density that are caused by quantum fluctuations in the inflaton field [74].

The fluctuations in the CMB can be described by their power spectrum. The measured amplitude of the fluctuations and the scale dependence of the power spectrum can be used to constrain models of inflation [72, 73, 75]. Furthermore, the non-detection of tensor modes puts an upper bound on the value of the Hubble parameter during inflation [76, 77].

It is a remarkable fact that even the simplest models, where inflation is caused by a single scalar field, can correctly predict the power spectrum of fluctuations as observed in the CMB [77]. There are many different models for scalar field inflation [78]. In chapter 3 we will not stick to a specific model, but in chapter 4 we will study the case where the Higgs is the inflaton.

1.3 Outline of this thesis

In this thesis we focus on two stages of the early universe. The topic of Part I is reheating: the phase connecting inflation to HBB evolution. In chapter 2 we show why studying the reheating phase is interesting and sketch how the energy of the inflaton field is transferred to SM particles. Chapter 3 addresses a problem that arises from the running of the Higgs self-coupling λ, which becomes negative at energy scales above 10^{11} GeV. Efficient production of Higgs modes during preheating would cause the Higgs field to end up in an energetically favorable vacuum at $\varphi \gg 246\,\mathrm{GeV}$, which is in contradiction with observations. In chapter 4 we study reheating after inflation caused by the Higgs field. We focus on production of Higgs modes and gauge modes, as these are most efficiently produced.

The topic of Part II is electroweak baryogenesis. Chapter 5 sums up the necessary conditions for baryogenesis. We then show how the baryon asymmetry can be obtained during the electroweak phase transition and give an overview of the computation of the baryon asymmetry. The central question of chapter 6 is whether electroweak baryogenesis can be studied in the framework of the Standard Model Effective Field Theory. We focus on the contribution from top quarks to the baryon asymmetry, but find that this does not result in a value of the baryon asymmetry that is consistent with observations. In chapter 7 we will then study the importance of leptons for generating the baryon asymmetry.

Part I

Reheating the universe after inflation

Chapter 2

Introduction to reheating

Immediately after the end of inflation, the dominant constituent of the universe is the inflaton field that is oscillating at the bottom of its potential. The densities of all other particles have been diluted to practically zero during inflation. We have seen in the introduction that inflation should connect to standard HBB cosmology. The energy of the inflaton field must be transferred to the SM degrees of freedom. The successful predictions of BBN give a lower bound on the energy scale at which this transition needs to be complete. To explain BBN, the universe needs to be radiation-dominated and the SM particles in chemical equilibrium at $T_{\rm BBN}$. We therefore know that the transfer of energy from the inflaton field to the SM particles, as well as their thermalization, must have completed before the era of Big Bang Nucleosynthesis.

The process of energy transfer from the inflationary sector to the standard model particles and the subsequent thermalization, is referred to as reheating. In early studies of reheating it was assumed that the inflaton decays into SM particles through perturbative interactions [79–81]. It was realized in Refs. [82–89] that the coherent oscillations of the inflaton field can lead to a phase of resonant particle production. This phase is referred to as the preheating stage. For some inflationary models, preheating is so efficient that the inflaton field can transfer all of its energy during this stage. In other cases some early resonant energy transfer takes place, but perturbative decays are needed for reheating to complete.

In this introductory chapter we will first motivate why the reheating phase is interesting to study. We will then lay out some basics of particle production.

2.1 Why is studying reheating important?

Even though the reheating phase can not be probed directly, it is an interesting phase to study, for a variety of reasons.

2.1.1 Reheating temperature

The end state of reheating is a universe filled with SM particles in equilibrium (as we will see below, DM might be produced during reheating as well). Typically, the reheating temperature, $T_{\rm reh}$, is estimated from the energy density at the end of reheating, $\rho_{\rm reh}$, through the relation

$$\rho_{\rm reh} = \frac{\pi^2}{30} g_*(T_{\rm reh}) T_{\rm reh}^4 \,, \tag{2.1}$$

where $g_*(T_{\rm reh})$ is the number of relativistic degrees of freedom at the reheating temperature.

As mentioned above, the value of the reheating temperature is constrained by the predictions of Big Bang Nucleosynthesis (see section 1.2.2.3). Taking the temperature at which BBN took place as a lower bound on the reheating temperature gives $T_{\rm reh} > T_{\rm BBN} \approx 1\,\text{MeV}$. When the effect of the relic neutrino background on the abundances of light elements is taken into account, the constraint becomes slightly stronger: $T_{\rm reh} \gtrsim 4\,\text{MeV}$ [90, 91].

2.1.2 Expansion rate after inflation

In section 1.2.1 we introduced the equation of state parameter w

$$w = \frac{P}{\rho} \,, \tag{2.2}$$

which determines the time-dependence of the scale factor and the dependence on the scale factor of the energy density.

Since the Hubble parameter is defined as the logarithmic derivative of the scale factor, the above relation determines how the comoving size of the horizon or inverse Hubble scale $(aH)^{-1}$ depends on the scale factor a. The (smallest) momentum scale k of the modes of the fluctuations in the CMB that are observed today is given by the current value of the Hubble scale: $k = a_0 H_0$. The amplitude of this mode was set when it became superhorizon during inflation, which happened when the momentum was equal to the Hubble scale during inflation: $k = aH$.

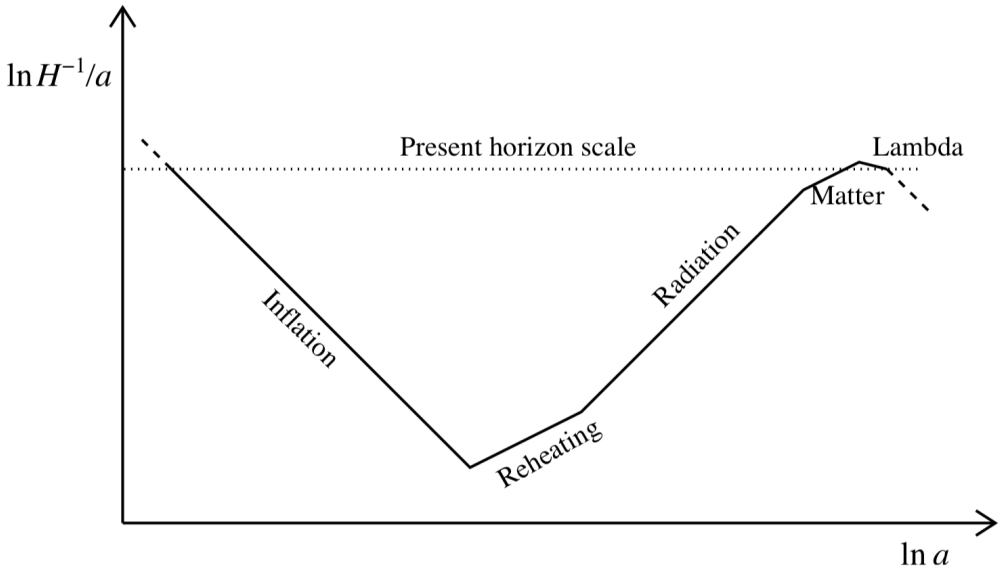

FIGURE 2.1: The logarithm of the Hubble scale as a function of the scale factor during and after inflation, illustrating how the dependence of the Hubble scale on the scale factor varies for the different epochs. The dashed lines show extrapolations to the past and future. Figure copied from Ref. [92].

For a given model of inflation, the local properties of the potential can be determined from observations of the CMB. In order to use CMB-observables to constrain inflationary models, one must know at what moment during inflation the perturbations that are observed today were formed. This moment determines the value of the inflationary potential, which in turn gives the values of the observable primordial tilt and tensor-to-scalar ratio. To find this moment during inflation, the expansion history after inflation should be known. Knowing the equation of state *after* inflation tells us how many e-folds passed since the end of inflation until now. This determines the amount of e-folds between the generation of the perturbation at $k = aH$ and the end of inflation, as is clearly explained in Refs. [92, 93]. This is illustrated in figure 2.1, that shows the expansion history during the different epochs (with different equations of state) that the universe went through.

The equation of state during reheating depends on the shape of the inflationary potential. For example, an inflaton oscillating in a quadratic potential gives rise to a matter-like equation of state $w = 0$ and an inflaton oscillating in a quartic potential to a radiation-like equation of state $w = 1/3$. When reheating completes and the universe becomes radiation-dominated, the equation of state relaxes to $w = 1/3$. The expansion history is thus affected by the shape of the potential and the duration of reheating.

Figure 2.2 shows how the uncertainty in the expansion history after inflation affects the comparison of different inflationary models to CMB-observables. The small dots show the predictions for the

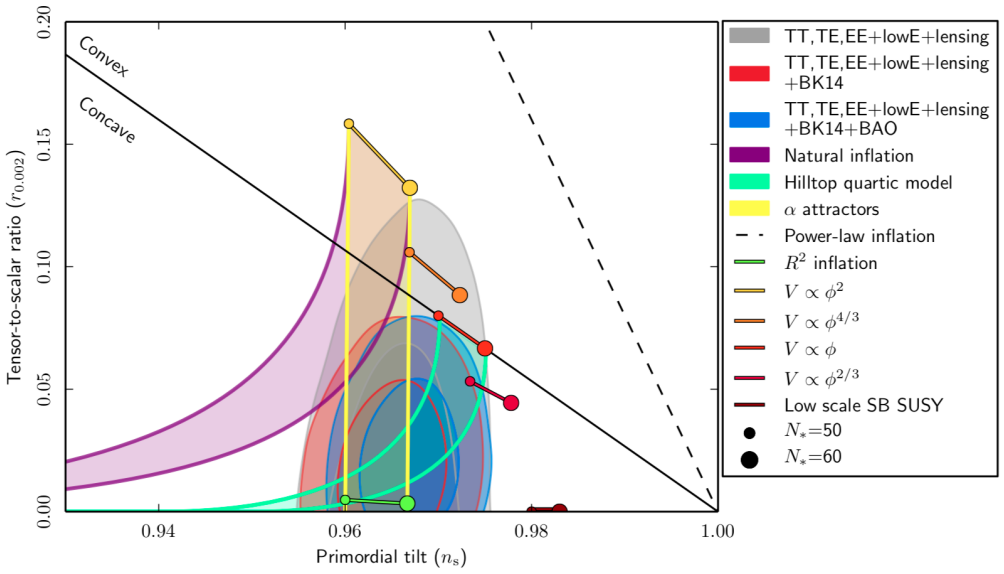

FIGURE 2.2: 68% and 95% confidence level regions for the primordial tilt n_s and tensor-to-scalar ratio r at $k = 0.002\,\mathrm{Mpc}^{-1}$ from *Planck* 2018 data alone (gray regions) and in combination with BICEP2/Keck Array 2014 data (red regions) and BICEP2/Keck Array 2014 and Baryon Acoustic Oscillation data (blue regions). The confidence intervals are compared with predictions for n_s and r for different inflationary models. Figure copied from Ref. [77].

primordial tilt n_s and tensor-to-scalar ratio r for the cases when the CMB-modes were formed 50 e-folds before the end of inflation and the large dot shows the prediction if the perturbations were formed 60 e-folds before the end of inflation. A better understanding of reheating would decrease the uncertainty in the evolution after inflation and would therefore shrink the uncertainty in comparisons like figure 2.2.

2.1.3 Higgs vacuum stability

The possible decay of the electroweak vacuum during preheating is the topic of chapter 3. In this chapter, we consider a Higgs potential with a quartic coupling that runs negative at large energy scales. This implies that the electroweak vacuum that we live in today is not the energetically favorable vacuum, but that there is a state of even lower energy, the 'true vacuum' [94–100]. Decay to this true vacuum state would lead to rapidly growing bubbles with negative cosmological constant [101–105], that would take over the entire universe, which is clearly inconsistent with the universe that we live in. We study the production of Higgs quanta during reheating – in a model where the Higgs is not the inflaton – to determine whether in that model the Higgs field decays to the true vacuum state or not. Determining whether the Higgs vacuum remains stable during reheating can be a consistency check for models of inflation and BSM physics.

2.1.4 Generation of the baryon asymmetry

There are mechanisms for generating the baryon asymmetry of the universe during reheating. One example is the class of Grand Unified Theories (GUTs), in which the $SU(3)_C \times SU(2)_L \times U(1)_Y$-symmetry group of the SM is part of a larger symmetry group above the GUT energy scale. Above this scale, quarks and leptons are part of the same multiplets, and therefore baryon number B is not a conserved quantity, which allows for the generation of baryon number. Violation of B implies that the proton is not absolutely stable. Experiments aiming to observe proton decay so far have only put lower bounds on the lifetime of the proton, which severely constrains the simplest GUT, where the SM gauge group is a subgroup of $SU(5)$ [106]. In fact, non-supersymmetric $SU(5)$ is completely ruled out by the non-detection of proton decay [107]. Other symmetry groups that are still allowed by experiment and that can also break into the SM are for example $SO(10)$ (which also contains right-handed neutrinos), E_6, E_7 and E_8. Baryogenesis in GUTs can be realized when a heavy boson X is produced nonperturbatively during the preheating phase. The baryon asymmetry is generated when the unstable particle X decays into SM particles [108, 109].

Another possibility for generating the baryon asymmetry during preheating is the Cold Electroweak Baryogenesis model [110, 111]. Here, inflation happens at the electroweak scale (which is orders of magnitude lower than the inflationary scale in most other models). B-violating electroweak sphaleron transitions are active during preheating and the baryon asymmetry is formed. When reheating ends, the temperature of the universe is so low that B-violating processes have become inefficient, such that the generated baryon asymmetry remains.

In this part of the thesis we will not consider the possibility of generating the baryon asymmetry during reheating. Part II of this thesis treats the generation of the baryon asymmetry during the electroweak phase transition, assuming that reheating has already completed.

2.1.5 Dark matter production

It should not come as a surprise that the dark matter abundance can also be generated during the reheating phase. Two examples of dark matter candidates that can be produced during reheating:

- WIMPzillas [112, 113] are very heavy ($10^{12} - 10^{16}\,\mathrm{GeV}$) nonthermal dark matter candidates that are very long-lived. At the end of inflation, these particles can be produced gravitationally or through a direct coupling to the inflaton field. Decay of WIMPzilla particles could produce cosmic rays with ultra-high energies [114].

- Scalar fields that are non-minimally coupled to gravity can be produced during reheating through tachyonic resonance [115] (see also section 2.2.3.3). If the couplings of these scalars to the SM are small, they are long lived, and can form all of the observed dark matter (and escape all direct, indirect and collider searches [116]).

2.2 Particle production during reheating

In this section we will lay out the behavior of the inflaton field after inflation and the possible particle production mechanisms. Even though the equations governing the behavior of the inflaton field and the produced particles will mostly be solved numerically in the upcoming chapters, some intuition can be gained from analytic estimates. We will present these analytical estimates for single-field inflation in the upcoming part, following the analyses of Refs. [89, 117]. Other useful reviews of particle production after inflation are Refs. [118, 119].

2.2.1 Oscillating inflaton field

The equation of motion of the inflaton field is given by:

$$\ddot{\chi} + 3H\dot{\chi} + V_{,\chi} = 0\,, \tag{2.3}$$

where χ denotes the classical background value of the inflaton and the subscript $,\chi$ a derivative with respect to the field χ. The behavior of the inflaton field depends on the details of the potential. For concreteness, we will consider a quadratic potential

$$V(\chi) = \frac{1}{2}m^2\chi^2\,, \tag{2.4}$$

which is a good approximation for many inflationary models during reheating. At the end of inflation the field oscillates with decreasing amplitude. The evolution of the inflaton field asymptotes to

$$\chi(t) = X(t)\sin(mt)\,, \qquad X(t) \propto \frac{1}{mt}\,, \tag{2.5}$$

as is shown in figure 2.3.

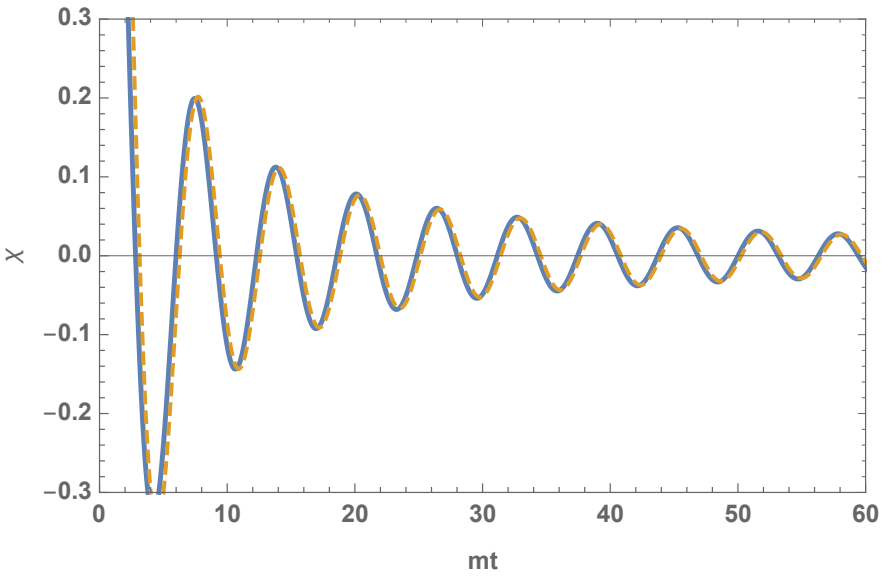

FIGURE 2.3: Numerical solution to eq. (2.3) for a quadratic potential with $m = 10^{-5} m_{\rm pl}$ (solid blue). The approximation of eq. (2.5) is shown in dashed orange.

2.2.2 Perturbative inflaton decay

Initially, particle production after inflation was described by perturbative decays of the inflaton field [80, 81]. As an example we consider an inflaton field that is coupled to a scalar field η and a spinor field ψ, with interaction term:

$$\mathcal{L}_{\rm int} = -\sigma \chi \eta^2 - h \chi \bar{\psi} \psi, \tag{2.6}$$

where σ is a mass scale and h is a dimensionless coupling. The $\sigma\chi\eta^2$-term for example arises from spontaneous symmetry breaking. Provided that the mass of the inflaton is larger than twice the mass of its decay product, the inflaton can decay into pairs of η- and ψ-particles, with the following decay rates [120]

$$\Gamma_{\chi \to \eta\eta} = \frac{\sigma^2}{8\pi m}\,, \qquad \Gamma_{\chi \to \bar{\psi}\psi} = \frac{h^2 m}{8\pi}\,. \tag{2.7}$$

Perturbative decay will only become efficient once the decay rates become comparable to the Hubble expansion rate

$$\Gamma_{\rm tot} \gtrsim H\,, \tag{2.8}$$

where $\Gamma_{\rm tot}$ is the sum of the perturbative decay rates. For realistic values of the couplings and masses, $\Gamma_{\rm tot} \ll H$ at the onset of reheating. As the universe expands, H decreases until it becomes equal to the decay rate. Using $H^2 = \frac{\rho}{3m_{\rm pl}^2}$ and eq. (2.1) gives the reheating temperature:

$$T_{\rm reh} \approx \left(\frac{90}{g_* \pi^2} \sqrt{m_{\rm pl} \Gamma_{\rm tot}} \right)\,. \tag{2.9}$$

The perturbative approach does not give a complete description of the reheating process. As we will see below, resonant particle production can be much more efficient than perturbative decays. In some cases, this so-called preheating phase is so efficient that the inflaton field rapidly transfers all of its energy before the resonance shuts off. Alternatively, the inflaton looses some of its energy during the preheating phase, but remains the dominant contribution to the energy budget of the universe when the resonance shuts off. In this case, reheating completes much later, through the perturbative decay described above.

2.2.3 Resonant particle production

The first reason why particle production can be much more efficient than the perturbative production, is that the decay of the inflaton field is a collective process – the inflaton quanta do not decay independently of each other. The second reason is that Bose condensation effects in the decay products can strongly enhance the production (this effect is not present for fermions). These effects are relevant for the initial phase of reheating, preheating. This phase should thus be studied in a non-perturbative analysis.

Let's consider production of the field η with mass m_η and coupling to the inflaton as in eq. (2.6). We first consider the regime $m_\eta > \sqrt{2\sigma X}$ [1]. In order to make analytic progress, we neglect the expansion of space, i.e. we take a=1. The mode equation of the η-field is given by

$$\ddot{\eta}_k + \left[k^2 + m_\eta^2 + 2\sigma X \sin(mt)\right] \eta_k \equiv \ddot{\eta}_k + \omega_k^2(t)\eta_k = 0\,. \tag{2.10}$$

The number density per k-mode is

$$n_k = \frac{\omega_k}{2}\left(\frac{|\dot{\eta}_k|^2}{\omega_k^2} + |\eta_k|^2\right) - \frac{1}{2}\,, \tag{2.11}$$

and the full number density n_η and energy density ρ_η can be obtained by integrating over all k-modes:

$$n_\eta = \frac{1}{2\pi^2}\int_0^\infty dk k^2 n_k\,, \qquad \rho_\eta = \frac{1}{2\pi^2}\int_0^\infty dk k^2 \omega_k n_k\,. \tag{2.12}$$

[1] If we allow $m_\eta < \sqrt{2\sigma X}$, for small k-modes the effective η-mass squared becomes negative during part of the oscillation. This is the tachyonic resonance regime that is described in section 2.2.3.3

In order to solve eq. (2.10), we make a change of variables and rewrite eq. (2.10) in the form of a Mathieu equation [121, 122]

$$\begin{aligned} &\eta_k'' + [A_k - 2q\cos 2z]\,\eta_k = 0\,, \\ &A_k = 4\frac{k^2 + m_\eta^2}{m^2}\,, \quad q = \frac{4\sigma X}{m^2}\,, \quad z = \frac{mt}{2}\,, \end{aligned} \tag{2.13}$$

where a prime denotes derivative with respect to z. The solutions to the Mathieu equation can be described by the stability and instability bands of figure 2.4. Modes with values of A_k and q lying in an instability band display exponential growth:

$$\eta_k \propto \exp\left[\mu_k z\right]\,. \tag{2.14}$$

As becomes clear from figure 2.4, the range of k-modes that gets resonantly enhanced depends on q. For small values of $q \ll 1$ only a small range of k-modes gets resonantly produced. This regime is called narrow resonance. For larger values of $q > 1$, a wider range of k-modes gets enhanced – this is called the broad resonance regime. Both cases are described below.

2.2.3.1 Narrow resonance

Narrow resonance occurs when $q \ll 1$. Only k-modes for which $A_k \approx n^2$, with n an integer, get enhanced. The first resonant band at $A_k \approx 1$ is the most important one and occurs for momenta in the range $k = \frac{m}{2}\left(1 \pm \frac{q}{2}\right)$. The rate of exponential growth for k-modes in the first instability band is given by

$$\mu_k = \sqrt{\left(\frac{q}{2}\right)^2 - \left(\frac{2k}{m} - 1\right)^2}\,. \tag{2.15}$$

The growth of the particle number density in the fastest growing mode is shown in the left panel of figure 2.5.

The well-understood picture of narrow resonance in Minkowski space does not completely carry over to an expanding universe. Due to gravitational redshift, k-modes might not remain in the instability bands for a long enough time to get exponentially enhanced. This leads to the additional requirement for resonant production:

$$q^2 m \gtrsim H\,, \tag{2.16}$$

which is typically not satisfied at the end of inflation for $q \ll 1$, such that the narrow resonance does not take off. At a later stage of reheating narrow resonance can nevertheless become important [84].

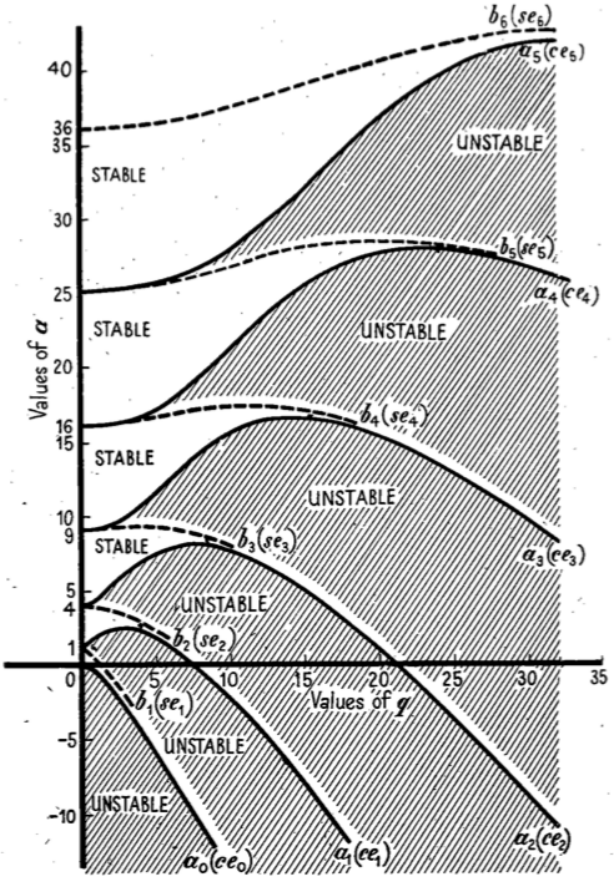

FIGURE 2.4: Stability and instability bands of the Mathieu equation (2.13). The horizontal axis shows the value of q and the vertical axis shows the value of A_k. The white regions correspond to stable solutions while the shaded areas correspond to exponentially growing solutions. Figure copied from Ref. [121].

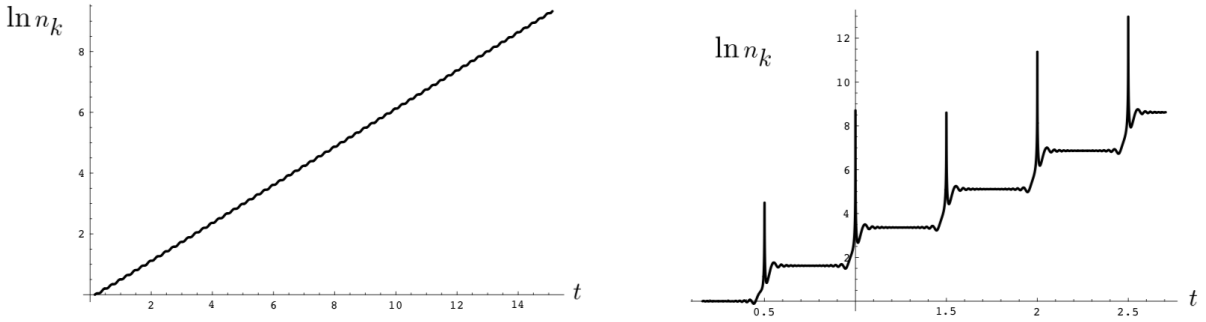

FIGURE 2.5: Number density in the fastest growing k-mode as a function of time during parametric resonance. The left panel shows narrow resonance for $q \approx 0.1$ and the right panel shows broad resonance for the potential of eq. (2.4). In both cases the expansion of spacetime is neglected. Time is shown in units of $\frac{m}{2\pi}$. Figure copied from Ref. [89].

2.2.3.2 Broad resonance

It is clear from figure 2.4 that the gray instability bands become wider for $q > 1$. This is therefore called the broad resonance regime. In this regime, particle production is typically very efficient. Modes with momentum k get resonantly produced when the adiabaticity condition

$$\frac{d\omega_k}{dt} \gtrsim \omega_k^2 \,, \tag{2.17}$$

is violated. In our toy model, these bursts of particle production happen when the (inflaton-dependent) mass of the decay product becomes very small, as the inflaton field crosses zero. In chapter 4 we will see an example of particle production where the violation of adiabaticity is not caused by a small mass, but by the derivative of the mass becoming large. The right panel of figure 2.5 shows the time dependence of the particle number density in the broad resonance regime. In contrast to the narrow resonance case, particles are only produced when $\chi(t) \approx 0$ and the number density remains approximately constant between two subsequent bursts. An analytic treatment of broad resonance in a static spacetime can be found in Refs. [89, 117].

Again, taking the expansion of the universe into account, the picture changes. Since the amplitude of the inflaton field now decreases with time, q decreases and the resonance becomes more narrow. Explosive particle production can however still occur. The theory of broad resonance in an expanding universe is called 'stochastic resonance'. We will not pursue it any further in this introduction, since we will solve our mode equations numerically in the upcoming chapters.

2.2.3.3 Tachyonic resonance

The narrow and broad resonance cases described above correspond to the regime $A_k \leq 2q$. In this regime ω_k^2 is always positive and (in the broad resonance case) particle production occurs when eq. (2.17) is satisfied. If we drop the condition that $m_\eta > \sqrt{2\sigma X}$, k-modes with

$$k^2 < 2\sigma X - m_\eta^2 \,, \tag{2.18}$$

have $\omega_k^2 < 0$ during part of the oscillation. The 'tachyonic resonance' that occurs during this period can be extremely efficient [123–126]. An extensive analytical and numerical study of tachyonic preheating is given in Ref. [124]. Tachyonic resonance can occur in theories with trilinear couplings,

like our example eq. (2.6), but also for fields coupling to the spacetime Ricci tensor R, as we will see in chapter 3.

Chapter 3

Electroweak stability and non-minimal coupling

3.1 Introduction

No evidence for physics beyond the Standard Model has been found so far at the Large Hadron Collider or any other experiment. This opens up the possibility that the SM is valid up to a very high energy scale (for example the GUT scale). If true, our universe might be metastable. Indeed, with the particle content of the SM, the Higgs quartic coupling λ runs to negative values at large energy scales, and the Higgs potential develops a second minimum in addition to the electroweak minimum. For the best fit values of the top quark and Higgs mass the quartic Higgs coupling becomes zero $\lambda(\mu_{\rm cr}) = 0$ at a scale $\mu_{\rm cr} \sim 10^{11}$ GeV, although stability of the SM up to the Planck scale is only excluded at the 2-3σ level [94–100]. In this chapter we take the instability of the Higgs potential at face value, and consider its cosmological consequences.

The presence of the global minimum at large field values poses no danger at present as the metastable vacuum can only decay via a slow tunnelling process, and has a lifetime that is much longer than the age of the universe. Within a cosmological context the longevity of our vacuum is no longer assured. If the Hubble scale H during inflation is comparable to or larger than the maximum of the Higgs potential, then vacuum decay is no longer suppressed as the Higgs field can quantum fluctuate over the potential barrier [101–105]. This is a concern for large field inflationary models such as chaotic inflation and Starobinsky type inflation. It was pointed out that stability during inflation can be ensured if one includes a (positive) non-minimal coupling ξ between the Ricci scalar and the Higgs field $\mathcal{L} \supset \frac{1}{2}R(m_{\rm pl}^2 - 2\xi\Phi^\dagger\Phi)$ [127–129], as this induces an effective stabilizing Higgs mass. The vacuum is stable during inflation if $\xi \gtrsim 3/8$, but even smaller couplings $\xi \gtrsim 0.01$ are admissible

depending on post-inflationary evolution [128]. The non-minimal coupling to gravity is allowed by all symmetries, in fact such a term will be generated by loop effects, although it is not clear whether it will have the right sign and size (in chapter 4 we will see that the same coupling with a different sign can lead to completely different behavior).

This is not the end of the story though. After inflation, as the inflaton starts oscillating at the bottom of its potential, production of Higgs particles can be very efficient. The effective Higgs mass, induced by the non-minimal coupling, oscillates between positive and negative values, leading to tachyonic resonance. The produced Higgs quanta contribute to the effective Higgs mass and the energy momentum tensor — this is similar to temperature corrections in a thermal bath, although the Higgs spectrum is highly non-thermal — and both effects can affect vacuum stability [130]. Preheating is efficient if

$$q_0 \equiv \frac{3}{4}\left(\xi - \frac{1}{6}\right)\frac{\chi_0^2}{m_{\rm pl}^2} \gtrsim \mathcal{O}(5), \tag{3.1}$$

with χ_0 the inflaton field value at the end of inflation. In this case particle production is explosive, and within a few inflaton oscillations the produced quanta will completely dominate the Higgs mass. As this all happens at high scales $H > \mu_{\rm cr}$ the quantum contribution to the effective mass is negative and destabilizes the vacuum [130–134].

For smaller q_0-values results are less clear, and there is no consensus in the literature on the fate of our vacuum, mainly because different criteria for stability are used [130–134]. Even though in this case particle production is not efficient enough initially to destabilize the vacuum, this may still happen eventually as the classical potential redshifts away faster than the quantum corrections due to Higgs production. If the Higgs mass is dominated by the production term only after the Hubble scale has dropped below the critical value $H < \mu_{\rm cr}$, the quantum contribution to the effective mass is positive around the maximum of the potential, and thus will only raise the barrier separating the true and false vacuum. Nevertheless, tunnelling to the true vacuum may be enhanced by the non-zero energy density. Although a full calculation is needed to assert this effect, we expect decay to be fast when the energy density becomes of the order of the maximum of the potential. For small q_0 we will use this as our criterion for stability.

Arguably the most interesting part of parameter space is $q_0 \lesssim 1$. From a naturalness point of view order one couplings ξ are favored, and for both chaotic and Starobinksy type inflation models $\chi_0 \sim m_{\rm pl}$, which implies $q_0 = \mathcal{O}(1)$. One of the main points of this chapter is that exactly for these q_0-values the effective Higgs mass and especially the energy density will depend sensitively on the choice of vacuum, and no definite statements about stability can be made.

The Higgs mass, which gets a one-loop correction proportional to the Higgs two-point Green function, as well as the energy density can be split in a divergent vacuum piece, which is absorbed in counterterms and leads to the running of the couplings, and a finite piece due to Higgs excitations on top of the vacuum. Different choices of vacuum can be viewed as different renormalization schemes, as they lead to different renormalization conditions defining the physical couplings. In a cosmological setting where the background energy density in the inflaton field is changing with time, the vacuum choice is not well-defined. Usually, the zeroth order adiabatic vacuum is chosen. In the asymptotic regions where the system is (nearly) time independent — at initial times during slow roll inflation and at late times after inflaton decay — it reduces to the usual in/out vacua. Moreover, if the background is slowly changing with time the production of high momentum modes is exponentially suppressed, supporting the vacuum interpretation [135].

The high momentum modes are adiabatic during at least part of the inflaton oscillation, and these moments in time can be used to evaluate the Green function. The problem with the current set-up is that smaller momentum modes $k < k_n$ violate the nth order adiabaticity condition and are never adiabatic. Since k_n increases with time, the contribution of these non-adiabatic modes to the Higgs mass and energy density increases with time until they fully dominate the result. A direct way to monitor the vacuum dependence is to compare quantities calculated using the zeroth and second order adiabatic vacuum.

Of course, the electroweak vacuum is either stable or unstable, this cannot depend on the choice of vacuum. However, the problem is in defining the renormalized couplings in the theory — which is necessary to find a critical coupling below which the vacuum is stable — as different vacuum choices correspond to different counterterms. As usual this freedom can be fixed by measuring the couplings. However, this measurement has to be done *during* preheating, since different adiabatic vacua only give different results during preheating and not in the adiabatic initial and final states. Moreover, even if such a measurement was in principle possible, one would also need to use non-adiabatic methods to calculate the Green function for the results to be useful.

This chapter is organized as follows. In the next section we introduce the Lagrangian and derive the equations of motion for the inflaton and Higgs field. In section 3.3 we then discuss the one-loop corrections to the effective potential and energy density, which are defined via an adiabatic renormalization scheme. Semi-analytic approximations of the effective Higgs mass and energy density are given in section 3.4, as well as a comparison with the numerical results. In section 3.5 we study the adiabaticity conditions and compute the vacuum dependence of the quantities of interest. In

section 3.6 we formulate our criteria for vacuum stability, discuss relevant time scales and corroborate our analytic results with numerical calculations. We end with concluding remarks.

Notation. The relevant equations depend on the combination $(\xi - 1/6)$, for which we introduce the shorthand notation

$$\hat{\xi} \equiv \left(\xi - \frac{1}{6}\right). \tag{3.2}$$

Time is measured in number of inflaton oscillations T. The frequency of the Higgs perturbations is periodic with frequency $\delta T = \frac{1}{2}$. To indicate a particular time during an oscillation, we use the notation $T \hat{=} \frac{1}{4}$, meaning $T = \frac{1}{4} \bmod \frac{1}{2}$.

The inflaton background is an oscillating function with a time-dependent amplitude $A(T)$. The initial conditions for the inflaton field amplitude and scale factor at $T = 0$ are denoted by $A(0) = A_0$ and $a(0) = a_0$. We will also need the amplitude and scale factor at $T = 1/4$, which are denoted by $A(\frac{1}{4}) = A_{1/4}$ and $a(\frac{1}{4}) = a_{1/4}$. Finally, after a few oscillations the amplitude and scale factor are well approximated by $A(T) = A_T/T$ and $a(T) = a_T T^{2/3}$, with normalization constants A_T and a_T. The values for all of them are taken from the numerical solution of the classical background. For future reference we list them here

$$\{A_0,\, a_0\} = \{\frac{1}{2} m_{\rm pl},\, 1\}, \quad \{A_{1/4},\, a_{1/4}\} \approx \{0.1 m_{\rm pl},\, 1.3\}, \quad \{A_T,\, a_T\} \approx \{0.25 m_{\rm pl},\, 1.7\}. \tag{3.3}$$

3.2 Classical action

We study a Higgs field that is non-minimally coupled to the Ricci scalar. We are interested in the behavior during preheating, the period just after the end of inflation when the inflaton is oscillating in its potential, and the inflaton field still dominates the energy density. The Lagrangian is given by[1]

$$\frac{\mathcal{L}}{\sqrt{-g}} = \frac{1}{2}\left(m_{\rm pl}^2 - 2\xi \Phi^\dagger \Phi\right) R + \mathcal{L}_{\rm SM} + \mathcal{L}_{\rm inf}, \tag{3.4}$$

with Φ the SM Higgs doublet. We are interested in values of ξ that ensure stability during inflation, which requires $\xi \geq 3/8$ [128].

[1] In principle one should also add a quartic interaction term between the inflaton field χ and the Higgs field $\mathcal{L} \supset \sqrt{-g}\, \kappa^2 \chi^2 |\Phi|^2$, which is allowed by the symmetries. We will assume that the coupling κ is small, and neglect this term. In Refs. [131, 134] the effect of a direct interaction term between the inflaton and Higgs is studied.

3.2.1 Inflaton background

For the inflaton we take a quadratic potential

$$\frac{\mathcal{L}_{\rm inf}}{\sqrt{-g}} = -\frac{1}{2}(\partial\chi)^2 - \frac{1}{2}m_\chi^2\chi^2. \tag{3.5}$$

This is a good approximation for many inflationary models soon after the end of inflation, as for small field values $\chi \ll m_{\rm pl}$ the potential is generically dominated by the quadratic term. However, since most of the Higgs fluctuations are produced during the first few inflaton oscillations, where deviations from the quadratic potential can be significant, for example in Starobinksy inflation, more precise calculations may require a model-dependent inflaton potential.

The inflaton dominates the energy density in the universe. The Hubble constant and Ricci scalar can then be expressed in terms of the inflaton field:

$$3H^2m_{\rm pl}^2 \simeq \frac{1}{2}\dot\chi^2 + \frac{1}{2}m_\chi^2\chi^2, \qquad R = 6\left(\dot H + 2H^2\right) \simeq \frac{1}{m_{\rm pl}^2}(-\dot\chi^2 + 2m_\chi^2\chi^2). \tag{3.6}$$

The equation of motion for the inflaton is:

$$\ddot\chi + 3H\dot\chi + m_\chi^2\chi = 0. \tag{3.7}$$

We choose initial conditions at time $t_0 = 2\pi/m_\chi$ for the inflaton field and scale factor

$$A_0 \equiv \chi(t_0) = \frac{1}{2}m_{\rm pl}, \quad \dot\chi(t_0) = 0, \quad a(t_0) = 1. \tag{3.8}$$

We take $m_\chi = 10^{-5}m_{\rm pl}$ for the inflaton mass, which is the right order of magnitude for both chaotic inflation with a quadratic potential and Starobinsky inflation[2] ; in both models $\chi \sim m_{\rm pl}$ at the end of inflation, in agreement with eq. (3.8).

[2]Starobinsky inflation [136] with a non-minimally coupled Higgs field is described by $\frac{\mathcal{L}}{\sqrt{-g}} \supset \frac{1}{2}(m_{\rm pl}^2R + \frac{1}{6M^2}R^2) - \xi R\Phi^\dagger\Phi$. Using an auxiliary field $\psi = \frac{1}{6M}R$ and a conformal transformation [137], the resulting Einstein frame Lagrangian in the limit $\xi\Phi^\dagger\Phi \ll m_{\rm pl}^2$ is the same as eq. (3.4) when transformed to the Einstein frame. The potential for the canonically normalized inflaton field (defined via $e^{\sqrt{2/3}\chi/m_{\rm pl}} = 1 + 2\frac{\psi}{Mm_{\rm pl}^2}$) is quadratic for small field values, as in eq. (3.5).

After a few oscillations the inflaton background is very well approximated by a periodic cosine function with a decreasing amplitude[3]

$$\chi \approx \frac{A_T \cos(2\pi T)}{T}, \tag{3.9}$$

with amplitude $A_T \approx 0.25 m_{\rm pl}$, which is determined by a fit to the numerical solution. The number of inflaton oscillations T is approximated by

$$T \approx \frac{m_\chi t}{(2\pi)} - 1. \tag{3.10}$$

After the first few oscillations the inflaton starts to behave as a cold dark matter fluid, i.e., averaged over an oscillation the inflaton has zero pressure and the energy density redshifts as $\rho_\chi \propto a^{-3}$. The scale factor grows as $a \propto t^{2/3}$, which can be written as

$$a \simeq a_T T^{2/3}, \tag{3.11}$$

with $a_T \approx 1.7$. At late times the Ricci scalar and Hubble constant evolve as

$$R = \frac{A_T^2 m_\chi^2 (1 + 3\cos(4\pi T))}{2 m_{\rm pl}^2 T^2} + \mathcal{O}(T^{-3}), \qquad H^2 = \frac{A_T^2 m_\chi^2}{6 m_{\rm pl}^2 T^2} + \mathcal{O}(T^{-3}). \tag{3.12}$$

3.2.2 Mode equation for the Higgs field

The relevant part of the Lagrangian for the production of Higgs modes is

$$\frac{\mathcal{L}}{\sqrt{-g}} = \frac{1}{2}\left(m_{\rm pl}^2 - 2\xi|\Phi|^2\right) R - |D_\mu \Phi|^2 - V + ... \tag{3.13}$$

with the Higgs potential

$$V = \mu^2 \Phi^\dagger \Phi + \lambda (\Phi^\dagger \Phi)^2. \tag{3.14}$$

During preheating μ^2 is very small compared to the effective mass generated by the coupling to R, and will be neglected in our computations. We concentrate on the production of the radial Higgs field, and neglect all other SM particles. In unitary gauge $\Phi^\dagger \Phi = \Phi_R^2/2$, with Φ_R a real scalar that can be split in a background field plus fluctuations:

$$\Phi_R(\vec{x}, t) = \varphi(t) + h(\vec{x}, t). \tag{3.15}$$

[3]The phase is actually shifted at late times and a better approximation is $\chi \approx (A_T/T)\cos(2\pi T - \frac{\pi}{8})$. However, the phase is irrelevant for most considerations, and for simplicity we drop it.

We are interested in the regime of small Higgs field values $\xi\varphi^2 \ll m_{\rm pl}^2$, then to leading order the results are the same in the Einstein and Jordan frame. This allows to treat gravity as a classical background. The FLRW metric for a homogeneous isotropic universe is

$$\mathrm{d}s^2 = -\mathrm{d}t^2 + a^2(t)\mathrm{d}\vec{x}^2 = a^2(\tau)\left(-\mathrm{d}\tau^2 + \mathrm{d}\vec{x}^2\right). \tag{3.16}$$

The conformal time τ is defined via $\mathrm{d}\tau = \mathrm{d}t/a(t)$. Derivatives with respect to cosmic time t are denoted by an overdot and derivatives with respect to conformal time by a prime.

Using conformal time and defining 'conformal' fields

$$\bar{\varphi} = a\varphi, \quad \bar{h} = ah, \quad \bar{V} = a^4 V, \tag{3.17}$$

the action for the fluctuations becomes (where we neglected the quartic self-interaction term)

$$\begin{aligned} S &\supset \frac{1}{2}\int \mathrm{d}^3x\mathrm{d}t a^3\left[\dot{h}^2 + \frac{(\nabla h)^2}{a^2} - \xi R h^2 - V_{\varphi\varphi}h^2\right] \\ &= \frac{1}{2}\int \mathrm{d}^3x\mathrm{d}\tau\left[\left(\partial_\tau\bar{h}\right)^2 + (\nabla\bar{h})^2 - M^2\bar{h}^2 - 2\frac{a'}{a}\bar{h}\partial_\tau\bar{h} + \left(\frac{a'}{a}\right)^2\bar{h}^2 - \frac{1}{6}a^2R\bar{h}^2\right] \\ &= \frac{1}{2}\int \mathrm{d}^3x\mathrm{d}\tau\left[\left(\partial_\tau\bar{h}\right)^2 + (\nabla\bar{h})^2 - M^2\bar{h}^2\right], \end{aligned} \tag{3.18}$$

with the background-dependent, and thus time-dependent, effective mass term

$$M^2 = a^2\left(\left(\xi - \frac{1}{6}\right)R(t) + V_{\varphi\varphi}\right). \tag{3.19}$$

In the second step we switched to conformal time and fields. To get the final expression we integrated by parts and further used that $(a'/a) = aH$, $R = 6(\dot{H} + 2H^2)$, and $\partial_\tau(a'/a) = (aH)^2 + a^2\dot{H}$. The system is now equivalent to that of a harmonic oscillator with a time-dependent frequency in Minkowski space, and we can apply the usual flat space methods. The field $\bar{h}$ can be expanded in mode functions

$$\bar{h} = \int \frac{\mathrm{d}^3\vec{k}}{(2\pi)^3}\left(a_{\vec{k}}U_k(t)\mathrm{e}^{i\vec{k}.\vec{x}} + a^\dagger_{\vec{k}}U_k^*(t)\mathrm{e}^{-i\vec{k}.\vec{x}}\right), \tag{3.20}$$

that satisfy the mode equation:

$$U_k'' + \omega_k^2 U_k = 0, \quad \omega_k^2 = k^2 + M^2. \tag{3.21}$$

The term $a^2V_{\varphi\varphi} = \bar{V}_{\bar{\varphi}\bar{\varphi}} = 3\lambda\bar{\varphi}^2$ in the effective mass (3.19) will be neglected, because it only becomes

important once the classical Higgs field is close to the value at the maximum. For smaller field values, it does not play an important role. In order to find out *whether* the classical field obtains values as big as the value at the maximum, we thus do not need the effect of the $3\lambda\bar{\varphi}^2$-term. Our approximation becomes unreliable for larger field values, but that is not the regime that we are interested in.

3.3 Quantum effective action

In the previous section we outlined the behavior of the classical inflaton field, which dominates the energy density, and gave the classical mode equations for the Higgs fluctuations. In this section we will discuss the one-loop corrections to the effective action and mode equation for the Higgs field, and the contribution of the Higgs modes to the energy density.

In non-equilibrium systems we are mostly interested in expectation values, which can be calculated using the CTP formalism [138–142]. The effective action and energy density only depend on the equal-time Green function, which we define with appropriate boundary conditions. More details can be found for example in Refs. [143–146].

3.3.1 Green Function

We start off by defining the Higgs Green function, which will enter the quantum corrected effective potential. As follows from the action for the fluctuations (3.18), the rescaled Green function $\bar{G}(\tau, x; \tau', x') \equiv \langle T\bar{h}(x,\tau)\bar{h}(x',\tau')\rangle$ satisfies the Green function equation

$$\left[\partial_\tau^2 - \nabla^2 + M^2\right]\bar{G}(\tau, x; \tau', x') = -i\delta(\tau, x; \tau', x'). \tag{3.22}$$

Now we Fourier transform $\bar{G}(\tau, x; \tau', x') = \int \frac{\mathrm{d}^3k}{(2\pi)^3}\bar{G}_k(\tau,\tau')\mathrm{e}^{i\vec{k}.(\vec{x}-\vec{x}')}$, and make the Ansatz

$$\bar{G}_k(\tau,\tau') = c\left[U_k(\tau)U_k^*(\tau')\Theta(\tau-\tau') + U_k^*(\tau)U_k(\tau')\Theta(\tau'-\tau)\right], \tag{3.23}$$

with $\Theta(\tau-\tau')$ the Heaviside step function. Substituting this into eq. (3.22), and using the mode equation (3.21), we find

$$c = -\frac{i}{\mathcal{W}_k}, \quad \text{with} \quad \mathcal{W}_k = U_k'(\tau)U_k^*(\tau) - U_k^{*'}(\tau)U_k(\tau). \tag{3.24}$$

The Wronskian is time independent, $\partial_\tau \mathcal{W}_k = 0$, and is fixed by the initial conditions:

$$U_k(0) = u_k, \quad U_k'(0) = -i\omega_{k,0} U_k(0), \quad \mathcal{W}_k = -2i\omega_{k,0}|u_k|^2, \tag{3.25}$$

with $\omega_{k,0} = \omega_k(\tau_0)$. We will take $u_k = 1$. Note that different normalizations are used in the literature (e.g. $u_k = 1/\sqrt{2\omega_{k,0}}$ [130, 131, 145]); however, in all cases the ratio $U_k(\tau_0)/U_k'(\tau_0)$ is the same, which assures that the normalization drops out of the final result, and is thus arbitrary. The effective potential only depends on the equal-time Green function. In terms of the mode functions [145, 146]:

$$\bar{G}(\tau) = \langle \bar{\varphi}(\tau)^2 \rangle = -\int \frac{\mathrm{d}^3 k}{(2\pi)^3} \frac{i}{\mathcal{W}_k} |U_k|^2 = \int \frac{\mathrm{d}^3 k}{(2\pi)^3} \frac{1}{2\omega_{k,0}} |U_k|^2. \tag{3.26}$$

In the rest of this chapter we are only interested in the equal-time Green function, and for notational convenience the explicit time-dependence of $\bar{G}$ is often dropped.

3.3.2 Energy density

The fluctuations U_k give a contribution to the energy-momentum tensor. The energy density can be split into a classical part (dominated by the inflaton contribution) and a quantum part. We are interested in the energy density of the Higgs fluctuations in the Einstein frame. There are two equivalent ways to derive this: either work in the Jordan frame and treat the Ricci scalar as a classical background source, or perform a conformal transformation to the Einstein frame and derive the energy density in that frame. We use the former method, but we stress that both methods give exactly the same result in the small field limit $\xi\varphi^2 \ll m_{\mathrm{pl}}^2$. The action for the Higgs fluctuations was given in eq. (3.18). In terms of the mode functions the (conformal) energy density derived from this action is

$$\bar{\rho} = \int \frac{d^3 k}{(2\pi)^3} \bar{\rho}_k = \int \frac{d^3 k}{(2\pi)^3} \frac{1}{4\omega_{k,0}} \left(|U_k'|^2 + \omega_k^2 |U_k|^2 \right). \tag{3.27}$$

3.3.3 Adiabatic Renormalization of $\bar{G}$ and $\bar{\rho}$

The (equal-time) Green function $\bar{G}$ and the energy density $\bar{\rho}$ are UV-divergent and need to be regularized. A convenient method for renormalization in an expanding universe is the method of adiabatic renormalization [135, 147–149]. The renormalized quantities are defined by subtracting the nth order adiabatic approximation of the quantity of interest from the divergent expression. The

quantity of interest is thus defined with respect to the nth order adiabatic vacuum. This renormalization procedure is particularly easy to implement, and widely used in preheating studies, and thus also in the Higgs studies [130–134]. The downside of this method is that the renormalization conditions for the couplings and fields in the theory are only implicitly defined, making it harder to define the renormalized couplings [150]. In fact, although for the non-interacting scalar theory adiabatic subtraction is equivalent to redefining the constants of the original action [149], new counterterms are needed in the interacting non-equilibrium theory [150, 151].

The Higgs mode functions behave adiabatically if the frequency satisfies the adiabaticity conditions

$$\epsilon_n \equiv \left| \frac{\partial_\tau^n \omega_k}{\omega_k^{n+1}} \right| \ll 1. \tag{3.28}$$

Usually only the first two conditions $n = 1, 2$ are considered, but we will show that it is important to look at the full tower. In the adiabatic limit, the solution to the mode equation (3.21) can be approximated by the WKB-solution:

$$v_k = \sqrt{\frac{\omega_{k,0}}{W_k}}\, \mathrm{e}^{-i\int^\tau W_k(\tau')d\tau'}, \tag{3.29}$$

where W_k satisfies the non-linear equation

$$W_k^2(\tau) = \omega_k^2(\tau) - \frac{1}{2}\left(\frac{W_k''}{W_k} - \frac{3}{2}\frac{W_k'^2}{W_k^2} \right). \tag{3.30}$$

In a slowly varying spacetime, this can be solved iteratively. The zeroth and second order WKB-solutions are given by:

$$\begin{aligned} \left(W_k^{(0)}\right)^2 &= \omega_k^2\,, \\ \left(W_k^{(2)}\right)^2 &= \omega_k^2 - \frac{1}{2}\left(\frac{\omega_k''}{\omega_k} - \frac{3}{2}\frac{\omega_k'^2}{\omega_k^2} \right). \end{aligned} \tag{3.31}$$

In general, the difference between the nth and $(n+2)$th frequency $W_k^{(n)}$ is of the order of the adiabaticity parameters ϵ_{n+1} and ϵ_{n+2}. Expanding the Higgs field in the adiabatic mode functions

$$\bar{h} = \int \frac{\mathrm{d}^3\vec{k}}{(2\pi)^3} \left(a_{\vec{k},\mathrm{ad}}^{(n)} v_k^{(n)}(t) \mathrm{e}^{i\vec{k}.\vec{x}} + a_{\vec{k},\mathrm{ad}}^{(n)\,\dagger} v_k^{(n)*}(t) \mathrm{e}^{-i\vec{k}.\vec{x}} \right), \tag{3.32}$$

defines the adiabatic vacuum via $a_{\vec{k},\mathrm{ad}}^{(n)} |0^{(n)}\rangle = 0$ [135]. All orders of the adiabatic vacuum reduce to the usual in/out vacua in the static asymptotic regions. Since the high momentum modes behave adiabatically, as the k^2-term is the dominant term in ω_k, the production of high momentum modes

is suppressed, as is expected in the vacuum.

Since large momentum modes are increasingly adiabatic, the exact mode functions approach the WKB solution in the UV limit. It follows that the divergences in $\bar{G}$ and $\bar{\rho}$ can be cancelled by subtracting from the Green function and the energy density the corresponding expression in the WKB-approximation:

$$\bar{G}^{(n)}_{\rm ren} = \bar{G} - \bar{G}^{(n)}_{\rm ad}, \qquad \bar{\rho}^{(n)}_{\rm ren} = \bar{\rho} - \bar{\rho}^{(n)}_{\rm ad}, \tag{3.33}$$

which gives

$$\bar{G}^{(n)}_{\rm ren} = \int \frac{d^3k}{(2\pi)^3} \frac{1}{2\omega_{k,0}} \left(|U_k|^2 - |v^{(n)}_k|^2 \right) = \int \frac{d^3k}{(2\pi)^3} \left(\frac{1}{2\omega_{k,0}} |U_k|^2 - \frac{1}{2W^{(n)}_k} \right), \tag{3.34}$$

and

$$\bar{\rho}^{(n)}_{\rm ren} = \int \frac{d^3k}{(2\pi)^3} \left[\frac{1}{4\omega_{k,0}} \left\{ |U_k'|^2 + \omega_k^2 |U_k|^2 \right\} - \frac{1}{4} \left\{ \left(\frac{1}{4} \frac{(W^{(n)'}_k)^2}{(W^{(n)}_k)^3} + W^{(n)}_k \right) + \frac{\omega_k^2}{W^{(n)}_k} \right\} \right]. \tag{3.35}$$

For the Green function the adiabatic subtraction term $\bar{G}^{(n)}_{\rm ad}$ removes all divergences for $n \geq 0$. Since the degree of divergence is higher for the energy density it seems that one has to go to higher order $n \geq 2$ to also remove the log-divergence. However, since $\bar{\rho}^{(n)} - \bar{\rho}^{(0)}$ is finite for $n \geq 2$, the UV-behavior is the same for all orders; this implies that the zeroth order adiabatic vacuum works just as well for regularizing the integral.

In a time-dependent background the adiabatic vacuum $|0^{(n)}\rangle$ is not an eigenstate of the Hamiltonian, and it does not minimize the energy density in adiabatic mode v_k at a given time τ_p [152]:

$$\bar{\rho}^{(n)}_{k,\,\rm ad}(\tau_p) = \frac{1}{4} \left(\frac{1}{4} \frac{(W^{(n)'}_k)^2}{(W^{(n)}_k)^3} + W^{(n)}_k + \frac{\omega_k^2}{W^{(n)}_k} \right) = \frac{1}{2} \omega_k(\tau_p) + \mathcal{O}\left(\epsilon_1, ..., \epsilon_n\right) . \tag{3.36}$$

Only when the adiabaticity conditions $\epsilon_n \ll 1$ are satisfied, the adiabatic energy density is slightly higher than the minimum value $\rho_k(\tau_p)|_{\rm min} = \frac{1}{2}\omega_k(\tau_p)$. Thus for the k-modes that violate the adiabaticity condition the adiabatic vacuum is not a good vacuum.

In many previous works on preheating in the Higgs system the adiabatic particle number density was used as a measure for the efficiency of preheating. The zeroth order adiabatic particle number density can be defined as $n^{(0)}_k = \rho^{(0)}_k / \omega_k$. This approach thus has the same issues with the choice of vacuum.

The WKB-approximation cannot be used for negative frequencies. The renormalized Green function and energy density are only defined at times for which $W_k^2 > 0$ and the lower bound τ_- of the integral in the WKB-solution at time τ should be chosen such that $W_k^2 > 0$ between τ_- and τ. To formally extend the Green function and energy density in the tachyonic regions one can take absolute values of the various terms in $\bar{G}_{\rm ad}$, $\bar{\rho}_{\rm ad}$; this is also what is (implicitly) done in the definition of adiabatic particle number used in previous studies [130–134].

3.3.4 Effective potential

To find the one-loop effective potential we use the tadpole method [143–146]. The equation of motion for the conformal background field can be found by requiring the tadpole to vanish: $\langle\bar{\varphi}\rangle = 0$. This gives

$$\bar{\varphi}'' + a^2(\xi - \frac{1}{6})R\bar{\varphi} + \bar{V}_{\bar{\varphi}} + \frac{1}{2}\partial_{\bar{\varphi}}(\bar{m}^2_{\bar{\varphi}})\bar{G}(\tau) + ... = 0, \tag{3.37}$$

where $G(\tau)$ is the equal-time Green function of the conformal Higgs field. Since the Higgs is the only field that is produced directly during preheating, we neglect contributions to the equation of motion from the other fields, as denoted by the ellipses. Further, for the Higgs potential (3.14) one has $\bar{V}_{\bar{\varphi}} \simeq \lambda\bar{\varphi}^3$ and $\partial_{\bar{\varphi}}(\bar{m}^2_{\bar{h}}) = \bar{V}_{\bar{\varphi}\bar{h}\bar{h}}$. In a (nearly) static background, integrating the equation of motion gives the usual Coleman-Weinberg correction to the effective potential [153]. Including explicit counterterms[4] this gives

$$\bar{V}_{\rm eff} = \frac{1}{2}a^2\left(\xi + \delta\xi - \frac{1}{6}\right)R\bar{\varphi}^2 + \frac{(\lambda+\delta\lambda)\bar{\varphi}^4}{4} + 3\lambda\bar{\varphi}^2\bar{G}(\tau) + ...\,, \tag{3.38}$$

Now we split the Green function into a vacuum part and a part due to excitations on top of the adiabatic vacuum $\bar{G} = \bar{G}^{(n)}_{\rm ad} + \bar{G}^{(n)}_{\rm ren}$, according to the adiabatic renormalization scheme (3.34). The divergent vacuum part can be absorbed in the counterterms, together with the vacuum contribution of all other SM particles. In a static universe, defining appropriate renormalization conditions this gives the standard results for the renormalized couplings. In an adiabatically expanding universe this procedure can still be used at each moment in time since time derivatives only give small corrections. Although very easy to implement, the disadvantage of the adiabatic renormalization scheme is that it is hard to translate it into the explicit counterterms in the Lagrangian (3.38). The effective potential

[4]Since the non-minimal coupling is a non-renormalizable interaction between gravity and the Higgs field, one cannot treat gravity as a classical background in calculating the counterterms and RGE equation; rather a covariant method should be used [154]. Since the details are not important for our purposes, we neglect this complication.

can be renormalization-group (RG) improved to give

$$\bar{V}_{\rm eff} = \frac{1}{2}a^2\left(\xi(\mu) - \frac{1}{6}\right)R\bar{\varphi}^2 + \frac{\lambda(\mu)\bar{\varphi}^4}{4} + 3\lambda(\mu)\bar{\varphi}^2\bar{G}^{\rm ren}(\tau)\,, \tag{3.39}$$

with $\lambda(\mu)$, $\xi(\mu)$ the running couplings. In an expanding universe the renormalization scale can be taken as the mass of the top quark $m_t \sim \varphi$, or if higher, the Hubble scale

$$\mu \sim \max(H, \varphi). \tag{3.40}$$

The RGEs for the quartic coupling and all other SM couplings are the usual SM RGEs (see e.g. Ref. [95]), the RGE for the non-minimal coupling can be found in Ref. [154]. The boundary conditions are set by the measurement of the Higgs mass at the electroweak scale, and the value of ξ at the inflationary scale that can be extracted from the CMB. The term proportional to $\bar{G}^{(n)}_{\rm ren}(\tau)$ is the contribution to the effective potential due to Higgs quanta above the nth order adiabatic vacuum; this is analogous to how the effective potential receives thermal corrections in a plasma.

Different choices of vacuum, such as the zeroth and second order WKB vacuum eq. (3.31), correspond to different counterterms, and as a result the physical couplings are defined via different renormalization conditions. Since the different order vacua all coincide in the static asymptotic regions, the renormalization conditions only differ during preheating. As a result, to fully fix the theory one has to measure the couplings during this period. If preheating is efficient, the vacuum dependence of the result is relatively small and this is not a big problem. However, as we will see, if preheating is less efficient the vacuum dependence in the Green function and energy density grows with time, i.e. the differences $\bar{G}^{(0)} - \bar{G}^{(n)}$ and $\bar{\rho}^{(0)} - \bar{\rho}^{(n)}$ grow with time. Therefore, the ambiguity in the finite pieces of the counterterms, and thus in the definition of the physical couplings via a renormalization condition grows, and it becomes harder to extract a reliable critical coupling for stability. Note that the physics is independent of our choice of vacuum, the electroweak vacuum is either stable or not. The problem lies in the lack of a measurement of the couplings during preheating, and secondly in the application of equilibrium methods to a system that is not adiabatic.

We can read off the one-loop effective mass, which consists of the tree-level term (3.19) plus quantum correction due to the production of Higgs quanta:

$$M^2_{\rm eff} \simeq a^2\left(\xi(\mu) - \frac{1}{6}\right)R + 6\lambda\bar{G}^{\rm bg}(\tau) = a^2\hat{\xi}(\mu)R + 6\lambda\bar{G}^{\rm bg}(\tau)\,, \tag{3.41}$$

where we neglected the subdominant tree-level contribution from the quartic Higgs coupling, and used the notation of eq. (3.2).

If the mass squared is positive at small field values — either because the tree-level mass dominates, or because the quartic coupling is positive and the quantum correction to the mass is positive — the potential has a barrier separating the true and false vacua. We now assume that $H > \mu_{\rm cr} \sim 10^{11}$GeV, such that the coupling $\lambda(H) \sim -10^{-2}$ is negative and approximately field independent near the maximum of the potential. We then find that

$$\bar{V}_{\rm max} = \frac{1}{4}\frac{M_{\rm eff}^4}{|\lambda|}\,. \tag{3.42}$$

For a smaller Hubble constant, there will be corrections as the coupling $\lambda(\varphi)$ is field dependent, but these corrections are small in the regime that we are interested in.

Along the same lines one can define the energy density of the Higgs quanta on top of the adiabatic vacuum as $\rho_{\rm ren}^{(n)}$ as defined in eq. (3.35), where the couplings can be taken as the running couplings.

3.4 Higgs effective mass and energy density

In this section we will discuss the numerical results for the Higgs effective mass and energy density, and develop a semi-analytical understanding. More details on the numerical implementation are given in section 3.6.3.1. The results are for the zeroth order adiabatic vacuum. In the next section we look at the vacuum dependence, and discuss the difference with the higher order vacua.

3.4.1 Green function

For small enough comoving momentum k the frequency squared ω_k^2 of the Higgs modes oscillates between positive and negative values. Modes for which the frequency squared is negative are produced in tachyonic preheating, see section 2.2.3.3 and Refs. [123, 124]. Modes for which the frequency is positive but non-adiabatic are produced in a broad resonance, see section 2.2.3.2. Most quanta are produced in the first few oscillations.

We will estimate the contribution of the tachyonic and non-adiabatic modes to the Green function, guided by the numerical results. The first step is to write the mode equation (3.21) in the form of the Mathieu equation. To do so we approximate the inflaton field and its derivative during the first

oscillation as[5]

$$\chi \approx A(T)\cos(2\pi T), \quad \partial_T \chi \approx A(T)\partial_T \cos(2\pi T), \tag{3.43}$$

that is, we neglect the time-dependence of the amplitude in taking the derivative. If furthermore the time-derivative of the mode function is approximated by $\partial_\tau^2 U_k \approx (a m_\chi/(2\pi))^2 \partial_T^2 U_k$, the mode equation (3.21) can be written in the form of a Mathieu equation:

$$\partial_z^2 U_k + (\mathcal{A}_k - 2q\cos(2z))\, U_k = 0, \tag{3.44}$$

with

$$\mathcal{A}_k(T) = \frac{k^2}{a^2 m_\chi^2} + \frac{1}{2}\hat{\xi}A^2, \quad q(T) = \frac{3}{4m_{\rm pl}^2}\hat{\xi}A^2, \quad 2z = 4\pi T - \pi. \tag{3.45}$$

Note that the amplitude A, scale factor a, and thus the parameters $\mathcal{A}_k$, q are time dependent in the expanding universe. We define the efficiency parameter as the q-value at the initial time

$$q_0 \equiv q(0) = \frac{3}{4m_{\rm pl}^2}\hat{\xi}A_0^2. \tag{3.46}$$

Let's look at tachyonic preheating first. The small momentum modes are tachyonic $\omega_k^2 < 0$ during part of the inflaton oscillation. The frequency is most negative at times $T \approx T_p = \frac{1}{4} + \frac{1}{2}p$, with p an integer. It was estimated in Ref. [124] that during the pth burst of tachyonic particle production, the tachyonic mode functions grow approximately as[6]

$$|U_k(T_p)|^2 \sim \left(\frac{2\omega_{k,0}}{\omega_k}\right) \mathrm{e}^{4x\sqrt{q_p}}, \tag{3.47}$$

with x an order one constant. Since q decreases with time, the production is dominated by the first few times the frequency becomes tachyonic. Consider then the first burst of particle production at $T_{p=0} = 1/4$. Modes with $k \lesssim k_{\rm tach}$ are tachyonic at that time, with

$$k_{\rm tach} = \frac{2}{\sqrt{3}} a_{1/4} m_\chi \sqrt{q_{1/4}}\,, \tag{3.48}$$

[5] After a few oscillations the amplitude is well approximated by $A(T) \approx A_T/T$ as in eq. (3.9), but in the first few oscillations the amplitude decays faster and has a different time-dependence.

[6] The factor $(2\omega_{k,0}/\omega_k)$ enters because of our normalization of the mode functions.

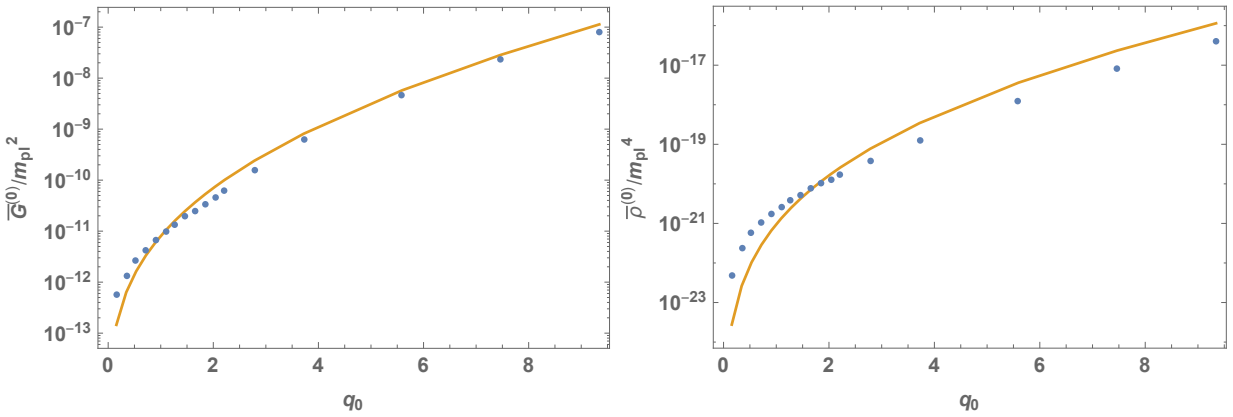

(A) Left graph: comparison between the numerically computed values of $\bar{G}^{(0)}$ (blue) and estimate (3.50) (orange) as a function of q_0. $\bar{G}^{(0)}$ was computed after 1.5 oscillations, except for the two largest values of q_0, where it was computed after 3 oscillations. Right graph: comparison between the numerically computed values of $\bar{\rho}^{(0)}$ (blue) and estimate (3.53) (orange) as a function of q_0. $\bar{\rho}^{(0)}$ was computed after 3.5 oscillations.

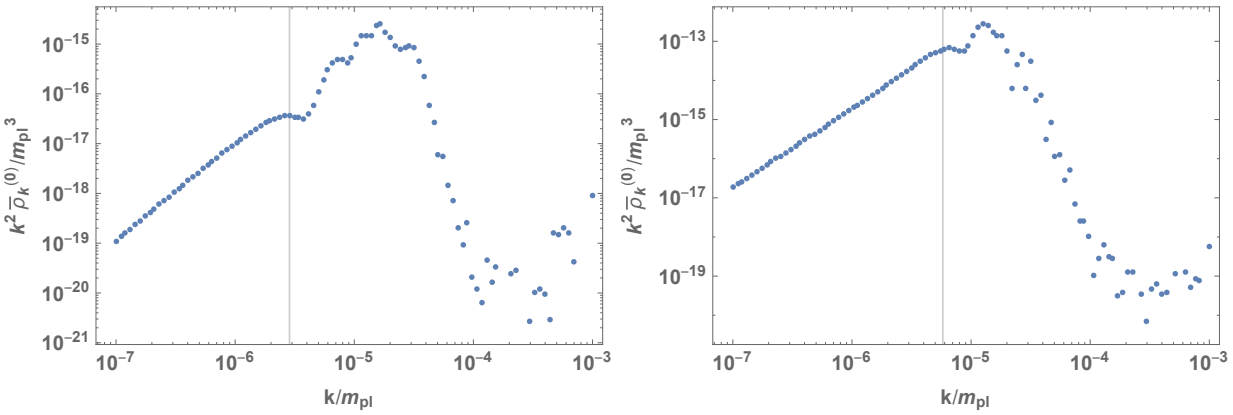

(B) $k^2\bar{\rho}_k^{(0)}$ as a function of k at $T = 3.5$ for $q_0 = 0.9$ (left graph) and $q_0 = 3.7$ (right graph). The vertical line indicates the value of k_{tach}.

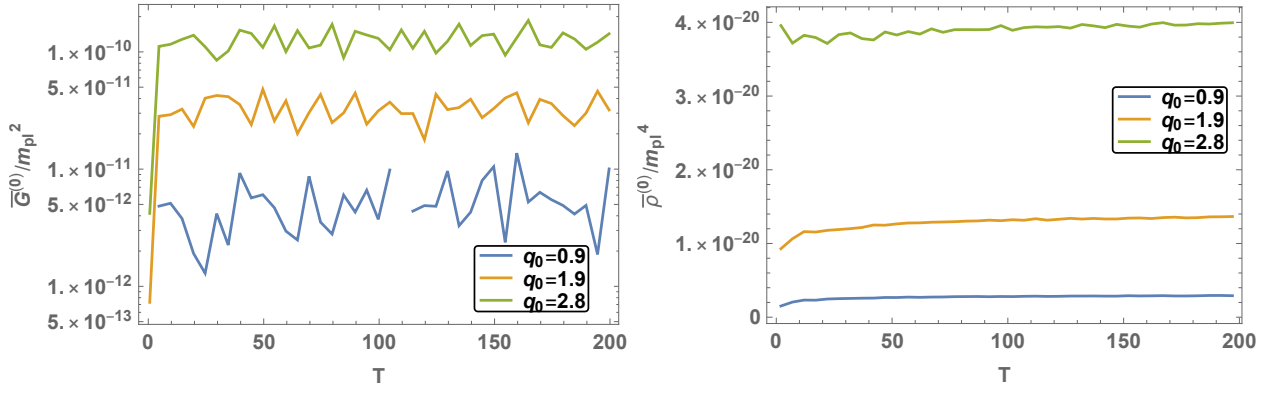

(C) Left graph: $\bar{G}^{(0)}$ as a function of time during the first 200 oscillations of the inflaton field. Right graph: $\bar{\rho}^0$ during the first 100 oscillations. $\bar{G}^{(0)}$ and $\bar{\rho}^{(0)}$ are plotted for $q_0 = 0.9$ (blue), $q_0 = 1.9$ (orange) and $q_0 = 2.8$ (green). The quantities are sampled with $\delta T = 5$, for values of T where the vacuum dependence is minimal.

FIGURE 3.1

where we introduced the shorthand $q_{1/4} = q(T = 1/4)$ and analogous notation for other time-dependent quantities. The first burst of production gives a contribution to the Green function (3.34)

$$\bar{G}^{(0)}(1/4) \sim \int^{k_{\rm tach}} \frac{\mathrm{d}^3k}{(2\pi)^3 2\omega_{k,0}} |U_k(1/4)|^2 \sim \frac{1}{2\pi^2} \int^{k_{\rm tach}} \mathrm{d}k\, k \mathrm{e}^{4x\sqrt{q_{1/4}}} \sim \frac{1}{2\pi^2} k_{\rm tach}^2 \mathrm{e}^{4x\sqrt{q_{1/4}}}. \tag{3.49}$$

Here we used that the integral is dominated by the modes with $k \sim k_{\rm tach}$, for which the approximation $\omega_k \sim k$ is valid. Particle production in the subsequent tachyonic intervals is subdominant. It follows that $\bar{G}^{(n)}$ approaches its asymptotic value after about one inflaton oscillation, and remains constant after that. The above approximation for the Green function is thus valid at late times as well. Relating $q_{1/4} = (A_{1/4}/A_0)^2 q_0$, the contribution of the tachyonic modes to the Green function can be approximated by

$$\bar{G}^{(0)}(T) \sim \frac{1}{2\pi^2} k_{\rm tach}^2 \mathrm{e}^{4x\sqrt{q_{1/4}}} \sim 5 \times 10^{-13} m_{\rm pl}^2 q_0 \mathrm{e}^{c\sqrt{q_0}}, \tag{3.50}$$

where in the 2nd step we used $m_\chi = 10^{-5} m_{\rm pl}$ and eq. (3.3), and defined $c = 4x\sqrt{q_{1/4}/q_0}$.

We fit the growth factor c to the numerical results

$$c \approx 3.5. \tag{3.51}$$

The left panel of figure 3.1a shows a comparison between the numerically computed values of $\bar{G}^{(0)}$ and the approximation (3.50). The approximation agrees with the numerical result within a factor of two over the whole range $q_0 = 0.15 - 9.3$, corresponding to $\xi = 1 - 50$. The left panel of figure 3.1c shows the large time behavior of the Green function in the zeroth order adiabatic vacuum. The graphs show that $\bar{G}^{(0)}$ remains approximately constant after the initial amplification, confirming our assumption that production is completely dominated by the first few oscillations.

3.4.2 Energy density

Analogously to the Green function, the energy density is produced in the first few oscillations and remains constant afterwards, as confirmed by the numerical results shown in figure 3.1c.

The contribution of the tachyonic modes to eq. (3.35) is estimated as

$$\begin{aligned} \bar{\rho}^{(0)}(T) &\sim \frac{1}{8\pi^2} \int^{k_{\rm tach}} k dk \, \left\{ |U_k'|^2 + \omega_k^2 |U_k|^2 \right\} \Big|_{T=\frac{1}{4}} \sim \frac{1}{4\pi^2} \int^{k_{\rm tach}} k^3 dk \, |U_k(1/4)|^2 \\ &\sim \frac{1}{4\pi^2} k_{\rm tach}^4 \mathrm{e}^{c\sqrt{q_0}}. \end{aligned} \tag{3.52}$$

In the 2nd step we used that the modes $k \sim k_{\rm tach}$ dominate the integral, analogously to the approximation made in the Green function. Moreover, we assumed equipartition and used $|U_k'|^2 \sim k^2|U_k|^2$, which agrees with the numerical results.

Numerically, we fit

$$\bar{\rho}^{(0)} \sim 2.8 \times 10^{-23} m_{\rm pl}^4 q_0^2 {\rm e}^{c\sqrt{q_0}}. \tag{3.53}$$

The numerical fit is about a factor 15 larger than estimate (3.52), which includes tachyonic modes only. The growth factor c is given by eq. (3.51). This indicates that the energy density and Green function are dominated by the same mode functions.

In the right panel of figure 3.1a a comparison between the numerically computed values of $\bar{\rho}^{(0)}$ after 3.5 inflaton oscillations and approximation (3.53) is shown. For $q_0 > 2$ the estimate and numerical result agree within a factor of two, but for smaller q_0 estimate (3.53) underestimates the numerical result by a larger margin.

There are several effects that can explain the factor 15 difference between the analytic and numerical result. First of all, the approximation $\omega_k \approx k$ could be slightly off. Secondly, the assumption that the production of modes after the first oscillation is negligible does not completely hold for larger q_0. Furthermore, we did not take into account the contribution of non-tachyonic modes. Figure 3.1b shows $k^2\bar{\rho}_k^{(0)}$ as a function of k at $T = 3.5$. As expected, the resonance is most efficient for the larger value of q_0. The right graph shows that for $q_0 = 3.7$ the distribution is peaked at a k_* that is slightly larger than $k_{\rm tach}$. The left graph shows that for $q_0 = 0.9$ the difference between $k_{\rm tach}$ and the most dominant mode k_* is approximately a factor 5. This implies that there is a significant contribution of modes that are non-adiabatic, but never tachyonic. This leads to the conclusion that for $q_0 \lesssim 1$, broad resonance plays a role that is more important than tachyonic resonance.

These three effects should in principle also apply to our estimate of $\bar{G}^{(0)}$. However, we did not need any multiplicative factor for our fit of $\bar{G}^{(0)}$, which suggests that the effects approximately cancel in this case.

3.5 Adiabaticity and vacuum dependence

The adiabatic vacuum is a good vacuum for high-momentum modes, for which the adiabaticity parameters defined in eq. (3.28) are small at least during part of the inflaton oscillation. However, for smaller momenta, adiabaticity is violated at all times. If these momenta give a significant

contribution to the Green function and/or energy density, this introduces a large vacuum dependence and as a result $\bar{G}$ and $\bar{\rho}$ have different values for different orders of adiabatic vacuum.

In this section we will discuss the adiabaticity condition and the vacuum dependence of the Green function and energy density, which are both input to determine the stability of the vacuum, as laid out in section 3.6.1.

3.5.1 Adiabaticity conditions

After a few oscillations the inflaton background is very well approximated by expression (3.9). The frequency for the Higgs modes (3.21) becomes

$$\omega_k^2 \simeq k^2 + \frac{1}{2}A_T^2 a_T^2 m_\chi^2 \hat{\xi} T^{-2/3}\left(1+3\cos(4\pi T)\right) + \mathcal{O}(T^{-5/3}). \tag{3.54}$$

The frequency is periodic with $\delta T = 1/2$. In the rest of this section we will use the notation $T\hat{=}1/4$ to denote $T = 1/4 \bmod 1/2$.

Modes with $k < k_n$ violate the nth-order adiabaticity condition $\epsilon_n > 1$, which involves n derivatives of the frequency. Keeping only the leading term at large T this gives the estimate

$$k_n \sim a_T m_\chi \left(4\times 2^{(n-2)}\left(\frac{A_T}{A_0}\right)^2 q_0\right)^{\frac{1}{(n+2)}} T^{\frac{2(n-1)}{3(n+2)}} \times \begin{cases} |\sin(4\pi T)|^{\frac{1}{(n+2)}} & n \text{ odd}, \\ |\cos(4\pi T)|^{\frac{1}{(n+2)}} & n \text{ even}, \end{cases} \tag{3.55}$$

with $A_T/A_0 \approx 0.2$, see eq. (3.3). Since even orders are proportional to a cosine, and odd orders to a sine, k_n cannot be minimized simultaneously for all n. At every moment during the inflaton oscillations there are modes that violate some of the adiabaticity conditions. The momentum cutoff k_n grows, and as time goes by more modes become non-adiabatic. At early times all k_n are similar for $q_0 = 1 - 10$, but the larger the order n the faster k_n grows with time. Explicitly, parametrizing $k_n \propto T^\alpha$ this gives $\alpha = \{0, 1/6, 4/15, 1/3\}$ for $n = \{1, 2, 3, 4\}$.

The left top plot in figure 3.2a shows the exact critical k_n for which $\epsilon_n = 1$ (using eq. (3.9) as the inflaton background) for $n = 1, .., 4$ during a time interval $\delta T = 1/2$; this is compared with our approximation (3.55) . The approximation works well (it becomes more accurate with larger T), except for parts close to the critical points $T\hat{=}3/8, 1/2, 5/8$ where either the sine or the cosine goes to zero.

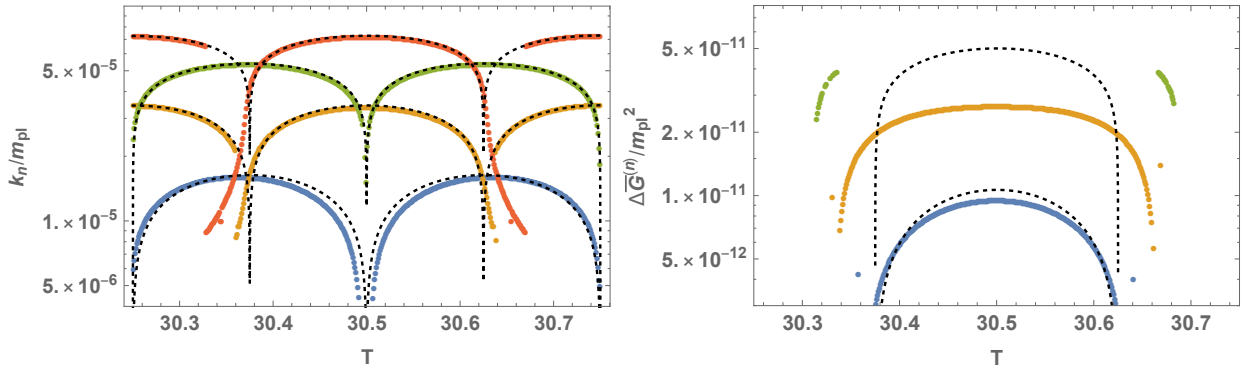

(A) The left plot shows k_n for which $\epsilon_n = 1$ during a time interval $\delta T = 1/2$. The blue, orange, green and red line correspond to $n = 1, 2, 3, 4$ respectively, and the black dotted lines the analytical approximation (3.55). The right plot shows $\Delta\bar{G}^{(n)}$; the blue, orange and green points correspond to $n = 2, 4, 6$. Only points with $\mathrm{Im}(\Delta\bar{G}^{(n)}) < 0.01\mathrm{Re}(\Delta\bar{G}^{(n)})$ are shown. The black dotted lines correspond to the approximation (3.58).

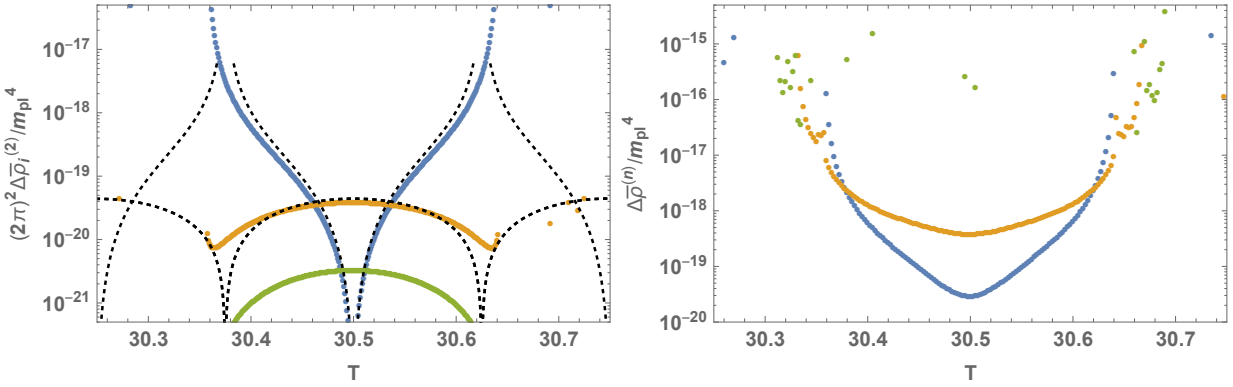

(B) The left plot shows $(2\pi)^2\Delta\bar{\rho}_i^{(2)}$, blue, orange, and green lines are for $i = 1, 2, 3$ respectively, and the black dotted line corresponds to eq. (3.61). The right plot shows $\Delta\bar{\rho}^{(n)}$; the blue, orange and green points correspond to $n = 2, 4, 6$. Only points with $\mathrm{Im}(\bar{\rho}^{(n)}) > 0.01\mathrm{Re}(\Delta\bar{\rho}^{(n)})$ are shown. All plots are for $\hat{\xi} = 10$.

FIGURE 3.2

For the above estimate we only included the classical contribution to the effective mass (3.41). Taking into account the quantum correction, even if larger than the tree-level term, will have negligible effect. As discussed in the previous subsection $\bar{G}$ is nearly constant at late times, and the time-derivative of ω_k is still given by the time-derivative of the tree-level term. Further, for the q_0 values of interest $k_n^2 > M_{\rm eff}^2$, and one can use the approximation $\omega_k \sim k$; the backreaction will not change this either.

If we compare the non-adiabatic modes with the tachyonic modes (3.48), we see that $k_{\rm tach} < k_n$. The tachyonic modes give a an exponentially enhanced contribution to the Green function and energy density, signifying particle production. The larger the enhancement, i.e., the larger q_0, the smaller the effect of the different adiabatic subtractions. However, since k_n grows with time, at sufficiently late times the vacuum dependence of $\bar{G}$ and $\bar{\rho}$ always become substantial. This is what we will discuss next.

3.5.2 Green function

We now approximate the vacuum dependence of the Green function. The nth adiabatic order frequency is schematically of the form

$$\left(W_k^{(n)}\right)^2 = \omega_k^2 + f^{(n)}(\epsilon_1, \epsilon_2, ..., \epsilon_n), \tag{3.56}$$

that is, $f^{(n)}$ contains terms up to n derivatives of the frequency ω_k. The highest derivative term dominates, and thus $W^{(n)} > W^{(n-2)}$ for modes $k < k_n$ for which $\epsilon_n > 1$. Consider the difference between the Green functions of the zeroth and nth order adiabatic vacuum. This is approximately

$$\begin{aligned}\Delta\bar{G}^{(n)} \equiv \bar{G}^{(n)} - \bar{G}^{(0)} &= \int \frac{d^3k}{(2\pi)^3}\left(\frac{1}{2W_k^{(0)}} - \frac{1}{2W_k^{(n)}}\right) \approx \frac{1}{4\pi^2}\int^{k_n} \mathrm{d}k\, \frac{k^2}{W_k^{(0)}} \\ &\sim \frac{1}{8\pi^2}k_n^2\,.\end{aligned} \tag{3.57}$$

In the last step we used that $W_k^{(0)} = \omega_k \sim k$, which is a good approximation for the modes that dominate the integral. Comparing with the exact result, we can fit the constant of proportionality

$$\Delta\bar{G}^{(2)} \approx \frac{1}{8\sqrt{2}\pi^2}k_2^2, \quad \Delta\bar{G}^{(4)} \approx \frac{1}{16\pi^2}k_4^2, \quad \Delta\bar{G}^{(6)} \approx \frac{1}{16\sqrt{2}\pi^2}k_6^2. \tag{3.58}$$

The top right plot in figure 3.2a shows the exact $\Delta\bar{G}^{(n)}$ for $n = 2, 4, 6$ and our approximation (3.58) over a time interval $\delta T = 1/2$. We only show points for which the imaginary part of $\Delta\bar{G}^{(n)}$ is less than 1%. That is, the modes that dominate the integral are all non-tachyonic $W_k^{(n)} > 0$ and the adiabatic vacuum is defined for them, but we allow that a fraction of the smaller k-modes (that give a subdominant contribution) are tachyonic. The vacuum dependence of the Green function grows with time and for larger adiabatic order. However, one cannot take the order to infinity and claim that the vacuum dependence is arbitrarily large, as for larger n the frequency is tachyonic $(W_k^{(n)})^2 < 0$ for more k-modes and the Green function becomes increasingly less well-defined. Indeed, the plot already shows that for $n = 6$ the imaginary part of the Green function exceeds 1% during most of the time interval, also at times where lower order vacua and $\bar{G}^{(2)}, \bar{G}^{(4)}$ are still well-defined.

The second observation is that the vacuum dependence $\Delta\bar{G}^{(n)}$ is minimized for $T\hat{=}1/8, 3/8$, in accordance with our estimate (3.55) as k_{2n} vanishes here. It seems that zooming in on this time instant the vacuum dependence can be made arbitrarily small. However, this is not the case, as in this limit more and more k-modes become tachyonic, and at some point the Green function is no longer well-defined. This still puts a lower bound on the vacuum dependence. Moreover, at these

time instants the frequencies are still non-adiabatic (only the even adiabaticity parameters vanish), and this vanishing is more a coincidence rather than a consequence of adiabaticity. Indeed, as we will see next, the vacuum dependence of the energy density is minimized at different time instants, and one cannot make both of them arbitrarily small at the same time.

3.5.3 Energy density

Define the vacuum dependence of the energy density via

$$\Delta\bar{\rho}^{(n)} \equiv \bar{\rho}^{(n)} - \bar{\rho}^{(0)}, \tag{3.59}$$

i.e. we compare the zeroth and nth order adiabatic vacuum. To find an analytic approximation it is useful to look at the different terms in $\bar{\rho}_{\rm ad}$ separately

$$\begin{aligned}\bar{\rho}^{(n)}_{\rm ad} &= -\frac{1}{4}\int \frac{d^3k}{(2\pi)^3}\left\{\frac{1}{4}\frac{(W_k^{(n)'})^2}{(W_k^{(n)})^3} + \left(W_k^{(n)} + \frac{k^2}{W_k^{(n)}}\right) + \frac{\hat{\xi}a^2R}{W_k^{(n)}}\right\} \\ &= \bar{\rho}_1^{(n)} + \bar{\rho}_2^{(n)} + \bar{\rho}_3^{(n)}.\end{aligned} \tag{3.60}$$

For definiteness, concentrate on the $n = 2$ vacuum; the results can be generalized to higher order vacua. The term $\Delta\bar{\rho}_3$ is subdominant for $T \gtrsim \sqrt{q_0}$ and is neglected. The term $\Delta\bar{\rho}_2$ is dominated by the modes $k \sim k_2$ for which $W^{(0)} \sim W^{(2)}$, and can be estimated by

$$|\Delta\bar{\rho}_2^{(2)}| \sim \frac{1}{4\pi^2}\int^{k_2} \mathrm{d}k\, k^2 \times \frac{k}{2} \sim \frac{1}{64\pi^2}k_2^4, \tag{3.61}$$

where the factor $1/2$ is matched to the numerical solution. The term $\Delta\bar{\rho}_1$ is also dominated by modes $k \sim k_2$, as the integrand is peaked for these momenta. We estimate

$$|\Delta\bar{\rho}_1^{(2)}| \approx \frac{1}{32\pi^2}\int^{k_2} k^2\mathrm{d}k\,\frac{(W_k^{(2)'})^2}{(W_k^{(2)})^3} \sim \frac{(W_k^{(2)'})^2\big|_{k\sim k_2}}{32\pi^2(3/2)^{3/2}} \sim \frac{1}{256\sqrt{6}}\frac{k_3^{10}}{k_2^6}, \tag{3.62}$$

where once again the numerical factors are matched to the numerical solution. It should not surprise that k_3 enters this estimate, as this term involves an extra time derivative and thus depends on the 3rd adiabaticity parameter.

The different contributions to $\Delta\bar{\rho}^{(2)}$ and the analytical approximation (3.61) and (3.62) are shown in the bottom left plot in figure 3.2b. The total vacuum dependence of $\Delta\bar{\rho}^{(n)}$ is shown in the bottom

right plot for $n = 2, 4, 6$. Just as for the Green function, only the time instants are shown where the imaginary contribution is less than 1%.

Both approximations agree well with the numerical result away from the critical points $T \hat{=} \frac{3}{8}, \frac{1}{2}, \frac{5}{8}$. However, in these limits increasingly more modes become tachyonic, and the energy density is at some point not well-defined. The vacuum dependence grows with the order of the vacuum n, but just as for the Green function case one cannot take arbitrary large n as these vacua are tachyonic and not defined during most of the time (some of the scattered points, mostly for $\Delta\bar{\rho}^{(6)}$, are a numerical artefact as the integrand behaves wildly for these points).

$\Delta\bar{\rho}^{(n)}$ is minimized for $T \hat{=} \frac{1}{2}$ and blows up at the other critical points $T \hat{=} \frac{3}{8}, \frac{5}{8}$.

In the following we will use $\bar{G}^{(2)}$ and $\bar{\rho}^{(2)}$ as an estimate for the vacuum dependence. Away from the critical points to a good approximation

$$\Delta\bar{G}^{(2)} \sim \frac{1}{8\sqrt{2}\pi^2} k_2^2, \quad \Delta\bar{\rho}^{(2)} \sim \max\left[\frac{1}{64\pi^2} k_2^4,\ \frac{1}{256\sqrt{6}} \frac{k_3^{10}}{k_2^6}\right]. \tag{3.63}$$

3.6 Vacuum stability

In this section we discuss the implications of our results for the vacuum stability. In the next subsection we first discuss the criteria for stability. In section 3.6.2 we analytically determine all the relevant time scales, which we compare with the numerical results in section 3.6.3.

3.6.1 Criteria for stability

The qualitative form of the potential depends sensitively on the Hubble scale. If the Hubble scale is larger than the critical scale $H > \mu_{\rm cr} \sim 10^{11}$GeV it follows from eq. (5.33) that $\lambda(\mu) < 0$ for all Higgs field values $\varphi < H$. This is the case at early times, after a sufficiently small number of inflaton oscillations. Using eq. (3.12) the critical time is given by[7]

$$T_{\rm crit} \sim 25 \left(\frac{A_0}{0.5 m_{\rm pl}}\right) \left(\frac{m_\chi}{10^{-5} m_{\rm pl}}\right) \left(\frac{4.2 \times 10^{-8} m_{\rm pl}}{\mu_{\rm cr}}\right), \tag{3.64}$$

with A_0 the initial inflaton amplitude. There are then two possibilities for the vacuum to decay.

- The quantum corrections to the effective mass (3.41) dominate before $T_{\rm crit}$.

[7] Here we used that the ratio A_T/A_0 is approximately constant for different A_0.

As we have seen the Green function is nearly constant after a few oscillations. As a consequence, if the coupling is negative, the quantum correction to the effective Higgs mass is then always negative. If it exceeds the (oscillating) tree-level contribution the vacuum is destabilized, since there is no barrier. The vacuum can only remain stable if the following criterion is satisfied

$$\textbf{condition 1}: \qquad 6|\lambda|\bar{G}^{\rm ren}(\tau) \lesssim a^2\hat{\xi}R_{\rm max}, \quad \text{for } T < T_{\rm crit}, \tag{3.65}$$

with $R_{\rm max}$ the maximum value of the Ricci scalar during an inflaton oscillation.

- The energy density becomes larger than the potential barrier separating the electroweak and true vacuum.

  If the tree-level term dominates the effective mass the potential is an oscillating function with a barrier separating the two vacua. If the quantum correction to the effective mass comes to dominate at late times $T > T_{\rm crit}$, this only enhances the barrier, as the quantum correction to the effective mass is positive at $\varphi < \mu_{\rm cr}$.

  The tunnelling process is expected to be enhanced if the energy density in the Higgs modes exceeds the height of barrier, potentially leading to rapid decay.[8] In addition to the first criterion, we thus have a second criterion for vacuum stability:

$$\textbf{condition 2}: \qquad \bar{\rho}^{\rm ren} < \bar{V}_{\rm max}, \tag{3.66}$$

  with $\bar{V}_{\rm max}$ given in eq. (3.42).

In the literature, many different criteria for stability are used [130–134]. Even though the details may differ, all agree that for large non-minimal coupling $q_0 \gtrsim \mathcal{O}(5)$ particle production is efficient and the electroweak vacuum is destabilized within a couple of inflaton oscillations, since the stability condition (3.65) is violated.

For smaller couplings particle production is initially not efficient enough to destabilize the vacuum. As the classical background redshifts faster than the quantum correction, the energy density may become larger than the effective barrier of the potential at late times, and the condition (3.66) is violated. However, as we will see, the vacuum dependence of the energy density grows with time, and this makes it hard to make definite statements for small $q_0 \sim \mathcal{O}(1)$.

[8] Although a full calculation is needed to assert whether this is indeed the case. It should be noted that both the energy density and the potential are oscillating functions.

3.6.2 Time scales

In this section we discuss the relevant time scales, starting with some effects we have neglected (inflaton and Higgs decay), and ending with estimates for when the Green function and energy density become large, when the vacuum dependence becomes important, and when the stability criteria are violated.

3.6.2.1 Inflaton decay

Even though the inflaton decay rate is model dependent, we can make some general statements.

The inflaton oscillates until decay. If it decays via very efficient preheating (into a field other than the Higgs field), the total number of oscillations are $T \lesssim 10^3 - 10^4$ [89]. Perturbative decay is slower. The inflaton cannot be coupled too strongly to other fields, as otherwise loop corrections would spoil the flatness of the potential. This gives a bound $T \gtrsim 10^6$ corresponding to a maximum reheating temperature $T_R \lesssim 10^{12}$GeV; but the number of oscillations can be much larger, for example if the coupling is of gravitational strength and $\Gamma_\chi \sim m_\chi^3/m_{\rm pl}^2$, decay happens after $T \sim 10^9$ oscillations, with a maximum reheating temperature $T_R \lesssim 7 \times 10^{10}$GeV.

After inflaton decay the universe is dominated by a relativistic fluid, and $R \approx 0$. The classical contribution to the Higgs mass vanishes. However, already before complete decay, there are temperature corrections to both the Higgs mass and the energy density, just like the non-thermal preheating corrections discussed in this chapter. The net effect is that the thermal corrections generically stabilize the vacuum — see Refs. [101, 128] for the exact bounds. For non-perturbative decay, there is an intermediate non-thermal stage before thermal equilibrium is reached; during this stage the Ricci scalar is non-vanishing. Although a dedicated study will be needed to determine the exact bounds in this case, it is likely that perturbative inflaton decay also helps to stabilize the vacuum.

In the next subsections we will discuss the critical q_0 value below which the electroweak vacuum is stable, assuming inflaton decay is late and only happens after all relevant time-scales. Since inflaton decay generically stabilizes the electroweak vacuum, fast decay can only raise the critical q_0 value.

3.6.2.2 Higgs decay

The Higgs decays when $\Gamma \sim H$, provided decay is kinematically allowed. The condition for decay is

$$aH \sim \alpha M_{\rm eff}, \tag{3.67}$$

with $\alpha = y^2/(4\pi)$ and y a Yukawa/gauge coupling. For the top quark and gauge couplings $\alpha \sim (1-5)\times 10^{-2}$ at scales $\mu_{\rm cr}$, and for the bottom quark, tau and Higgs self coupling $\alpha \sim 10^{-4} - 10^{-5}$. The fermion/gauge boson mass in conformal time, the equivalent of $M_{\rm eff}$ for the Higgs field (3.41), only has a contribution from the Higgs fluctuations $M_y \sim y\sqrt{\bar{G}}$. Averaged over one oscillation $H^2 \sim R \sim A^2 m_\chi^2/a^3$, as follows from eq. (3.12).

Consider first the case that the tree-level term dominates the Higgs mass $M_{\rm eff}$. The Higgs is much heavier than the SM particles, and decay into top quarks and gauge bosons is kinematically possible. Decay only happens for $\sqrt{\xi}\alpha > 1$, so only for large couplings $\xi \gtrsim 10^4$.

In the opposite limit that quantum corrections dominate the Higgs mass, decay is kinematically allowed if $M_{\rm eff} > 2M_y$. Since both the mass of the Higgs and the mass of the decay products scale with $\sqrt{\bar{G}}$, decay into top quark and EW gauge bosons is impossible. Decay into lighter fields is still allowed, in particular decay into b-quarks, tau-leptons and Higgs will dominate. The Higgs decays when

$$\frac{\lambda \bar{G}}{a^2 \xi R} \gtrsim \frac{1}{\alpha^2 \xi} \gtrsim \frac{10^8}{\xi}, \tag{3.68}$$

where we used $\alpha \lesssim 10^{-4}$ in the last step.

Perturbative Higgs decay only happens at late times for the ξ couplings of interest, and can be neglected for our purposes.

3.6.2.3 Large Green function corrections

At late times the maximum value of the classical mass during an oscillation can be approximated by

$$M_{\rm eff}^2|_{\rm class} = a^2 \hat{\xi} R|_{\rm max} = \frac{2A_T^2 a_T^2 m_\chi^2 \hat{\xi} T^{-\frac{2}{3}}}{m_{\rm pl}^2} + \mathcal{O}(T^{-\frac{5}{2}}), \tag{3.69}$$

where we used eq. (3.12). The quantum contribution to the mass $M^2_{\rm eff}|_{\rm quant} = 6\lambda\bar{G}$ becomes of the same order as the classical contribution at time

$$T_{\rm G} \approx 5 \times 10^5 \left(\frac{10^{-2}}{\lambda}\right)^{3/2} {\rm e}^{-\frac{3}{2}c\sqrt{q_0}}, \tag{3.70}$$

where we used eq. (3.50), and c is given in eq. (3.51). We find $T_G \approx \{4 \times 10^3,\, 7 \times 10^2,\, 13,\, 0.2\}$ for $q_0 = \{1,\, 2,\, 5,\, 10\}$. Preheating is efficient and the vacuum is destabilized if the quantum correction dominates already when $H > \mu_{\rm cr}$, see our first stability condition (3.65). This requires $T_G < T_{\rm crit}$, with $T_{\rm crit}$ given in eq. (3.64):

$$T_{\rm G} \lesssim T_{\rm crit} \quad \Rightarrow \quad q_0 \gtrsim q_0^{\rm crit} = 4.5 \;\; (\text{or } \xi \gtrsim 24). \tag{3.71}$$

This is reasonably close to the value $q_0^{\rm crit} \approx 3.7$ that we find numerically.

3.6.2.4 Large energy density

For $T > T_{\rm crit}$ the potential always has a barrier; decay may still be possible if the energy density exceeds the maximum of the potential, see our second stability condition (3.66). The interesting parameter region is $q_0 < q_0^{\rm crit}$. In that case the energy density becomes larger than $V_{\rm max}$ at a time

$$T_\rho \sim 2 \times 10^3 {\rm e}^{-\frac{3}{4}c\sqrt{q_0}} \left(\frac{10^{-2}}{|\lambda|}\right)^{3/4}, \tag{3.72}$$

where we used approximation (3.53). The energy density becomes large before the quantum correction to the Green function becomes large, that is $T_\rho < T_G$, and the above time-scale was derived using the tree-level potential. Taking $|\lambda| = 10^{-2}$, $T_\rho \approx \{2 \times 10^2,\, 55,\, 6,\, 0.8\}$ for $q_0 = \{1,\, 2,\, 5,\, 10\}$.

3.6.2.5 Large vacuum dependence

We focus on the difference between the zeroth and second order adiabatic vacuum, as a measure of the vacuum dependence of the results. The vacuum dependence becomes of the same order as the Green function itself if

$$\frac{\Delta\bar{G}^{(2)}}{\bar{G}^{(0)}} > 1 \quad \Rightarrow \quad T > T_{\Delta G} = 6 \times 10^{-3} q_0^{3/2} {\rm e}^{3c\sqrt{q_0}}, \tag{3.73}$$

where we took $\cos(4\pi T) \sim 1$. This gives $T_{\Delta G} = \{80,\, 10^5,\, 10^8\}$ for $q_0 = \{1,\, 2,\, 5\}$. $T_{\Delta G} < 1$ for $q_0 \lesssim 1$. The Green function enters the first stability criterion (3.65) for effective preheating, which is valid if the vacuum decays within the first 25 oscillations and $q_0 > q_0^{\rm crit} = 4.5$. It follows from eq. (3.73) that the vacuum dependence of the results is small in this case.

If we compute the energy density at the instants where the vacuum dependence is minimized, $T \hat{=} \frac{1}{2}$, we have $\Delta\bar{\rho}^{(2)} = \frac{1}{64\pi^2} k_2^4$ and the vacuum dependence of the energy density becomes sizeable when

$$\frac{\Delta\bar{\rho}^{(2)}}{\bar{\rho}^{(0)}} > 1 \quad \Rightarrow \quad T > T_{\Delta\rho} = 0.21 e^{\frac{3}{2}c\sqrt{q_0}} q_0^2. \tag{3.74}$$

This gives $T_{\Delta\rho} \approx \{40,\, 10^3,\, 3\times 10^5\}$ for $q_0 = \{1,\, 2,\, 5\}$. The energy density enters the second stability criterion (3.66) for $q_0 < q_0^{\rm crit}$. Demanding that

$$T_\rho < T_{\Delta\rho} \quad \Rightarrow \quad q_0 \gtrsim 1.3 \quad (\text{or } \xi \gtrsim 7). \tag{3.75}$$

However, $V_{\rm max}$, $\bar{\rho}$ and $\Delta\bar{\rho}$ are all oscillating functions. We can not expect that an interpolation between the points where the vacuum dependence of $\bar{\rho}$ is minimized gives a proper description of $\bar{\rho}$ during the whole oscillation, or of the oscillation averaged $\bar{\rho}$. For an accurate determination of the tunnelling rate to the true vacuum, information at other time instants may be needed.

Moving slightly away from $T \hat{=} \frac{1}{2}$, the vacuum dependence is given by $\Delta\bar{\rho}^{(2)} = \frac{1}{256\sqrt{6}} \frac{k_3^{10}}{k_2^6}$ and $T_{\Delta\rho}$ becomes much smaller. Taking $T \hat{=} \frac{1}{2} + 0.05$ as an example, we get:

$$\frac{\Delta\bar{\rho}^{(2)}}{\bar{\rho}^{(0)}} > 1 \quad \Rightarrow \quad T > T_{\Delta\rho} = 0.27 e^{\frac{3}{5}c\sqrt{q_0}} q_0^{9/10}, \tag{3.76}$$

which gives $T_{\Delta\rho} \approx \{2,\, 10,\, 10^2\}$ for $q_0 = \{1,\, 2,\, 5\}$. Demanding again that $T_\rho < T_{\Delta\rho}$ gives the stronger bound

$$T_\rho < T_{\Delta\rho} \quad \Rightarrow \quad q_0 \gtrsim 2.8 \quad (\text{or } \xi \gtrsim 15). \tag{3.77}$$

Numerically we find $q_0 \sim 0.9$ (or $\xi \sim 5$) when we look at the vacuum dependence at $T \hat{=} \frac{1}{2}$, and $q_0 \sim 2.2$ (or $\xi \sim 12$) for $T \hat{=} \frac{1}{2} + 0.05$.

3.6.3 Numerical results

In this section we present the results of our numerical calculation, which serves as a check for the analytical results discussed in the previous sections. We focus on the calculation of the Higgs Green

function and energy density, and in particular on their vacuum dependence by calculating them in both the zeroth and second order vacuum eq. (3.31).

3.6.3.1 Numerical implementation

Since our aim is not so much on getting the most accurate results, but rather on investigating the vacuum dependence, we have made some simplifying assumptions to speed up the numerics.

First of all, we neglect the Higgs mass term and quartic Higgs coupling. The electroweak scale mass is negligible during preheating. The quartic coupling only becomes important near the maximum of the potential, but can be neglected for smaller field values. Since we are only interested in the question whether the EW vacuum is destabilized, and not in the exact dynamics of the Higgs after crossing the barrier, we can neglect this interaction. This is supported by numerical simulations in the literature (see e.g. Ref. [131]).

Secondly, we neglect backreaction. It can be checked that the backreaction on the inflaton equation of motion of the produced particles is small. The backreaction for the Higgs mode equation becomes important once the barrier disappears and M^2_{eff} becomes negative. At this point the vacuum is already destabilized.

Thirdly, we neglect the interaction of the Higgs with all other SM particles and also other inflaton interactions (which should be there for complete decay of the inflaton). As discussed in section 3.6.2, Higgs decay happens on large time-scales and can be neglected; inflaton decay is model dependent, but is expected to only increase stability.

Since the inflaton background is formulated in cosmic time (see eq. (3.7)), we solve for the Higgs modes in cosmic time as well. The mode functions satisfy the differential equation:

$$\ddot{U}_k + H\dot{U}_k + \frac{\omega_k^2}{a^2}U_k = 0, \qquad \omega_k^2 = k^2 + a^2(\xi - \frac{1}{6})R. \tag{3.78}$$

As suggested in Ref. [145], we write the mode functions as

$$U_k = e^{-i\omega_{k,0}\tau}(1 + g_k), \qquad g_k(t_0) = \dot{g}_k(t_0) = 0. \tag{3.79}$$

These g_k-functions satisfy the mode equation:

$$\ddot{g}_k + \left(H - \frac{2i\omega_{k,0}}{a}\right)\dot{g}_k = -\left(\xi - \frac{1}{6}\right)\left(R - \frac{a^2(t_0)}{a^2}R(t_0)\right)(1 + g_k). \tag{3.80}$$

The mode equations are solved numerically in Mathematica. The g_k-modes are numerically more stable for large k than the U_k-modes.

We are interested in the quantities $\bar{\rho}^{(n)}$ and $\bar{G}^{(n)}$, which are obtained by integrating over U_k-modes. In order to keep the computation time manageable, the integral is replaced by a sum. Typically we compute U_k and $\dot{U}_k$ for 100 values of k lying on a logarithmic scale between $10^{-7}m_{\rm pl}$ and $10^{-3}m_{\rm pl}$. The mode functions do not vary significantly with k for k as small as $10^{-7}m_{\rm pl}$. Furthermore, the contribution for small k is suppressed by the factor k^2 from the Jacobian, so our lower boundary is effectively zero. The contribution of the large k modes decreases exponentially beyond a certain cutoff (much smaller than $k = 10^{-3}m_{\rm pl}$), due to the adiabatic renormalization, and these modes can be neglected.

Since we use the adiabatic approximation for renormalization, our expressions for $\bar{\rho}$ and $\bar{G}$ are only properly defined when $W_k^2(t) > 0$. In order to have a continuous graph, we either interpolate between values of T for which $W_k^2(t) > 0$ when we focus on large time scales, or, when we focus on shorter time scales, we take the absolute value of the renormalization terms in eq. (3.34).

3.6.3.2 Results

Large q_0, immediate decay of the Higgs Preheating is efficient for $q_0 \gg 1$, or equivalently $\xi \gg 1$, and leads to decay of the electroweak vacuum. We show the results for $q_0 = 9.3$ ($\xi = 50$) in figure 3.3a. We plotted both the maximum of the oscillating tree-level contribution to the effective Higgs mass and the negative one-loop contribution. Within one inflaton oscillation the latter dominates and the first criterion for stability (3.65) is violated: the potential does not have a maximum anymore and the Higgs will inevitably roll down to the true minimum. It should be noted that once that happens, our results are inaccurate, since it is no longer justified to neglect the quartic term from the potential. We tested for vacuum dependence, by calculating the quantum correction in both the zeroth and second order adiabatic vacuum eq. (3.31). Only during the first half of the first oscillation we can see a difference between the zeroth and second order adiabatic renormalization, but the final result is nearly vacuum independent, as expected from eq. (3.73).

Large-T behavior of $\bar{G}$ and $\bar{\rho}$. For smaller values of q_0, preheating is less efficient, and the initial production of Higgs modes is not enough to let the Higgs decay within the first few oscillations.

As was shown in figure 3.1c, the Green function and energy density remain approximately constant after the initial amplification. Due to the different scaling of the classical and one-loop contribution,

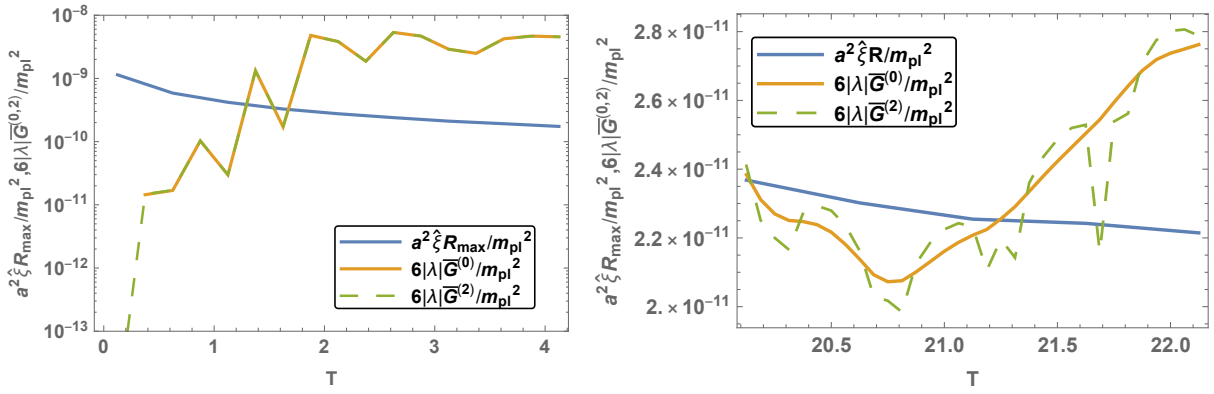

(A) Left: $q_0 = 9.3$. Tree-level contribution $a^2\hat{\xi}R$ (blue) and one-loop contribution $6|\lambda|\bar{G}$ (orange and green) to the effective Higgs mass for the first few oscillations. The $a^2\hat{\xi}R$-term oscillates in reality, but in this graph we show an interpolation between the maxima. The solid orange line shows the result for $\bar{G}$ in the zeroth order adiabatic vacuum, the dashed green line shows the second order result. In order to have a continuous plot, we take the absolute value of the renormalization terms in eq. (3.34). $\bar{G}$ is sampled with $\delta T = 1/4$. Right: $q_0 = 3.7$. (Interpolation between the maxima of) tree-level contribution $a^2\hat{\xi}R$ (blue) and one-loop contribution $6|\lambda|\bar{G}$ (orange and green) to the effective Higgs mass at $T \approx 21$. The solid orange line shows the result for $\bar{G}$ in the zeroth order adiabatic vacuum, the dashed green line shows the second order result. In order to have a continuous plot, we take the absolute value of the renormalization terms in eq. (3.34). $\bar{G}$ is sampled with $\delta T = 1/16$.

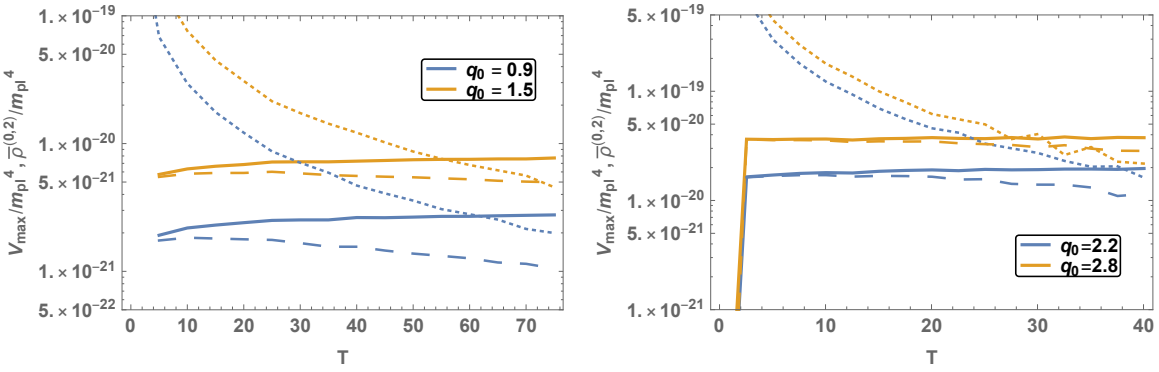

(B) Interpolation of the maxima of $\bar{\rho}$ and $\bar{V}_{\max}$ as a function of time. The solid line shows $\bar{\rho}^{(0)}$, the dashed line shows $\bar{\rho}^{(2)}$, the dotted line shows $\bar{V}_{\max}$ in the zeroth order vacuum (the second order result looks identical). Left: $q_0 = 0.9$ (blue) and $q_0 = 1.5$ (orange). $\bar{\rho}$ and $\bar{V}_{\max}$ are sampled with $\delta T = 5$, starting at $T = 0$, such that the vacuum dependence is minimized. Right: $q_0 = 2.2$ (blue) and $q_0 = 2.8$ (orange). $\bar{\rho}$ and $\bar{V}_{\max}$ are sampled with $\delta T = 2.5$, starting at $T = 0.05$.

FIGURE 3.3

the first stability criterion might still be violated before H becomes smaller than the instability scale $\mu_{\rm cr}$ even if q_0 was not large enough to lead to immediate Higgs decay.

Figure 3.3a shows the tree-level and one-loop mass entering the first stability criterion (3.65) at $T \approx 21$ for $q_0 = 3.7$ ($\xi = 20$). The graph shows that the one-loop contribution indeed becomes larger than the tree-level contribution, resulting in decay of the Higgs. The difference between $\bar{G}$ in the two vacua is approximately 50 times smaller than $\bar{G}$ itself. Since the Hubble constant becomes smaller than $\mu_{\rm cr}$ around $T = 25$, the first criterion for stability will not be violated for values of $q_0 \lesssim 3.7$. This value of q_0 is reasonably close to the estimated value of $q_0^{\rm crit} = 4.5$.

Comparison of $\bar{V}_{\max}$ and $\bar{\rho}$ for $q_0 < 3.7$. For $q_0 < 3.7$, the Green function contribution does not become dominant before $T = 25$, so we need to look at the second stability criterion (3.66) to determine the fate of the Higgs.

The left plot of figure 3.3b shows a comparison between $\bar{\rho}^{(0)}$, $\bar{\rho}^{(2)}$ and $\bar{V}_{\max}$ for $q_0 = 0.9, 1.5$ ($\xi = 5, 8$) for values $T \hat{=} \frac{1}{2}$ where the vacuum dependence is minimized. The computation of $\bar{V}_{\max}$ is done in the zeroth order vacuum, but the vacuum dependence of $\bar{V}_{\max}$ is in any case subdominant. For $q_0 = 1.5$, $\bar{\rho}$ becomes comparable to $\bar{V}_{\max}$ when the vacuum dependence is still rather small, implying that there is a possibility of vacuum decay (remember though that $\bar{\rho}$ oscillates). For $q_0 = 0.9$, $\Delta\bar{\rho}^{(2)}$ becomes comparable to $\bar{\rho}^0$ at the same time when $\bar{\rho}^{(0)} = \bar{V}_{\max}$. As a consequence, we can not determine whether the Higgs decays. Our critical value of q_0 agrees reasonably well with the estimated value of $q_0 \approx 1.3$. We conclude that for $q_0 \lesssim 0.9$ (or $\xi \lesssim 12$) we can not draw vacuum-independent conclusions about the stability of the Higgs.

The right graph of figure 3.3b gives an even stricter bound on the value of q_0 for which vacuum-independent statements can be made. $\bar{\rho}$ and $\bar{V}_{\max}$ are determined at $T \hat{=} \frac{1}{2} + 0.05$. We then find that no vacuum-dependent statements can be made for $q_0 \lesssim 2.2$.

3.7 Conclusion

In this chapter we studied the stability of the Higgs field during preheating in the presence of a non-minimal coupling between the Higgs field and the Ricci scalar. After inflation the inflaton oscillates in its potential and the effective Higgs mass squared oscillates between positive and negative values. Higgs modes with momentum k such that $\omega_k^2 < 0$ during part of the inflaton oscillation are produced

through tachyonic preheating; in addition non-adiabatic modes are produced in a broad parametric resonance. The produced Higgs modes contribute to the effective potential and the energy density.

Vacuum decay can now occur in two ways. First, if preheating is very efficient it leads to explosive particle production and within a few oscillations the effective Higgs mass is dominated by the one-loop corrections. At early times the Hubble exceeds the critical renormalization scale and the Higgs coupling is negative $\lambda(\mu \sim H) < 0$, and consequently the effective Higgs mass is negative. The Higgs will inevitably roll down to the true minimum. Secondly, if preheating is less efficient, the one-loop contribution may still dominate at late times as the background term redshifts away faster. At late times and for smaller Hubble scale, the effective potential will always have a barrier separating the true and false vacuum. However, the energy density may become comparable or larger than the maximum of the potential, making tunnelling to the true vacuum likely.

Particle production is dominated by the initial times, where the Higgs mass becomes most negative. This allows to approximate the Green function and energy density by the contribution during the first oscillation, as it remains (nearly) constant afterwards. We presented the semi-analytic approximations in section 3.4. We compared the analytical estimate of the Green function and energy density with the numerical values for values of the efficiency parameter q_0 between 0.16 and 9.3 (ξ between 1 and 50) and found an agreement up to a factor of 2 for most values of q_0.

The results are defined with respect to the nth order adiabatic vacuum. The adiabatic vacuum is a good vacuum for high momentum modes, for which the adiabaticity parameters defined in eq. (3.28) are small at least during part of the inflaton oscillation. However, for smaller momenta, adiabaticity is always violated. We found that the contribution of the non-adiabatic momenta to the Green function and/or energy density grows with time, and thus the vacuum dependence grows with time. Since different choices of vacua correspond to different renormalization conditions, there is thus an uncertainty in the values of the renormalized couplings — and in the definition of the critical coupling for vacuum stability — which can only be fixed (in theory) by a measurement during preheating.

Our main results are that for $q_0 \gtrsim 3.7$ preheating is efficient and the vacuum decays at early times when $H > \mu_{\rm cr}$. This is in agreement with results in the literature [130–134]. Since decay is rapid, vacuum effects are negligible in this case.

For $0.9. \lesssim q_0 \lesssim 3.7$ the Higgs potential always has a barrier, but the energy density becomes of the order of the barrier height before the results are swamped by uncertainties due to the vacuum choice.

For $q_0 \lesssim 0.9$ however, no definite statements can be made. This bound becomes stricter if we compare $\bar{\rho}$ and $\bar{V}_{\max}$ at time instants where the vacuum dependence of $\bar{\rho}$ is not minimized. When the energy density becomes large enough for the vacuum to be in peril, the vacuum dependence is already large (the difference in energy density for different vacua is larger than the energy density itself calculated in the zeroth order vacuum). As a consequence there is a large uncertainty in the definition of the effective couplings, and thus any attempt to determine a critical coupling for stability is hampered by that. Note that this is arguably the most interesting part of parameter space, as order one couplings and initial conditions such as in chaotic or Starobinsky inflation lead to $q_0 = \mathcal{O}(1)$.

Chapter 4

Preheating after Higgs inflation: self-resonance and gauge boson production

4.1 Introduction

In this chapter we study the production of Standard Model particles after inflation caused by the Higgs field. The intriguing possibility of identifying the Higgs field with the scalar field driving inflation requires a non-minimal coupling between the Higgs field and the Ricci curvature scalar $\mathcal{L} \supset \frac{1}{2}R(m_{\rm pl}^2 + 2\xi\Phi^\dagger\Phi)$ [155]. We are already familiar with this coupling from chapter 3, but note that the non-minimal-coupling term needed for Higgs inflation has a different sign than the term used in chapter 3 (see eq. (3.4)). In both chapters we study positive values of ξ.

Since Higgs inflation is not feasible for negative values of the Higgs self-coupling λ, in this chapter we will assume that it is positive. The measured value of the amplitude of scalar perturbations determines the value of λ/ξ^2. The inherent ambiguity in the running of λ at high energies, due to our incomplete knowledge of possible new physics between the TeV and inflationary scales, leads to an ambiguity in the exact value of the required non-minimal coupling [156–160]. While simple estimates like $\lambda_{\rm infl} = \mathcal{O}(0.01)$ lead to the requirement of $\xi = \mathcal{O}\left(10^4\right)$, smaller values of λ can allow for much smaller non-minimal couplings. We will remain agnostic about the exact running of the Standard Model couplings at high energies and instead explore a broad parameter range[1]

[1]For inflation on the flat plateau one should consider $\xi \gtrsim 440$ (e.g. [161]). In models of hilltop or inflection point inflation, smaller values of ξ are possible, although UV corrections are expected to be larger. A discussion of the effects of UV corrections, as well as initial conditions, in Higgs inflation can be found for example in Refs. [162, 163]. In order to provide a treatment of Higgs inflation as complete as possible without referring to specific unknown physics, we choose to consider a broad range of non-minimal couplings that go below $\xi \approx 400$.

covering $10 \lesssim \xi \lesssim 10^4$.

A basic feature of inflationary models with non-minimal couplings is that they provide universal predictions for the spectral observables n_s and r, largely independent of the exact model parameters and initial conditions [164, 165]. These observables fall in line with the Starobinsky model [136] as well as with the large family of α-attractors [166–170]. Even after the latest Planck release [77], these models, which predict $n_s = 1 - 2/N_*$ and $r = \mathcal{O}(1/N_*^2)$, continue to be compatible with the data for modes that exit the horizon at $N_* \simeq 55$ e-folds before the end of inflation.

Higgs inflation provides a unique opportunity to study the transition from inflation to radiation domination, since the couplings of the Higgs-inflaton to the rest of the SM are known. Detailed analyses of reheating in Higgs inflation were first performed in Refs. [171, 172] and extended in Ref. [173] using lattice simulations. However, as discussed later in Refs. [174–176] and independently in Ref. [177], multi-field models of inflation with non-minimal couplings to gravity can exhibit more efficient preheating behavior than previously thought, due to the contribution of the field-space structure to the effective mass of the fluctuations. Furthermore, it was shown in Refs. [174–176] that, in non-minimally coupled models, preheating efficiency can be vastly different for different values of the non-minimal coupling, even if these values lead to otherwise identical predictions for CMB observables. We will thus perform a detailed study of preheating in Higgs inflation, extending the results of Refs. [171, 172, 174–177], in order to distinguish between Higgs inflation models with different values of the non-minimal coupling.

Because of the appeal of Higgs inflation as an economical model of realizing inflation within the particle content of the Standard Model, the unitarity cutoff scale of the theory has been extensively studied [159, 160, 178–190] (see also Ref. [191] for a recent review). For large values of the Higgs vev, like the ones appearing during inflation on the flat plateau, the appropriate unitarity cutoff scale is $m_{\rm pl}/\sqrt{\xi}$, while for small values of the Higgs vev it must be substituted by $m_{\rm pl}/\xi$.

In section 4.2, we introduce a simplified model of a complex Higgs field coupled to an Abelian gauge field. We also discuss the relation to the full SM gauge sector. In section 4.3 we study self-resonance of Higgs modes. Section 4.4 deals with the evolution of the gauge fields during and after Higgs inflation. At the end of this section we also address the unitarity scale. The effect of decays and scattering processes that involve the produced Higgs and gauge bosons are summarized in section 4.5 and observational consequences in 4.6. Concluding remarks follow in section 4.7. This chapter is a modified version of our work [2]. We will occasionally omit some details and refer to the original paper.

4.2 Abelian model and formalism

We build on the formalism of Ref. [192] for the evolution of non-minimally coupled multi-field models, as it was applied in Refs. [164, 193, 194] during inflation and in Refs. [174–176] during preheating. The electroweak sector consists of a complex Higgs doublet, expressed using 4 real-valued scalar fields in $3+1$ spacetime dimensions:

$$\Phi = \frac{1}{\sqrt{2}} \begin{pmatrix} \theta^1 + i\theta^2 \\ \varphi + h + i\theta \end{pmatrix} , \tag{4.1}$$

where φ is the background value of the Higgs field, h denotes the Higgs fluctuations and θ, θ^1 and θ^2 are the Goldstone modes. In order to study decay into gauge bosons, we add the $SU(2)_L$ and $U(1)_Y$ gauge sectors. We will start by closely examining a simplified Abelian model as a proxy for the full electroweak sector, consisting of the complex scalar field

$$\Phi = \frac{1}{\sqrt{2}}(\varphi + h + i\theta), \tag{4.2}$$

and a $U(1)$ gauge field only. We discuss the relation between this simplified Abelian model and the equations of the full Higgsed electroweak sector in section 4.2.3.

In order to connect our notation to that of Ref. [192] we identify $\phi^1 = \varphi + h$ and $\phi^2 = \theta$. We will start by deriving the equations of motion for general ϕ^I-fields for notational simplicity. We use upper-case Latin letters to label field-space indices, $I, J = 1, 2, 3, 4$ (or just $I, J = 1, 2$ in the Abelian case); Greek letters to label spacetime indices, $\mu, \nu = 0, 1, 2, 3$; and lower-case Latin letters to label spatial indices, $i, j = 1, 2, 3$.

We first consider $U(1)$ symmetry with the corresponding gauge field B_μ. The Lagrangian in the Jordan frame is given by

$$S_J = \int d^4x\sqrt{-\tilde{g}}\Big[f(\Phi,\Phi^\dagger)\tilde{R} - \tilde{g}^{\mu\nu}(\tilde{\nabla}_\mu\Phi)^\dagger\tilde{\nabla}_\nu\Phi - \frac{1}{4}\tilde{g}^{\mu\rho}\tilde{g}^{\nu\sigma}F_{\mu\nu}F_{\rho\sigma} - \tilde{V}(\Phi,\Phi^\dagger)\Big] . \tag{4.3}$$

The covariant derivative $\tilde{\nabla}_\mu$ is given by

$$\tilde{\nabla}_\mu = \tilde{D}_\mu + ieB_\mu, \tag{4.4}$$

where $\tilde{D}_\mu$ is a covariant derivative with respect to the space-time metric $\tilde{g}_{\mu\nu}$ and e is the coupling constant. The corresponding field strength tensor[2] is

$$F_{\mu\nu} = \tilde{D}_\mu B_\nu - \tilde{D}_\nu B_\mu. \tag{4.5}$$

By performing a conformal transformation

$$\tilde{g}_{\mu\nu}(x) \to g_{\mu\nu}(x) = \frac{2}{m_{\rm pl}^2} f(\Phi, \Phi^\dagger)\, \tilde{g}_{\mu\nu}(x), \tag{4.6}$$

the action in the Einstein frame becomes

$$\begin{aligned} S = \int d^4x\sqrt{-g}\Bigg[& \frac{m_{\rm pl}^2}{2} R - g^{\mu\nu}\Big(\frac{1}{2}\mathcal{G}_{IJ}(\Phi,\Phi^\dagger) D_\mu\phi^I D_\nu\phi^J + \frac{m_{\rm pl}^2}{2f(\Phi,\Phi^\dagger)} \\ & \Big((ieB_\mu\Phi)^\dagger (ieB_\nu\Phi) + ie(-B_\mu\Phi^\dagger D_\nu\Phi + B_\nu(D_\mu\Phi^\dagger)\Phi)\Big)\Big) - V(\Phi,\Phi^\dagger) - \frac{1}{4} g^{\mu\rho} g^{\nu\sigma} F_{\mu\nu} F_{\rho\sigma}\Bigg], \end{aligned} \tag{4.7}$$

with

$$V(\Phi,\Phi^\dagger) = \frac{m_{\rm pl}^4}{4f^2(\Phi,\Phi^\dagger)} \tilde{V}(\Phi,\Phi^\dagger), \tag{4.8}$$

and

$$\mathcal{G}_{IJ}(\Phi,\Phi^\dagger) = \frac{m_{\rm pl}^2}{2f(\Phi,\Phi^\dagger)} \left[\delta_{IJ} + \frac{3}{f(\Phi,\Phi^\dagger)} f(\Phi,\Phi^\dagger)_{,I}\, f(\Phi,\Phi^\dagger)_{,J}\right], \tag{4.9}$$

as in Refs. [192, 193]. The subscript $,I$ denotes a derivative with respect to the field ϕ^I. The potential in the Jordan frame is the usual Standard Model Higgs potential

$$\tilde{V}(\Phi,\Phi^\dagger) = \lambda\left(\Phi^\dagger\Phi - \frac{1}{2}v_0^2\right)^2 \simeq \lambda\left(\Phi^\dagger\Phi\right)^2, \tag{4.10}$$

where the Higgs vacuum expectation value $v_0 = 246\,\text{GeV}$ can be safely neglected at field values that arise during inflation and preheating. Hence the Higgs potential can be adequately modeled by a pure quartic term.

[2]The tensor $F_{\mu\nu}$ is defined with lower indices. In that case it does not matter whether partial or covariant derivatives are used. However, when working with $\tilde{F}^{\mu\nu}$ it *does* matter, since the metric does not commute with partial derivatives. So $\tilde{F}^{\mu\nu}$ is given by $\tilde{F}^{\mu\nu} = \tilde{g}^{\mu\rho}\tilde{g}^{\nu\sigma}F_{\rho\sigma} = \tilde{g}^{\mu\rho}\tilde{g}^{\nu\sigma}(\tilde{D}_\rho B_\sigma - \tilde{D}_\sigma B_\rho) = \tilde{D}^\mu B^\nu - \tilde{D}^\nu B^\mu$.

For the sake of readability, we will drop the arguments of $\mathcal{G}, V$ and f from now on. Varying the action with respect to the scalar fields ϕ^I, the corresponding equation of motion for ϕ^I is

$$\begin{aligned}
&\Box\phi^I + g^{\mu\nu}\Gamma^I_{JK}\partial_\mu\phi^J\partial_\nu\phi^K + \mathcal{G}^{IJ}\left(\left(\frac{m_{\rm pl}^4}{4\xi f}e^2B^2\right)_{,J} - V_{,J}\right) + ie\frac{m_{\rm pl}^2}{2f^2}f_{,J}\,\mathcal{G}^{IJ}\Big(-B^\mu\Phi^\dagger D_\mu\Phi \\
&+ B^\mu(D_\mu\Phi^\dagger)\Phi\Big) - iem_{\rm pl}^2\mathcal{G}^{IJ}\left(-\frac{1}{2f}B^\mu\Phi^\dagger{}_{,J}\,D_\mu\Phi + D_\mu\left(\frac{1}{2f}B^\mu\Phi^\dagger\right)\Phi_{,J}\right. \\
&\left. - \Phi^\dagger{}_{,J}\,D_\mu\left(\frac{1}{2f}B^\mu\Phi\right) + \frac{1}{2f}B^\mu\left(D_\mu\Phi^\dagger\right)\Phi_{,J}\right) = 0.
\end{aligned} \tag{4.11}$$

We work to first order in fluctuations, in both the scalar fields and spacetime metric. The gauge fields have no background component, thus we only treat them as first-order perturbations. We consider scalar metric perturbations around a spatially flat FLRW metric,

$$\begin{aligned}
ds^2 &= g_{\mu\nu}(x)\,dx^\mu dx^\nu \\
&= -(1+2A)dt^2 + 2a\,(\partial_i\mathcal{B})\,dx^i dt + a^2\left[(1-2\psi)\delta_{ij} + 2\partial_i\partial_j E\right]dx^i dx^j,
\end{aligned} \tag{4.12}$$

where $a(t)$ is the scale factor. We may always choose a coordinate transformation and eliminate two of the four scalar metric functions that appear in eq. (4.12). We work in the longitudinal gauge, where $\mathcal{B}(x) = E(x) = 0$. Furthermore, in the absence of anisotropic pressure perturbations, the remaining two functions are equal $A(x) = \psi(x)$.

We also expand the fields,

$$\phi^I(x^\mu) = \varphi^I(t) + \delta\phi^I(x^\mu). \tag{4.13}$$

Note that for Higgs inflation only ϕ^1 has a background value, $\varphi(t)$, whereas the background value of ϕ^2 is zero.

We may then construct generalizations of the Mukhanov-Sasaki variable that are invariant with respect to spacetime gauge transformations up to first order in the perturbations [192, 195–197]:

$$Q^I = \delta\phi^I + \frac{\dot\varphi^I}{H}\psi. \tag{4.14}$$

The background equation of motion for φ^I is unchanged with respect to models with multiple scalar fields and no gauge bosons

$$\mathcal{D}_t\dot\varphi^I + 3H\dot\varphi^I + \mathcal{G}^{IJ}V_{,J} = 0\,, \tag{4.15}$$

and

$$\begin{aligned} H^2 &= \frac{1}{3m_{\rm pl}^2}\left[\frac{1}{2}\mathcal{G}_{IJ}\dot{\varphi}^I\dot{\varphi}^J + V(\varphi^I)\right], \\ \dot{H} &= -\frac{1}{2m_{\rm pl}^2}\mathcal{G}_{IJ}\dot{\varphi}^I\dot{\varphi}^J, \end{aligned} \tag{4.16}$$

where overdots denote derivatives with respect to t, and the Hubble parameter is given by $H(t) = \dot{a}/a$. Covariant derivatives with respect to the field-space metric are given by $\mathcal{D}_J A^I = \partial_J A^I + \Gamma^I_{\ JK} A^K$ for a field-space vector[3] A^I, from which we may construct the (covariant) directional derivative with respect to cosmic time,

$$\mathcal{D}_t A^I = \dot{\varphi}^J \mathcal{D}_J A^I = \dot{A}^I + \Gamma^I_{\ JK}\dot{\varphi}^J A^K\,, \tag{4.17}$$

where the Christoffel symbols $\Gamma^I_{\ JK}(\varphi^L)$ are constructed from $\mathcal{G}_{IJ}(\varphi^K)$.

We now specify our analysis to the case of a complex Higgs field with background $\varphi(t)$ and fluctuations $h(t,\vec{x})$ and $\theta(t,\vec{x})$ as in eq. (4.2). The equation of motion for the gauge-invariant fluctuation Q^I is identical to the case without the presence of a gauge-field [174–176, 192], up to terms that mix θ and B_μ:

$$\begin{aligned} &\mathcal{D}_t^2 Q^I + 3H\mathcal{D}_t Q^I + \left[\frac{k^2}{a^2}\delta^I_J + \mathcal{M}^I_{\ J}\right] Q^J \\ &- e\frac{m_{\rm pl}^2}{2f}\mathcal{G}^{IJ}\frac{d\theta}{d\phi^J}\left(2B^\mu\partial_\mu\varphi + (D_\mu B^\mu)\varphi + 2fB^\mu\varphi D_\mu\left(\frac{1}{2f}\right)\right) = 0, \end{aligned} \tag{4.18}$$

where we define the mass-squared matrix by

$$\mathcal{M}^I_{\ J} \equiv \mathcal{G}^{IK}\left(\mathcal{D}_J\mathcal{D}_K V\right) - \mathcal{R}^I_{\ LMJ}\dot{\varphi}^L\dot{\varphi}^M - \frac{1}{m_{\rm pl}^2 a^3}\mathcal{D}_t\left(\frac{a^3}{H}\dot{\varphi}^I\dot{\varphi}_J\right), \tag{4.19}$$

and $\mathcal{R}^I_{\ LMJ}$ is the Riemann tensor constructed from the field-space metric $\mathcal{G}_{IJ}(\varphi^K)$. The term in eq. (4.19) proportional to $1/m_{\rm pl}^2$ arises from the coupled metric perturbations through expanding Einstein's field equations to linear order and using eq. (4.14). It hence vanishes in the limit of an infinitely rigid spacetime $m_{\rm pl} \to \infty$. In the single field attractor [164, 174, 193], the background field motion proceeds along a straight single-field trajectory $\varphi(t)$. $\mathcal{G}^{IJ}$ and $\mathcal{M}^{IJ}$ are then diagonal

[3] Examples of field-space vectors include $A^I = \delta\phi^I$ and $A^I = \dot{\varphi}^I$.

at background order, so the equations of motion for the first order fluctuations h and θ do not mix:

$$\begin{aligned}
&\mathcal{D}_t^2 Q^h + 3H\mathcal{D}_t Q^h + \left[\frac{k^2}{a^2} + \mathcal{M}^h{}_h\right] Q^h = 0, \\
&\mathcal{D}_t^2 Q^\theta + 3H\mathcal{D}_t Q^\theta + \left[\frac{k^2}{a^2} + \mathcal{M}^\theta{}_\theta\right] Q^\theta \\
&- e\frac{m_{\rm pl}^2}{2f}\mathcal{G}^{\theta\theta}\left(2B^\mu\partial_\mu\varphi + (D_\mu B^\mu)\varphi + 2fB^\mu\varphi D_\mu\left(\frac{1}{2f}\right)\right) = 0,
\end{aligned} \tag{4.20}$$

where

$$Q^h = h + \frac{\dot\varphi}{H}\Psi, \qquad Q^\theta = \theta. \tag{4.21}$$

We see that only the Higgs fluctuations, generated along the direction of background motion, are coupled to the metric perturbations Ψ. In the language of Refs. [174–176], the Higgs fluctuations correspond to adiabatic modes.

The equations are simplified if we replace $Q^I \to X^I/a(t)$ and use covariant derivatives with respect to conformal time τ instead of cosmic time. We multiply the equations by a^3 and obtain:

$$\mathcal{D}_\tau^2 X^h + (k^2 + a^2(\mathcal{M}^h{}_h - \frac{1}{6}R\mathcal{G}^h{}_h))X^h = 0, \tag{4.22}$$

$$\mathcal{D}_\tau^2 X^\theta + (k^2 + a^2(\mathcal{M}^\theta{}_\theta - \frac{1}{6}R\mathcal{G}^\theta{}_\theta))X^\theta - ea^3\frac{m_{\rm pl}^2}{2f}\mathcal{G}^{\theta\theta}(2B^0\dot\varphi + (D_\mu B^\mu)\varphi - \frac{\dot f}{f}B^0\varphi) = 0\,. \tag{4.23}$$

Variation of the action with respect to the gauge field gives

$$D_\nu F^{\nu\mu} - \frac{m_{\rm pl}^2 e^2}{f}\Phi^\dagger\Phi B^\mu + ie\frac{m_{\rm pl}^2}{2f}g^{\mu\nu}(\Phi^\dagger\partial_\nu\Phi - (\partial_\nu\Phi^\dagger)\Phi) = 0. \tag{4.24}$$

Since there is no background value for the gauge field, the first order perturbation equation is:

$$D_\nu F^{\nu\mu} - \frac{m_{\rm pl}^2 e^2}{2f}\varphi^2 B^\mu + e\frac{m_{\rm pl}^2}{2f}g^{\mu\nu}(\theta\partial_\nu\varphi - \varphi\partial_\nu\theta) = 0, \tag{4.25}$$

where we used eq. (4.2) and we stress again that $F^{\nu\mu}$ is defined using covariant derivatives.

Until now we have worked in full generality, not choosing a gauge. Hence we are in principle working with more degrees of freedom than needed. We will distinguish two frequently used gauges: unitary and Coulomb gauge. The equation of motion of X^h is unaffected by the gauge choice.

4.2.1 Unitary gauge

In unitary gauge $\theta = 0 = X^\theta$. We go to Fourier space, with convention $f(x) = \int \frac{d^3\mathbf{k}}{(2\pi)^{3/2}} f_\mathbf{k} e^{-i\mathbf{k}\cdot\mathbf{x}}$ and split the field into a transverse ($B_k^\pm$) and longitudinal (B_k^L) mode:

$$\vec{B}_\mathbf{k} = \hat{\epsilon}^L_\mathbf{k} B^L_\mathbf{k} + \hat{\epsilon}^+_\mathbf{k} B^+_\mathbf{k} + \hat{\epsilon}^-_\mathbf{k} B^-_\mathbf{k} \,, \tag{4.26}$$

with

$$i\mathbf{k}\cdot\hat{\epsilon}^L_\mathbf{k} = |\mathbf{k}|, \qquad \mathbf{k}\cdot\hat{\epsilon}^\pm_\mathbf{k} = 0 \,. \tag{4.27}$$

The equations of motion for the transverse and longitudinal modes become (see Ref. [2] for a derivation):

$$\begin{aligned} &\partial_\tau^2 B^\pm_\mathbf{k} + (k^2 + a^2 \frac{m_{\rm pl}^2 e^2}{2f}\varphi^2) B^\pm_\mathbf{k} = 0 \,, \\ &\partial_\tau^2 B^L_\mathbf{k} + 2\left(\frac{\partial_\tau\varphi}{\varphi} - \frac{\partial_\tau f}{2f} + \frac{\partial_\tau a}{a}\right) \frac{k^2}{k^2 + \frac{m_{\rm pl}^2 a^2}{2f} e^2\varphi^2} \partial_\tau B^L_\mathbf{k} + (k^2 + a^2 \frac{m_{\rm pl}^2 e^2}{2f}\varphi^2) B^L_\mathbf{k} = 0 \,. \end{aligned} \tag{4.28}$$

4.2.2 Coulomb gauge

In Coulomb gauge ($\partial_i B^i = 0$), the Goldstone mode θ remains an explicit dynamical degree of freedom and the equation of motion for X^θ is:

$$\begin{aligned} &\mathcal{D}_\tau^2 X^\theta - 2e^2 \frac{m_{\rm pl}^4}{4f^2} \mathcal{G}^{\theta\theta} \frac{\varphi(\partial_\tau\varphi - \frac{\partial_\tau f}{2f}\varphi + \frac{\partial_\tau a}{a}\varphi)}{\frac{k^2}{a^2} + \frac{m_{\rm pl}^2 e^2\varphi^2}{2f}} \mathcal{D}_\tau X^\theta \\ &+ \left(k^2 + a^2(\mathcal{M}^\theta{}_\theta - \frac{1}{6} R \mathcal{G}^\theta{}_\theta) + e^2 \frac{m_{\rm pl}^4}{4f^2} \mathcal{G}^{\theta\theta} \Big(a^2\varphi^2 + 2 \frac{(\partial_\tau\varphi - \frac{\partial_\tau f}{2f}\varphi + \frac{\partial_\tau a}{a}\varphi)(\partial_\tau\varphi + \frac{\partial_\tau a}{a}\varphi)}{\frac{k^2}{a^2} + \frac{m_{\rm pl}^2 e^2}{2f}\varphi^2} \right. \\ &\left. + 2 \frac{\partial_\tau\varphi\varphi(\partial_\tau\varphi - \frac{\partial_\tau f}{2f}\varphi + \frac{\partial_\tau a}{a}\varphi)}{\frac{k^2}{a^2} + \frac{m_{\rm pl}^2 e^2}{2f}\varphi^2} \Gamma^\theta_{h\theta} \Big) \right) X^\theta = 0 \,. \end{aligned} \tag{4.29}$$

We must demand that physical observables are identical in the two gauges, and derive a relation between $\theta_\mathbf{k}$ in Coulomb gauge and $B^L_\mathbf{k}$ in unitary gauge. $X^h_\mathbf{k}$ and $B^\pm_\mathbf{k}$ are already identical in the two gauges. The longitudinal component of the electric field[4] is given by

$$E^L_\mathbf{k} = \dot{B}^L_\mathbf{k} - k B_{0,\mathbf{k}}. \tag{4.30}$$

[4]The gauge field being studied is not the $U(1)_Q$ of the electromagnetic sector. However, we will use the familiar nomenclature found in electromagnetism.

In unitary and Coulomb gauge we get

$$\text{Unitary:}\quad E^L_{\mathbf{k}} = \frac{m_{\rm pl}^2 e^2}{2f}\varphi^2 \frac{\dot{B}^L_{\mathbf{k}}}{\frac{k^2}{a^2}+\frac{m_{\rm pl}^2 e^2}{2f}\varphi^2}\,, \qquad \text{Coulomb:}\quad E^L_{\mathbf{k}} = -k\frac{m_{\rm pl}^2 e}{2f}\frac{\theta_{\mathbf{k}}\dot{\varphi}-\varphi\dot{\theta}_{\mathbf{k}}}{\frac{k^2}{a^2}+\frac{m_{\rm pl}^2 e^2}{2f}\varphi^2}. \tag{4.31}$$

Since E_L should not depend on the gauge, we can use these expressions to solve for B_L in terms of θ. We obtain

$$B^L_{\mathbf{k}} = \frac{k}{e\varphi}\theta_{\mathbf{k}}. \tag{4.32}$$

It is interesting to note that there is no ξ-dependent term in the relation of $\theta_{\mathbf{k}}$ to $B^L_{\mathbf{k}}$. It is a straightforward algebraic exercise to show that by using eq. (4.32), the equation of motion for $B^L_{\mathbf{k}}$ and $\theta_{\mathbf{k}}$ can be transformed into each other, providing a useful check for our derivation.

During preheating, when the background inflaton field oscillates, the unitary gauge becomes ill-defined at the times where $\varphi(t) = 0$, as can be seen for example in the transformation relation of eq. (4.32). We will perform preheating simulations is the Coulomb gauge, which is always well-defined.

4.2.3 Full $SU(2)_L \times U(1)_Y$-sector

In section 3 of Ref. [2] we compute the equations of motion for the full Higgsed electroweak sector. To first order in fluctuations non-Abelian effects are absent and the equations of motion derived above can easily be translated to the full electroweak case. The equations of motion of the background field φ and the Higgs boson h do not change. The photon does not couple to the Higgs field and its equation of motion $D_\nu F^{\nu\mu} = 0$ is therefore unaffected.

In unitary gauge the relevant degrees of freedom are the transverse and longitudinal polarizations of the W- and Z-bosons. Their equations of motion are identical to eqs. (4.28) with the replacement $e^2 \to \frac{g^2}{2}$ for the W and $e^2 \to \frac{g^2}{4\cos^2\theta_W}$ for the Z, where g is the $SU(2)$ coupling constant and θ_W the Weinberg angle.

In Coulomb gauge the equations of motion for the transverse polarizations of W and Z are the same as in unitary gauge. The equation of motion of the Goldstone mode θ is obtained from eq. (4.29) by the replacement $e^2 \to \frac{g^2}{4\cos^2\theta_W}$. The equations for the other Goldstone modes $\phi^I = \theta^1, \theta^2$ are obtained from eq. (4.29) by replacing $e^2 \to \frac{g^2}{4}$ and the field-space-dependent quantities $\mathcal{G}^{\theta\theta} \to \mathcal{G}^{\phi^I\phi^I}$ and $\Gamma^{\theta}_{h\theta} \to \Gamma^{\phi^I}_{h\phi^I}$.

For simplicity, we will work with the Abelian equations derived in section 4.2 in the rest of this chapter.

4.2.4 Single-field attractor and parameter choices

For Higgs inflation, the function $f(\Phi, \Phi^\dagger)$ is given by [155]:

$$f(\Phi, \Phi^\dagger) = \frac{m_{\rm pl}^2}{2} + \xi \Phi^\dagger \Phi. \tag{4.33}$$

For typical values of Higgs inflation $\lambda = \mathcal{O}(0.01)$ and correspondingly $\xi \sim 10^4$. If we consider a different RG flow for the self-coupling λ, through the introduction of unknown physics before the inflationary scale, or different boundary conditions at the EW scale, λ will become smaller or larger at inflationary energies. Since, as we will show below, the combination λ/ξ^2 is fixed by the amplitude of the scalar power spectrum, a larger or smaller value of λ during inflation will lead to a correspondingly larger or smaller value of the non-minimal coupling ξ. We will consider values of ξ in the range $10 \leq \xi \leq 10^4$. The inflationary predictions for the scalar and tensor modes for non-minimally coupled models with $\xi \geq 10$ fall into the large-ξ single-field attractor regime, as described for example in Ref. [164]. This results in very simple expressions for the scalar spectral index n_s, the tensor-to-scalar ratio r and the running of the spectral index α as a function of the number of e-folds at horizon-crossing N_*

$$n_s \simeq 1 - \frac{2}{N_*} - \frac{3}{N_*^2}\,, \quad r \simeq \frac{12}{N_*^2}\,, \quad \alpha = \frac{dn_s}{d\ln k} \simeq -\frac{2}{N_*^2}\left(1 + \frac{3}{N_*}\right). \tag{4.34}$$

The values for the spectral observables given in eq. (4.34) correspond to single-field background motion. Multi-field non-minimally coupled models of inflation at large ξ show a very strong single-field attractor behavior. The strength of the attractor was analyzed in Ref. [193] for the case of an $SO(N)$-symmetric model, similar to Higgs inflation without gauge fields. The more general case of two-field inflation with generic potential parameters is given in Refs. [174, 194], showing that the single-field attractor becomes stronger for larger ξ and that it persists not only during inflation but also during the (p)reheating era. For generic initial conditions, the isocurvature fraction $\beta_{\rm iso}$ is exponentially small for random potentials, while for a symmetric potential $\beta_{\rm iso} = \mathcal{O}(10^{-5})$, as is shown in Ref. [194]. As briefly discussed in section 4.4.1 and more extensively in section 5A of Ref. [2], during inflation, the gauge bosons are very massive compared to the Hubble scale, making the single-field attractor behavior of Higgs inflation stronger than the one described in Ref. [193] for

the scalar symmetric case. Hence the use of a single-field motion $\varphi(t)$ for the background is well justified during and after Higgs inflation.

The dimensionless power spectrum of the (scalar) density perturbations is measured to be

$$A_s \simeq 2 \times 10^{-9} \,. \tag{4.35}$$

Using the tensor-to-scalar ratio from eq. (4.34) with $N_* = 55$ yields $r \simeq 3.3 \times 10^{-3}$, and hence the tensor power spectrum becomes

$$\frac{\mathcal{P}_T}{m_{\rm pl}^2} = \frac{2H^2}{\pi^2 m_{\rm pl}^2} = r \times A_s \simeq 6.6 \times 10^{-12} \,. \tag{4.36}$$

Given that the Hubble scale during inflation is approximately [155]

$$H_{\rm infl}^2 \simeq \frac{\lambda}{12\xi^2} m_{\rm pl}^2 \,, \tag{4.37}$$

the Higgs self-coupling and non-minimal coupling must obey the relation

$$\frac{\lambda}{\xi^2} \simeq 5 \times 10^{-10} \,. \tag{4.38}$$

We keep the value of the Hubble scale fixed and determine the value of λ that corresponds to each ξ through eq. (4.38).

4.3 Higgs self-resonance

We now focus on the Higgs fluctuations, neglecting the effects of Goldstone modes and gauge fields. In our linear analysis the Higgs fluctuations do not couple to the gauge field. The equation of motion for the rescaled fluctuations $X^h(x^\mu) \equiv a(t) Q^h(x^\mu)$ is

$$\mathcal{D}_\tau^2 X_{\mathbf{k}}^h + \omega_h^2(k,\tau) X_{\mathbf{k}}^h = 0 \,, \tag{4.39}$$

where the effective frequency is defined as

$$\frac{\omega_h^2(k,\tau)}{a^2} = \frac{k^2}{a^2} + m_{{\rm eff},h}^2 \,. \tag{4.40}$$

For notational simplicity and connection to earlier work [174–176] we define the various contributions to the effective mass of the Higgs fluctuations

$$m^2_{\rm eff,h} \equiv \mathcal{M}^h{}_h - \frac{1}{6}R = m^2_{1,h} + m^2_{2,h} + m^2_{3,h} + m^2_{4,h}\,, \tag{4.41}$$

where $\mathcal{M}^h{}_h$ was defined in eq. (4.19) and

$$\begin{aligned}
m^2_{1,h} &= \mathcal{G}^{hh}(\mathcal{D}_\varphi\mathcal{D}_\varphi V)\,, &(4.42)\\
m^2_{2,h} &= -\mathcal{R}^h{}_{LMh}\dot\varphi^L\dot\varphi^M\,, &(4.43)\\
m^2_{3,h} &= -\frac{1}{m^2_{\rm pl}a^3}\mathcal{D}_t\left(\frac{a^3}{H}\dot\varphi^2\mathcal{G}_{hh}\right)\,, &(4.44)\\
m^2_{4,h} &= -\frac{1}{6}R = (\epsilon-2)H^2\,, &(4.45)
\end{aligned}$$

where ϵ is the slow-roll parameter $\epsilon = -\dot H/H^2$. For the case of fluctuations along the straight background trajectory, as are Higgs fluctuations, the Riemann contribution $m^2_{2,h}$ vanishes identically. As described in Ref. [36] and further utilized in Ref. [174], the mode-functions can be decomposed using the vielbeins of the field-space metric. In the single-field attractor the decomposition of $X^h_{\mathbf{k}}$ into creation and annihilation operators is trivial

$$\hat X^h = \int \frac{d^3k}{(2\pi)^{3/2}}\left[v_k e_1{}^h\,\hat a_{\mathbf{k}}e^{i\mathbf{k}\cdot\mathbf{x}} + v_k^* e_1{}^h\,\hat a^\dagger_{\mathbf{k}}e^{-i\mathbf{k}\cdot\mathbf{x}}\right]\,, \tag{4.46}$$

where $e_1{}^h = \sqrt{\mathcal{G}^{hh}}$. Since the vielbeins obey the parallel transport equation $\mathcal{D}_\tau e_1{}^h = 0$, the equation of motion for the mode function $v_{\mathbf{k}}$ becomes

$$\partial^2_\tau v_{\mathbf{k}} + \omega^2_h(k,\tau)v_{\mathbf{k}} = 0\,. \tag{4.47}$$

We solve the equation in cosmic, rather than conformal time, which is better suited for computations after inflation

$$\ddot v_{\mathbf{k}} + H\dot v_{\mathbf{k}} + \frac{\omega^2_h(k,t)}{a^2}v_{\mathbf{k}} = 0\,, \tag{4.48}$$

where the frequency is defined in eq. (4.40).

We examine the two dominant terms of the effective mass, the one arising from the potential ($m^2_{1,h}$) and the one arising from the coupled metric perturbations ($m^2_{3,h}$). The latter is often overlooked in studies of preheating, perhaps because it is vastly subdominant during inflation. It arises by combining the equation of motion for $\delta\phi$ and the metric perturbation ψ, defined through eq. (4.12),

in conjunction with the definition of the Mukhanov-Sasaki variables, given in eq. (4.14).

The expression for $m_{1,h}^2$ normalized by the Hubble scale is

$$\begin{aligned}\frac{m_{1,h}^2}{H^2(t)} =& \frac{12m_{\rm pl}^2\left(\xi\varphi^2\left(12\xi m_{\rm pl}^2 - 2\xi(6\xi+1)\varphi^2 + m_{\rm pl}^2\right) + 3m_{\rm pl}^4\right)}{\varphi^2\left(\xi(6\xi+1)\varphi^2 + m_{\rm pl}^2\right)^2} \\ \simeq& -\frac{4m_{\rm pl}^2}{\xi\varphi^2} + \frac{4m_{\rm pl}^4}{\xi^2\varphi^4} + \mathcal{O}\left(\frac{m_{\rm pl}^6}{\xi^3\varphi^6}\right),\end{aligned} \tag{4.49}$$

where we used $\xi \gg 1$ in expressions such as $(6\xi + 1) \simeq 6\xi$. Furthermore, since we are at first interested in studying the behavior during inflation, where analytic progress can be made, we use $\xi\varphi^2 \gg m_{\rm pl}^2$ as an approximation. As we will see, this works reasonably well even close to the end of inflation. We can use the single-field slow-roll results

$$-N = \frac{3}{4}\frac{\xi\varphi^2}{m_{\rm pl}^2} + \frac{1}{8}\frac{\varphi^2}{m_{\rm pl}^2} + \mathcal{O}\left(\log\frac{\varphi}{m_{\rm pl}}\right), \tag{4.50}$$

where we went beyond lowest order in $\xi\varphi^2$ and we measure the number of e-folds from the end of inflation, meaning that negative values correspond to the inflationary era[5]. This leads to

$$\frac{m_{1,h}^2}{H^2(t)} \simeq \frac{3}{N} + \frac{9}{4N^2} + \mathcal{O}\left(\frac{1}{N^3}\right). \tag{4.51}$$

If we minimize m_1^2 as a function of $\delta = \sqrt{\xi}\varphi$, the field amplitude that minimizes the mass is

$$\delta_{\rm min} = \sqrt{2}m_{\rm pl} + \mathcal{O}\left(\frac{1}{\xi}m_{\rm pl}\right), \tag{4.52}$$

or equivalently $N_{\rm min} \simeq -1.5$. For the minimization we used the full expression for the effective mass and only took the Taylor expansion for large ξ at the end. We can see that, for $\xi \gg 1$ the minimum of m_1^2 is independent of ξ and thus occurs at the same value of δ, which will also be the same value of N, in the approximation of eq. (4.50). In general, the function $m_{1,h}^2(N)/H^2$ shows no appreciable difference for different values of $\xi \gg 1$ during inflation. This can be easily seen by substituting eq. (4.50) into eq. (4.49). As shown in Ref. [175], this behavior persists during the time of coherent inflaton oscillations.

[5]We neglected the contributions coming from the lower end of the integral leading to eq. (4.50).

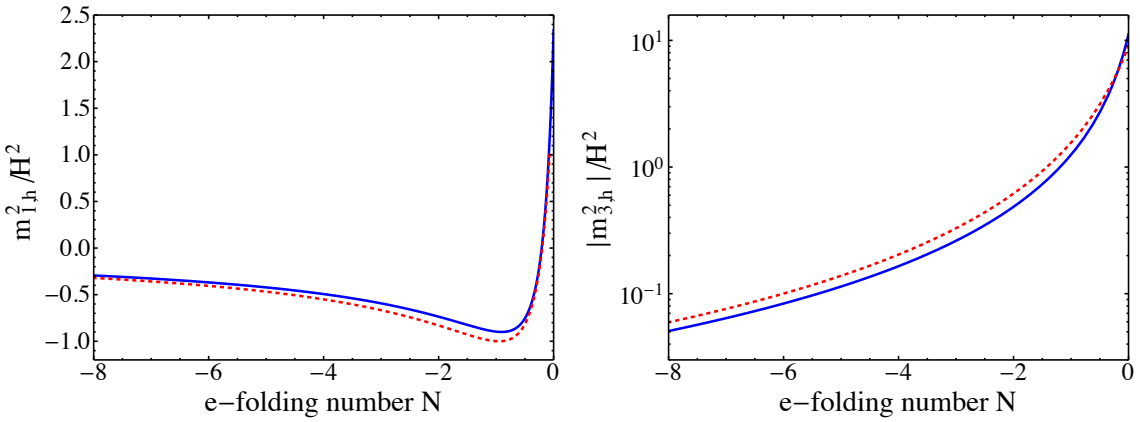

FIGURE 4.1: The components of the effective mass of the Higgs fluctuations $m^2_{1,h}$ and $m^2_{3,h}$ rescaled by the Hubble scale. The blue curves show the numerical curves for $\xi = 10$ and the red dashed lines the approximate analytic expressions of eqs. (4.51) and (4.54) respectively.

The mass component arising from the metric fluctuations is

$$m^2_{3,h} = -\frac{\left(\xi(6\xi+1)\varphi^2 + m^2_{\rm pl}\right)\dot{\varphi}\left(H(t)(\epsilon(t)+3)\dot{\varphi} + 2\ddot{\varphi}\right)}{H(t)\left(\xi\varphi^2 + m^2_{\rm pl}\right)^2} \simeq -\frac{18\dot{\varphi}^2}{\varphi^2}\,, \tag{4.53}$$

where the last approximation holds during inflation. Using the slow-roll expression for $\dot{\varphi}$ we get that during inflation

$$\frac{m^2_{3,h}}{H^2(t)} \simeq -\frac{9}{2N^2}\,. \tag{4.54}$$

This contribution is clearly subdominant to $m^2_{1,h}$, hence it can be safely neglected during inflation. However, $|m^2_{3,h}|$ grows near the end of inflation, since it is proportional to $\dot{\varphi}^2$, which at the end of inflation is given by

$$\dot{\varphi}^2_{\rm end} = \mathcal{G}^{\varphi\varphi}V = \frac{\lambda m^2_{\rm pl}\varphi^4}{4\left(6\xi^2\varphi^2 + \xi\varphi^2 + m^2_{\rm pl}\right)} \simeq \frac{\lambda m^2_{\rm pl}\varphi^2}{24\xi^2}\,. \tag{4.55}$$

It has been numerically shown in Ref. [174] that the field value at the end of inflation is $\sqrt{\xi}\varphi_{\rm end} \simeq 0.8 m_{\rm pl}$, leading to

$$\dot{\varphi}^2_{\rm end} \simeq \frac{0.8^2\lambda}{24\xi^3} m^4_{\rm pl} \simeq \frac{2\lambda}{75\xi^3} m^4_{\rm pl}\,. \tag{4.56}$$

Numerically we get $m^2_{3,h}/H^2(t) \simeq -11$ at the end of inflation, in rough agreement with the approximate expressions given above.

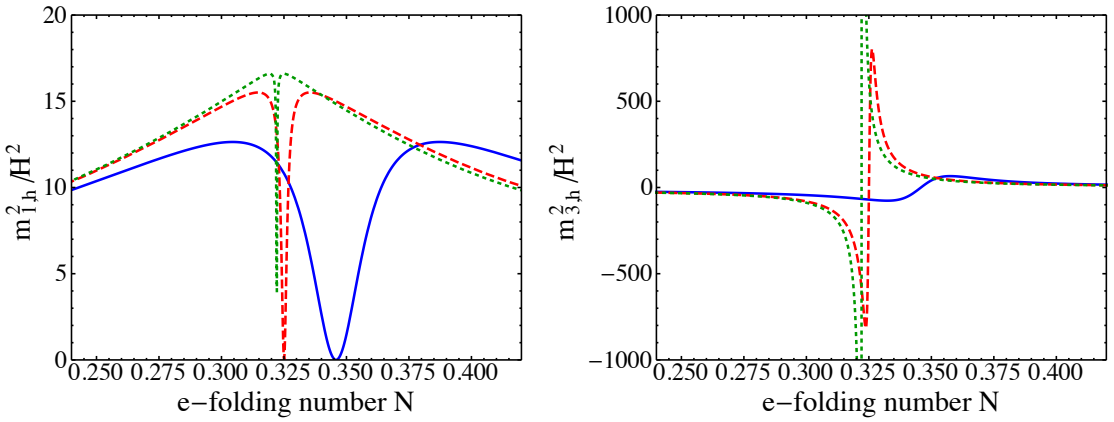

FIGURE 4.2: The ratio of the components of the effective mass of the Higgs fluctuations $m^2_{1,h}$ (left) and $m^2_{3,h}$ (right) rescaled by the Hubble scale at the end of inflation. The blue, red dashed and green dotted curves correspond to $\xi = 10, 10^2, 10^3$ respectively.

The numerical results for $\xi = 10$ are shown in figure 4.1, along with the approximate analytical expressions that we derived. We only show the $\xi = 10$ case, since all cases with higher values of the non-minimal coupling exhibit visually identical results. After the end of inflation the two dominant components of the effective mass of the Higgs fluctuations evolve differently for different values of ξ. In Ref. [175] the behavior of $m^2_{1,h}$ was analyzed in the static universe approximation. It was shown that for $\xi \gtrsim 100$ the effective mass component $m^2_{1,h}$ quickly approaches a uniform shape regardless of the value of ξ. The consequence of that is that the Floquet chart for the inflaton self-resonance also approaches a common form for $\xi \gtrsim 100$. This can be seen in the left panel of figure 4.2, where $m^2_{1,h}$ is very similar between $\xi = 100$ and $\xi = 10^3$, but different for $\xi = 10$. The coupled metric fluctuations component of the effective mass has a similar shape for $\xi = 100$ and $\xi = 10^3$, but for $\xi = 10$ it is significantly less pronounced, as seen in the right panel of figure 4.2.

4.3.1 Superhorizon evolution and thermalization

An important notion when dealing with (p)reheating is the transfer of energy from the inflaton condensate to the radiation degrees of freedom. Naively, one must compute all the power concentrated in the wave numbers that are excited above the vacuum energy (different than the adiabatic vacuum at any time) and compare that to the energy density stored in the condensate. However, when dealing with inflationary perturbations, one must keep in mind that computations should refer to modes, whose length-scales are relevant to the dynamics being studied. For curvature perturbations,

the use of a finite box was described in Ref. [198]. For preheating, since thermalization proceeds through particle interactions, the relevant length-scales are those that allow for particle interactions, hence subhorizon scales, or short wavelengths.

The parametric excitation of long-wavelength modes has been extensively studied [83, 199–207]. It has been demonstrated that the coupled metric fluctuations lead to an enhancement of –particularly– long-wavelength modes [200, 202, 203, 205, 207], which is larger than the one computed using a rigid background. Furthermore, the amplification of long-wavelength modes, even on super Hubble scales, does not violate causality, as discussed for example in Refs. [199, 200, 202, 203, 207]. Intuitively, the inflaton condensate has a super-Hubble correlation length and can thus consistently affect super-Hubble modes.

While UV modes encounter the complication of possibly being excited for wavenumbers that exceed the unitarity bound (this doesn't occur for Higgs modes), the IR modes have a different conceptual difficulty: since thermalization occurs when particles interact and exchange energy, in order to lead to a thermal distribution, modes that are superhorizon are 'frozen-in' and hence cannot take part in such processes[6]. Hence, it is normal to only consider modes that have large enough physical wave numbers, that place them inside the horizon at the instant in time that we are considering. Modes that have longer wavelengths are frozen outside the horizon and do not contribute to the thermalization process. They should be summed over and added to the local background energy density. We will skip this last step, as their contribution is subdominant, compared to the energy density stored in the inflaton condensate. In figure 4.3 we see the evolution of the comoving Hubble radius, that is determined from the background field φ, neglecting any backreaction from decay products. The Hubble radius shrinks during inflation and grows after inflation ends. We also see that different values of ξ lead to different post-inflationary evolution, which is expected, since the effective equation of state of the background dynamics after inflation depends strongly on ξ, as shown in Ref. [174]. More specifically, large non-minimal couplings $\xi \gtrsim 100$ lead to a prolonged period of matter-domination-like expansion, which can last for several e-folds in the absence of backreaction. As we will see in the next sections, the majority of the parametric resonance effects occur for $N \lesssim 3$ e-folds, placing the entirety of the reheating dynamics inside the matter-dominated background era for large values of ξ. In order to take into account the relevant wavenumbers consistently, we use an

[6]Generically in multi-field models, one would not expect the curvature perturbations to remain frozen in when stretched outside the Hubble radius, since multi-field interactions can generate non-adiabatic pressure, which in turn will source changes in the gauge-invariant curvature perturbations on arbitrarily long length-scales. However, in models like Higgs inflation that feature strong single-field attractor dynamics during inflation, the non-adiabatic pressure effectively vanishes and the long-wavelength modes remain frozen in, akin to the expected behavior in simple single-field models. Details on the single-field attractor in such models can be found in Refs. [164, 174, 193].

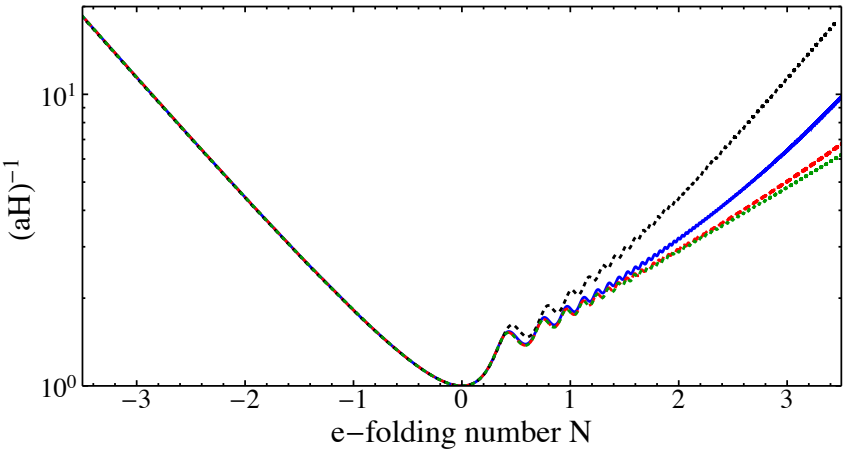

FIGURE 4.3: The size of the comoving Hubble radius during and after inflation for $\xi = 10, 10^2, 10^3, 10^4$ (black, blue, red and green respectively). The curves are normalized such that $(aH)^{-1} = 1$ at the end of inflation.

adaptive code, that only sums up the contribution of modes that are inside the horizon at the point in time when computing the energy density of the Higgs field fluctuations.

4.3.2 Preheating

We now move to the computation of the energy density in the Higgs particles that are produced during preheating, for which we solve eq. (4.40) numerically. Again we use cosmic time rather than conformal time. A detailed analysis was already performed in Ref. [176]. However, all computations were initialized at the end of inflation, thereby neglecting the amplification of long-wavelength modes during the last e-folds of inflation. We initialize all computations at 4.5 e-folds before the end of inflation, in order to ensure that all relevant modes are well described by the Bunch-Davies (BD) vacuum solution

$$v_{k,h} \simeq \frac{1}{\sqrt{2k}} e^{-ik\tau} \,. \tag{4.57}$$

We see in the right panel of figure 4.4 that at early times (before the end of inflation), the energy density in Higgs modes (indicated by the solid blue line) decays as a^{-4} (indicated by the dotted line), in keeping with the expectation for modes in the BD state. However, approximately one e-fold before the end of inflation, the evolution of the energy density in Higgs modes departs from a^{-4}, because the low k-modes are enhanced with respect to the BD spectrum. This enhancement occurs

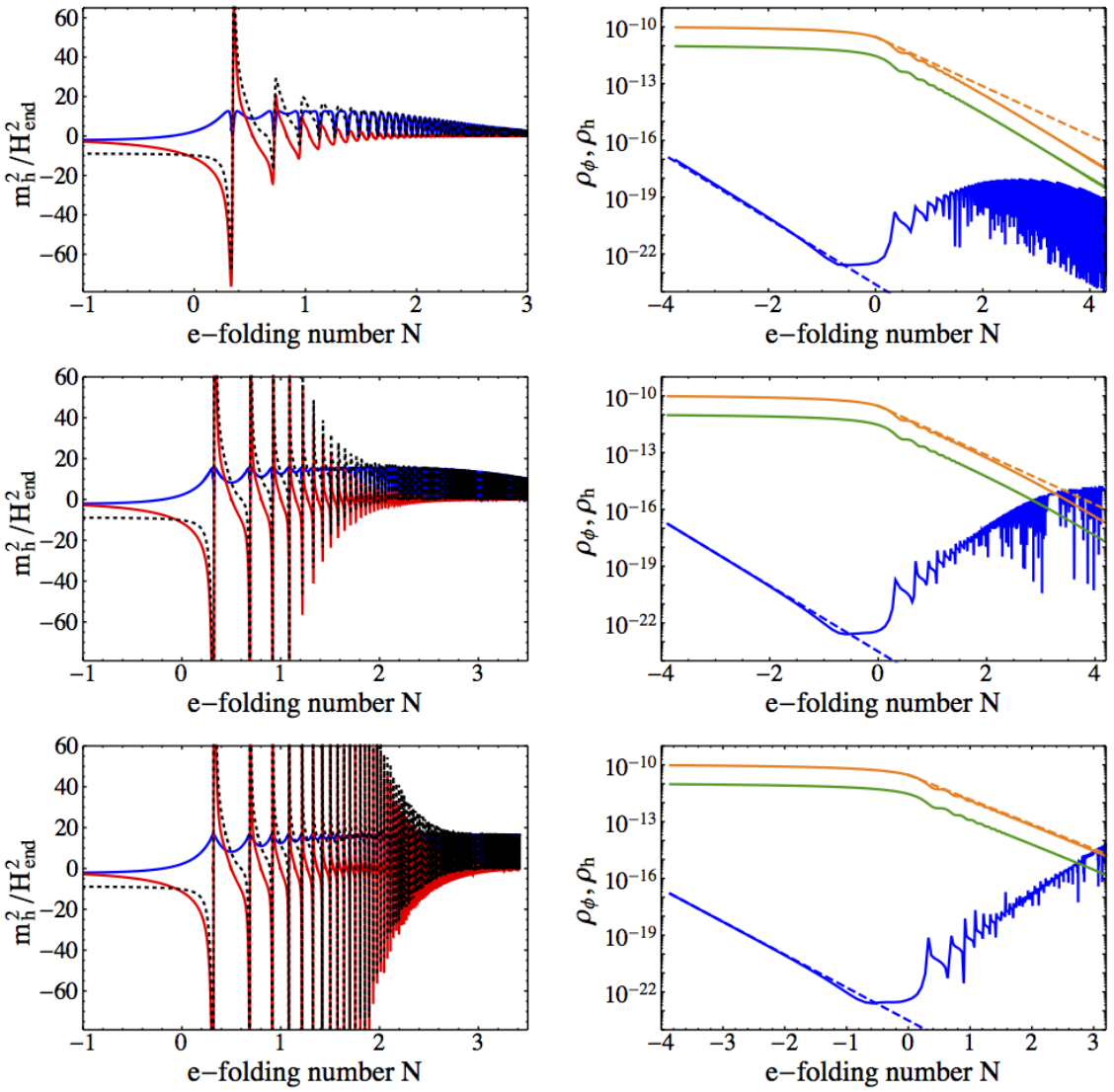

FIGURE 4.4: *Left:* The effective mass-squared (black-dotted), along with the contributions from the potential (blue) and the coupled metric perturbations (red).
Right: The energy density in the background Higgs condensate (orange) and the Higgs fluctuations (blue) for $\xi = 10, 10^2, 10^3$ (top to bottom) in units of $m_{\rm pl}^4$. The green line shows 10% of the background energy density, which is used as a proxy for the limit of our linear analysis. The orange-dashed line is $\rho_0 a^{-4}$, corresponding to the red-shifting of the background energy density during radiation-dominated expansion.

because $m_{{\rm eff},h}^2 < 0$, an early tachyonic amplification phase driven largely by the effect of coupled metric perturbations. An immediate consequence of this fact is that one would underestimate the true amount of growth by starting the computation in a BD-like vacuum state at the end of inflation.

The right panels of figure 4.4 present the results for the energy transfer into Higgs particles for $\xi = 10, 10^2, 10^3$. Preheating completes when the energy density in the Higgs fluctuations (blue line) becomes equal to the energy density of the background field (orange line). However, the linear analysis is expected to break down when the energy density of the Higgs fluctuations becomes comparable to that of the inflaton field. As an indicator of the validity of the linear theory, which neglects backreaction of the excited modes onto the background, the green line shows 10% of the energy density of the inflation field.

For all values of ξ studied, the system exhibits an amplification of inflaton (Higgs) fluctuations. This is mainly caused by the periodic negative contribution of $m^2_{3,h}$ to the effective mass-squared $m^2_{\text{eff},h}$, which is plotted in the left panel of figure 4.4. This is the term arising from considering the effect of the coupled metric perturbations at linear order. As shown in Ref. [176] and further reiterated in figure 4.4, the amplification driven by $m^2_{3,h}$ lasts longer for larger values of ξ. Specifically, the time at which the tachyonic resonance regime stops scales as $t \sim \sqrt{\xi} H^{-1}_{\text{end}}$, as shown in Ref. [176]. However, for $\xi > 100$ the differences are irrelevant (in the simplified linear treatment), since the universe will have preheated already by $N \simeq 3$ e-folds. Hence for $\xi > 100$, self-resonance of the Higgs field leads to predictions for the duration of preheating that are almost independent of the exact value of ξ.

After the tachyonic resonance has shut off (and if preheating has not completed yet), the modes undergo parametric resonance, driven by the oscillating effective mass term $m^2_{1,h}$. However, for very long-wavelength modes $k \simeq 0$, the Floquet exponent vanishes [175], and the amplification is polynomial in time rather than exponential, hence significantly weaker. As shown in Ref. [175] the maximum Floquet exponent in the static universe approximation is $\mu_{k,\max} T \approx 0.3$, where T is the background period. Using the relation $\omega/H \simeq 4$, which was derived in Ref. [174] for $\omega = 2\pi/T$, the maximum Floquet exponent is expressed as $\mu_k \sim 0.5H$. Hence the Floquet exponent is too small to lead to an efficient amplification of Higgs fluctuations in an expanding universe. Thus the early time tachyonic resonance, driven by the coupled metric fluctuation is crucial for preheating the universe through Higgs particle production.

For $\xi = 10$ the situation is significantly different. Both tachyonic resonance, due to the coupled metric fluctuations encoded in $m^2_{3,h}$, as well as parametric resonance due to the potential term $m^2_{1,h}$ become inefficient earlier, leading to a slower growth of the fluctuations and the energy density that they carry and an incomplete preheating.

However, for smaller values of the non-minimal coupling $\xi = \mathcal{O}(10)$ one must take into account another important feature, namely the evolution of the background. As shown in Ref. [174], larger

values of ξ put the universe into a prolonged matter-dominated state ($w = 0$). This means that the energy density of the background condensate redshifts as $a^{-3} = e^{-3N}$. For small values of ξ, however, the universe passes briefly through the background (average) equation of state $w = 0$ and after the first e-fold approaches $w \simeq 1/3$. Figure 4.5 shows the evolution of the energy density in Higgs modes for the marginal case of $\xi = 30$. We see that the fluctuation energy density in the Higgs modes would be always smaller than the background, if the background evolved with $w \simeq 0$, as indicated by the orange dashed line. However, the fact that the background energy density redshifts faster ($w \simeq 1/3$) allows for complete preheating. Simply put, non-minimal couplings in the 'intermediate' regime of $\xi = \mathcal{O}(10)$ exhibit a shorter period of tachyonic-parametric amplification, while at the same time following a background evolution of $\rho_\phi \sim e^{-4N}$.

We distinguish two time points relevant for preheating: $N_{\rm reh}$ is the time at which the energy density in the linear fluctuations equals the background energy density, which we take as the time of complete preheating and $N_{\rm br}$ is the time at which the energy density in the linear fluctuations equals 10% of the background energy density, which is the point at which backreaction effects may become important. We have numerically found that self-resonance of the Higgs field becomes insufficient to preheat the universe at $\xi < 30$. In particular, the results for $N_{\rm reh}(\xi)$ can be fitted by a simple analytical function, as shown in figure 4.6:

$$N_{\rm reh}(\xi) \simeq \frac{21}{\xi(1 + 0.016\xi)} + 3\,, \tag{4.58}$$

for $\xi \gtrsim 30$, where complete preheating is possible, at least in the linear approximation that we use. For $\xi > 100$, $N_{\rm reh}$ becomes largely independent of ξ, as expected from the results of figure 4.4. As a final note, we must say that the results were insensitive to the exact value of the maximum wavenumber considered. This is due to the fact that the small (but subhorizon) wavenumbers $k = \mathcal{O}(H_{\rm end})$ are exponentially amplified and dominate the fluctuation energy density shortly after the end of inflation. Hence we do not need to implement any scheme to subtract the vacuum contribution from large-k modes, since it is vastly subdominant for any reasonable UV cutoff.

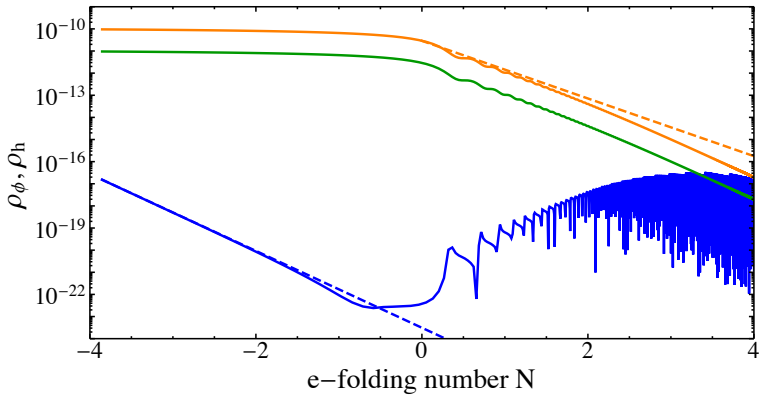

FIGURE 4.5: The energy density in the background Higgs condensate (orange) and the Higgs fluctuations (blue) for the marginal case of $\xi = 30$ (top to bottom) in units of $m_{\rm pl}^4$. The green line shows 10% of the background energy density, which is used as a proxy for the limit of our linear analysis. The orange-dashed line is $\rho_0 a^{-4}$, corresponding to the red-shifting of the background energy density during radiation-dominated expansion.

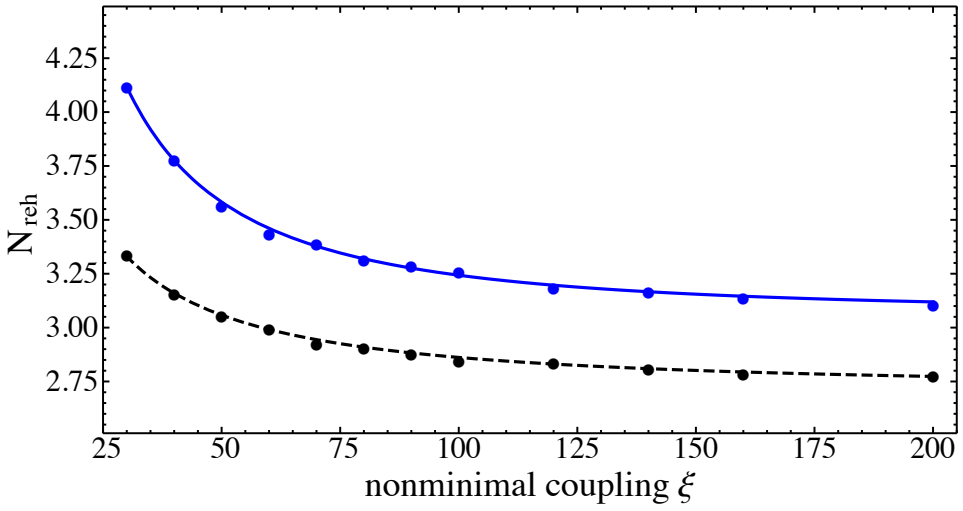

FIGURE 4.6: The number of e-folds after inflation when the energy density in the Higgs fluctuations equals the background energy density $N_{\rm reh}$ (blue solid) or 10% of the background energy density $N_{\rm br}$ (black dashed).

4.4 Gauge / Goldstone boson production

4.4.1 Initial conditions for preheating

In section 5A of Ref. [2] we use the equations of motion derived in the Abelian model in unitary gauge, in order to study the evolution of gauge fields during inflation. The unitary gauge is well-defined in this period, since $\varphi(t)$ does not vanish. The values of $B_{\mathbf{k}}^{\pm,L}$ at the end of inflation, when $t = t_{\rm in}$, serve as initial conditions for preheating. Especially for initializing lattice simulations, which are increasingly expensive to start deeper within inflation, accurate knowledge of the spectrum of gauge fields at the end of inflation is essential. During preheating, unitary gauge is not well-defined at moments when $\varphi(t) = 0$, so we use Coulomb gauge. In order to determine the initial condition for $\theta_{\mathbf{k}}$, we will use eq. (4.32), which relates $B_{\mathbf{k}}^{L}$ in unitary gauge to $\theta_{\mathbf{k}}$ in Coulomb gauge.

During inflation we find that the transverse modes are canonically normalized and conformally coupled at early times and the modes therefore follow the Bunch-Davies vacuum solution. At late times they become heavy and thus suppressed. The longitudinal gauge modes are of greater interest, since they will be amplified during preheating. It turns out that they follow the adiabatic WKB-solution until the end of inflation. The longitudinal modes are very heavy during inflation (as compared to the Hubble scale). This enhances the single-field attractor behavior.

Using eq. (4.32) to translate the solution for the longitudinal mode in unitary gauge to the Goldstone mode in Coulomb gauge, we find

$$\theta_{\mathbf{k}}(t_{\rm in}) = \frac{1}{\sqrt{2}} \frac{e\varphi(t_{\rm in})}{k} \frac{1}{\sqrt{b_L(k,t_{\rm in})}\sqrt{\omega_L(k,t_{\rm in})}}\,, \tag{4.59}$$

$$\dot{\theta}_{\mathbf{k}}(t_{\rm in}) = -i\,\frac{\omega_L(k,t_{\rm in})}{a(t_{\rm in})} \times \theta_k(t_{\rm in}) \tag{4.60}$$

with

$$b_L(k,\tau) = \left(1 + \frac{k^2 2f}{m_{\rm pl}^2 a^2 e^2 \varphi^2}\right)\,, \qquad \omega_L^2(k,\tau) = k^2 + a^2 \frac{m_{\rm pl}^2}{2f} e^2 \varphi^2\,. \tag{4.61}$$

If we focus on the case of $k|\tau| \gg \sqrt{\frac{12\xi}{\lambda}} e \equiv x_c$, where the initial conditions for preheating are

$$\theta_{\mathbf{k}}(\tau_{\rm in}) \approx \frac{e\phi}{x_c} \frac{\tau_{\rm in}}{\sqrt{2k}}\,, \tag{4.62}$$

$$\dot{\theta}_{\mathbf{k}}(\tau_{\rm in}) \approx \theta_{\mathbf{k}}(\tau_{\rm in}) \times \left(\frac{i\,k}{a(\tau_{\rm in})}\right)\,, \tag{4.63}$$

we find that for large wavenumbers the coupling constant e drops out of the initial conditions for the θ field (since $x_c \propto e$), hence the decoupling limit is trivially obtained. For $k|\tau| < x_c$ it is slightly more complicated to see that, since for $e \to 0$ we get $x_c \to 0$, hence that region shrinks into nonexistence as we take the decoupling limit. Also, we would have to compute the expressions for $x_c \ll 1$ before we send $e \to 0$ in that case. Since the case of $e \ll 1$ does not apply to Higgs inflation, we will not pursue it further.

4.4.2 Preheating

We start by rewriting eq. (4.29) in a somewhat more compact way

$$\begin{aligned} &\mathcal{D}_\tau^2 X^\theta - \partial_\tau \log\left(1+\frac{\tilde{m}_B^2}{k^2}\right)\mathcal{D}_\tau X^\theta \\ &\quad + \left[k^2 + a^2 m_{\mathrm{eff},\theta}^2 + \tilde{m}_B^2 + \left(\frac{\partial_\tau \varphi}{\varphi} + \frac{\partial_\tau a}{a} - \frac{\partial_\tau f}{2f}\right)\partial_\tau \log\left(1+\frac{\tilde{m}_B^2}{k^2}\right)\right] X^\theta = 0\,, \end{aligned} \tag{4.64}$$

where we defined the gauge field mass

$$\tilde{m}_B^2 \equiv e^2\varphi^2 \frac{m_{\mathrm{pl}}^2}{2f} a^2\,, \tag{4.65}$$

and $X^\theta = a(t)\cdot\theta$. We normalize the scale factor as $a = 1$ at the end of inflation. The effective mass of the Goldstone mode θ in the absence of gauge fields is

$$m_{\mathrm{eff},\theta}^2 \equiv \mathcal{M}^\theta{}_\theta - \frac{1}{6}R = m_{1,\theta}^2 + m_{2,\theta}^2 + m_{3,\theta}^2 + m_{4,\theta}^2\,, \tag{4.66}$$

with

$$m_{1,\theta}^2 = \mathcal{G}^{\theta\theta}(\mathcal{D}_\theta\mathcal{D}_\theta V)\,, \tag{4.67}$$

$$m_{2,\theta}^2 = -\mathcal{R}^\theta{}_{hh\theta}\,\dot{\varphi}^2\,, \tag{4.68}$$

$$m_{3,\theta}^2 = 0, \tag{4.69}$$

$$m_{4,\theta}^2 = -\frac{1}{6}R = (\epsilon - 2)H^2\,. \tag{4.70}$$

The numerical solution of eq. (4.64) was again performed in cosmic rather than conformal time and the computations were initialized at the end of inflation, according to eq. (4.59) and eq. (4.60).

We can follow the quantization method described in Ref. [174] and utilized in section 4.3 for the study of Higgs self-resonance:

$$\hat{X}^\theta = \int \frac{d^3k}{(2\pi)^{3/2}} \left[z_k e_2{}^\theta \, \hat{a}_{\mathbf{k}} e^{i\mathbf{k}\cdot\mathbf{x}} + z_k^* e_2{}^\theta \, \hat{a}_{\mathbf{k}}^\dagger e^{-i\mathbf{k}\cdot\mathbf{x}} \right] , \tag{4.71}$$

where $e_2{}^\theta = \sqrt{\mathcal{G}^{\theta\theta}}$. Using the vielbein decomposition again, the covariant derivatives are effectively substituted by partial ones

$$\begin{aligned} &\partial_\tau^2 z_k - \partial_\tau \log(1+\tilde{m}_B^2/k^2) \cdot \partial_\tau z_k \\ &\quad + \left(k^2 + a^2 m_{\mathrm{eff},\theta}^2 + \tilde{m}_B^2 + \frac{1}{2}\partial_\tau \log\left(\tilde{m}_B^2 \sqrt{\frac{2f}{m_{\mathrm{pl}}^2}} \right) \partial_\tau \log\left(1 + \frac{\tilde{m}_B^2}{k^2} \right) \right) z_k = 0 \, . \end{aligned} \tag{4.72}$$

In order to eliminate the first-derivative term we can use the rescaled variable $\tilde{z}_k$, defined as

$$z_k = \sqrt{1 + \frac{\tilde{m}_B^2}{k^2}} \, \tilde{z}_k \equiv T \cdot \tilde{z}_k \, , \tag{4.73}$$

leading to

$$\partial_\tau^2 \tilde{z}_k + \omega_z^2 \, \tilde{z}_k = 0 \, , \tag{4.74}$$

where

$$\omega_z^2 = k^2 + a^2 m_{\mathrm{eff},\theta}^2 + \tilde{m}_B^2 + \frac{1}{2}\partial_\tau \log\left(\tilde{m}_B^2 \sqrt{\frac{2f}{m_{\mathrm{pl}}^2}} \right) \partial_\tau \log(T^2) + \frac{\partial_\tau^2(\tilde{m}_B^2)}{2k^2T^2} - \frac{3}{4}\frac{(\partial_\tau \tilde{m}_B^2)^2}{k^4 T^4} \, , \tag{4.75}$$

where $\tilde{m}_B^2$ is larger than $m_{1,\theta}^2$ and $m_{4,\theta}^2$. As discussed extensively in Refs. [174–176] for the case of a purely scalar multi-field model with large non-minimal couplings to gravity, the field-space manifold is asymptotically flat for large field values and exhibits a curvature 'spike' at the origin $\varphi(t) \simeq 0$. This 'Riemann spike' is exhibited in the effective mass of the isocurvature modes $m_{\mathrm{eff},\theta}^2$, more specifically in the $m_{2,\theta}^2$ component, which is subdominant for all times away from the zero-crossings of the background value of the inflaton field $\varphi(t)$. We will not reproduce the entirety of the Floquet structure of this model, both because we do not wish to repeat the analysis of [175], and because, as we will see in the subsequent section, the first zero-crossing of $\varphi(t)$ is the only relevant one for preheating through gauge modes.

In order to estimate the maximum excited wavenumber k_{max}, we consider the following approximation, containing only the dominant terms

$$\omega_{z,\,\mathrm{approx}}^2 \equiv k^2 + a^2 m_{2,\theta}^2 + \tilde{m}_B^2 \, , \tag{4.76}$$

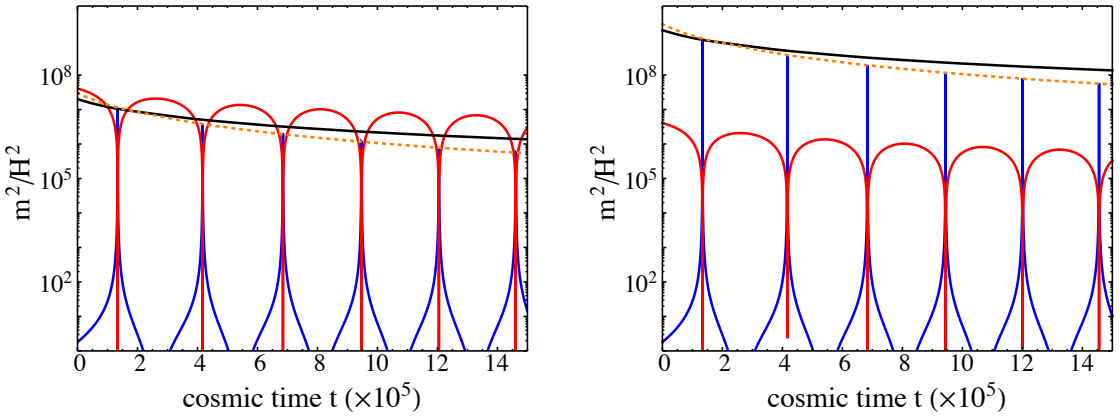

FIGURE 4.7: Dominant components of the effective frequency-squared for $\xi = 10^3$ (left) and $\xi = 10^4$ (right). Color coding is as follows: $\tilde{m}_B^2/a^2$ (red), $m_{2,\theta}^2$ (blue) and k^2/a^2 (black) for the maximum excited wavenumber $k_{\max}$. The orange-dotted curve shows the scaling a^{-3}.

where $\tilde{m}_B^2$ dominates over all subsequent terms in eq. (4.75) for large k. Figure 4.7 shows the three contributions to $\omega_{z,\,\text{approx}}^2$ for $\xi = 10^3, 10^4$ for $k = k_{\max}$. As shown in Ref. [176], the scaling of the spike in the effective mass is

$$\frac{m_{2,\theta}^2\big|_{\max}}{\langle H(t)\rangle^2} = \mathcal{O}(10)\xi^2\,, \tag{4.77}$$

where $\langle H(t)\rangle$ is a time-averaged version of the Hubble scale over the early oscillatory behavior. The range of excited wavenumbers is given by the relation

$$k^2 \lesssim a^2\, m_{2,\theta}^2\big|_{\max}\,, \tag{4.78}$$

assuming that the spike of $m_{2,\theta}^2$ dominates over $\tilde{m}_B^2$ near $\varphi(t) = 0$. Each subsequent inflaton zero-crossing affects a smaller range of wavenumbers, since $m_{2,\theta}^2 \propto H^2 \propto \rho_{\text{infl.}} \propto a^{-3}$, where we assumed $w = 0$ for the averaged background evolution. Altogether $k_{\max}^2 \propto a^{-1}$, hence the maximum excited wavenumber shrinks for every subsequent inflaton oscillation. The maximum comoving wavenumber after the first inflaton zero-crossing, where $a(t) \approx 1$, is

$$k_{\max}^2 = \mathcal{O}(10)\xi^2 H_{\text{end}}^2 = \mathcal{O}(1)\lambda\, m_{\text{pl}}^2\,, \tag{4.79}$$

where we used eq. (4.37) and $H_{\text{end}} \approx 0.5 H_{\text{infl}}$. This is in agreement with Ref. [177]. We focus primarily on the first inflaton zero-crossing, since the produced gauge bosons will decay into fermions between two subsequent background zero-crossings, hence Bose enhancement is lost. This was shown

in Refs. [171, 172] and will be discussed in section 4.5.

The second dominant component of the gauge field effective frequency-squared is $\tilde{m}_B^2$, which scales simply as

$$\frac{\tilde{m}_B^2/a^2}{H_{\rm end}^2} = \frac{m_{\rm pl}^2 e^2}{2f}\varphi^2 \frac{1}{H_{\rm end}^2} = \mathcal{O}(1)\frac{\xi}{\lambda} = \mathcal{O}(1)\frac{10^{10}}{\xi}\,, \tag{4.80}$$

where the $\lambda - \xi$ relation given in eq. (4.38) was used at the last step. We can see that for $\xi = 10^3$ the maxima of the two contributions $\tilde{m}_B^2$ and $m_{2,\theta}^3$ are similar, as shown in figure 4.7 .

Computing the energy density transferred from the inflaton condensate into the gauge field modes requires more attention than the corresponding computation of section 4.3 for the Higgs self-resonance. In the case of Higgs self-resonance, the range of excited wavenumbers is $k_{\rm max}^h \sim H$. A naive computation of the energy density in the local adiabatic (WKB) vacuum for the same modes gives $\rho_{BD} \sim k_{\rm max}^4 \sim H^4$ which is 10 orders of magnitude smaller than the background energy density[7]. In that case we do not need to subtract this unphysical vacuum contribution from the energy density of the Higgs modes, since the energy density in the parametrically amplified modes is exponentially larger.

For the case of gauge fields the maximum wavenumber up to which modes can be excited is given in eq. (4.79). The vacuum energy density in these modes, naively computed, is $\rho_{\rm BD} \sim k_{\rm max}^4 \sim \lambda^2 m_{\rm pl}^4$. The total energy density in the inflaton field is $\rho_{\rm infl} = 3H^2 m_{\rm pl}^2$ leading to $\rho_{\rm BD}/\rho_{\rm infl} \sim \lambda\,\xi^2 \sim 10^{-10}\xi^4$. This is much greater than unity for large values of the non-minimal coupling. We thus need to remove the unphysical vacuum contribution to the energy density using the adiabatic subtraction scheme [135]. In this scheme we compare the wave-function of the gauge fields to the instantaneous adiabatic vacuum, computed in the WKB approximation, isolating the particle number for each wavenumber k. The particle number corresponding to a mode v_k is given by:

$$n_k = \frac{\omega_k}{2}\left(\frac{|\dot{v}_k|^2}{\omega_k^2} + |v_k|^2\right) - \frac{1}{2}\,. \tag{4.81}$$

A drawback of this method is that the particle number is only well-defined when the adiabaticity condition holds $\dot{\omega}_k/\omega_k^2 \ll 1$, thus we cannot define the particle number in the vicinity of the Riemann spike, when $\varphi(t) = 0$[8].

[7] Any computation that does not involve vacuum subtraction, including lattice simulations such as Refs. [208, 209], deals with classical quantities and computes the energy density of the vacuum modes as if they were physical. Such a computation is valid as long as the unphysical energy density of the vacuum modes is vastly subdominant.

[8] Ref. [177] computed the particle number, working in the Jordan frame, arriving at similar results. The energy of the gauge fields was subsequently computed using the value of the gauge field mass directly on the Riemann spike. We refrain from using $m_{2,\theta}^2\big|_{\rm max}$ as an indicator of the gauge field mass, since the particle number is not a well-defined

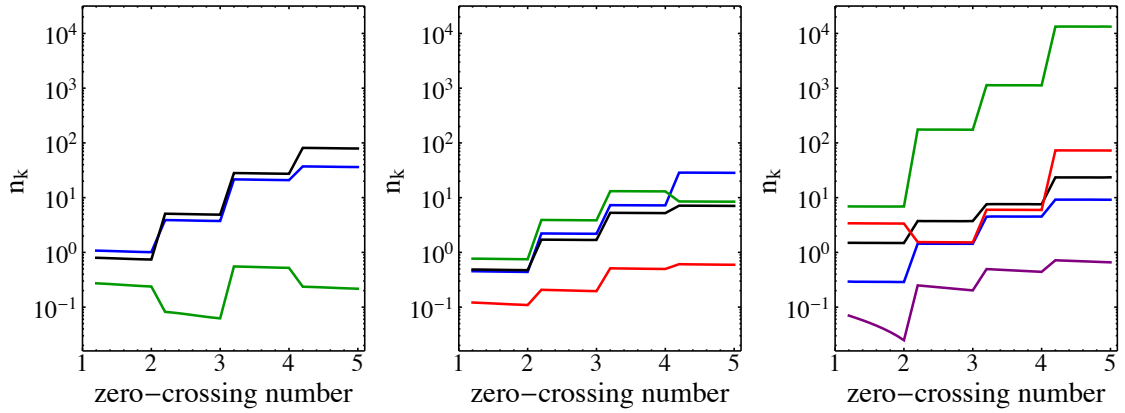

FIGURE 4.8: The particle number density for $k/H_{\rm end} = 1, 150, 550, 2600, 28000$ (blue, black, green, red and purple respectively). From left to right: $\xi = 10^2, 10^3, 10^4$. If a colored curve is missing from a panel, the corresponding wavenumber is not excited.

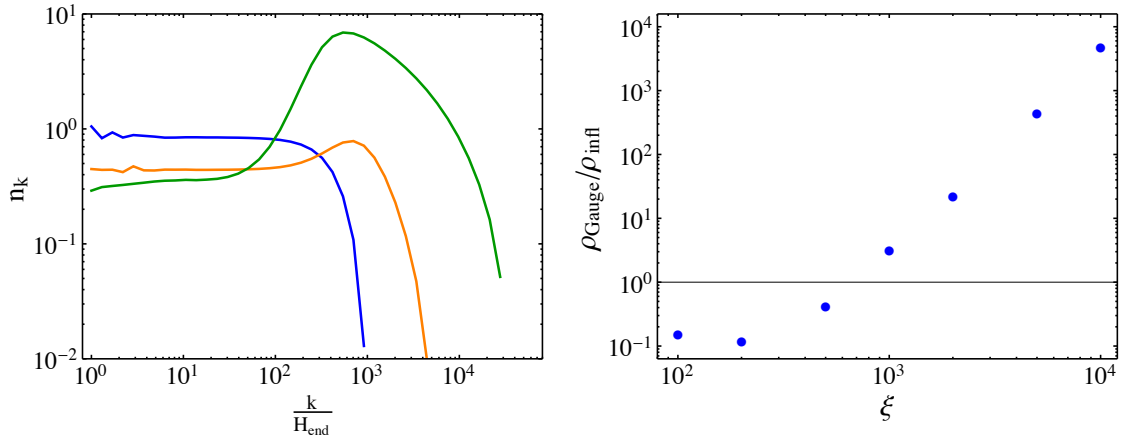

FIGURE 4.9: Left: The particle number density after the first inflaton zero-crossing for $\xi = 10^2, 10^3, 10^4$ (blue, orange and green respectively)
Right: The ratio of the energy density in gauge fields to the background inflaton energy density as a function of the non-minimal coupling ξ after the first zero-crossing. We see that for $\xi \gtrsim 10^3$ gauge boson production can preheat the universe after one background inflaton zero-crossing, hence it is much more efficient than Higgs self-resonance.

The energy density is easily computed through the particle number as

$$\rho^{L,\theta} = \int \frac{d^3k}{(2\pi)^3} n_k \omega_k \,. \tag{4.82}$$

quantity there. For $\xi \approx 10^3$, the two contributions to the gauge field mass, $m^2_{2,\theta}$ and $\tilde{m}^2_B$ are comparable, as shown in figure 4.7, which does not hold for other values of ξ.

Both the particle number and the energy density can be computed equally well using the field $\theta_{\mathbf{k}}$ or $B^L_{\mathbf{k}}$, since the only moment for which the longitudinal gauge fields are not defined is when $\varphi(t) = 0$. At this instant we cannot define the particle number either way, since there is no well-defined adiabatic vacuum. Figure 4.8 shows the evolution of the particle number density for a few values of the comoving wavenumber after the first few inflaton zero-crossings, neglecting the effect of particle decays, as described in section 4.5. The left panel of figure 4.9 shows the particle number density per k-mode for $\xi = 10, 10^2, 10^3$ after the first inflaton zero-crossing. The condition of eq. (4.79) for the maximum excited wavenumber $k_{\rm max}$ is evident.

At this point, it is worth performing a simple estimate of the energy density that can be transferred to the gauge field modes away from the first point $\varphi(t) = 0$.

$$\rho = \int \frac{d^3k}{(2\pi)^3} n_k \omega_k \sim \langle n \rangle \, \tilde{m}_B \, k^3_{\rm max} \sim \langle n \rangle \left(\frac{10^5}{\sqrt{\xi}} H_{\rm end} \right) \left(\lambda^{3/2} m^3_{\rm pl} \right) \sim \langle n \rangle m^4_{\rm pl} 10^{-15} \xi^{5/2} \,, \tag{4.83}$$

where $\langle n \rangle$ is the average occupation number. The background inflaton energy density is $\rho_{\rm infl} = 3H^2 m^2_{\rm pl} \sim 10^{-11} m^4_{\rm pl}$, hence for $\xi \gtrsim 10^3$ the transfer of energy is enough to completely drain the inflaton condensate within one zero-crossing of $\varphi(t)$, if we take the particle number shown in figure 4.9 into account. The right panel of figure 4.9 shows the ratio of the energy density in gauge fields to the background energy density of the inflaton after the first zero-crossing. Obviously, values of $\rho_{\rm gauge}/\rho_{\rm infl} > 1$ are not physical but signal the possibility of complete preheating.

4.4.3 Unitarity scale cut-off

So far we have computed the excitation of gauge field modes of arbitrary wavenumber $k < m_{\rm pl}$. However the unitarity scale sets a limit above which no analytical (perturbative) treatment can be trusted. The unitarity scale for Higgs inflation and more generally for non-minimally coupled models, has received extensive attention in the literature. We will follow the analysis of Ref. [190], where a field-dependent unitarity scale was derived in both the Jordan and Einstein frames.

The unitarity scale at the end of inflation is $k_{\rm UV,1} \equiv m_{\rm pl}/\sqrt{\xi}$, which becomes $k_{\rm UV,2} \equiv m_{\rm pl}/\xi$ for even smaller values of the background Higgs field. It is straightforward to estimate the relation of the unitarity scale to the maximum excited wavenumber

$$\frac{k_{\rm UV,1}}{k_{\rm max}} = \frac{1}{\sqrt{\xi\lambda}} \sim \frac{5 \times 10^4}{\xi^{3/2}} \,, \tag{4.84}$$

$$\frac{k_{\rm UV,2}}{k_{\rm max}} = \frac{1}{\xi\sqrt{\lambda}} \sim \frac{5 \times 10^4}{\xi^2} \,. \tag{4.85}$$

We see that, depending on the value of the non-minimal coupling ξ, the wavenumber of the produced gauge bosons can exceed the field-dependent unitarity scale. New physics is needed above the unitarity scale and it is not clear how this new physics will change particle production for such large wavenumbers. We do not wish to propose any UV completion of the Standard Model in order to address the dynamics above the unitarity scale. We will instead provide a conservative estimate of the energy density in gauge bosons in the presence of unknown UV physics that suppresses particle production with large wavenumbers (above the unitarity scale). Simply put, we will compute the energy density by introducing a UV cut-off at $k_{\mathrm{UV},1}$ or $k_{\mathrm{UV},2}$.

If we consider the UV cut-off at $k_{\mathrm{UV},1}$, both $\xi = 10^3$ and $\xi = 10^4$ preheat entirely after one inflaton zero-crossing, since $k_{\mathrm{UV},1} \gtrsim k_{\mathrm{max}}(\xi = 1000)$, as can be seen from figure 4.9. If instead we place the UV cut-off at $k_{\mathrm{UV},2}$, the gauge fields do not carry enough energy to completely preheat the universe after one inflaton zero-crossing, regardless of the value of the non-minimal coupling ξ. We thus conclude that preheating into gauge fields is very sensitive to unknown UV physics, since the majority of the energy density is carried by high-k modes, whose number density in a UV-complete model can be much different than the one computed here. It is worth noting that the excitation of Higgs fluctuations occurs entirely below the unitarity scale, hence it is not UV sensitive. We will not consider any UV cut-off for the remainder of this chapter, unless explicitly stated.

4.5 Scattering, decay and backreaction

So far we have computed the parametric excitation of particles, either Higgs or gauge bosons, from the oscillating Higgs condensate during preheating. With the exception of the brief discussion in section 4.3.1, the interactions of the resulting particles have been completely ignored. However, as discussed in Refs. [171, 172], certain types of decays of the produced particles can suppress Bose enhancement and thus effectively shut off preheating. In Ref. [2] we carefully study the effects of the following decays and scattering processes:

A. the decay of Higgs particles into gauge bosons and fermions,

B. the scattering of Higgs particles into gauge bosons and fermions,

C. the decay of parametrically produced gauge bosons,

D. the scattering of gauge bosons into fermions and Higgs bosons and

E. possible effects arising from non-Abelian interactions of the produced W- and Z-bosons.

Any of the above mentioned processes can suppress or shut off the resonances. We summarize the results of Ref. [2] here.

4.5.1 Higgs decay

Decay of the Higgs into a pair of fermions f or gauge bosons B requires $m_h > 2m_{f,B}$. The fermion masses are

$$m_f^2 = \frac{y_f^2}{2}\frac{\varphi^2}{2f}\,, \tag{4.86}$$

while the gauge boson masses were extensively studied in section 4.4.2. Comparing the Higgs mass to the fermion and gauge boson masses shows that away from the zero-crossings of φ the only decay that is kinematically allowed is a decay into an electron-positron pair. The corresponding decay rate is given by

$$\Gamma = \frac{y_f^2}{8\pi} m_h\,. \tag{4.87}$$

For the electron, the small Yukawa coupling gives $\Gamma \ll H$, such that the decay is not efficient. We have checked that the instants where $\varphi \approx 0$ – and decay into other fermions is kinematically possible – are too short for significant Higgs decay to occur. We therefore conclude that perturbative decays do not shut off the self-resonance.

4.5.2 Higgs scattering

Due to the large number density, Higgs scatterings might be more efficient than decays. For Higgs scattering into pairs of bosons/fermions the kinematical constraint is weakened by a factor 2: $m_h > m_{f,B}$. As we saw above, kinematical constraints are significant, and we therefore only consider Higgs scattering into electron-positron pairs. The scattering rate is

$$\Gamma = n\sigma v\,, \tag{4.88}$$

where n is the Higgs number density, σ the interaction cross-section and v the velocity of the Higgs. We find that, despite the large number density, scattering is inefficient, $\Gamma \ll H$, due to the small cross-section $\sigma \propto y_e^4/(m_h^2)$. We also note that other scattering diagrams that could lead to Higgs depletion suffer from the same suppression factors as the tree-level scattering: light fermions have small Yukawa couplings, while heavy ones will lead to suppression factors from the fermion loops.

4.5.3 Gauge decay

Following Refs. [171, 172] the decay width of the W and Z bosons to fermions is given by

$$\Gamma_W = \frac{3g^2}{16\pi} m_W \,, \tag{4.89}$$

$$\Gamma_Z = \frac{g_2^2}{8\pi^2 \cos^2\theta_W} m_Z \left(\frac{7}{2} - \frac{11}{3}\sin^2\theta_W + \frac{49}{9}\sin^4\theta_W \right) , \tag{4.90}$$

where the decay widths are obtained by summing over all allowed decay channels into SM fermions. The decay of the Z boson to a pair of Higgs particles proceeds similarly. Using the gauge boson mass given in eq. (4.80), we see that $\Gamma_{W,Z}/H \gg 1$ and we find that decays into fermions completely deplete the produced gauge boson population within far less than a period of background oscillations. We estimate that the effect of particle decay *during* the Riemann spike is not strong enough to significantly affect the production of gauge bosons at the first zero-crossing. Hence, in order for the gauge bosons to be able to preheat the universe, the energy density in the gauge fields must be equal to the energy density in the inflaton condensate already after the first zero-crossing.

4.5.4 Gauge scattering

Instead of decaying into fermions, gauge bosons can also scatter into Higgs particles or fermion-antifermion pairs. The scattering rate is again given by $\Gamma = n\sigma v$, where v and n are now the velocity and number density of the gauge bosons respectively. We estimate

$$\frac{\Gamma}{H} \simeq \frac{10^5}{\xi^{3/2}} \,. \tag{4.91}$$

Since $\Gamma/H \lesssim 1$ for $\xi \gtrsim 10^3$, gauge field scatterings are not important for large values of ξ.

4.5.5 Non-Abelian effects

Since we are using an Abelian $U(1)$-gauge field as a proxy for preheating into SM W- and Z-bosons, we estimate the possible non-Abelian effects. As long as the linear analysis holds, the electroweak sector can be decomposed into 3 almost identical Abelian copies. However, once the the gauge field modes become sufficiently populated, their true non-Abelian nature cannot be neglected. Using a

Hartree-type approximation we can define the non-Abelian contribution to the gauge field mass-squared as $m^2_{\rm non-Abelian} \sim g^2\langle AA\rangle$. We estimate

$$\langle A^2\rangle \simeq 10^{-10}\xi m^2_{\rm pl}\,, \tag{4.92}$$

which does not dominate over the Riemann spike for $\xi \gtrsim 10^3$. We thus expect the explosive transfer of energy from the inflaton to the gauge fields for $\xi \gtrsim 10^3$ to persist even in the full $SU(2)_L \times U(1)_Y$ sector.

4.6 Observational consequences

As mentioned in section 2.1, observing reheating is difficult due to the inherently small length scales involved. However, there are two important quantities that can be used to connect reheating to particle physics processes or CMB observables: the reheat temperature $T_{\rm reh}$ and the number of e-folds of an early matter dominated epoch in the expansion history of the universe $N_{\rm matter}$.

4.6.1 Reheating temperature

The reheat temperature is computed using the Hubble scale at the instant when $\rho_{\rm infl} = \rho_{\rm rad}$ as

$$3m^2_{\rm pl}H^2 = \rho = \frac{\pi^2}{30g_*}T^4_{\rm reh}\,, \tag{4.93}$$

where $g_* = 106.75$ is the number of relativistic degrees of freedom at high energies. For instantaneous reheating from gauge field production, which happens for $\xi \gtrsim 1000$, the Hubble scale is $H \simeq H_{\rm end}$. For $\xi \lesssim 1000$ preheating proceeds through Higgs self-resonance, leading to a smaller value of the energy density as shown in figure 4.4. The monotonic increase of the reheat temperature $T_{\rm reh}$ as a function of the non-minimal coupling ξ is shown in figure 4.10. It must be noted that eq. (4.93) assumes the immediate transition to a thermal state after preheating has ended. For the case of Higgs self-resonance, this will occur through efficient scattering of Higgs bosons to the rest of the SM. For the case of instantaneous preheating to gauge fields, the situation is more complicated. In that case the number density of gauge bosons is not exponentially large, as is usually the case in preheating. On the contrary, the transfer of energy to gauge fields is done primarily through the production of fewer high-momentum modes $k_{\rm max} \sim \sqrt{\lambda}m_{\rm pl}$. A fraction of the produced W- and Z-bosons will decay to leptons, while another fraction will decay into quarks and antiquarks that

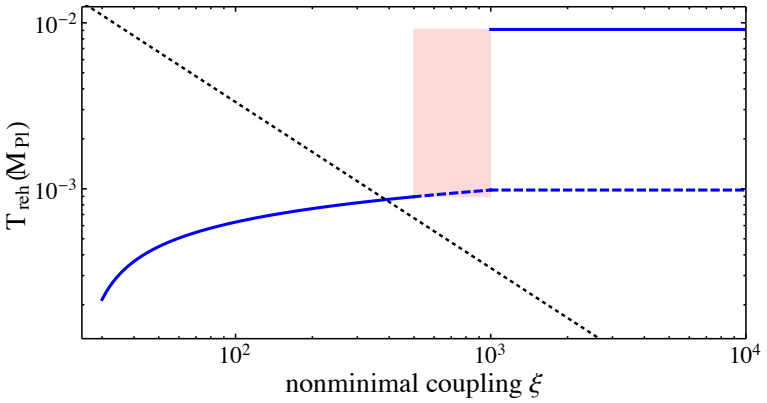

FIGURE 4.10: Reheat temperature in units of $m_{\rm pl}$ as a function of the non-minimal coupling ξ. The discontinuity at $\xi \simeq 10^3$ occurs due to the instantaneous preheating to gauge fields. The light red region represents the uncertainty of the exact threshold of instantaneous preheating to gauge fields. The black-dotted line corresponds to the unitarity scale constraint. The blue-dashed line shows the reheat temperature due entirely to Higgs self-resonance, assuming gauge boson production above the unitarity scale is suppressed due to unknown UV physics.

will eventually hadronize. The approach to thermal equilibrium will thus be more complicated. We leave the study of the thermalization process for future work and we use eq. (4.93) as an estimate of the reheat temperature, under the assumption of efficient thermalization.

However, a high reheat temperature may pose a challenge for any computation that goes beyond the linearized analysis that we presented, due to possible conflicts with the unitarity scale. Since thermalization of the reheating products will result in a blackbody spectrum, we can take the typical momentum involved to be $k \sim 3T_{\rm reh}$, which is thus the typical momentum exchange in particle scatterings inside the plasma. Since complete reheating means that the inflaton condensate will have completely decayed, the unitarity scale is $k_{\rm UV,2} \equiv m_{\rm pl}/\xi$. The typical particle momenta are below the unitarity scale for $3T < k_{\rm UV,2}$. As shown in figure 4.10, for $\xi \lesssim 300$, the resulting plasma has a low enough temperature to avoid processes that exceed the unitarity scale, at least neglecting the tail of the thermal spectrum. For $\xi \gtrsim 300$, the unitarity scale $k_{\rm UV,2}$ will be exceeded by the typical wavenumbers in the system, provided that thermalization is efficient. Finding out whether the unitarity scale is indeed violated for $\xi \gtrsim 300$ requires a more extensive study of the thermalization phase.

4.6.2 Number of matter-dominated e-folds

The duration of the reheating stage can have observational consequences, as was explained in section 2.1.2. The values of the spectral observables n_s and r are related to the time N_* when the CMB-relevant modes exited the horizon during inflation. For Higgs inflation and related models the CMB observables are given by $n_s \simeq 1 - 2/N_* - 3/N_*^2$ and $r \simeq 12/N_*^2$. Depending on the speed of the transition from the end of inflation to radiation-dominated expansion of the universe, the observationally relevant N_* may vary, shifting the predictions for n_s and r.

The number of matter-dominated e-folds of post-inflationary expansion is a non-monotonic function of the non-minimal coupling. For $\xi \gtrsim 10^3$, instantaneous reheating leads to a universe filled with gauge field modes of high wavenumbers, hence the universe transitions immediately to radiation domination (assuming no UV suppression). We must note that the decay of the inflaton condensate makes the gauge fields light, hence relativistic. For small values of the non-minimal coupling $\xi = \mathcal{O}(10)$, the background evolves as $w \approx 1/3$, hence the evolution of the universe is that of radiation domination soon after the end of inflaton, even if preheating is not efficient. Hence $N_{\rm matter} = 0$ for both large and $\mathcal{O}(10)$ values of the non-minimal coupling. There is an intermediate region of $\xi = \mathcal{O}(100)$, where preheating happens through self-resonance and the background evolves following an average equation of state of $w \approx 0$ [174] before preheating completes. In that regime of non-minimal couplings $N_{\rm matter} \approx N_{\rm reh} \approx 3$, slightly shifting the predictions of the CMB compared to the approximation of instantaneous reheating [119], where the equation of state is assumed to transition from $w = -1/3$ at the end of inflation to $w = 1/3$ immediately afterwards.

4.7 Conclusions

Higgs inflation is an appealing way to realize inflation within the particle content of the Standard Model, by coupling the Higgs field non-minimally to the gravity sector with a large value of the non-minimal coupling. We analyzed the non-perturbative decay of the Higgs condensate into Higgs bosons and electroweak gauge fields, finding distinct behavior for different ranges of values of the non-minimal coupling ξ.

The self-resonance of the Higgs field leads to preheating after $N_{\rm reh} \simeq 4$ e-folds for values of the non-minimal coupling $\xi \gtrsim 30$. For large values $\xi > 100$ the inflaton can transfer all of its energy into non-relativistic Higgs modes within $N_{\rm reh} \approx 3$, independently of the exact value of the non-minimal coupling. The dominant contribution to the parametric excitation of Higgs modes is the effect of

coupled metric fluctuations. In order to accurately capture the amplitude of the Higgs wavefunction, the computation must be initiated before the end of inflation.

The excitation of gauge bosons is much more dramatic, reminiscent of the purely scalar case of preheating in multi-field inflation with non-minimal couplings [174–176]. Gauge fields are excited after the first zero-crossing of the inflaton field, up to wavenumbers $k_{\rm max} \sim \sqrt{\lambda} m_{\rm pl}$. This leads to the possibility of the inflaton condensate transferring the entirety of its energy density to W- and Z-bosons immediately after the end of inflation, leading to instantaneous preheating. W- and Z-bosons will efficiently decay into SM fermions, ultimately filling the universe with a thermal plasma. Estimates of perturbative decay and non-Abelian effects show that gauge field production is robust against both for $\xi \gtrsim 10^3$.

The use of Coulomb, rather than unitary gauge for our computations allows us to tie the results to the purely scalar case studied in Refs. [174–176], as well as apply the results to other models with curved field-space manifolds. One such example is another version of Higgs and Higgs-like inflation, proposed in Ref. [210]. In that model, the necessary non-minimal coupling is small and negative, accompanied by a minimum of the Higgs potential at a large vacuum expectation value during inflation.

Another modification of Higgs inflation is based on the possible existence of an inflection point in the Higgs inflation potential [211–213]. The possibility of primordial black hole production in critical Higgs inflation has been proposed in Ref. [214]. It was however shown that large curvature fluctuations in Higgs inflation are hard or impossible to produce without violating observational limits on the tensor-to-scalar ratio and the running of the spectral tilt [215, 216], unless one postulates a large running of the non-minimal coupling ξ that is not found in the renormalization group flow of the Standard Model non-minimally coupled to gravity. Recent studies of Higgs inflation involving non-minimal couplings in the Palatini formulation of gravity [217, 218] can also have different preheating phenomenology. Exploring the preheating phenomenology of these models is interesting and can be performed using the techniques applied here. Such analyses can provide unique handles in order to probe the Higgs potential at energy scales that are out of reach for the LHC and any future accelerator.

Part II

Electroweak Baryogenesis

Chapter 5

Introduction to Electroweak Baryogenesis

The second part of this thesis focuses on a longstanding problem in particle physics and cosmology. Measurements show that there is an excess of matter over antimatter in our universe. The baryon asymmetry of the universe (BAU) is quantified by the ratio of of the baryon number density n_B (1/3 the number of quarks minus 1/3 the number of antiquarks) over the entropy density s. This quantity has been determined by two independent methods [11, 219]

$$Y_B = \frac{n_B}{s} = \begin{cases} 8.2\text{-}9.4 \times 10^{-11} & \text{Big Bang Nucleosynthesis}\,, \\ 8.65 \pm 0.09 \times 10^{-11} & \text{Planck}\,, \end{cases} \tag{5.1}$$

which are in good agreement.

If we assume that the universe started in a matter-antimatter symmetric state, the Standard Model can not explain how the observed baryon asymmetry was formed. Assuming that the universe started out with an overdensity of baryons does not solve the problem either: inflation would have washed out any initial density. Explaining the prevalence of baryons over antibaryons in our present universe thus requires a new mechanism to generate this asymmetry. This process is referred to as 'baryogenesis'. In the next section we will introduce the necessary conditions for baryogenesis and give examples of models that satisfy these conditions. We will then focus on a specific framework, electroweak baryogenesis, and explain how to fulfil the necessary condition of a first-order electroweak phase transition in section 5.2. In section 5.3 and 5.4 we derive the transport equations for the particles in the plasma. In section 5.5 we show how we compute the resulting baryon asymmetry. In this part of the thesis we use a metric with signature $(+,-,-,-)$.

5.1 Conditions for baryogenesis

5.1.1 Sakharov conditions

In 1967 Andrei Sakharov wrote down three conditions for successful baryogenesis [220]:

- **B violation**

  This condition is rather obvious: to go from a universe with no net baryon density to a universe with nonzero baryon number density, there should be some process in which baryon number is created. The standard model fulfils this condition through the non-perturbative electroweak sphaleron process [221, 222]. The electroweak sphaleron transition violates $B + L$ (baryon + lepton number). At low energies sphaleron transitions are exponentially suppressed but they are active at temperatures above the electroweak scale [223]. Extensive treatments of electroweak sphalerons in the context of baryogenesis can for example be found in Refs. [224–227].

- **C- and CP-violation**

  Violation of baryon number alone is not a sufficient condition. If C (charge) and CP (charge-parity) would be conserved, each baryon-number generating process would have a C- or CP-conjugate process that generated negative baryon number at the same rate. C- and CP-violation is thus a second condition for successful baryogenesis. The electroweak sector of the standard model violates C and the CKM-matrix accommodates CP-violation as well. The amount of CP-violation is however not sufficient to produce the observed baryon asymmetry [228–230].

- **Out-of-equilibrium dynamics**

  If the above two conditions were satisfied, but the relevant processes were in thermal equilibrium, baryogenesis would not occur. Deviation from thermal equilibrium is needed to ensure that baryon-number-generating processes do not have the same rate as their opposite processes, which destroy baryon number. An example of an out-of-equilibrium process is a first-order phase transition. For the measured value of the Higgs boson mass the electroweak phase transition is not first order [231–236]. The QCD phase transition is not first order either, so the condition of out-of-equilibrium dynamics is not satisfied in the standard model.

5.1.2 Models for baryogenesis

Understanding why baryons are more abundant than antibaryons thus requires BSM physics. There is a large range of BSM models that could explain the observed baryon asymmetry. In section 2.1.4 we already introduced two models in which the baryon asymmetry is generated during reheating (GUT-scale baryogenesis and Cold Electroweak Baryogenesis). Another important class of models are leptogenesis models. In this framework the SM is extended by heavy right-handed Majorana neutrinos. The out-of-equilibrium decay of these heavy particles generates a lepton asymmetry, which is (partly) converted into a baryon asymmetry by the electroweak sphalerons [237]. Leptogenesis is an attractive framework, since the heavy Majorana neutrinos could also explain the small left-handed neutrino masses through the see-saw mechanism [238–240].

The disadvantage of most leptogenesis and GUT baryogenesis models is that the BSM physics lives at a very high energy scale, decoupled from the electroweak scale. Such scenarios will be difficult to probe in current and upcoming experiments (although measurements of neutrinoless double beta decay would be a hint of leptogenesis). In this part of the thesis we will focus on the electroweak baryogenesis (EWBG) scenario [226, 227, 241], where the baryon asymmetry is generated during the electroweak phase transition. In this case, the scale of BSM physics cannot be much higher than the electroweak scale which makes the scenario more testable. In particular, searches for new scalars, precision measurements of Higgs couplings, and electric dipole moment (EDM) experiments all probe different aspects of EWBG scenarios.

5.1.3 Electroweak baryogenesis in a nutshell

The mechanism of EWBG is as follows. The Sakharov condition of out-of-equilibrium dynamics is satisfied if the electroweak phase transition is first order. The phase transition proceeds via the formation of bubbles of broken Higgs vacuum, which subsequently expand to eventually fill up all of space. The quarks and leptons in the plasma collide with the walls of the expanding bubbles. If these interactions violate CP, the transmission and reflection coefficients are different for particles and antiparticles. The net result is that an overdensity of left-handed particles over antiparticles builds up in front of the bubble wall. The $(B + L)$-violating electroweak sphaleron transitions only act on electroweak doublets, and transform this 'chiral asymmetry' into a net baryon number in front of the bubble. The produced baryons are then swept up by the expanding bubble. Inside the bubble the baryon number is preserved as the electroweak sphaleron processes are strongly suppressed in the broken vacuum. For reviews of EWBG, see for example Refs. [224–227].

5.2 The electroweak phase transition

For the measured value of the Higgs mass, the EWPT in the SM is a cross-over such that the Sakharov condition demanding an out-of-equilibrium process is not satisfied [231–236]. The SM Higgs potential needs to be supplemented by BSM physics that changes the phase transition to a first-order phase transition. We will use an effective dimension-six operator to parameterize the new physics:

$$\mathcal{L} \supset -\kappa(\Phi^\dagger\Phi)^3\,, \tag{5.2}$$

from the SM-EFT Lagrangian, where $\kappa = 1/\Lambda^2$ with Λ the scale of new physics. We define the components of the Higgs field as

$$\Phi = \frac{1}{\sqrt{2}}\begin{pmatrix} \theta^1 + i\theta^2 \\ \varphi + h + i\theta \end{pmatrix}\,, \tag{5.3}$$

with θ^i the Goldstone bosons, h the Higgs field, and φ the background field, the tree-level classical potential in terms of φ is given by

$$V_0 = \frac{\mu^2}{2}\varphi^2 + \frac{\lambda}{4}\varphi^4 + \frac{\kappa}{8}\varphi^6\,. \tag{5.4}$$

5.2.1 The finite-temperature Higgs potential

In order to describe the phase transition we need to include loop corrections to the potential. The one-loop effective potential can be split into the zero-temperature Coleman-Weinberg potential and the finite-temperature contribution. The former can be resummed to get the renormalization group improved effective potential where the couplings are running with scale. For the analysis of EWBG we use the coupling values at the renormalization scale $M = m_Z$, and for simplicity neglect all running effects and threshold corrections. The calculation of the finite temperature contribution V_T is reviewed in Appendix A.1 of Ref. [3]. We can write the one-loop effective potential as $V_{\text{eff}} = V_{\text{RG}} + V_T$, with V_{RG} the RG-improved potential, and

$$V_{\text{eff}} = \frac{\mu^2}{2}\varphi^2 + \frac{\lambda}{4}\varphi^4 + \frac{\kappa}{8}\varphi^6 + \sum_X n_X \frac{T^4}{2\pi^2} J_B(m_X^2/T^2) - \sum_f n_f \frac{T^4}{2\pi^2} J_F(m_f^2/T^2)\,, \tag{5.5}$$

where we take μ, λ and κ at the renormalization scale. The sums are over all bosons X and fermions f that couple to the Higgs. We only include the fermion contribution from the top quark. n_X and

n_f denote the numbers of degrees of freedom and are given by $n_{\{h,\theta,W,Z,t\}} = \{1, 3, 6, 3, 4N_c\}$, with N_c the number of colors. The functions $J_{B,F}$ are given by

$$J_{B,F}\left(m^2/T^2\right) = \int_0^\infty dk k^2 \log\left[1 \mp e^{\left[-\sqrt{k^2+m^2/T^2}\right]}\right], \tag{5.6}$$

with the upper (lower) sign for bosons (fermions). In the high-temperature expansion (see eq. (A.11) of Ref. [3] for the expansion of J_B and J_F) the potential becomes

$$V_{\text{eff}} = \left(\frac{\mu^2}{2} + \frac{a_T}{2}T^2\right)\varphi^2 + \left(\frac{\lambda}{4} + \frac{b_T}{4}T^2\right)\varphi^4 + \frac{\kappa}{8}\varphi^6 + \mathcal{O}(T\varphi^3)\,, \tag{5.7}$$

where

$$a_T = \frac{1}{16}\left(\frac{4m_h^2}{v_0^2} + 3g^2 + g'^2 + 4y_t^2 - 12v_0^2\kappa\right), \qquad b_T = \kappa\,, \tag{5.8}$$

with m_h and v_0 the zero-temperature Higgs mass and Higgs vev, respectively. For simplicity, we will use this high-temperature expansion to determine the allowed values of κ, and to find the Higgs profile across the bubble wall that is used for the calculation of the baryon asymmetry. In addition, we neglect higher-loop corrections due to ring diagrams (usually called daisy resummation), and as mentioned above evaluate all running couplings at the scale of the Z-boson mass, and neglect further running and threshold effects. The results are not significantly different from those obtained with the full potential [242], in which all these effects are included. The simplified potential is sufficient for the goals of the upcoming two chapters: testing the SM-EFT framework and comparing the contributions of different fermions to the baryon asymmetry.

5.2.2 Nucleating bubbles

At very high temperatures the effective Higgs potential only has a minimum at $\varphi = 0$, while for lower temperatures a second minimum appears. In a potential that allows for a first-order EWPT the two minima are degenerate at some critical temperature T_c. The value of the field φ in the second minimum is denoted by v_c. We find degenerate minima for κ in the range $1.6 < (\kappa \times \text{TeV}^2) < 4.3$, in agreement with Refs. [242, 243].

The EWPT proceeds by the formation of bubbles of broken vacuum. If larger than some critical size, these bubbles expand and eventually fill up the entire universe. While bubbles can already form at the critical temperature, their rate may be too small for the phase transition to complete. The temperature at which tunnelling to the true vacuum proceeds is called the nucleation temperature T_N. To obtain this temperature we follow the discussion in Refs. [242, 244].

The tunnelling rate is $\Gamma \propto e^{-S_E}$, with S_E the Euclidean action for the so-called bounce solution φ_b [245]. At temperatures T greater than the inverse bubble radius R^{-1}, the bounce solution is $O(3)$-symmetric [246] and obeys the equation

$$\frac{d^2\varphi_b}{dr^2} + \frac{2}{r}\frac{d\varphi_b}{dr} - \frac{\partial V_{\text{eff}}(\varphi_b, T)}{\partial \varphi_b} = 0\,, \tag{5.9}$$

with boundary conditions

$$\varphi_b(r \to \infty) = 0 \quad \text{and} \quad \frac{d\varphi_b(r=0)}{dr} = 0\,. \tag{5.10}$$

$\varphi_b(r)$ gives the field profile of a static bubble, with r the distance from the center of the bubble. The corresponding Euclidean action factorizes into $S_E = S_3/T$, with

$$S_3 = 4\pi \int dr r^2 \left[\frac{1}{2}\left(\frac{d\varphi_b}{dr}\right)^2 + V_{\text{eff}}(\varphi_b, T)\right]\,. \tag{5.11}$$

Nucleation happens when the probability of creating a single bubble within one horizon is of order one [247], which leads to the condition

$$\frac{S_3}{T_N} \simeq 140\,. \tag{5.12}$$

The field value at the center of the bubbles at T_N is denoted by v_N. We point out that v_N is slightly smaller than the field value at the minimum of the potential. The difference between v_N and the field value at the minimum is larger when there is a large difference between the potential in the true and the false vacuum.

We use the Mathematica Package 'AnyBubble' [248] to solve the bounce equation (5.9) and compute S_3 for $\kappa = 2$, 2.5, and $3\,\text{TeV}^{-2}$. Figure 5.1 shows S_3/T as a function of temperature. For $\kappa \gtrsim 3\,\text{TeV}^{-2}$, the minimum of the potential at $\varphi = 0$ persists until $T = 0$, which is reflected in the figure by the lower bound on S_3/T. The nucleation rate is never large enough, and φ gets trapped in the symmetric vacuum. For $\kappa \lesssim 1.8\,\text{TeV}^{-2}$ the minimum at $\varphi = 0$ changes into a maximum before bubbles have had time to nucleate, and the EWPT is not first order.

In order to preserve the baryon number that was formed in the broken phase, the sphaleron transitions should be suppressed inside the bubble. The rate of sphaleron transitions inside the bubble is proportional to $\exp\left[-E_{\text{sph}}(T_N)/T_N\right]$, with the sphaleron energy $E_{\text{sph}}(T_N)$ being proportional to v_N. We therefore demand the additional condition for baryogenesis $v_N/T_N \gtrsim 1$ and refer to Refs. [249, 250] for a more detailed discussion. We find that this is automatically assured for all

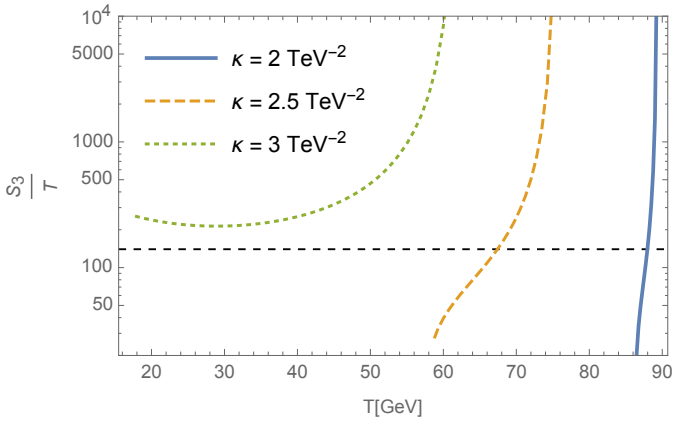

FIGURE 5.1: S_3/T as a function of temperature for three values of κ. The horizontal line indicates $S_3/T = 140$, the approximate value for which bubbles nucleate. The graph shows that nucleation is impossible for $\kappa \gtrsim 3\,\text{TeV}^{-2}$.

values of κ for which a first-order phase transition is possible in the first place. The strength of the phase transition and the value of v_N/T_N increases with κ.

To summarize, only for a narrow range of values for κ do we satisfy all criteria for successful baryogenesis:

$$1.8 \lesssim (\kappa \times \text{TeV}^2) \lesssim 3\,. \tag{5.13}$$

If we write $\kappa = \Lambda^{-2}$ this corresponds to the scale $0.58\,\text{TeV} < \Lambda < 0.75\,\text{TeV}$.

Finally, we briefly discuss the bubble profile which is needed to calculate the baryon asymmetry. The bounce solution $\varphi_b(r)$ is the initial time ($t = 0$) bubble profile. In the rest frame of the bubble, the solution at later times is $\varphi_b(\tilde{z})$ with $\tilde{z} = |r - v_w t|$, with v_w the radial velocity of the bubble wall. We can define a new variable

$$z = r_c - \tilde{z} = r_c - |r - v_w t|\,, \tag{5.14}$$

with r_c the location of the bubble wall defined via $\varphi_b(r_c) = \varphi_b(0)/2$. In terms of this new coordinate the bubble wall is located at $z = 0$, with the broken phase at $z > 0$ and the symmetric phase at $z < 0$, which matches a convention often used in the literature. We can now write the bubble profile solution $\varphi_b(\tilde{z}(z))$ as a function of z. To calculate the baryon asymmetry the wall curvature is usually neglected, and the bubble is approximated by a plane located at $z = 0$; in this approximation r can be replaced by the coordinate perpendicular to the wall, and z is extended to $\pm\infty$.

In the literature the bubble profile is often parametrized by a kink solution [251]

$$\varphi_b^{\text{kink}} = \frac{v_N}{2}\left(1 + \tanh\frac{z}{L_w}\right)\,, \tag{5.15}$$

where L_w is a measure of the width of the bubble wall. The numerical solution can be fit to this parametrization to extract L_w. We will use the kink solution in chapter 7.

5.3 CP-violating source terms

The number densities of the plasma particles in the presence of an expanding bubble are governed by transport equations. To obtain a baryon asymmetry, these equations need to include a CP-violating (CPV) source term that drives the chiral asymmetry. We will use dimension-six CPV operators from the Standard Model Effective Field Theory (SM-EFT) that we will specify in chapters 6 and 7. For definiteness we will now consider a CPV top-Higgs interaction:

$$\mathcal{L}_6^{\text{CPV}} = -\frac{i}{\Lambda_{\text{CP}}^2}\bar{Q}_L y_t \tilde{\Phi} t_R (\Phi^\dagger \Phi) + \text{h.c.}\,, \tag{5.16}$$

where Q_L denotes the left-handed doublet of the third generation and t_R the right-handed top. Φ denotes the Higgs doublet and $\tilde{\Phi}^a = \epsilon^{ab}\Phi^{b*}$. Λ_{CP} is the scale of new physics. We will just sketch the derivation of the transport equations, focusing on how this source term depends on the bubble wall profile. More details can be found in Ref. [252], the methods of which we follow.

The quantum transport equations are derived in the finite temperature Closed-Time-Path formalism [138, 139, 253–256]. Starting from the Schwinger-Dyson equation a transport equation for the number current of top quarks can be derived

$$\begin{aligned}\partial_\mu j_i^\mu(x) = -\int d^3z \int_{-\infty}^{x_0} dz_0 \ \text{Tr}\Big[&\Sigma_i^>(x,z)S_i^<(z,x) - S_i^>(x,z)\Sigma_i^<(z,x) \\ &+ S_i^<(x,z)\Sigma_i^>(z,x) - \Sigma_i^<(x,z)S_i^>(z,)\Big]\,,\end{aligned} \tag{5.17}$$

with $i = L, R$ for the left- and right-handed top quark respectively. Here S^λ are the fermionic Wightman functions (see Ref. [252] for the explicit definitions), and Σ^λ the corresponding self-energies defined below in eq. (5.20).

In the bubble background the fermion mass is space-time dependent as it depends on the Higgs background $\varphi_b(z)$. To deal with this complication, the self-energies are calculated in the 'vev-insertion approximation' (VIA) [257–260], which amounts to treating the field-dependent part of the mass as a perturbation. The zero-temperature top mass m_t can be split into a real and imaginary part (indicated by superscripts), and likewise for the thermal corrections δm_t. The quadratic Lagrangian for the top quarks is split into a free part, independent of the bubble profile, and a field-dependent

interaction part, according to

$$\mathcal{L}^{\text{free}} \supset \sum_{i=L,R} \bar{t}_i \left(i\not{\partial} - \delta m_i^{\text{Re}}(T) \right) t_i \,, \tag{5.18}$$

$$\mathcal{L}^{\text{int}} \supset -\left[m_t^{\text{Re}}(\varphi_b) + i \left(m_t^{\text{Im}}(\varphi_b) + \delta m_t^{\text{Im}}(\varphi_b, T) \right) \right] \bar{t}_L t_R + \text{h.c.} \equiv -\frac{\mathscr{g}_t(T, \varphi_b)}{\sqrt{2}} \bar{t}_L t_R + \text{h.c.} \,. \tag{5.19}$$

The $\mathscr{g}_t$-functions defined above, which parameterize the interaction strength, depend on the specific CPV-interaction and will be given in chapters 6 and 7. The $\delta m_i^{\text{Re}}(T)$ are the usual SM thermal masses [261]. They can be viewed as one-loop thermal corrections to the massless propagator. Since these corrections do not depend on the space-time dependent Higgs profile, they can be resummed and included in the full propagator $S_i^{\lambda}(\delta m_i^{\text{Re}})$, which is constructed from the free Lagrangian. The $\delta m_i^{\text{Im}}(\varphi_b, T)$ are the one-loop thermal corrections to the CPV m_i^{Im}-vertex. All the terms in $\mathscr{g}_t$ are field dependent, and therefore treated as a perturbation. The imaginary part of the mass is space-time dependent in the bubble background, and cannot be rotated away by a chiral transformation if it is non-linear in the field. Its presence leads to different dispersion relations for left- and right-handed particles, and consequently different forces act on them as they scatter with the bubble wall. This is the physical underpinning of the appearance of a source term, denoted by $S^{\not{\text{CP}}}$, in the transport equations that drives the chiral asymmetry. Based on this discussion, we expect $S^{\not{\text{CP}}} \propto \text{Im}(\mathscr{g}_t' \mathscr{g}_t^*)$, where a prime denotes a derivative with respect to z, the distance from the center of the bubble wall. This specific combination of $\mathscr{g}_t$ and $\mathscr{g}_t'$ arises as the source should be proportional to $\mathscr{g}_t'$, depend on the phase of $\mathscr{g}_t$, and be quadratic in $\mathscr{g}_t$ as the diagram for $t_L \to t_L$ scattering requires at least two mass insertions. This dependence is confirmed by the explicit derivation, which we will now sketch.

We consider the transport equation for the right-handed top quark t_R. The self-energy Σ_R^{λ} obtains a contribution from the diagram with two mass insertions

$$\Sigma_R^{\lambda}(x, y) = -\frac{1}{2} \mathscr{g}_t(x) \mathscr{g}_t^*(y) P_R S_L^{\lambda}(x, y) P_L \,, \tag{5.20}$$

with $P_{L,R}$ the left- and right-handed projection operators. Using eq. (5.20) in the transport equation (5.32), we can separate the right-hand side into a real and imaginary part, corresponding to the

CP-conserving relaxation term and the CPV source

$$\begin{aligned}\partial_\mu j^\mu_R(x) &= \frac{1}{4}\int d^3z \int_{-\infty}^{x_0} dz_0 \;\left[\not{g}_t(x)\not{g}_t(z)^* + \not{g}_t(x)^*\not{g}_t(z)\right]\;\mathrm{Re}\,\mathrm{Tr}\left[S^>_{L,xz}S^<_{R,zx} - S^<_{L,xz}S^>_{R,zx}\right]_{\mathrm{Tr}(m)=0}\\ &+ \frac{1}{4}\int d^3z \int_{-\infty}^{x_0} dz_0\, i\left[\not{g}_t(x)\not{g}_t(z)^* - \not{g}_t(x)^*\not{g}_t(z)\right]\;\mathrm{Im}\,\mathrm{Tr}\left[S^>_{L,xz}S^<_{R,zx} - S^<_{L,xz}S^>_{R,zx}\right]_{\mathrm{Tr}(m)=0}\\ &= S^{\mathrm{CP}}_R(x) + S^{\not{\mathrm{CP}}}_R(x)\,,\end{aligned} \tag{5.21}$$

where we used the short-hand $S^{\lessgtr}_{i,xz} = S^{\lessgtr}_i(x,z)$. The subscript $\mathrm{Tr}(m)=0$ indicates that the mass can be set to zero in the trace of the propagators[1]. The analogous equation can be written down for the left-handed fermion, with $S^{\mathrm{CP}}_L(x) = -S^{\mathrm{CP}}_R(x)$ and $S^{\not{\mathrm{CP}}}_L(x) = -S^{\not{\mathrm{CP}}}_R(x)$.

In the limit that the typical time scale for thermalization of the fermions is much faster than the time scale on which the Higgs profile changes, we can expand[2]

$$\begin{aligned}\lim_{z\to x}\left[\not{g}_t(x)\not{g}_t(z)^* + \not{g}_t(x)^*\not{g}_t(z)\right] &\approx 2|\not{g}_t(x)|^2\,,\\ \lim_{z\to x}\left[\not{g}_t(x)\not{g}_t(z)^* - \not{g}_t(x)^*\not{g}_t(z)\right] &\approx 2iv_w\mathrm{Im}[\not{g}_t'(x)\not{g}_t(x)^*](x^0-z^0)\,,\end{aligned} \tag{5.23}$$

and the $\not{g}_t$-dependent parts can be taken outside the z-integral in eq. (5.21). This gives the result we are after, as it factors out the explicit dependence on the bubble-wall profile. We find that $S^{\mathrm{CP}}_R \propto |\not{g}_t|^2$, explicitly

$$S^{\mathrm{CP}}_R = \Gamma^+(\mu_L+\mu_R) + \Gamma^-(\mu_L-\mu_R)\,, \tag{5.24}$$

with $\mu_{L,R}$ the chemical potentials of left- and right-handed top quarks respectively. The rates $\Gamma^\pm$ are given by

$$\begin{aligned}\Gamma^\pm = \frac{6}{T^2}\times\frac{N_c}{4\pi^2 T}|\not{g}_t|^2\int\frac{k^2\mathrm{d}k}{\omega_L\omega_R}\mathrm{Im}\Bigg[&-\frac{(h(\mathcal{E}_L)\mp h(\mathcal{E}^*_R))}{\mathcal{E}^*_R-\mathcal{E}_L}\left(\mathcal{E}_L\mathcal{E}^*_R - k^2\right)\\ &+\frac{(h(\mathcal{E}_L)\mp h(\mathcal{E}_R))}{\mathcal{E}_L+\mathcal{E}_R}\left(\mathcal{E}_L\mathcal{E}_R + k^2\right)\Bigg]\,,\end{aligned} \tag{5.25}$$

[1] Inserting eq. (5.20) into eq. (5.32) gives a trace of a product of propagators and projection operators, which in Fourier space is of the form $\mathrm{Tr}\left[P_L(\not{p}+m_i)P_R(\not{q}+m_j)\right] = \frac{1}{2}\mathrm{Tr}\left[\not{p}\not{q}\right]$. By defining

$$S^\lambda_i(x)\big|_{\mathrm{Tr}(m)=0} = \int\frac{\mathrm{d}^4k}{(2\pi)^4}\mathrm{e}^{ik.x}\hat{S}^\lambda_i(k)(\not{k}+m)\Big|_{\mathrm{Tr}(m)=0} = \int\frac{\mathrm{d}^4k}{(2\pi)^4}\mathrm{e}^{ik.x}\hat{S}^\lambda_i(k)\not{k}\,, \tag{5.22}$$

(5.21) can be neatly split into a CP-conserving and CPV part.

[2] Here we used that Taylor expanding $\lim_{z\to x}\left[\not{g}_t(x)\not{g}_t(z)^* - \not{g}_t(x)^*\not{g}_t(z)\right]$, the $\not{g}_t^*\partial_i\not{g}_t$ term vanishes when substituted in the integral in eq. (5.21) because of spatial isotropy, and thus only the term proportional to the time-derivative $\not{g}_t^*\partial_0\not{g}_t = v_w\not{g}_t^*\not{g}_t'$ contributes [252].

with T the temperature, $h(x) = e^{x/T}(e^{x/T}+1)^{-2}$ the derivative of the Fermi-Dirac distribution $n_f(x) = (e^{x/T}+1)^{-1}$ and

$$\omega_i = \sqrt{k^2 + (\delta m_i^{\rm Re})}\,, \qquad \mathcal{E}_i = \omega_i - i\Gamma_t\,, \tag{5.26}$$

with Γ_t the thermal width. We will set Γ^+ to zero, which is a good approximation, and switch to the notation $\Gamma_M \equiv \Gamma^-$. The expression for the CPV source term is

$$\begin{aligned} S_R^{\not{CP}} = \frac{v_w N_c}{2\pi^2}\mathrm{Im}[\not{g}_t' \not{g}_t^*] \int \frac{k^2 \mathrm{d}k}{\omega_L \omega_R} \mathrm{Im}\Bigg[& \frac{(n_f(\mathcal{E}_L) - n_f(\mathcal{E}_R^*))}{(\mathcal{E}_L - \mathcal{E}_R^*)^2}\left(\mathcal{E}_L \mathcal{E}_R^* - k^2\right) \\ & + \frac{(n_f(\mathcal{E}_L) + n_f(\mathcal{E}_R) - 1)}{(\mathcal{E}_L + \mathcal{E}_R)^2}\left(\mathcal{E}_L \mathcal{E}_R + k^2\right)\Bigg]\,. \end{aligned} \tag{5.27}$$

The '-1' term in the numerator on the second line gives a divergent contribution that survives in the zero-temperature limit where the distributions n_f are Boltzmann suppressed. This divergence is absorbed by the counterterms of the zero-temperature renormalized action, or equivalently, this term can be removed by normal ordering the operators [262].

In the computation of these terms we have neglected collective plasma excitations (hole modes) [263–265]. The expressions for the source terms and relaxation rates for any fermion f can be obtained by using $\not{g}_f$ and the quantities ω_i and $\mathcal{E}_i$ corresponding to the fermion f. In appendix A the thermal widths, thermal masses and couplings needed for the computation of the CPV source and relaxation rates are listed. For leptons we set $N_c = 1$.

An alternative approach for the computation of the source terms is the semi-classical method of Refs. [266–268], which uses the WKB expansion, and is also valid for large Yukawa couplings. The source term does not depend on the thermal corrections. The expression found in Ref. [268] (multiplied by $T^3/6$ to match our conventions) for a fermion f is

$$S_f^{\rm WKB} = \frac{c v_w N_c D_f}{24}(|\not{g}_f|^2 \theta'_{\not{g}_f})''\,, \tag{5.28}$$

with $c = \mathcal{O}(1)$, D_f the diffusion constant, and $\theta_{\not{g}_f} = \arg(\not{g}_f)$. Since it is third order in the derivative expansion it is a factor $(L_w T_N)^{-2} \sim 10^{-2}$ suppressed with respect to the source in eq. (7.4), where we used the benchmark values listed in Appendix A. Including all numerical factors negates this suppression: for the benchmark values of chapters 6 and 7 we find that the semi-analytical and VIA source terms are of the same order of magnitude $S_f^{\rm WKB}/S_f = 0.2 - 5$, with the larger values obtained for leptons (which have larger diffusion constants). For definiteness, in the upcoming chapters we will use the source term in eq. (5.27) (and also the CP-conserving relaxation rate) derived in VIA for

all fermions. The qualitative results on the applicability of the SM-EFT and the role of leptons in EWBG will not depend on this, and the results can straightforwardly be adapted to different source terms.

Apart from the just derived CP-conserving rate Γ_M and CP-violating source term $S^{\not{\text{CP}}}$, the SM Yukawa interaction also enters the transport equations. The 3-point $\bar{t}_L t_R h$-interactions is kinematically forbidden (the same is the case for other fermions), so we include the 4-point $\bar{t}_L t_R h g$ interaction, which has an extra gluon line [269]:

$$\Gamma_Y = \Gamma_Y^{(4)} = \frac{\zeta_3}{6\pi^2} g_s^2 |\not{g}_t|^2 T \ln\left(\frac{8T^2}{m_q^2}\right) , \tag{5.29}$$

where we take for the typical mass scale $m_q = \delta m_t^{\text{Re}}$, or the appropriate mass when we consider a different fermion. Like above, the expression for Γ_Y neglects collective plasma excitations.

Finally, another rate that goes into the transport equations is the strong sphaleron rate [270]

$$\Gamma_{ss} = 14\kappa' \alpha_s^4 T , \tag{5.30}$$

where we take $\kappa' = 1$. Strong sphaleron interactions only affect quarks.

5.4 Quantum Boltzmann transport equations

We are now ready to write down the quantum Boltzmann transport equations for a system with CP-violating sources for top and bottom quark as well as the tau lepton, generalizing the results of Refs. [252, 271]. From these equations we can compute the density of left-handed particles. This density sources the electroweak sphaleron transition that generates a net baryon number. We denote the net number density — meaning the number density of particles minus antiparticles — of third-generation quarks by $t = n_{t_R}$, $b = n_{b_R}$, $q = n_{t_L} + n_{b_L}$, the third-generation leptons by $\nu = n_{\nu_R}$, $\tau = n_{\tau_R}$, $l = n_{\nu_L} + n_{\tau_L}$, and similarly for the lighter generations; the Higgs number density is given by $h = n_{\Phi^0} + n_{\Phi^+}$.

Gauge interactions and Higgs self-interactions are fast compared to the relevant time scales and are therefore assumed to be in thermal equilibrium, implying that the chemical potentials of the up and down components of $SU(2)_L$ doublets are equal. The same holds for the components of the Higgs doublet. First- and second-generation Yukawa interactions are slow and are therefore neglected; we justify this approximation in chapter 7. Consequently, the light leptons effectively decouple. The

light quarks still participate in strong sphaleron interactions, which means their densities are related via

$$q_1 = q_2 = -2u = -2d = -2s = -2c\,, \tag{5.31}$$

and we only require one equation to describe them. We choose the u-quark. Here q_i denotes the first- and second-generation left-handed doublet, and u, d, s, c the right-handed quarks. If we neglect the bottom Yukawa interactions, we have the further simplification $u = b$.

Weak sphaleron processes are also slow and baryogenesis can be modeled as a two-step process, where in the first step a chiral asymmetry is generated, which in a second step is converted into a baryon asymmetry [257, 268]. We argue in section 7.3 that this two-step approach even works for a lepton source scenario, where the relevant tau-Yukawa interaction rate can be small compared to the weak sphaleron rate. The conversion of the chiral asymmetry into a baryon asymmetry is described in section 5.5.

With the above considerations the full set of transport equations becomes

$$\begin{aligned}
\partial_\mu q^\mu &= +\Gamma_M^{(t)}\mu_M^{(t)} + \Gamma_M^{(b)}\mu_M^{(b)} + \Gamma_Y^{(t)}\mu_Y^{(t)} + \Gamma_Y^{(b)}\mu_Y^{(b)} - 2\,\Gamma_{\rm ss}\,\mu_{\rm ss} - S_t - S_b\,,\\
\partial_\mu t^\mu &= -\Gamma_M^{(t)}\mu_M^{(t)} - \Gamma_Y^{(t)}\mu_Y^{(t)} + \Gamma_{\rm ss}\,\mu_{\rm ss} + S_t\,,\\
\partial_\mu b^\mu &= -\Gamma_M^{(b)}\mu_M^{(b)} - \Gamma_Y^{(b)}\mu_Y^{(b)} + \Gamma_{\rm ss}\,\mu_{\rm ss} + S_b\,,\\
\partial_\mu l^\mu &= +\Gamma_M^{(\tau)}\mu_M^{(\tau)} + \Gamma_Y^{(\tau)}\mu_Y^{(\tau)} - S_\tau\,,\\
\partial_\mu \nu^\mu &= 0,\\
\partial_\mu \tau^\mu &= -\Gamma_M^{(\tau)}\mu_M^{(\tau)} - \Gamma_Y^{(\tau)}\mu_Y^{(\tau)} + S_\tau\,,\\
\partial_\mu h^\mu &= +\Gamma_Y^{(t)}\mu_Y^{(t)} - \Gamma_Y^{(b)}\mu_Y^{(b)} + \Gamma_Y^{(c)}\mu_Y^{(c)} - \Gamma_Y^{(\tau)}\mu_Y^{(\tau)}\,,\\
\partial_\mu u^\mu &= +\Gamma_{\rm ss}\mu_{\rm ss}\,.
\end{aligned} \tag{5.32}$$

The S_f denote the flavor-diagonal CPV sources for third-generation fermions that we derived in section 5.3, with $f = t, b, \tau$. The relaxation rates $\Gamma_M^{(f)}$, Yukawa rates $\Gamma_Y^{(f)}$, and strong sphaleron rate $\Gamma_{\rm ss}$, redistribute and/or wash out the generated chiral asymmetry. The lepton sector mirrors the quark sector in the above equations, with the important difference that the leptons do not have strong sphaleron transitions, and the right-handed neutrino decouples.

The chemical potentials (strictly speaking, these are rescaled chemical potentials, as we have factored out a factor $6/T^2$) corresponding to the interaction rates $\Gamma_M^{(f)}$, $\Gamma_Y^{(f)}$ and $\Gamma_{\rm ss}$ are

$$\begin{aligned}
\mu_M^{(t)} &= \left(\frac{t}{k_t} - \frac{q}{k_q}\right), & \mu_Y^{(t)} &= \left(\frac{t}{k_t} - \frac{q}{k_q} - \frac{h}{k_h}\right), \\
\mu_M^{(b)} &= \left(\frac{b}{k_b} - \frac{q}{k_q}\right), & \mu_Y^{(b)} &= \left(\frac{b}{k_b} - \frac{q}{k_q} + \frac{h}{k_h}\right), \\
\mu_M^{(\tau)} &= \left(\frac{\tau}{k_\tau} - \frac{l}{k_l}\right), & \mu_Y^{(\tau)} &= \left(\frac{\tau}{k_\tau} - \frac{l}{k_l} + \frac{h}{k_h}\right), \\
\mu_{\rm ss} &= \sum_{i=1}^{3}\left(\frac{2q_i}{k_{q_i}} - \frac{u_i}{k_{u_i}} - \frac{d_i}{k_{d_i}}\right).
\end{aligned} \tag{5.33}$$

The $k_i(m_i/T)$-functions relating the chemical potentials to the number densities are defined via $n_i = T^2\mu_i k_i/6 + \mathcal{O}(\mu_i^3)$ and their expression is:

$$k_i(m/T) = k_i(0)\frac{c_{F,B}}{\pi^2}\int_{m/T}^{\infty} dx x \frac{e^x}{(e^x \pm 1)^2}\sqrt{x^2 - \frac{m^2}{T^2}}\,, \tag{5.34}$$

where $c_{F(B)} = 6\,(3)$ and the $+(-)$ sign in the denominator is for fermions (bosons), and

$$k_{Q_L}(0) = 6\,, \quad k_{q_R}(0) = 3\,, \quad k_{L_L}(0) = 2\,, \quad k_{l_R}(0) = 1\,, \quad k_\Phi(0) = 4\,, \tag{5.35}$$

where Q_L (L_L) denotes any left-handed quark (lepton) doublet, q_R (l_R) any right-handed quark (lepton) singlet and Φ the Higgs doublet.

It is easiest to work in the rest frame of the bubble, where the Higgs profile is only a function of $z = r_c - |r - v_w t|$ as in eq. (5.14), and we can express all space-time derivatives in terms of z-derivatives. In the diffusion approximation the current can be written as $j_i^\mu = (n_i, -D_i\vec{\nabla}n_i)$ with n_i the number densities and D_i the diffusion coefficients. In addition, we neglect the curvature of the bubble wall, and model the bubble wall as a plane located at $z = 0$ [272]. With these approximations

$$\partial_\mu n_f^\mu(x) \simeq v_w n_f' - D_f\vec{\nabla}^2 n_f \simeq v_w n_f' - D_f n_f''\,, \tag{5.36}$$

where the last expression is valid for the planar approximation, and where a prime denotes a derivative with respect to z. The diffusion coefficients are listed in appendix A.

Since the left- and right-handed quarks have approximately equal diffusion constants, baryon number is locally conserved on the time scale of the transport equations such that

$$t + b + q + c + s + q_2 + u + d + q_1 = t + b + q = 0\,. \tag{5.37}$$

In the second expression we used that the light quarks are only produced via strong sphalerons eq. (5.31). Local baryon number conservation can be used to eliminate the transport equation for the bottom quark. The set of transport equations can be further simplified by neglecting the slower rates, but which rates can be neglected depends on the chosen source term. If bottom Yukawa interactions are neglected we have $b = u$, and the number densities of all quarks directly follow from (q, t). If bottom Yukawa interactions are included we additionally have to solve the u-equation.

In contrast, lepton number is only conserved globally [273]. Right-handed leptons diffuse more easily than left-handed leptons since right-handed leptons do not interact through $SU_L(2)$-interactions, and therefore $D_l \neq D_\tau$. As we will see in chapter 7, for our set-up it is a reasonably good approximation to neglect this difference and assume local lepton number conservation as well.

5.5 Electroweak sphalerons

The electroweak sphalerons convert the chiral asymmetry into a baryon asymmetry. The corresponding rate is slower than all other relevant interaction rates and thus decouples from the transport equations. The only exception is the lepton Yukawa rate and we discuss this case in section 7.3. The density of left-handed fermions that sources the electroweak sphaleron transitions is given by $n_L = \sum_i (q_i + l_i)$, and is determined by solving the transport equations (5.32). The baryon asymmetry becomes (see Appendix B of Ref. [4] for a derivation)

$$Y_B = \frac{n_b}{s} = -\frac{3\Gamma_{\rm ws}}{2sD_q\alpha_+}\int_{-\infty}^{0} \mathrm{d}z\, n_L \mathrm{e}^{-\alpha_- z}\,, \qquad \alpha_\pm = \frac{v_w \pm \sqrt{4D_q\Gamma_{\rm ws}\mathcal{R} + v_w^2}}{2D_q}\,. \tag{5.38}$$

Here $s = 2\pi^2/(45) g_{*S} T^3$ is the entropy density, $g_{*S} = 106.75$ the entropy degrees of freedom at the electroweak scale, $D_q \simeq 6/T$ the quark diffusion constant, $\mathcal{R} = 15/4$ the SM relaxation term, and $\Gamma_{\rm ws} = 6\kappa\alpha_w^5 T$ the electroweak sphaleron rate with $\kappa \sim 20$ and $\alpha_w = g^2/(4\pi)$ [274–276]. In the limit $4D_q\Gamma_{\rm ws}\mathcal{R} \ll v_w^2$, the result reduces to a more familiar form

$$Y_B = \frac{n_b}{s} = -\frac{3\Gamma_{\rm ws}}{2v_w s}\int_{-\infty}^{0} n_L(z)\, e^{z\,\mathcal{R}\Gamma_{\rm ws}/v_w}\,. \tag{5.39}$$

This approximation works well for $v_w \geq 0.02$. We integrate the asymmetry over the broken phase ranging from $z = -\infty$ to the center of the bubble wall at $z = 0$ where $\varphi_b = v_N/2$. Other integration regions can be chosen, for instance $-\infty < z < -L_w$ [252, 273]. This gives a percent-level difference for the asymmetry generated by a lepton source, but can give an $\mathcal{O}(1)$ difference for the top source.

It would be optimal to integrate over the full region using the field-dependent $\Gamma_{\rm ws}(\varphi_b)$, but this requires a better understanding of the electroweak sphaleron rate.

Chapter 6

Electroweak baryogenesis and the Standard Model Effective Field Theory

6.1 Introduction

The failure of the SM to produce the observed baryon asymmetry and the wish to connect baryogenesis to the EW scale have led to a large number of SM extensions that can lead to successful EWBG. Depending on the BSM details, such as the particle content and symmetries, different tests are required and each scenario requires a detailed phenomenological study. It would be a great advantage if the crucial aspects of all these models can be tested in a single framework. In principle, the SM Effective Field Theory (SM-EFT) could provide such a framework [242, 243, 277–282] as it provides a model-independent parametrization of BSM physics. The SM-EFT assumes that any BSM degrees of freedom are sufficiently heavy, such that they can be integrated out and that their low-energy effects can be captured by effective gauge-invariant operators containing just SM degrees of freedom. While an infinite number of effective operators exist, they can be organized by their dimension. The higher the dimension of the operators, the more suppressed their low-energy effects are by powers of E/Λ, where E is a typical low-energy scale, such as the electroweak scale, and Λ the scale of BSM physics. The first operators relevant for EWBG appear at dimension-six. If the SM-EFT is suitable for the description of EWBG, it would provide an attractive framework as the dimension-six operators have to a large extent been connected to low- and high-energy experiments already, while the EFT operators can be easily matched to specific UV-complete models. Pedagogical reviews of EFTs and the SM-EFT can be found for example in Refs. [283–287].

The applicability of the SM-EFT requires a perturbative expansion in E/Λ, which is potentially dangerous for EWBG applications. Extending the SM scalar potential with a dimension-six cubic interaction to ensure a strong first-order EWPT requires a relatively low scale $\Lambda \lesssim 800$ GeV [243], which can lead to a mismatch between calculations in the SM-EFT and specific UV-complete models, see for instance Ref. [280] for an analysis of the singlet-extended SM. Furthermore, EDM constraints on dimension-six CP-violating (CPV) operators potentially relevant for EWBG are typically in the multi-TeV range [288–291]. This difference in scale can be accommodated by assuming a different threshold for the CPV dimension-six operators such that $\Lambda_{\rm CP} > \Lambda$ [278]. In this way, it might be possible to use EFT techniques for the CPV sector despite the relatively low scale required for a strong first-order EWPT.

In this chapter we investigate a related issue of the EFT approach to EWBG. As mentioned, the EFT approach requires that the effects of higher-dimensional operators are suppressed with respect to the lower-dimensional ones. For energies around the electroweak scale and $\Lambda \simeq 800$ GeV, the expansion parameter $(E/\Lambda)^2$ seems at first sight to be sufficiently small for a perturbative expansion. In practice, the necessity of a first-order phase transition requires a fine balance between dimension-two, -four, and -six contributions to the Higgs potential. While no such balance is necessary for the CP-violating sector, successful EWBG requires an interplay of the scalar and CPV sectors, such that formally higher-order corrections to the latter might become relevant as well. To study this, we consider two specific EFTs which can be related via the classical equations of motion (EOMs). EOMs can be applied to EFTs to reduce the number of operators in the EFT basis [292]. Operators related via EOMs lead to identical observables up to higher-order corrections in the EFT expansion. That is, if the EFT is working satisfactory the two EFTs under investigation should lead to the same baryon asymmetry modulo small corrections. The main goal of our work is to perform a detailed test of this hypothesis.

A somewhat similar study was performed in Ref. [282], where it was concluded that the derivative operators in the EFT can no longer be eliminated by EOMs without explicitly specifying the dynamics of the phase transition. We improve on these results by carefully investigating — both analytically and numerically — the redundancy of the operators in the EFT, including important thermal effects. We also improve the EDM phenomenology with respect to Ref. [282], which neglected several relevant contributions.

Our study allows us to pin down where and how the EFT approach breaks down for the application of EWBG. We find that scenarios that are identical up to higher-order dimension-eight corrections lead to large differences in the baryon asymmetry. The breakdown of the EFT is not specific to the EWBG

calculation and in principle also arises at zero temperature where certain CPV interactions get $\mathcal{O}(1)$-corrections from dimension-eight operators. However, these interactions are largely unconstrained, and as far as the EDM phenomenology is concerned the scenarios that are related by the EOMs are equivalent. In the context of EWBG, however, we find that dimension-eight corrections strongly modify the strength of the CPV source term that drives the creation of the matter-antimatter asymmetry. While this modification is partially washed out due to SM processes that are active during the phase transition, it still leads to a reduction of the matter-antimatter asymmetry by a factor of order five. Higher-dimensional CPV operators can therefore not be neglected.

This chapter is organized as follows. In section 6.2 we introduce the SM-EFT operators we consider and how they are related via the EOMs. We also obtain the EDM constraints on the CPV operators. In section 6.3 we briefly discuss the parameters related to the EWPT. In section 6.4 we give the simplified set of transport equations relevant to our sources of CP violation. The baryon asymmetry is calculated in section 6.5. With the calculated asymmetries we test the impact of formally higher-order corrections, and identify the source for the breakdown of the EFT expansion. We summarize, conclude, and give an outlook in section 6.6. This chapter is based on Ref. [3], but some of the details have been left out. Whenever this is the case, we will refer to the relevant section of Ref. [3].

6.2 Effective scenarios for electroweak baryogenesis

We use the same notation for the SM Lagrangian as in eq. (1.4) [1]. We add a gluon term to the covariant derivative

$$D_\mu = \partial_\mu - ig_s G^a_\mu \frac{\lambda^a}{2} - igA^i_\mu \frac{\tau^i}{2} - ig' \frac{Y}{2} B_\mu \,, \tag{6.1}$$

where g_s is the $SU(3)_C$ coupling constant and $\lambda^a/2$ are the $SU(3)$ generators. The gluon field strength is

$$G^a_{\mu\nu} = \partial_\mu G^a_\nu - \partial_\nu G^a_\mu - g_s f^{abc} G^b_\mu G^c_\nu \,, \tag{6.2}$$

with f^{abc} the $SU(3)$ structure constant. The hypercharge assignments, Y, are 1/3, 4/3, $-2/3$, -1, -2, and 1 for Q_L, u_R, d_R, L_L, e_R, and Φ, respectively.

In eq. (1.4) we have suppressed fermion generation indices, but note that the Yukawa matrices are general 3×3 matrices in flavor space. We are mainly interested in interactions of the third generation

[1] Please note that we use a metric with different signature now. This leads to a sign change in the kinetic term.

of quarks. We neglect the Yukawa couplings to light fermions, but make an exception for the electron Yukawa which plays an important role when considering EDM constraints. We have left out the topological theta terms which play no role in our discussion.

The full set of dimension-six gauge-invariant operators was constructed in Ref. [293] and updated in Ref. [294]. There exist a large set of operators but only relatively few have impact on EWBG [279, 282]. Here, we consider two specific scenarios, which we label by scenario **A** and **B**, in which we consider a small subset of dimension-six operators:

A Here we extend the SM Lagrangian by two dimension-six operators

$$\mathcal{L}_6^{(A)} = -\kappa(\Phi^\dagger\Phi)^3 - \left[C_Y\,\bar{Q}_L y_t \tilde{\Phi}\, t_R\,(\Phi^\dagger\Phi) + \text{h.c.}\right], \tag{6.3}$$

where $\kappa \sim \Lambda^{-2}$ and $C_Y \sim \Lambda_{\text{CP}}^{-2}$ are couplings of the dimension-six operators. Q_L and y_t denote, respectively, the left-handed doublet of the third-generation quarks and the (33)-component of the up-type Yukawa-coupling matrix. As we have seen in section 5.2 the first term in eq. (6.3) modifies the scalar potential and can be used to ensure a strong first-order EWPT. The second term is a dimension-six modification of the top Yukawa coupling which causes a misalignment between the top-quark mass and the top-Higgs coupling such that the latter can obtain a physical CPV phase. In fact, for simplicity we consider a purely imaginary coupling $C_Y = i\tilde{c}_Y$, with $\tilde{c}_Y^* = \tilde{c}_Y$. This particular choice of dimension-six operators has been well studied [277, 278, 281, 282] and is sometimes called the minimal EWBG scenario [278].

B In this scenario we add the same modification to the scalar potential, but consider a different CPV structure. We use

$$\mathcal{L}_6^{(B)} = -\kappa(\Phi^\dagger\Phi)^3 - \alpha\left[C_{DD}\,\bar{Q}_L D^2\tilde{\Phi}\, t_R + C_{DD}\left(\bar{Q}_L^a t_R\right)\,\epsilon^{ab}\,\left(\bar{e}_L^b y_e e_R\right) + \text{h.c.}\right], \tag{6.4}$$

where e_L and y_e denote, respectively, the lepton doublet of the first generation and the real electron Yukawa coupling. α is a real constant introduced for normalization purposes. The second term provides the dimension-six CPV source for EWBG, while the third term describes a CPV top-electron coupling and is introduced for later convenience. As in scenario **A** we consider a purely imaginary coupling $C_{DD} = i\tilde{c}_{DD}$, with $\tilde{c}_{DD}^* = \tilde{c}_{DD}$.

It is possible to relate the two scenarios via the classical EOM for the scalar field [292]. From the Euler-Lagrange equations we obtain

$$(D^2\Phi^*)^a \;=\; -\mu^2(\Phi^*)^a - 2\lambda(\Phi^\dagger\Phi)(\Phi^*)^a - 3\kappa(\Phi^\dagger\Phi)^2(\Phi^*)^a + \epsilon^{ab}\bar{t}_R y_t Q_L^b - \bar{e}_L^a y_e e_R\,, \tag{6.5}$$

where we neglected the Yukawa couplings to other fermions and a term proportional to $\Lambda_{\rm CP}^{-2}$. Applying the EOM to eq. (6.4) shifts the Lagrangian into[2]

$$\mathcal{L}_6^{(B)} \to \mathcal{L}_6^{(\rm EOM)} = -\kappa(\Phi^\dagger\Phi)^3 + \alpha\left[\mu^2 C_{DD}\,\bar{Q}_L\,\tilde{\Phi}\,t_R + 2\lambda C_{DD}\,\bar{Q}_L\,\tilde{\Phi}\,t_R\,(\Phi^\dagger\Phi) + C_8O_8\right]\,, \tag{6.6}$$

where the top-electron term in eq. (6.4) has cancelled and the dimension-eight piece is given by

$$C_8O_8 = 3\,\kappa\,C_{DD}\,\bar{Q}_L\,\tilde{\Phi}\,t_R\,(\Phi^\dagger\Phi)^2\,, \tag{6.7}$$

which scales as $\sim \Lambda^{-2}\Lambda_{\rm CP}^{-2}$. If the EFT is working satisfactory this term should give rise to small corrections compared to the dimension-six terms in eq. (6.6). It is possible to simplify eq. (6.6) by redefining the Q_L and t_R in order to absorb the $\mu^2 C_{DD}$ term into the SM top-Yukawa coupling. The resulting Lagrangian then becomes

$$\mathcal{L}_6^{(\rm EOM)} = -\kappa(\Phi^\dagger\Phi)^3 + \alpha\left[2\lambda C_{DD}\,\bar{Q}_L\,\tilde{\Phi}\,t_R\,(\Phi^\dagger\Phi) + C_8O_8\right]\,, \tag{6.8}$$

which is of the same form as eq. (6.3) modulo the higher-order correction. For now, we will not remove the $\mu^2 C_{DD}$ piece and keep the form of eq. (6.6), mainly because it provides a cleaner relation between $\mathcal{L}_6^{(\rm EOM)}$ and the derivative of the scalar potential.

6.2.1 Zero-temperature phenomenology

We now discuss experimental constraints on the dimension-six Lagrangians. We begin with the Lagrangian in scenario **A**. We assume the scalar field picks up a vacuum expectation value $v_0 = 246$ GeV, and work in this section in the unitarity gauge $\Phi = (0,\, v_0 + h)^T/\sqrt{2}$, where h denotes the Higgs boson with zero-temperature mass $m_h \simeq 125$ GeV. Because of the modified scalar potential, in both scenarios the relations between the parameters μ^2 and λ on the one hand and v_0 and m_h^2 on

[2]Here we used that $C_{DD}\,(\bar{Q}_L t_R)(\bar{t}_R Q_L) + \text{h.c.} = 0$, for purely imaginary C_{DD}.

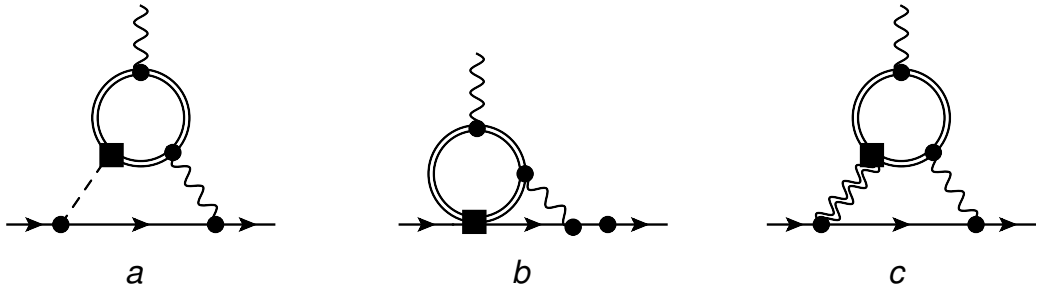

FIGURE 6.1: Two-loop diagrams contributing to the electron EDM. Single (double) lines denote the electrons (top quarks), dashed lines the Higgs boson, and wavy single (doubles) lines the photons (Z-bosons). Circles denote SM vertices, while squared denotes CPV dimension-six vertices. Only one topology for each diagram is shown.

the other, are modified by the κ term. At zero temperature we can express

$$\mu^2 = -\frac{1}{2}\left(m_h^2 - \frac{3}{2}\kappa v_0^4\right) , \qquad \lambda = \frac{1}{2}\left(\frac{m_h^2}{v_0^2} - 3\kappa v_0^2\right) . \tag{6.9}$$

Effects of the dimension-six κ interaction in particular induce deviations of the Higgs cubic and quartic interactions with respect to SM predictions. This manifests in processes such as double Higgs production, see e.g. Refs. [295, 296] for recent discussions. At the moment, such processes have not been accurately measured and current constraints on κ are weak.

In scenario **A**, the dimension-six term in eq. (6.3) gives a contribution to the top mass. We define the real top mass by [3]

$$m_t = \frac{v_0 y_t}{\sqrt{2}}\left(1 + \frac{v_0^2}{2} C_Y\right) . \tag{6.10}$$

Although this relation implies that y_t obtains a small imaginary part $\sim \mathcal{O}(\Lambda_{\rm CP}^{-2})$, this imaginary part only enters observables at $\mathcal{O}(\Lambda_{\rm CP}^{-4})$ which can be neglected. As such, from now on we use $y_t = \sqrt{2} m_t / v_0 \simeq 1$. The interactions between top quarks and Higgs bosons become

$$\begin{aligned} \mathcal{L}_h^{(\rm A)} &= -\frac{m_t}{v_0}\bar{t}_L t_R\, h - m_t C_Y\, \bar{t}_L t_R \left(v_0 h + \frac{3}{2}h^2 + \frac{1}{2}\frac{h^3}{v_0}\right) + \text{h.c.} \\ &= -\frac{m_t}{v_0}\bar{t}t\, h - m_t \tilde{c}_Y\, \bar{t}\, i\gamma^5 t \left(v_0 h + \frac{3}{2}h^2 + \frac{1}{2}\frac{h^3}{v_0}\right) . \end{aligned} \tag{6.11}$$

The top-Higgs interactions pick up a CPV component which can be probed in EDM experiments. In particular, the strongest constraint comes from the ACME experiment using the polar molecule

[3] Note that this definition differs from the m_t in the discussion above eqs. (5.18) and (5.19), where m_t denotes the finite temperature complex mass.

ThO, which sets a strong limit on the electron EDM[4] $d_e \leq 1.1 \times 10^{-29}\, e\,\text{cm}$ at 90% c.l. [297]. Please note that while Ref. [3], on which this chapter is based, was written, the most stringent bound was still $d_e \leq 8.7 \times 10^{-29}\, e\,\text{cm}$ at 90% c.l. [298]. In this chapter we have updated the results to the most recent constraint.

The dominant contribution to the electron EDM from the CPV top-Higgs couplings arises from the two-loop Barr-Zee diagram[5] in figure 6.1a [299] and is given by

$$\frac{d_e^{(\mathrm{A})}}{e} = -\frac{32 N_c}{9}\frac{\alpha_{em}}{(4\pi)^3} g(x_t)\, m_e\, \tilde{c}_Y\,, \tag{6.12}$$

in terms of the number of colors $N_c = 3$, the electron mass m_e, $x_t = (m_t/m_h)^2$, and the two-loop function

$$g(x_t) = \frac{x_t}{2}\int_0^1 dx\, \frac{1}{x(1-x)-x_t}\log\left(\frac{x(1-x)}{x_t}\right) \simeq 1.4\,. \tag{6.13}$$

The electron EDM limit then sets the strong constraint $|v_0^2 \tilde{c}_Y| < 0.001$. If we assume $|\tilde{c}_Y| = \Lambda_{\mathrm{CP}}^{-2}$, we obtain $\Lambda_{\mathrm{CP}} > 7.1$ TeV. In these expressions we have for simplicity neglected QCD renormalization-group effects that mildly affect the constraints for quarks [288, 289, 300].

In scenario **B**, the analysis is slightly more complicated. After electroweak symmetry breaking and assuming a purely imaginary C_{DD}, the CPV operators relevant for the EDM calculation become

$$\begin{aligned}
\mathcal{L}_h^{(\mathrm{B})} &= -\frac{\alpha \tilde{c}_{DD}}{\sqrt{2}}\,\bar{t} i\gamma^5 t\left(D^2 h + \frac{m_e}{v_0}\bar{e}e\right) - \frac{\alpha \tilde{c}_{DD}}{\sqrt{2}}\,\bar{t}t\,\bar{e} i\gamma^5 e \\
&= -\frac{\alpha \tilde{c}_{DD}}{\sqrt{2}}\,\bar{t} i\gamma^5 t\left(\partial^2 h + \frac{m_e}{v_0}\bar{e}e\right) - \frac{\alpha \tilde{c}_{DD}}{\sqrt{2}}\bar{t}t\left(M_Z \partial^\mu Z_\mu + \bar{e} i\gamma^5 e\right) + \dots\,,
\end{aligned} \tag{6.14}$$

in terms of the Z-boson mass, M_Z, and the dots denote interactions with two or more gauge bosons, which play no role in the EDM calculation. The last two terms in section 6.2.1 contribute to diagrams 6.1b and 6.1c and mutually cancel (this was the reason to include the CPV top-electron coupling in eq. (6.4)). The first two terms contribute to diagrams 6.1a and 6.1b. The contributions can be combined by using $k^2/(k^2 - m_h^2) = 1 + m_h^2/(k^2 - m_h^2)$ inside the loop, and together become

$$\frac{d_e^{(\mathrm{B})}}{e} = -\frac{32 N_c}{9}\frac{\alpha_{em}}{(4\pi)^3} g(x_t)\, m_e \left(-\tilde{c}_{DD}\frac{\alpha m_h^2}{\sqrt{2} v m_t}\right)\,, \tag{6.15}$$

[4]This limit assumes negligible contributions to the ThO observable from CPV semi-leptonic operators. This is justified in our scenarios as these semi-leptonic operators are only induced at loop level and strongly suppressed by small Yukawa couplings.

[5]We neglect diagrams where the internal photon is replaced by a Z-boson. These are suppressed by the electron-Z vector coupling $\sim (-1/4 + \sin^2\theta_W)$, where $\sin^2\theta_W \simeq 0.23$ is the square of the sine of the Weinberg angle.

which is of the same form as eq. (7.5), but with the replacement $\tilde{c}_Y \to -(\alpha m_h^2)/(\sqrt{2}v_0 m_t)\tilde{c}_{DD}$. By specifying α, we can ensure the same electron EDM predictions in the two scenarios. In what follows below, we will use

$$\alpha = -\frac{\sqrt{2}m_t v_0}{m_h^2}\,, \qquad \tilde{c}_Y = \tilde{c}_{DD} = \frac{1}{\Lambda_{\rm CP}^2}\,, \tag{6.16}$$

with the constraint $\Lambda_{\rm CP} > 7.1$ TeV from the limit on the electron EDM.

In section 6.2 we argued that scenario **A** and **B** are the same apart from higher-order corrections. So where are these higher-order corrections in the EDM calculation? To answer this question it is useful to look at eq. (6.6), which is the CPV Lagrangian after applying the EOM to scenario **B**. The physical real top mass is now given by

$$m_t = \frac{v_0}{\sqrt{2}}\left[y_t - \alpha C_{DD}\left(\mu^2 + \lambda v_0^2 + \frac{3}{4}\kappa v_0^4\right)\right] = \frac{v_0}{\sqrt{2}}\,y_t\,, \tag{6.17}$$

where the last equality follows from eq. (6.9). After setting α to its value in eq. (6.16), the interactions between top quarks and Higgs bosons become

$$\mathcal{L}_h^{(\rm EOM)} = -\frac{m_t}{v_0}\bar{t}t\,h - m_t\tilde{c}_{DD}\,\bar{t}\,i\gamma^5 t\left[v_0 h + \frac{3}{2}h^2\left(1 + \frac{2\kappa v_0^4}{m_h^2}\right) + \frac{1}{2}\frac{h^3}{v_0}\left(1 + \frac{12\kappa v_0^4}{m_h^2}\right)\right] + \cdots\,, \tag{6.18}$$

where the dots denote terms with four and five Higgs bosons. Comparing this to (6.11), we see that the dimension-eight corrections, $\sim \tilde{c}_{DD}\kappa$, only affect interactions with two or more Higgs bosons. These terms only contribute to the electron EDM at three loops and these contributions are therefore strongly suppressed. As such, as far the EDM phenomenology is concerned, scenarios **A** and **B** are essentially identical.

The CPV top-Higgs interactions give rise to the EDMs and chromo-EDMs of light quarks via very similar Barr-Zee diagrams. Another two-loop diagram involving a Higgs exchange inside a closed top-loop connected to external gluons, gives rise to a CPV three-gluon operator, the so-called Weinberg operator [301]. The quark (chromo-)EDMs and Weinberg operator in turn give rise to EDMs of the neutron and diamagnetic atoms such as ^{199}Hg and ^{225}Ra. With current experimental sensitivities, these limits are not competitive with the limit from the electron EDM. Furthermore, the hadronic and nuclear EDMs are sensitive to theoretical uncertainties due to hadronic and nuclear matrix elements. A much more detailed discussion can be found in Refs. [289, 302].

Finally, the CPV top-Higgs coupling can be directly probed in collider experiments, see e.g. Refs. [303–306]. However, for the foreseeable future, the resulting limits are significantly weaker than EDM constraints [302].

6.3 Bubble profile

Using the methods described in section 5.2.2 we determine a benchmark bubble profile φ_b, with parameters

$$\text{Benchmark}: \quad \kappa = 2\,\text{TeV}^{-2}, \quad T_N = 88\,\text{GeV}\,, \quad v_N = 144\,\text{GeV}, \quad v_w = 0.05\,, \tag{6.19}$$

that we will use to obtain the numerical results of section 6.5. The value for κ corresponds to a cutoff scale $\Lambda = 0.71\,\text{TeV}$ and we have checked that other values of κ consistent with a first-order EWPT lead to similar conclusions. Fitting to the kink solution (5.15), we estimate the width of the bubble wall to be $L_w T_N \simeq 9$. In vacuum the bubble wall would expand at the speed of light, but plasma interactions reduce the bubble wall velocity. The calculation of v_w is beyond the scope of this chapter, we will use the benchmark value given above [307–310].

Comparing the kink solution (5.15) and the full numerical solution, for scenario **A** we obtain a difference of only 10% in the baryon asymmetry. In scenario **B**, however, where the baryon asymmetry depends on the Laplacian of φ_b, the kink solution gives very different results. The reason is that the Laplacian contains a term $\frac{2}{\tilde{z}}\partial\varphi_b/\partial\tilde{z}$, which, when integrated over $\tilde{z}$, is only convergent because of the boundary conditions in eq. (5.10), which guarantee that $\partial\varphi_b/\partial\tilde{z}$ goes to zero at $\tilde{z} = 0$. The kink solution, however, does not satisfy the boundary condition exactly and consequently the integral diverges. The divergence may be tamed by a suitable regulator[6], but we will not follow this approach here. To avoid the divergence in scenario **B**, we will not apply the kink solution for the bubble profile, but instead use the numerical bounce solution in section 6.5.

6.4 Transport equations

All three Sakharov conditions needed for the creation of a matter-antimatter asymmetry are present in the two scenarios outlined in section 6.2. The first-order EWPT proceeds via the nucleation of bubbles of the new vacuum, which is an out-of-equilibrium process. The left- and right-handed top quarks in the plasma scatter off the bubble wall differently due to the CPV interactions in eqs. (6.3) and (6.4). As a result, a chiral asymmetry is built in front of the bubble wall. The SM sphaleron transitions only act on the left-handed particles, and transform the chiral asymmetry into a baryon asymmetry. The net baryon charge thus created is swept up by the expanding bubble, and

[6]For example, one can add an extra term to the kink solution in eq. (5.15) that is small in the bubble wall region, but cancels the divergency at the center $z = r_c$.

remains conserved provided the phase transition is strong enough such that sphaleron transitions are suppressed in the broken phase inside the bubble.

The expressions for the CPV-source and relaxation rate Γ_M are given in section 5.3. For our dimension-six operators, the $\mathscr{g}_t$-functions introduced in eq. (5.19) are given by

$$\begin{aligned}
\mathscr{g}_{t,A}(\varphi_b) &= y_t\varphi_b + \frac{iy_t\tilde{c}_Y}{2}\left[\frac{1}{2}T^2\varphi_b + \varphi_b^3\right], \\
\mathscr{g}_{t,B}(\varphi_b) &= y_t\varphi_b + i\alpha\tilde{c}_{DD}\left[\Box\varphi_b + \frac{T^2}{16}(3g^2 + g'^2 + 4y_t^2)\varphi_b\right], \\
\mathscr{g}_{t,\mathrm{EOM}}(\varphi_b) &= y_t\varphi_b - i\alpha\tilde{c}_{DD}\left[\left(\mu^2 + \frac{T^2}{2}\lambda\right)\varphi_b + \left(\lambda + \kappa T^2\right)\varphi_b^3 + \frac{3\kappa}{4}\varphi_b^5\right],
\end{aligned} \tag{6.20}$$

where the labels $i = \{A, B, \mathrm{EOM}\}$ correspond to the CPV operators in scenarios **A** (6.3), **B** (6.4), and **B** after applying the EOM (6.6). We should use eq. (6.9) to substitute for μ^2 and λ in $\mathscr{g}_{t,\mathrm{EOM}}(\varphi_b)$. Since we are in the rest frame of the bubble wall, the derivative operator $\Box$ reduces to the three-dimensional Laplace operator in spherical coordinates (with a minus sign due to the metric).

To compare the asymmetries produced in scenarios **A** and **B** in a consistent way it is important to work at the same order in perturbation theory in both the Higgs and the CPV sector. Thus we have neglected daisy diagram and have included the one-loop thermal corrections to the CPV interactions, which were calculated in Appendix A of Ref. [3].

In the two scenarios under investigation, the CPV resides in the top sector only[7]. Since leptons are only produced by small Yukawa couplings they are not taken into account. In addition, it is assumed that the second generation quarks and right-handed bottom are exclusively produced through strong sphaleron interactions, as is common in EWBG studies with a CPV top source [277, 281, 282] We will test these assumptions in chapter 7.

In addition to the assumptions in section 5.4 of gauge interactions and Higgs self-interactions in thermal equilibrium we now also drop the Yukawa rates and the Γ_M of the bottom and tau. The transport equations of the leptons completely decouple and the density of right-handed bottom quarks follows from eq. (5.31) and local baryon number conversation (5.37). In this approximation, the total chiral asymmetry is $n_L = 5q + 4t$ [311].

[7] We neglect the CPV top-electron coupling that appears in scenario **B** (see eq. (6.4)) as it is proportional to the small electron Yukawa coupling.

The full set of transport equations (5.32) reduces to [252]

$$\begin{aligned}\partial^\mu (t+q)_\mu &= -\Gamma_{ss}\left(\frac{2q}{k_q} - \frac{t}{k_t} + \frac{(q+t)}{k_{\text{eff}}}\right), \\ \partial^\mu h_\mu &= \Gamma_Y \left(\frac{t}{k_t} - \frac{h}{k_h} - \frac{q}{k_q}\right), \\ \partial^\mu (2t+q+h)_\mu &= -\Gamma_M \left(\frac{t}{k_t} - \frac{q}{k_q}\right) + S_R^{\not{CP}}.\end{aligned} \tag{6.21}$$

Γ_M and Γ_Y are proportional to $|\not{g}_{t,i}|^2 = (y_t\varphi_b)^2 + \mathcal{O}(\Lambda_{\text{CP}}^{-4})$. The difference between scenario **A** and **B** lies thus solely in the source term (5.27).

Furthermore we have

$$k_{\text{eff}} \equiv \left(\frac{4}{k_{q_{1L}}} + \frac{4}{k_{q_{2L}}} + \frac{1}{k_{u_R}} + \frac{1}{k_{c_R}} + \frac{1}{k_{d_R}} + \frac{1}{k_{s_R}} + \frac{1}{k_b}\right)^{-1}, \tag{6.22}$$

which is often approximated by $1/k_{\text{eff}} \simeq 9/k_b$ [311].

The set of transport equations (6.21) reduces to ordinary differential equations in the planar wall approximation of eq. (5.36), and can be solved to find the net chiral asymmetry $n_L = 5q + 4t$. We determine the baryon number density by integrating over the symmetric phase, using eq. (5.39).

6.5 The baryon asymmetry and investigation of the SM-EFT expansion

In this section we compare the baryon asymmetry computed in scenario **A** and **B**, and use this as guidance to investigate the validity of the SM-EFT expansion. We solve the transport equations (6.21) with the semi-analytic method outlined in Appendix B.2 of Ref. [3] (see also Ref. [312]). This method approximates all rates by a step function, and ignores the variation over the bubble-wall width. In addition, since the source peaks in the broken phase, it is set to zero in the symmetric phase. We feed the solution for $n_L(x)$ into eq. (5.39) to obtain the baryon asymmetry. We use the benchmark Higgs profile described by eq. (6.19).

6.5.1 Interaction strength and source term

The expressions for the $\mathscr{g}_{t,i}$ corresponding to our different CPV scenarios are given in eq. (6.20). The baryon asymmetry in particular depends on the combination $S^{\not{CP}} \propto \delta_i \equiv \mathrm{Im}(\mathscr{g}'_{t,i}\mathscr{g}^*_{t,i})$ which enters the source term, and varies between the scenarios.

In order for δ_i to be nonzero, we require that $\mathscr{g}_{t,i}$ has both real and imaginary parts, and $\mathscr{g}_{t,i}$ must have at least one term that depends non-linearly on the background field. For instance, for a linear dependence, $\mathscr{g}_{t,i} = c\,\varphi_b$ with c any complex number, it is clear that $\delta_i = \mathrm{Im}(|c|^2)\varphi_b\varphi'_b = 0$. The requirement of a non-linear dependence reflects that a CP-phase in the SM dimension-four Yukawa term can be rotated away and is not physical, see also the discussion surrounding eq. (6.8). With these considerations we obtain in the different scenarios

$$\delta_A = \tilde{c}_Y y_t^2 \varphi_b^3 \varphi'_b\,, \tag{6.23}$$

$$\delta_B = -\alpha y_t \tilde{c}_{DD} \left(\varphi_b \varphi_b^{'''} - \varphi_b^{'}\varphi_b^{''} + \frac{2}{z-r_c}\varphi_b\varphi_b^{''} - \frac{2}{z-r_c}\varphi_b^{'2} - \frac{2}{(z-r_c)^2}\varphi_b\varphi_b^{'} \right), \tag{6.24}$$

$$\delta_{\mathrm{EOM}} = -\alpha\, y_t \tilde{c}_{DD} \left[2\left(\frac{m_h^2 - 3v_0^4\kappa}{2v_0^2} + \kappa T^2 \right) \varphi_b^3 \varphi_b^{'} + 3\kappa \varphi_b^5 \varphi_b^{'} \right]. \tag{6.25}$$

The results for $\mathscr{g}_{t,\mathrm{EOM}}$ were obtained by first applying the EOM to the tree-level Lagrangian of scenario **B**, and then calculating the one-loop thermal corrections to $\mathscr{g}_{t,\mathrm{EOM}}$. It was checked in Appendix A.2 of Ref. [3] (where the $\mathscr{g}_{t,i}$ are denoted as f_i) that the same result is obtained if we first calculate the thermal corrections in scenario **B** to determine $\mathscr{g}_{t,B}$, and then apply the one-loop equations of motion to obtain $\mathscr{g}_{t,\mathrm{EOM}}$. Since the bounce solution φ_b is a solution of the one-loop equations of motion, see eq. (5.9), it follows that $\mathscr{g}_{t,\mathrm{EOM}} = \mathscr{g}_{t,B}$ and the source terms are equivalent — just as expected. This is somewhat obscured by the form of δ_i given above, but it is apparent from the $\mathscr{g}_{t,i}$-functions given in equation (A.18) of Ref. [3]. For this comparison, we stress that it is important to consistently include thermal corrections to the effective potential and to the CPV operators.

The difference between scenario **A** and **B** arises from the difference between δ_A and δ_{EOM}. Normalizing the CPV operators such that they give the same EDM constraints by using eq. (6.16), this gives the relation

$$\delta_B = \delta_{\mathrm{EOM}} = \delta_A \left(1 + \kappa \frac{v_0^2}{m_h^2} \left(3(\varphi_b^2 - v_0^2) + 2T^2 \right) \right). \tag{6.26}$$

The scenarios thus differ by the terms proportional to $\kappa\,\delta_A$ that scale as $\mathcal{O}(\Lambda^{-2}\Lambda_{\mathrm{CP}}^{-2})$.

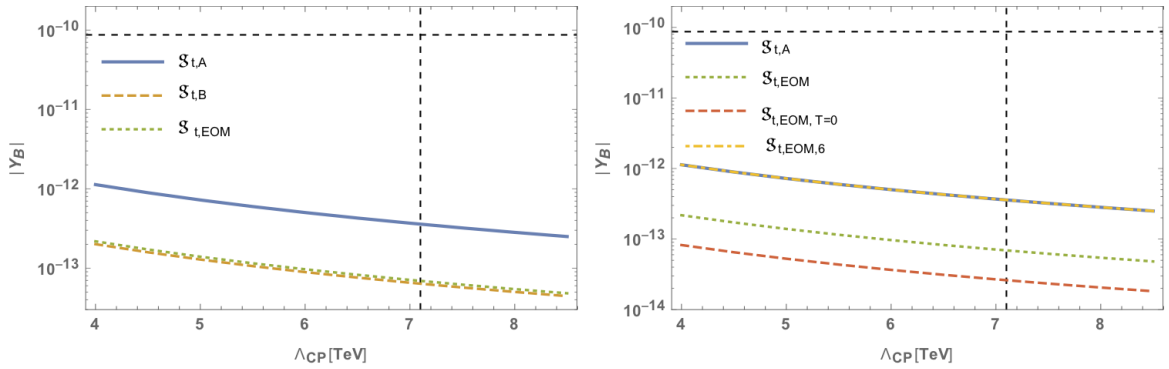

FIGURE 6.2: Absolute value of the baryon asymmetry for the considered dimension-six operators as a function of the effective CPV scale $\Lambda_{\rm CP}$. The vertical line indicates the experimental cutoff on $\Lambda_{\rm CP}$ and the horizontal line indicates the observed value of the baryon asymmetry.

6.5.2 Baryon asymmetry in scenario A and B

We will now discuss the baryon asymmetry in the two scenarios, starting with scenario **A**. We plot the baryon asymmetry as a function of $\Lambda_{\rm CP}$ in figure 6.2 in solid blue. The asymmetry measured by Planck is depicted by the dashed horizontal line, while the constraint on $\Lambda_{\rm CP}$ from EDM experiments ($\Lambda_{\rm CP} > 7.1$ TeV) is depicted by the vertical dashed line. Our results indicate that, given our approximation and input values, scenario **A** cannot produce the observed asymmetry for cutoff scales consistent with the EDM experiments. For the lowest allowed scale $\Lambda_{\rm CP} = 7.1$ TeV, corresponding to the most recent EDM constraint [297], the asymmetry is too small by roughly a factor 250.

The asymmetry in scenario **A** is much smaller than the observed value of Y_B. The computation should however be taken with a grain of salt. The baryon asymmetry is calculated using several approximations. For fermionic CPV sources in particular there are still a number of outstanding problems, see for example Refs. [226, 269]. Other issues are related to the accuracy of the vev-insertion approximation and the high-temperature expansion we applied in the calculation of the effective potential and the CPV source [313], and the uncertainty in the bubble wall velocity [307–309]. We therefore stress that our result for the baryon asymmetry suffers from significant theoretical uncertainties. An improvement of the formalism such that more accurate predictions can be made would of course be very relevant. But since the main goal of this chapter is to study the SM-EFT framework in the context of EWBG, we can live with these uncertainties as we are not too interested in the exact value of Y_B for now. Nevertheless, in chapter 7 we will investigate ways to enhance the value of the baryon asymmetry.

We now turn to scenario **B**. In this scenario the source is proportional to the much more complicated expression eq. (6.24) and depends also on the second and third derivative of the bubble profile. The

baryon asymmetry is obtained in the same way as in scenario **A** and is plotted in figure 6.2 in dashed yellow. The asymmetry is roughly five times smaller than in scenario **A** for the same values of $\Lambda_{\rm CP}$. The tension with EDM constraints is thus larger in scenario **B**.

Our results are obtained for the specific value of κ in eq. (6.19), which is expected to be representative for the narrow range in eq. (5.13) consistent with a first-order EWPT. We have checked that our results do not change qualitatively by small modifications of κ, but the exact difference between the value of the baryon asymmetry in scenarios **A** and **B** does depend on κ.

The large difference in the baryon asymmetry in the two scenarios points towards a breakdown of the SM-EFT expansion and indicates that the higher-order corrections in eq. (6.26) play an important role even though the power counting suggests that such effects are suppressed by $\mathcal{O}(v_N^2/\Lambda^2)$. In the next subsection we investigate the higher-order corrections in more detail.

6.5.3 Thermal corrections and dimension-eight effects

We study the difference between scenario **A** and **B** by dissecting $\delta_{\rm EOM}$ in eq. (6.25), which drives the CPV source after applying the EOM on scenario **B**. If we consider the complete $\delta_{\rm EOM}$, consisting of dimension-six and -eight (proportional to κ) contributions, we obtain the baryon asymmetry that is plotted in the left and right panel of figure 6.2 in dotted green. As it should, the asymmetry coincides with that of scenario **B**. The small differences of about 10% are due to numerical issues[8] related to the derivatives appearing in δ_B. The fact that the asymmetries agree provides a nontrivial check of our calculation.

If we now turn off dimension-eight contributions in $\delta_{\rm EOM}$, by setting $\kappa = 0$ in eq. (6.25), we reproduce the asymmetry in scenario **A**, as illustrated by the dotted-dashed yellow line in the right panel of figure 6.2. This is also expected as scenarios **A** and **B** are the same up to dimension-eight effects. The conclusion is that the formally higher-order terms in $\delta_{\rm EOM}$ proportional to $\sim \kappa\tilde{c}_{DD}$, reduce the obtained asymmetry by about a factor five and the EFT expansion explicitly fails. The dimension-eight terms can be separated into a temperature-independent and -dependent piece, and the dashed red line in the right panel of figure 6.2 is the result when we neglect the temperature-dependent piece of the CPV source. The difference with the full result is now roughly a factor 13 such that neglecting the temperature corrections to the CPV source is a poor approximation.

[8]The derivative terms in eq. (6.24) diverge in the limit $z \to r_c$ corresponding to the centre of the bubble, and the result is only finite once all terms are combined. Numerical errors arise if this cancellation is not perfect.

So what causes the breakdown of the EFT expansion? While the scale related to the $(\Phi^\dagger\Phi)^3$ term is not very high, $\Lambda = 0.71$ TeV, it is still significantly larger than any other scale, such as v_0, v_N, T_N, or particle masses, appearing in the computation. The problem is related to the demand of a strong first-order EWPT. The presence of a second minimum in the scalar potential requires a detailed balance between the dimension-two and -four terms in the SM Lagrangian and the $\kappa(\Phi^\dagger\Phi)^3$-term. This is the case for the zero-temperature potential as well as for the potential at the nucleation temperature T_N, but in the latter case the temperature corrections are included in the balancing act. This spoils the hierarchy between the dimension-four and -six terms in the effective potential, and thus after applying the EOMs for the Higgs field it spoils the hierarchy in the CPV sector.

This problem is not manifest in the EDM predictions in scenario **A** and **B**. The EDM constraints only depend on the linear top-Higgs coupling, which when expressed in terms of the physical masses, is the same in the two scenarios, and the higher-order terms (suppressed or not) are irrelevant. However, if we were able to accurately measure, for example, the CPV $h^2\,\bar{t}\,i\gamma^5\,t$-coupling, the two scenarios would give different predictions as can be seen by comparing eqs. (6.11) and (6.18); supposedly higher-order corrections in the EFT counting of the form $2\kappa v_0^4/m_h^2 \sim \mathcal{O}(1)$ give order-one corrections because of the balancing act in the Higgs potential.

The same breakdown of the EFT expansion occurs in the calculation of the baryon asymmetry. The difference between the obtained asymmetries in scenarios **A** and **B** arises from the dimension-eight terms in eq. (6.26). Figure 6.3 depicts the δ_{EOM} as a function of z. The green dotted line is the full result including all terms, the dashed red line ignores the temperature corrections, and the dotted-dashed yellow line ignores all dimension-eight effects and thus coincides with δ_A. The broken phase extends to $z \to \infty$, but φ_b' and consequently δ_i are only nonzero for $z < r_c \simeq 0.2\,\text{GeV}^{-1}$. The final baryon asymmetry depends on a weighted integral of the source over the broken phase[9].

The difference between the source with and without dimension-eight CPV interactions is not small at all. In fact, the peak value of δ_A is more than an order of magnitude larger than the peak value of δ_{EOM}. The right panel of figure 6.3 shows $\delta_{\text{EOM}}/\delta_A$ in the broken phase. The ratio goes from roughly -0.2 at $z = 0$ to 0.2 at $z = 0.2$. The difference mainly arises from zero-temperature contributions to δ_{EOM}, although the temperature corrections are non-negligible. Apart from the difference in overall scale, δ_{EOM} has a zero-crossing point which causes a partial cancellation between the positive and negative contributions in the integrand. The zero-crossing point emerges because the various terms in eq. (6.25) are of the same order and have opposite sign, which is related to the necessity of a

[9]See Appendix B.2 of Ref. [3] for more details on the solution to the transport equations. The source enters the solution through the β_i-parameters as given in eqs. (B.23) and (B.24).

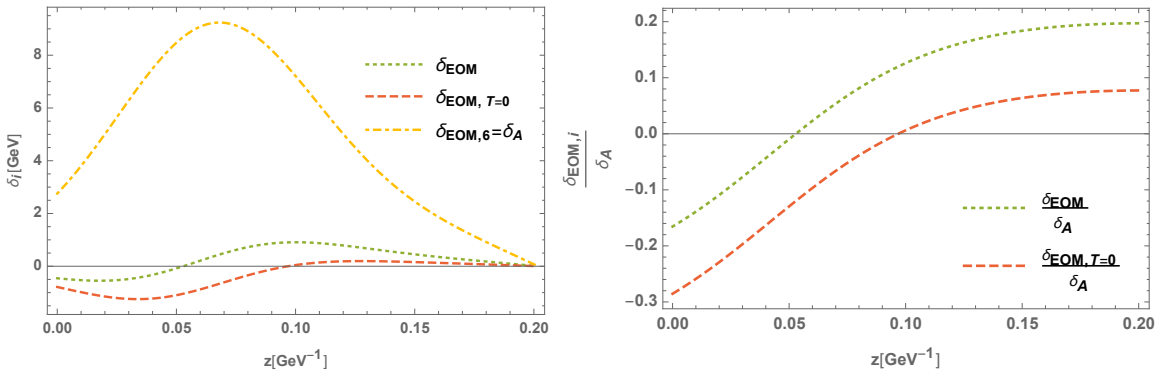

FIGURE 6.3: Left panel: $\delta_{\rm EOM}$ (green, dotted) and $\delta_{\rm EOM,6} = \delta_A$ (yellow, dotted-dashed) as a function of z in the broken phase. The difference arises from the terms proportional to $\kappa T^2\varphi_b^3$ and $\kappa\varphi_b^5$ in eq. (6.25). To see the relative importance of these two terms, we also plotted $\delta_{\rm EOM,\,T=0}$ (red, dashed), where the thermal corrections are neglected. Right panel: $\delta_{\rm EOM}/\delta_A$ in the broken phase. In dotted green the finite temperature corrections are included, in dashed red they are neglected.

second minimum in the potential. The cancellation is also present for $\delta_{\rm EOM,\,T=0}$, but occurs at a different value of z. On the other hand, δ_A is solely determined by the first term of eq. (6.25) and therefore has no cancellation between different contributions.

From figure 6.3 we can understand qualitatively why the asymmetry in scenario **B** is suppressed with respect to **A**. However, from the differences in the CPV source one would expect a larger difference in baryon asymmetry than the factor five we found and plotted in figure 6.2. Not only is the source in scenario **A** five to ten times larger over the whole range of relevant z-values, but there is also no zero-crossing and therefore no associated cancellation between different contributions. So what causes the relatively small difference in baryon asymmetry between scenarios **A** and **B** compared to the much larger difference in the CPV source?

The baryon asymmetry is produced as the electroweak sphaleron process converts the produced chiral asymmetry into a baryon asymmetry in the symmetric phase in front of the bubble wall. This chiral asymmetry n_L is calculated from the transport equations. In the symmetric phase the only non-zero rates on the r.h.s. of eq. (6.21) are the Yukawa and strong sphaleron interactions. Deep inside the symmetric phase these interactions are (approximately) in equilibrium, and consequently the combination of number densities

$$\left(\frac{2q}{k_q} - \frac{t}{k_t} + \frac{(q+t)}{k_{\rm eff}}\right) \simeq 0\,, \quad \left(\frac{t}{k_t} - \frac{h}{k_h} - \frac{q}{k_q}\right) \simeq 0\,, \qquad (z < z_{\rm eq})\,, \tag{6.27}$$

approximately vanish. Numerically, we find that this is an excellent approximation for $z_{\rm eq} \simeq -2\,{\rm GeV}^{-1}$. With these relations the chiral asymmetry can be written as $n_L = 5q + 4t = r_1 q$,

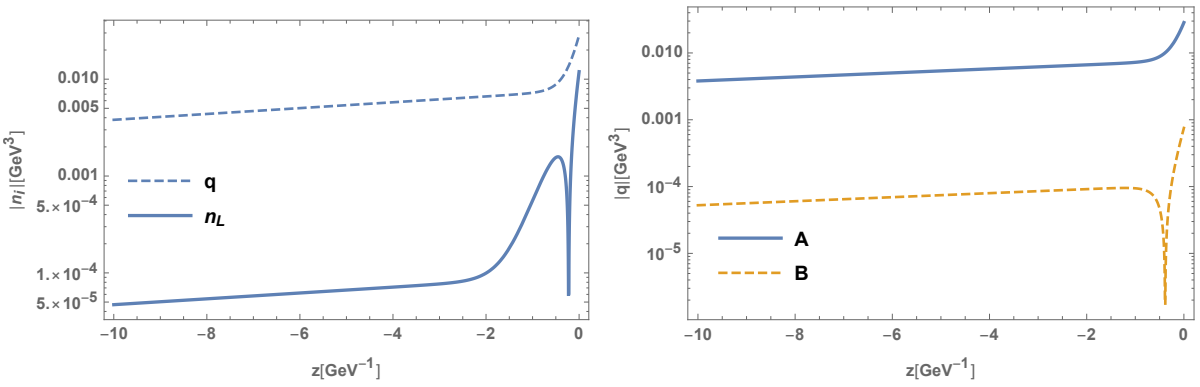

FIGURE 6.4: Left panel: absolute value of the number density q (dashed blue) and n_L (solid blue) in the symmetric phase for scenario **A**. The suppression of n_L is especially efficient for $z < -2\,\mathrm{GeV}^{-1}$. Right panel: absolute value of the number density q in the symmetric phase for scenario **A** (solid blue) and scenario **B** (dashed yellow). The density in scenario **A** is not only larger at the bubble wall at $z = 0$, but it has also diffused into the symmetric phase more effectively. The number densities t and h show similar behavior.

with

$$r_1 = 5 + \frac{4(2k_{\mathrm{eff}} + k_q)k_t}{k_q(k_{\mathrm{eff}} - k_t)}\,, \qquad (z < z_{\mathrm{eq}}). \tag{6.28}$$

The coefficient $r_1 = 0$ vanishes exactly in the massless limit, but also for our benchmark value it is small $r_1 \simeq -2 \times 10^{-2}$. The chiral asymmetry is thus much smaller than the individual number densities $n_L \ll h, q, t$, as was also noted in Refs. [314, 315].

The physical picture is as follows. The source term is non-zero inside the bubble and creates a chiral asymmetry, which then diffuses into the symmetric phase. However, on scales far away from the bubble $z < z_{\mathrm{eq}}$, the strong sphaleron and Yukawa transitions are in equilibrium and suppress the chiral asymmetry. This is shown in the left panel of figure 6.4, where the number density n_L is compared with q in scenario **A**. Electroweak sphaleron transitions transform the chiral asymmetry into a baryon asymmetry. However, this process is not efficient as only the small region right in front of the bubble $z_{\mathrm{eq}} < z < 0$ contributes significantly to the integral in eq. (5.39).

The above discussion is valid for both scenario **A** and **B**, which only differ by the source term that vanishes in the symmetric phase. It thus explains why in both scenarios baryogenesis is inefficient, and it is hard to obtain the observed asymmetry for cut-off scales consistent with EDM experiments. The difference, however, is that the source is much larger in scenario **A**. Consequently, the non-zero number densities diffuse into the symmetric phase more efficiently, as becomes clear from the right panel of figure 6.4, where the number density q is shown in the symmetric phase. If the cancellation in eq. (6.28) is not taken into account, and the chiral asymmetry would be estimated by $n_L \sim O(q)$

the obtained asymmetry would be much larger, as now the whole region $z < z_{\rm eq}$ contributes (and actually gives the dominant contribution).

The source in scenario **B** is much smaller, and consequently there is less diffusion of number densities into the symmetric phase. In effect, the number densities are peaked very close to the bubble wall and the wash-out of n_L due to the strong sphaleron and Yukawa interactions has a much smaller impact than for scenario **A**. This explains why the large difference in the CPV sources between scenarios **A** and **B** as shown in figure 6.3, are not completely transferred to large differences in the baryon asymmetry.

6.6 Discussion and conclusions

EWBG has been studied in many specific beyond-the-SM models. In this chapter, we have studied whether the crucial ingredients of EWBG can be studied without resorting to UV details of such models but instead by using effective operators to describe the EWPT and additional CP-violating sources. If applicable this would allow for a simple and model-independent description of a large class of models. Furthermore, specific SM extensions could be analyzed by matching to the EFT operators at the high-energy matching scale. As the SM-EFT operators can be and have been readily connected to low- and high-energy experiments this would allow for relatively easy tests of specific EWBG models. The main goal of this work was to study the effectiveness of the SM-EFT framework for EWBG.

The premise of the SM-EFT framework is that operators can be ordered by their dimension with higher-dimensional operators giving rise to suppressed contributions with respect to lower-dimensional ones. Based on this premise, it is possible to derive a minimal basis of operators at a given order in the EFT expansion, see for instance Refs. [293, 294], by applying EOMs. Certain operators are then redundant, up to higher-order corrections, and can be eliminated. In particular, the CPV operator in scenario **B** is usually removed from the basis. A full EFT analysis would then include all relevant dimension-six operators in a minimal basis. In this chapter we found that, for purposes of EWBG, the CPV operators in scenario **A** and **B** related by EOMs are not identical at all. The obtained baryon asymmetry differs by a large amount due to corrections from dimension-eight operators of the form

$$\mathcal{L}_8 = C_8\, \bar{Q}_L\, \tilde{\Phi}\, t_R\, (\Phi^\dagger \Phi)^2\,, \tag{6.29}$$

which therefore should be included in the analysis. In a general model-independent EFT approach there is then no, a priori, reason to not consider other dimension-eight operators that can contribute to the generation of the baryon asymmetry. The starting assumption of the SM-EFT approach is thus explicitly violated, and it is not possible to study EWBG and the related phenomenology in a fully model-independent way.

The breakdown of the effective field theory might be somewhat unexpected in view of the values of the scale of new physics required for successful baryogenesis. The scale corresponding to $\kappa = 2\,\text{TeV}^{-2}$ is $\Lambda = 0.71$ TeV while EDM experiments constrain $\Lambda_{\text{CP}} > 7.1$ TeV. There is no problem associated with the expansion in Λ_{CP}. While Λ is relatively low, it is still significantly larger than all other physical scales in the computation of the baryon asymmetry and a perturbative expansion might seem reasonable. However, in order for a first-order EWPT to occur, the $(\Phi^\dagger\Phi)^3$-term needs to strongly modify the scalar potential as the SM itself is not capable of providing such a phase transition. The parameters are thus chosen such that the dimension-four and the dimension-six terms at the minimum are approximately equal during the phase transition. We have calculated how this lack of hierarchy between dimension-four and -six contributions in the scalar sector is transferred to the CPV sector. We have shown that this leads to no problems for the low-energy EDM phenomenology which is, to a large extent, identical in the two scenarios. However, the CP-violating source which drives the generation of the baryon asymmetry is very different in the two scenarios leading to order-of-magnitude differences in particle number densities. Due to SM processes this large difference is not fully transferred to different baryon asymmetries, but nevertheless the total baryon asymmetry differs by a factor five in the two scenarios.

The difference in the baryon asymmetry raises the question whether EFT methods can still be useful for the study of EWBG. The breakdown of the EFT approach originates from the scalar sector, while the CPV sector is in principle better under control. One potential approach is then to consider a concrete UV-complete model for the phase transition, but keep the EFT approach for the CPV sector. For example, a modification of the Higgs sector that has been studied extensively in the literature [316–321] is the addition of a $\mathbb{Z}_2$-symmetric singlet S. A UV-completion has the advantage that there is no expansion in the problematic scale Λ, and the redundancy between the operators is maintained, but the price to pay is that the description of the electroweak phase transition is no longer model-independent. In addition, the EFT of the CPV sector needs to be extended to include effective operators that include the new singlet field. For a $\mathbb{Z}_2$-symmetric scenario, the first relevant operator is of the form $\mathcal{L} \sim \bar{Q}_L\tilde{\Phi}t_R|S|^2$ [322]. If the scalar field obtains a non-zero field value during the phase transition, these operators can give rise to a CPV phase contributing to EWBG that is

not significantly constrained by EDM experiments. The direct link between the baryon asymmetry and EDM experiments, which was present in the pure SM-EFT, is lost.

Another proposal, put forward in Ref. [282], is to work with the full set of dimension-six CPV operators, and to not use the EOMs to remove redundancies. In the context of this chapter, this means to treat the operators in scenario **A** and **B** as independent. Using a phenomenological description of the bubble wall in terms of a tanh-profile as in eq. (5.15), the Higgs sector can be specified by a few parameters, and thus kept generic. The disadvantage of this approach is that the physics leading to the phase transition can not be directly linked to collider experiments. Another problem is that the EDM or other low-energy experiments do not give constraints on the full set of dimension-six operators, since the redundancy is not broken at zero temperature such that observables only depend on a specific combination of operators that cannot be disentangled, even in principle. Finally, it is not clear how to match the EFT including redundant operators to a specific UV-complete model by an on-shell matching calculation at the high-energy scale.

In summary, we have investigated electroweak baryogenesis in the framework of the Standard Model EFT. We find that the EFT expansion breaks down due to the requirement of a strong first-order electroweak phase transition. We have shown that this also affects the expansion in the CP-violating sector of the EFT, such that higher-dimensional CP-violating operators cannot be a priori neglected. The pure Standard Model EFT is therefore not a suitable framework for electroweak baryogenesis. An extension of the EFT framework with additional scalar fields but effective CPV operators might be more suitable at the cost of losing model independence and a direct link to EDM phenomenology.

Chapter 7

The importance of leptons for electroweak baryogenesis

7.1 Introduction

We saw in the previous chapter that the baryon asymmetry from a dimension-six CPV top source is much smaller than the observed value of the baryon asymmetry. In this chapter we investigate why the top source is inefficient in generating the observed baryon asymmetry and explore the effects of including leptons.

We will use a relatively simple framework, inspired by effective field theory. The applicability of the SM-EFT is limited, as we saw in chapter 6, because new *light* degrees of freedom are necessary to obtain a strong first-order phase transition. In this chapter we mainly focus on the CPV dynamics and avoid the issue of the first-order phase transition by describing the bubble-wall profile in terms of the phenomenological tanh-function introduced in section 5.2.2.

As in chapter 6, we describe the required additional CPV by effective dimension-six CPV operators containing SM fields only. In principle the CPV dynamics could arise from effective operators involving any new fields that play a role in the phase transition [322], but as these are difficult to probe in experiments we ignore such interactions for now. In particular, we focus on effective dimension-six Yukawa interactions of various quarks and leptons as these are representative for popular classes of BSM models such as multi-Higgs models. Chapter 6 and similar studies in the literature have focussed on CPV in the top-quark sector [3, 278, 282], as the large top Yukawa coupling maximizes the CPV source term in the transport equations that describe the dynamics of the particle number densities. However, taking into account the most recent constraint on the

electric dipole moment of the electron [297], the 'top-source scenario' gives an asymmetry that is about two orders of magnitude too small to explain the baryon asymmetry [3].

The small value of the baryon asymmetry in the top-source scenario has prompted our current study of the general features of the solutions to the transport equations, to find ways to boost the asymmetry. The reasons for the inefficiency of the top-source scenario are threefold. First, the diffusion of the chiral asymmetry into the symmetric phase is not efficient for the strongly-interacting quarks [323]. Second, EDM measurements put strong constraints on CPV in the top sector [302] such that the strength of the CPV source term is limited. And third, the washout of the produced chiral asymmetry is significant for (top) quarks, as the top Yukawa and especially the strong sphaleron interactions effectively wash out the chiral asymmetry in the symmetric phase, except for regions very close to the bubble wall [314, 324]. These problems can potentially be overcome by looking at CPV source terms involving lighter fermions. For instance, EDM limits are less stringent for bottom quarks. While the CPV source term for bottom quarks is suppressed by the smaller Yukawa coupling, the washout rate due to Higgs interactions is suppressed accordingly. As such, the total baryon asymmetry is not a simple function of the size of the Yukawa coupling.

For leptons there can be even more advantages even though they have been neglected in many studies of EWBG. While the CPV source term is suppressed, leptons diffuse into the plasma much more easily [323], the EDM limits are less stringent for muon and tau CPV interactions [288], and the washout rate is less effective because leptons do not interact via strong sphalerons. Already in Refs. [273, 323, 325–327] the effect of leptons on EWBG was studied in a range of scenarios in which the lepton Yukawa coupling is enhanced significantly with respect to the SM values. We will show that even with the small SM Yukawa interactions, including leptons can dramatically change the baryon asymmetry in models with CPV source terms involving top quarks. In addition, we show that leptonic CPV source terms can be very efficient in producing the baryon asymmetry of the universe. Scenarios with a CPV leptonic source are also great diagnostic tools as the set of transport equations is relatively simple. We use this scenario to understand the parametric dependence of the baryon asymmetry on bubble wall parameters and the size of Yukawa couplings. This study confirms that the baryon asymmetry is not a simple function of the size of the Yukawa coupling. And while we focus on a particular set-up, the importance of leptons and the general mechanisms at play are more general.

As we will show, the role of leptons in EWBG depends on the effectiveness of the exchange of the chiral asymmetry between quarks and leptons. In the SM this exchange is not very efficient because of the small lepton Yukawa interactions. In various BSM models there can be more efficient

mechanisms, for example via the exchange of additional scalar fields. Such mechanisms can strongly boost the baryon asymmetry if the CPV source term is located in the quark sector by transferring the chiral asymmetry into the lepton sector, where it diffuses faster and suffers from less washout. Conversely, it can suppress the baryon asymmetry if the CPV source term is located in the lepton sector. We model this phenomenon by adding effective dimension-six quark-lepton interactions; this set-up qualitatively explains features of various models studied in recent literature [326, 327]. We also comment on the effect of possible new BSM quark-quark couplings, which may likewise boost the baryon asymmetry for a source located in the quark sector, as this coupling affects and limits the washout from strong sphaleron interactions.

This chapter is organized as follows. In the next section we introduce the set-up and briefly describe the first-order phase transition and bubble profile, the CPV dimension-six operators and the EDM and LHC constraints. We briefly touch upon the transport equations and the computation of the baryon asymmetry, but for the details we refer to sections 5.3, 5.4 and 5.5. We then identify the factors that suppress the value of the baryon asymmetry in the top-source scenario and motivate the importance of leptons. We also introduce a new top-lepton interaction. We start with a discussion of the tau-source scenario in section 7.3. The lepton sector almost completely decouples from the quark sector, and the baryon asymmetry can be computed analytically in this limit to good accuracy. We identify the important length scales, and discuss the physics and mechanisms at play. In section 7.4 we give the results for the top-source scenario. The equations to solve are more intricate, but the outcome can be understood qualitatively. We also comment on the viability of a bottom-source scenario and briefly discuss even lighter fermions. Finally, in section 7.5 we describe the effects of a new tau-top coupling on both the tau- and top-source scenario. We end with a discussion in section 7.6.

7.2 Set-up and methods

7.2.1 First-order phase transition

There are many BSM models that modify the Higgs sector such that the phase transition becomes first order. Well studied examples are the $\mathbb{Z}_2$-symmetric Higgs-singlet model [316–321] and two-Higgs doublet models [328–335]. In the previous chapter, we argued that a first-order electroweak phase transition cannot be described in a systematic EFT expansion and explicit light degrees of freedom

must be introduced. This unfortunately prohibits a model-independent approach, and it is necessary to pick a specific BSM model to implement the first-order phase transition.

Once a BSM model is chosen, one can solve the tunnelling equations of motion at the nucleation temperature T_N to find the so-called bounce solution φ_b [245]. We parameterize the Higgs doublet as $\Phi = (\Phi^+, \Phi^0)^T$ and in the bubble background $\langle \Phi^0 \rangle = \frac{1}{\sqrt{2}}\varphi_b(z)$. In this chapter, we will use the parametrization of eq. (5.15), which provides a reasonable description of the bubble-wall profile in many models. More complicated profiles can be studied in similar fashion. We do not expect our findings in this chapter to change significantly if more complicated profiles are applied. As in chapters 5 and 6 we use the planar wall approximation, in which curvature effects are neglected. Further, $v_N = v(T_N)$ is the vacuum expectation value of the Higgs field in the broken phase at the nucleation temperature T_N, and L_w the bubble width. In principle, these parameters should be determined by fitting the bounce solution of a BSM model to eq. (5.15). However, our prime interest is not the phase transition itself but the comparison of different sources of CP violation. We work with benchmark parameters $T_N = 88\,\text{GeV}$, $v_N = 152\,\text{GeV}$, and $L_w = 0.11\,\text{GeV}^{-1}$. For the velocity of the bubble wall we take the benchmark value $v_w = 0.05$. We will investigate how the produced asymmetry depends on these parameters.

7.2.2 Source of CP violation

We use the same CPV operator as in scenario **A** of chapter 6, but now also allow for CP-violation for lighter quarks and leptons. That is, we assume that apart from a modified scalar sector that ensures a first-order phase transition, other BSM degrees of freedom are sufficiently heavy and can be integrated out leading to effective operators. We consider the flavor-diagonal CPV dimension-six operators

$$\mathcal{L}_6 = -i\left[\bar{Q}_L\tilde{Y}_U\tilde{\Phi}\,u_R \;+\; \bar{Q}_L\tilde{Y}_D\Phi\,d_R \;+\; \bar{L}_L\tilde{Y}_L\Phi\,e_R\right](\Phi^\dagger\Phi) + \text{h.c.}\,, \tag{7.1}$$

in terms of the Higgs doublet Φ, the left-handed quark and lepton $SU(2)$ doublets Q_L and L_L, and the right-handed up, down, and lepton singlets u_R, d_R, and e_R. We have suppressed generation indices and consider the 3×3 matrices of Wilson coefficients $\tilde{c}_{U,D,L}$ to be diagonal and real (such that the operators are purely CP violating). The extension to include flavor-changing operators can be made straightforwardly. Again, we assume the dimension-six Yukawa couplings to be proportional to the SM Yukawa couplings $y_f/\sqrt{2} = m_f/v_0$ ($v_0 \simeq 246$ GeV is the zero-temperature vev) as is the

case in many BSM scenarios and suggested by minimal flavor violation

$$\tilde{Y}_U = \mathrm{diag}(y_u\tilde{c}_u,\, y_c\tilde{c}_c,\, y_t\tilde{c}_t)\,,\quad \tilde{Y}_D = \mathrm{diag}(y_d\tilde{c}_d,\, y_s\tilde{c}_s,\, y_b\tilde{c}_b)\,,\quad \tilde{Y}_L = \mathrm{diag}(y_e\tilde{c}_e,\, y_\mu\tilde{c}_\mu,\, y_\tau\tilde{c}_\tau)\,. \tag{7.2}$$

Finally, we write

$$\tilde{c}_f = \frac{s_f}{\Lambda_f^2}\,, \tag{7.3}$$

where $s_f = \pm 1$ is chosen to obtain a net number of baryons (rather than antibaryons) and Λ_f is the associated scale of new physics where the EFT breaks down. We stress that these operators are still just a subset of dimension-six SM-EFT CPV operators that can be constructed. The above operators are particularly efficient in generating a baryon asymmetry as they give rise to an effective CPV mass term during the phase transition, as we have seen in section 5.3. In addition to SM-EFT operators, in principle there can be CPV operators that include the unspecified light scalar degrees of freedom, which can only be included if we consider a specific UV completion of the scalar sector. We focus instead on the operators in eq. (7.1) as these can readily be constrained by EDM experiments.

The transport equations and the expressions for the relaxation rates and CPV source term are given in section 5.3. For later convenience, we define the function $J_f(T)$ through:

$$S_f = \frac{v_w N_c}{2\pi^2}\mathrm{Im}\left[g_f' g_f^*\right] J_f(T)\,, \tag{7.4}$$

where $J_f(T)$ is the integral in eq. (5.27) and the function g_f which was defined in eq. (5.19) should be computed for the appropriate fermion.

7.2.3 Experimental constraints on CP-violating dimension-six operators

The computation of the EDM constraint on the various CPV scales is analogous to the computation in section 6.2.1. As we will argue, for EWBG purposes the only relevant interactions are those involving the top, bottom, and tau and we mainly discuss these. Couplings to lighter fermions are too weak to create sufficient baryon asymmetry.

The contributions to the two-loop Barr-Zee diagrams of the top, bottom and tau fermions are given by [288, 289, 300]

$$\frac{d_e}{e} = -\frac{8\alpha_{em}}{(4\pi)^3} m_e \left[N_c Q_t^2\, g(x_t)\,\frac{s_t}{\Lambda_t^2} + N_c Q_b^2\, g(x_b)\,\frac{s_b}{\Lambda_b^2} + Q_\tau^2\, g(x_\tau)\,\frac{s_\tau}{\Lambda_\tau^2}\right]\,, \tag{7.5}$$

where Q_f denotes the fermion charge in units of e, $x_f = m_f^2/m_h^2$, and $g(x_f)$ the two-loop function

$$g(x_f) = \frac{x_f}{2}\int_0^1 dx\,\frac{1}{x(1-x)-x_f}\log\left(\frac{x(1-x)}{x_f}\right). \tag{7.6}$$

Numerically we have $g(x_t) \simeq 1.4$, $g(x_b) \simeq 2.7\cdot 10^{-2}$, $g(x_\tau) \simeq 7.7\cdot 10^{-3}$, and for lighter fermions the function roughly scales as $g(x_f) \sim x_f \log x_f$.

The recent constraint on the electron EDM from the ACME experiment $d_e \leq 1.1\times 10^{-29}\,e\,\text{cm}$ at 90% c.l. [297] puts a strong constraint on the CPV dimension-six top interaction $\Lambda_t \geq 7.1$ TeV, as we already saw in chapter 6. For the bottom and charm we find $\Lambda_b \geq 0.49$ TeV and $\Lambda_c \geq 0.41$ TeV and for the tau $\Lambda_\tau \geq 0.16$ TeV. For the lighter fermions no meaningful constraint can be set as the limit on Λ_f is lower than the electroweak scale. The tau coupling can in principle also be constrained by the limit on the tau EDM. However, while the contribution to the tau EDM from CPV tau-couplings is about a factor $\mathcal{O}(10^6)$ larger than the contribution to the eEDM, the experimental limit on the tau EDM is roughly a factor $\mathcal{O}(10^{11})$ weaker [336] and no significant constraints are obtained. The story is similar for the CPV μ-Higgs coupling and no significant constraint can be set. A CPV e-Higgs coupling, however, would lead to a large eEDM and we get a limit $\Lambda_e \geq 5.7$ TeV [337].

Additional constraints can be set by using experimental limits on hadronic EDMs. In this case, the analysis is more complicated and requires apart from several additional one- and two-loop diagrams also renormalization-group evolution factors and hadronic and nuclear matrix elements. A detailed study can be found in Refs. [289, 338]. With conservative values of matrix elements linking CP-odd quark-gluon operators to the neutron and Hg EDMs, we obtain $\Lambda_t \geq 0.7$ TeV, which is significantly weaker than the eEDM constraints, while no significant constraints can be set on Λ_b. For completeness we also give the EDM constraints for lighter quarks. Using conservative values for hadronic matrix elements there is no significant constraint for Λ_s and Λ_c, while $\Lambda_d \geq 1$ TeV and $\Lambda_u \geq 0.5$ TeV [289, 338]. Despite these weaker limits, we will see that EWBG is not efficient for CPV couplings involving light quarks.

The CPV fermion-Higgs couplings can also be probed at the LHC. At present, measurements of genuine CP-odd observables are not precise enough to set meaningful constraints. However, the CPV couplings modify also CP-even observables via contributions proportional to $\tilde{c}_f^2 \sim 1/\Lambda_f^4$. For example, the CPV tau-Higgs coupling modifies the $h\to\tau\tau$ branching ratio signal strength

$$\mu_{h\to\tau\tau} = \frac{\Gamma_{h\to\tau\tau}}{\Gamma_{h\to\tau\tau}^{SM}}\frac{\Gamma_h^{SM}}{\Gamma_h} = 1 + \frac{v^4}{\Lambda_\tau^4}\left(\frac{1}{1-4x_\tau}\right)\left(1 - \frac{m_H m_\tau^2}{8\pi v^2}\frac{(1-x_\tau)^{3/2}}{\Gamma_h^{\text{SM}}}\right), \tag{7.7}$$

where Γ_h denotes the total Higgs width in the presence of the CPV operators and $\Gamma_h^{\rm SM} \simeq 4.1$ MeV the predicted SM Higgs width. $\mu_{h\to\tau\tau}$ has been measured by ATLAS, $\mu_{h\to\tau\tau} = 1.09^{+0.18+0.27+0.16}_{-0.17-0.22.-0.11}$ [339]. Adding the uncertainties in quadrature gives the constraint $\Lambda_\tau \gtrsim 0.3$ TeV. Such limits are thus not very stringent. Similar analyses can be performed for other fermions, but in all cases the bounds on Λ_f are well below 1 TeV [289].

7.2.4 Transport equations

We use the set of transport equations given in eq. (5.32). If the new degrees of freedom that provide the first-order phase transition also couple to SM fermions additional interaction rates can appear in the transport equations. We model one such possible term by adding a $\Gamma_{\rm QL}$ that corresponds to a new top-tau interaction. This coupling will be motivated in section 7.2.5. It modifies the equations for q, t, l and τ, which we list here.

$$\begin{aligned}
\partial_\mu q^\mu &= +\Gamma_M^{(t)}\mu_M^{(t)} + \Gamma_M^{(b)}\mu_M^{(b)} + \Gamma_Y^{(t)}\mu_Y^{(t)} + \Gamma_Y^{(b)}\mu_Y^{(b)} - 2\,\Gamma_{\rm ss}\,\mu_{\rm ss} + \Gamma_{\rm QL}\,\mu_{\rm QL} - S_t - S_b\,,\\
\partial_\mu t^\mu &= -\Gamma_M^{(t)}\mu_M^{(t)} - \Gamma_Y^{(t)}\mu_Y^{(t)} + \Gamma_{\rm ss}\,\mu_{\rm ss} - \Gamma_{\rm QL}\,\mu_{\rm QL} + S_t\,,\\
\partial_\mu l^\mu &= +\Gamma_M^{(\tau)}\mu_M^{(\tau)} + \Gamma_Y^{(\tau)}\mu_Y^{(\tau)} - \Gamma_{\rm QL}\,\mu_{\rm QL} - S_\tau\,,\\
\partial_\mu \tau^\mu &= -\Gamma_M^{(\tau)}\mu_M^{(\tau)} - \Gamma_Y^{(\tau)}\mu_Y^{(\tau)} + \Gamma_{\rm QL}\,\mu_{\rm QL} + S_\tau\,.
\end{aligned} \tag{7.8}$$

The other transport equations in eq. (5.32) are unaffected. The chemical potential corresponding to the new interaction is

$$\mu_{\rm QL} = \left(\frac{l}{k_l} - \frac{\tau}{k_\tau} - \frac{q}{k_q} + \frac{t}{k_t}\right)\,. \tag{7.9}$$

In principle, we should also add a transport equation for the new light degrees of freedom added to the scalar sector. Generically, these new degrees of freedom equilibrate with the SM Higgs as significant interactions are required for a first-order phase transition, and the scalar degrees of freedom can be added to h which now denotes a combined number density.

The complete expressions for the interaction rates, source terms, masses, and other constants entering the equations can be found in section 5.3 and Appendix A. In this chapter we solve the transport equations numerically, with the boundary condition that the number densities vanish far away from the bubble wall. Details can be found in Appendix C of Ref. [4]. As an extra check we also solve the equations using the semi-analytical method that we used in chapter 6. Both approximations are reasonable, and for generic input parameters we find that the numerical and semi-analytical results

only differ by $\mathcal{O}(10\%)$. Unless otherwise stated, the results presented in the upcoming sections are those of the numerical calculation. We obtain the value of the baryon asymmetry from eq. (5.38).

7.2.5 Efficiency of quark/lepton source

A priori, one would expect the top source to give the largest baryon asymmetry. Since the CPV source term of eq. (7.4) is proportional to the Yukawa coupling squared, it is maximal for the top quark. Even if we had not assumed the dimension-six couplings to be proportional to y_f, the source would have a linear dependence on the Yukawa coupling. A first reason why the top-source scenario might nevertheless not be the most efficient mechanism to generate the BAU is also immediately apparent from eq. (7.4). The CPV source is suppressed by the square of the scale Λ_f. In section 7.2.3 we showed that the experimental bounds on Λ_f are rather strong for the top quark: $\Lambda_t \gtrsim 7.1\,\text{TeV}$. For the bottom quark and the tau lepton the bounds are much less severe: $\Lambda_b \gtrsim 0.5\,\text{TeV}$ and $\Lambda_\tau \gtrsim 0.3\,\text{TeV}$ respectively.

A second reason why leptons could be more efficient than quarks in generating the BAU is their larger diffusion coefficient. Since leptons only interact via the electroweak force they can diffuse further into the symmetric phase than the strongly interacting quarks [323]. This enhances the baryon asymmetry, as the electroweak sphalerons have more time to convert the lepton asymmetry into a baryon asymmetry before the bubble wall passes.

Finally, washout effects are also maximal for top quarks. The interactions mediated by the CP conserving part of the mass matrix relax the chiral asymmetry; the relaxation rate for this process is proportional to $\Gamma_M^{(f)} \propto |g_f|^2 = y_f^2\varphi_b^2 + \mathcal{O}(\Lambda_f^{-4})$, and thus largest for the top quark. The rate for Yukawa-type interactions (with radiation of an additional gluon or weak boson) is likewise maximized for the top quark $\Gamma_Y^{(f)} \propto y_f^2$.

More importantly, the strong sphaleron transitions are approximately in equilibrium in the symmetric phase except for regions close to the bubble wall [311, 314, 324] — we will estimate the size of this region in section 7.4.1 — and they very effectively wash out the chiral asymmetry in the quark sector, but leave leptons untouched. Indeed, if the strong sphaleron interactions are in thermal equilibrium the corresponding chemical potential eq. (5.33) vanishes $\mu^{ss} \simeq 0$. Neglecting the Yukawa interactions of the first- and second-generation quarks, and using baryon number conservation gives the relation

$$-4ua_1 + qa_2 + ba_3 \simeq 0\,, \tag{7.10}$$

where

$$a_1 = \frac{1}{2}\left(\frac{4}{k_{q_1}} + \frac{1}{k_u} + \frac{1}{k_d}\right), \quad a_2 = \left(\frac{2}{k_q} + \frac{1}{k_t}\right), \quad a_3 = \left(\frac{1}{k_t} - \frac{1}{k_b}\right). \tag{7.11}$$

The chiral asymmetry in quarks becomes

$$n_L^{(q)} \equiv \sum_{i=1}^{3} q_i = q - 4u = q\left(1 - \frac{a_2}{a_1}\right) - b\left(\frac{a_3}{a_1}\right), \tag{7.12}$$

where in the second and third steps we used eq. (5.31) and eq. (7.10), respectively. At zero temperature $(a_1, a_2, a_3) \propto (1, 1, 0)$ and the chiral asymmetry in quarks vanishes. At finite temperature there are corrections. For our benchmark point we find $n_L^{(q)} \simeq -0.01q - 0.01b$, and thus the chiral asymmetry in quarks is suppressed by roughly two orders of magnitude with respect to the individual quark densities. Note that we already studied this effect in section 6.5, but there we did not include the bottom quarks.

The above reasons ensure that the tau-source scenario is more effective at producing the baryon asymmetry than the top-source scenario. That is, despite the Yukawa suppression of the tau source we will obtain similar values of the total baryon asymmetries for $\Lambda_t \simeq \Lambda_\tau$.

The top Yukawa and especially the strong sphaleron interactions are very effective in washing out the chiral asymmetry in quarks. Hence, if, in the case of CP violation in the quark sector, part of the chiral asymmetry can be transferred to the leptons, which will escape the washout, the baryon asymmetry is increased. Leptons produced via the relatively small tau Yukawa interactions give the dominant contribution to the baryon asymmetry in the top-source scenario leading to a larger asymmetry up to an order of magnitude (see figure 7.3). The authors of Refs. [273, 315, 323] already pointed out that the contribution of tau leptons can be significant in the context of a two Higgs doublet model and the MSSM where the value of y_τ can be boosted by a large $\tan\beta$, but we stress that this Yukawa enhancement is not required for leptons to be very relevant. This relevance can be even enhanced in models with additional chiral-symmetry-breaking lepton-quark interactions, for instance via the exchange of new scalars. We discuss this in the next section.

7.2.6 Additional chiral-symmetry-breaking quark-lepton interactions

The importance of the leptons in the top-source case becomes even more pronounced in models with additional chiral-symmetry-breaking quark-lepton interactions. In our set-up we have added a dimension-six tau-top interaction to study this effect, but the qualitative results are insensitive to

the exact implementation. The dimension-six operator is given by

$$\mathcal{L}_{\mathrm{QL}} = \frac{1}{\Lambda_{\mathrm{QL}}^2}\bar{\tau}_L \tau_R \bar{t}_R t_L + \mathrm{h.c.}\,. \tag{7.13}$$

Using the methods of Ref. [325] we have calculated the rate associated to this interaction and obtain $\Gamma_{\mathrm{QL}} = \kappa_{\mathrm{QL}} T^5/\Lambda_{\mathrm{QL}}^4$ with κ_{QL} a factor of $\mathcal{O}(1)$. This interaction becomes important if it exceeds the SM tau Yukawa rate, which, for our benchmark point, is the case for $\Lambda_{\mathrm{QL}} \lesssim 3\,\mathrm{TeV}$.

For definiteness, we focus here on a new top-tau coupling but stress that a coupling to the muon or electron has a similar effect. If the CPV source is located in the quark sector, the baryon asymmetry can also be boosted by including a new coupling of the top to one of the lighter quarks (e.g. a top-charm coupling). In such a scenario the washout by strong sphalerons becomes less effective. Indeed, eq. (7.12) above was derived under the assumption that the light quarks are only produced via strong sphalerons and that their Yukawa interactions are negligible, such that eq. (5.31) holds. If, say, the new top-charm interaction is stronger than the strong sphaleron interactions, this is no longer the case, and the washout by strong sphalerons no longer implies a washout of the chiral asymmetry.

On the other hand, if the CPV source is located in the lepton sector, presence of the new top-tau interaction reduces the value of the baryon asymmetry. Part of the chiral asymmetry produced in the lepton sector now gets transported to the quark sector, where it gets washed out by strong sphalerons and top Yukawa interactions.

We describe the top-tau transfer here with an effective interaction, but larger interaction rates are possible if the coupling is via exchange of a light degree of freedom, for example the new scalar particle added to get a first-order phase transition [326, 327]. In such cases the scattering can be resonantly enhanced. To properly describe this requires the inclusion of the transport equation for the light particle with the corresponding interaction rates derived from renormalizable interactions. We expect that our effective interaction gives qualitatively similar results, even in the regime where Λ_{QL} is fairly small, and we therefore treat Λ_{QL} as a phenomenological parameter. We will show in section 7.5 that such interactions, even of modest strength, can drastically increase or reduce the baryon asymmetry depending on the nature of the CPV source.

7.3 Baryogenesis with a tau-lepton source

We start with a discussion of baryogenesis from a CPV tau source, and assume there is no new lepton-quark coupling (that is, we set $\Lambda_{\rm QL} \to \infty$). The value of the tau Yukawa coupling at the electroweak scale is small, $y_\tau \simeq 0.01$, with respect to the top Yukawa coupling, $y_t \simeq 1$. For reasons discussed in section 7.2.5, the tau could nevertheless be an interesting source of the baryon asymmetry.

In the present scenario, the lepton sector essentially decouples from the quark sector and the baryon asymmetry can be computed analytically to good accuracy. We start with discussing the analytical approximation and later compare it to the full numerical solution that *does* include effects of the quark sector. The analytical solution clarifies the dependence of the baryon asymmetry on parameters associated to the bubble wall and the leptonic Yukawa couplings. This relatively simple set-up provides insight into more complicated scenarios where analytical solutions are not possible.

7.3.1 Analytical approximation

The transport equations in eq. (5.32) contain separate equations for the third-generation left-handed doublet, l^μ, and the right-handed singlet, τ. Because the left- and right-handed tau leptons diffuse at different rates: $D_l = 100/T$ and $D_\tau = 380/T$ [273], in principle we have to treat these number densities separately. However, to a reasonable approximation we can ignore this difference and set $D_l = D_\tau = 100/T$, which implies $l = -\tau$. The lepton transport equation simply becomes

$$-D_l l'' + v_w l' + \bar{\Gamma} l - \Gamma_Y^{(l)} \frac{h}{k_h} = -S_\tau \,, \qquad \text{with} \qquad \bar{\Gamma} = \left(\Gamma_M^{(l)} + \Gamma_Y^{(l)}\right)\left(\frac{1}{k_\tau} + \frac{1}{k_l}\right). \tag{7.14}$$

CPV resides in the lepton sector and any non-zero density of Higgs particles can only be generated via interactions with leptons. Since the lepton Yukawa rate is relatively slow the Higgs density remains small and we can approximate $h \simeq 0$. In this limit, the leptons decouple completely and to find the chiral asymmetry we only have to solve eq. (7.14). This can be done using the semi-analytical solution that we used in chapter 6 (see section 6.5), which gives

$$l = -\frac{2\bar{S}}{(\sqrt{4D_l\bar{\Gamma}_B + v_w^2} + \sqrt{4D_l\bar{\Gamma}_S + v_w^2})} \mathrm{e}^{z/L_S} \,, \quad \text{for } \; z < 0 \,, \tag{7.15}$$

with $\bar{\Gamma}_{\{S,B\}}$ the rescaled interaction rates (7.14) in the symmetric and broken phase respectively, and

$$\begin{aligned} L_i &= \frac{2D_l}{\left(v_w + \sqrt{4D_l\bar{\Gamma}_i + v_w^2}\right)}\,, \\ \bar{S} &= \int_0^\infty \mathrm{e}^{-y/L_B} S_\tau(y)\mathrm{d}y = \frac{15 s_\tau}{128\pi^2}\frac{y_\tau^2}{\Lambda_\tau^2} v_w v_N^4 J_\tau(T)\left[1 - \frac{4(7+6\ln 2)}{45}\frac{L_w}{L_B} + \mathcal{O}\left(\frac{L_w^2}{L_B^2}\right)\right], \end{aligned} \tag{7.16}$$

and $i = \{S, B\}$. To get the second expression for $\bar{S}$, we used eqs. (5.15) and (7.4), and expanded in L_w/L_B. For a tau source, the leading order term dominates by far and we can set $L_w/L_B \simeq 0$.

Integrating the chiral asymmetry, $n_L = l$, as in eq. (5.38) gives the baryon asymmetry

$$Y_B = \frac{3\Gamma_{\rm ws}}{2v_w s}\frac{2\bar{S}}{(\sqrt{4D_l\bar{\Gamma}_B + v_w^2} + \sqrt{4D_l\bar{\Gamma}_S + v_w^2})}\frac{L_{\rm ws}L_S}{L_S + \frac{1}{2}L_{\rm ws}\left(1 + \sqrt{1 + \frac{4D_q}{L_{\rm ws}v_w}}\right)}\,, \tag{7.17}$$

with $L_{\rm ws} = v_w/(\mathcal{R}\Gamma_{\rm ws})$. Noting that $J_\tau < 0$, we have to pick $s_\tau = -1$ for the sign of the CPV coupling, to get the right sign for the baryon asymmetry. The last factor in eq. (7.17) arises from

$$I_Y \equiv \int \mathrm{d}z\, \mathrm{e}^{z\left(L_S^{-1} - \alpha_-\right)} = \frac{L_{\rm ws}L_S}{L_S + \frac{1}{2}L_{\rm ws}\left(1 + \sqrt{1 + \frac{4D_q}{L_{\rm ws}v_w}}\right)}\,, \tag{7.18}$$

with α_- as defined in eq. (5.38).

7.3.2 Comparison of approximations

We have calculated the total baryon asymmetry using different approximations:

1. The analytical solution in eq. (7.17) of the purely leptonic transport equation, eq. (7.14), where the Higgs and quark sectors are neglected. We call this solution $A(l)$.
2. A numerical solution of eq. (7.14) called $N(l)$.
3. A numerical solution that includes the Higgs and third-generation quarks called $N(l, h, q, t)$.
4. Finally, we investigate the different diffusion constants of left- and right-handed leptons. That is, we allow $D_l \neq D_\tau$ in $N(l, \tau)$. For numerical reasons we study this effect in the limit of a decoupled quark sector.

The entries in brackets in $A(...)$ and $N(...)$ denote the number densities for which we solve the transport equation explicitly in the respective approximation. In scenarios where the quark sector is

Approximation	A(l)	N(l)	N(l, h, q, t)	N(l, τ)
Y_B	6.8×10^{-11}	7.3×10^{-11}	7.3×10^{-11}	8.2×10^{-11}

TABLE 7.1: Baryon asymmetry Y_B for a tau CPV source obtained using various approximations as detailed in the main text. We used the benchmark values for the bubble-wall profile given in section 7.2.1 and $\Lambda_\tau = 1$ TeV.

considered, we apply local baryon conservation, eq. (5.37), and the relation in eq. (5.31) to account for the number densities of the bottom and lighter quarks.

The resulting baryon asymmetries in the various approximations for our benchmark point with $\Lambda_\tau = 1\,\text{TeV}$ and bubble-wall velocity $v_w = 0.05$ are given in table 7.1. Comparing N(l, τ) to N(l) shows that local lepton conservation is a reasonable approximation. More importantly, the analytical solution differs only $\sim 10\%$ from the numerical solutions with and without inclusion of the Higgs and quark sectors, that is from N(l, h, q, t) and N(l) respectively. The tau Yukawa coupling is sufficiently small that decoupling the Higgs and quark sectors is an excellent approximation.

In the left panel of figure 7.1 the various approximations are compared while varying the value of the tau Yukawa coupling. The decoupling approximation works well up to $y_\tau \lesssim 0.2$ while for larger values significant Higgs and quark densities are generated. The right panel of figure 7.1 shows that the analytical approximation holds over a large range of bubble-wall velocities, such that the conclusions are not restricted to just our benchmark values.

7.3.3 Parameter dependence

Having found that the analytical solution provides an excellent approximation, we can use it to understand how the baryon asymmetry depends on various parameters, such as the Yukawa coupling and the parameters associated to the bubble wall. It is useful to rewrite the solution for Y_B in eq. (7.17) in terms of various length scales

$$Y_B = \frac{3}{s\mathcal{R}} \frac{\bar{S}}{v_w L_{\text{ws}}} \frac{1}{\sqrt{1 + 4\frac{L_{\text{diff}}}{L_{\text{int}}^S}} + \sqrt{1 + 4\frac{L_{\text{diff}}}{L_{\text{int}}^B}}} \frac{L_{\text{ws}} L_S}{L_S + \frac{1}{2} L_{\text{ws}} \left(1 + \sqrt{1 + 4\frac{L_{\text{diff}}^q}{L_{\text{ws}}}}\right)}, \tag{7.19}$$

which are defined in table 7.2. L_S and L_B determine how far the asymmetry migrates into, respectively, the symmetric and broken phase. On larger length scales the asymmetry is exponentially suppressed by the $e^{-|z|/L_i}$-factor in eqs. (7.15) and (7.16). $L_{\text{diff}} = D_l/v_w$ is the diffusion length, which determines how far the asymmetry can diffuse into the symmetric phase before it is overtaken by the expanding bubble.

Length scale	Description	Benchmark value
$L_S = \frac{2L_{\rm diff}}{1+\sqrt{1+4L_{\rm diff}/L_{\rm int}^S}}$	migration length in symmetric phase	21.3
$L_B = \frac{2L_{\rm diff}}{1+\sqrt{1+4L_{\rm diff}/L_{\rm int}^B}}$	migration length in broken phase	9.8
$L_{\rm int}^S = v_w/\bar{\Gamma}_S$	interaction length in symmetric phase	313.3
$L_{\rm int}^B = v_w/\bar{\Gamma}_B$	interaction length in broken phase	7.0
$L_{\rm diff} = D_l/v_w$	lepton diffusion length	22.7
$L_{\rm diff}^q = D_q/v_w$	quark diffusion length	1.4
$L_{\rm ws} = v_w/(\mathcal{R}\Gamma_{\rm ws})$	weak sphaleron length	28.5
L_w	bubble-wall width	0.1

TABLE 7.2: Length scales (in units of GeV^{-1}) for a tau CPV source and their values for the benchmark values for the bubble-wall profile given in section 7.2.1 and $\Lambda_\tau = 1$ TeV.

The interaction lengths in the symmetric and broken phase are denoted by $L_{\rm int}^i = v_w/\bar{\Gamma}_i$ with $i = S, B$, respectively. If interactions are slow, $L_{\rm diff} \ll L_{\rm int}^i$, they can be neglected, and the migration scale is determined by diffusion $L_i \simeq L_{\rm diff}$. In the opposite limit of fast interactions, the symmetry is washed out over scales larger than $L_i \simeq \sqrt{L_{\rm diff} L_{\rm int}^i} = \sqrt{D_l/\bar{\Gamma}_i}$. In the broken phase, L_B has to be compared with the spatial extend of the source, which is set by the bubble-wall width L_w. For $L_w \ll L_B$ the source is not diluted by diffusion nor interactions and we can approximate $\bar{S}$ by the first term in eq. (7.16).

The conversion of the chiral number into a net baryon number through eq. (5.38) introduces additional length scales: the baryon/quark diffusion length scale $L_{\rm diff}^q = D_q/v_w$, and the scale on which the weak sphalerons act $L_{\rm ws} = v_w/(\mathcal{R}\Gamma_{\rm ws})$. In the limit $L_S \ll L_{\rm ws}$ the migration length, i.e., how far the chiral asymmetry migrates into the symmetric phase, determines the extend of the region in front of the bubble wall that contributes to the baryon asymmetry and the integral (7.18) becomes $I_Y \simeq L_S$. In the opposite limit, $L_{\rm ws} \ll L_S$, it seems necessary to include the weak sphaleron interactions directly in the transport equations, as there is no hierarchy between the sphaleron and Yukawa interactions, invalidating the two step procedure. However, although both processes may be important for the final asymmetry (depending on the bubble-wall velocity) they are still very far from equilibrium, and backreaction effects are small. It was checked numerically that the two-step procedure used to derive eq. (7.17) is a good approximation to the full coupled set of equations, see Appendix B of Ref. [4] for more details. We then find that in this regime the integral is cut off by $L_{\rm ws}$, the scale on which the weak sphalerons act, and $I_Y \simeq L_{\rm ws}(1+\sqrt{r})^{-1}$ in the parameter regime of interest, with

$$r = \frac{L_{\rm ws} L_{\rm diff}^q}{L_S^2} \overset{v_w \to 0}{=} \frac{D_q}{D_l} \frac{\bar{\Gamma}_S}{\mathcal{R}\Gamma_{\rm ws}}\,, \tag{7.20}$$

where the right-hand expression is valid in the small-velocity limit where r is maximal. For the tau Yukawa interactions $r \ll 1$ and we can neglect the baryon diffusion effects, and the approximation made in eq. (5.39) holds. This is no longer the case for the top- and bottom-source scenarios discussed in section 7.4, as can be anticipated from the above estimate. Replacing the tau Yukawa interaction with the top Yukawa or strong sphaleron interaction, and setting $D_l \to D_q$ gives $r \gg 1$.

The various length scales are listed in table 7.2, along with their value for the benchmark point. The length scales depend on bubble-wall parameters such as v_N and v_w that we can vary depending on the electroweak phase transition, and on SM parameters such as the tau Yukawa coupling, y_τ. We also consider variations in y_τ to see what would happen for source terms involving lighter SM fermions and to get some (limited) insight about what happens for heavier quarks, as further discussed in the next section. For all parameter choices, we have $L^B_{\rm int} \ll L^S_{\rm int}$ as $\Gamma^{(l)}_M$ greatly exceeds the Yukawa interaction rate in both the symmetric and broken phase. The solution for the baryon asymmetry can then be divided into three[1] different regions, depending on the chosen parameters and the resulting sizes of the relevant length scales:

a $L_{\rm diff} < L^B_{\rm int}, L^S_{\rm int}, L_{\rm ws}$ which corresponds to small Yukawa couplings and a large bubble-wall velocity. Interactions are slow and can be neglected, and the chiral asymmetry diffuses without washout $L_i \simeq L_{\rm diff}$. Since the diffusion length is much larger than the source width $L_{\rm diff} \gg L_w$ there is no dilution of the source and the expansion in eq. (7.16) is valid. In this regime, the baryon asymmetry becomes

$$Y_B \simeq \frac{3}{2s\mathcal{R}} \frac{\bar{S}}{v_w} \frac{L_{\rm diff}}{L_{\rm ws}} \propto \frac{y_\tau^2}{v_w^2} \frac{1}{\Lambda_\tau^2} \,. \tag{7.21}$$

The asymmetry decreases for large bubble-wall velocity, which can be understood as the faster the bubble moves, the less time there is for the chiral asymmetry to diffuse into the symmetric phase and to be converted into a baryon asymmetry. The asymmetry decreases quadratically with a smaller Yukawa coupling, which originates from the scaling of the source. In practice, the tau Yukawa coupling is slightly too large for the above scaling to hold for the benchmark velocity $v_w \simeq 0.05$.

b $L^B_{\rm int} < L_{\rm diff} < L^S_{\rm int}, L_{\rm ws}$. Interactions are now important in the broken phase and $L_B \simeq \sqrt{L^B_{\rm int} L_{\rm diff}}$. The dilution of the source in $\bar{S}$ is still a negligible effect, as $L_B \simeq L_w$ only holds for $\mathcal{O}(1)$ Yukawa couplings. The interactions in the broken phase, however, change the baryon

[1] In principle there exists a fourth region $L^S_{\rm int} \ll L_{\rm diff}$ and $L_S = \sqrt{L^S_{\rm int} L_{\rm diff}} \ll L_{\rm ws}$. This requires $\mathcal{O}(1)$ Yukawa couplings, for which our analytical approximation eq. (7.15) breaks down. As this is not the physical region of interest, we do not discuss this possibility further.

asymmetry into

$$Y_B \simeq \frac{3}{2s\mathcal{R}}\frac{\bar{S}}{v_w}\frac{\sqrt{L_{\rm diff}L^B_{\rm int}}}{L_{\rm ws}} \propto \frac{y_\tau}{v_w}\frac{1}{\Lambda^2_\tau}\,. \tag{7.22}$$

Y_B thus scales linearly with the Yukawa coupling and inversely with the bubble velocity. Here we see for the first time a violation of the naive y_f^2 scaling of the asymmetry.

c $L^B_{\rm int} < L_{\rm ws} < L_{\rm diff}, L^S_{\rm int}$ which corresponds to small velocities (and $y_\tau \lesssim 0.2$ such that the analytical approximation is valid). The baryon asymmetry

$$Y_B \simeq \frac{3}{2s\mathcal{R}}\frac{\bar{S}}{v_w}\sqrt{\frac{L^B_{\rm int}}{L_{\rm diff}}} \propto \frac{y_\tau v_w}{\Lambda^2_\tau}\,, \tag{7.23}$$

now scales linearly with both y_τ and v_w. The asymmetry decreases for small velocity, as in this limit the evolution approaches thermal equilibrium. We neglect the $L^S_{\rm int}$ dependence in the denominator in eq. (7.17) as it is subdominant to the $L^B_{\rm int}$ term.

Comparing eqs. (7.22) and (7.23) it follows that the asymmetry is maximized as a function of the velocity at the boundary of the two regimes, that is, for $L_{\rm ws} \sim L_{\rm diff}$. For the SM tau Yukawa coupling, region **a** corresponds to $v_w \gtrsim 0.1$, region **b** to $0.04 \lesssim v_w \lesssim 0.1$, and region **c** to $v_w \lesssim 0.04$.

The scaling of the asymmetry with bubble-wall velocity and Yukawa coupling are illustrated in figure 7.1. The left panel shows Y_B as a function of the Yukawa coupling y_τ. The vertical thick line gives the boundary between region **a** and **b**; region **c** does not occur for our benchmark velocity. In region **a**, on the left of the vertical thick line, the baryon asymmetry scales quadratically with the small Yukawa coupling, while in region **b**, on the right, the scaling is linear. The SM Yukawa value $y_\tau = 0.01$ falls in region **b**, and the baryon asymmetry for this value is indicated by a star (and corresponds to our benchmark number in table 7.1). The most relevant observation is that for $y_\tau \geq 0.005$, Y_B only grows linear with y_τ instead of the naively expected quadratic scaling. This confirms that CPV sources for fermions lighter than top quarks are less disadvantageous than might be expected.

The right panel shows Y_B as a function of the bubble-wall velocity v_w. Now the black lines divide, from right to left, regions **a**, **b**, and **c** that scale respectively as v_w^{-2}, v_w^{-1} and v_w. The boundary between **b** an **c** corresponds to the velocities for which $L_{\rm ws} \sim L_{\rm diff}$, approximately where the baryon asymmetry is maximized. Our benchmark point lies in scenario **b**, very close to the optimum value.

We end this section with a short discussion of how the baryon asymmetry depends on the dynamics of the first-order phase transition that we have parameterized by the bubble-wall profile eq. (5.15).

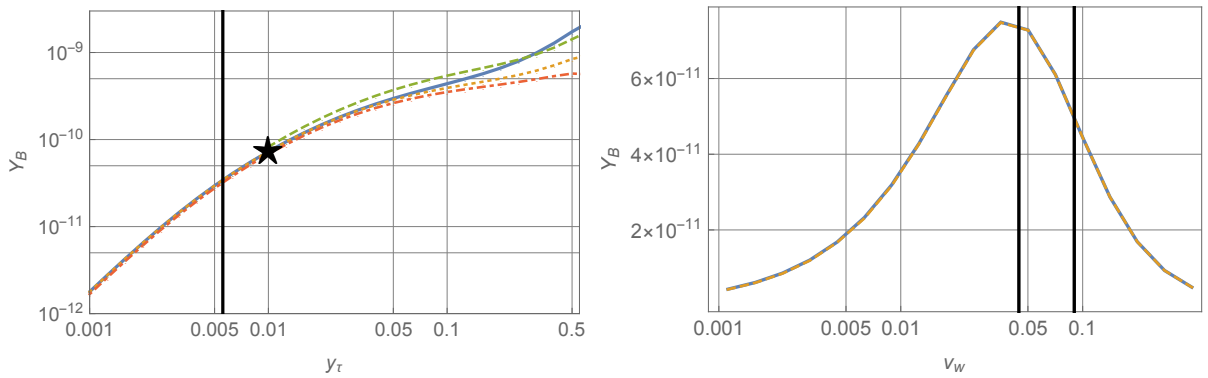

FIGURE 7.1: Left: Y_B as a function of the Yukawa coupling y_τ for the same four approximations as in Table 7.1 (solid blue: N(l,h,q,t), dotted orange: N(l), dashed green N(l,τ), dotdashed red: A(l)). The region left (right) of the vertical black line corresponds to region **a** (**b**). The star denotes the SM value of y_τ.
Right: Y_B as a function of the bubble-wall velocity v_w (solid blue: $N(l,h,q,t)$, dashed orange: N(l)). The left, middle and right regions corresponds to regions **c**, **b**, and **a**, respectively.

The bubble-wall width only enters the equations via the source. In the limit that $L_w/L_B \ll 1$, as appropriate for a tau source, the dependence on this parameter cancels. A larger bubble wall width gives a wider source but with a smaller amplitude, such that the total integrated source $\bar{S}$ remains the same.

The source scales as $\bar{S} \propto v_N^4$ with v_N the Higgs vev during nucleation; this power comes about because of the structure of our dimension-six CPV operator which involves three Higgs fields[2]. The relaxation rate $\Gamma_M^{(f)} \propto v_N^2$ depends on the vev as well. It thus follows that in region **a**, the baryon asymmetry scales as $Y_B \propto v_N^4$ and in region **b** as $Y_B \propto v_N^3$. For the SM tau Yukawa coupling we are in region **b**, but the velocity dependence of L_B cannot be fully neglected and numerically we find a scaling $Y_B \propto v_N^{3.2}$. Although the dependence on the vev is strong, we do not expect v_N to vary too much between different BSM models.

The dependence on the nucleation temperature T_N is harder to estimate, as many parameters, such as the thermal masses and thermal width, depend on the temperature. All interaction rates scale as $\Gamma_i \propto T$, except for $\Gamma_M \propto 1/T$; further $D_i \propto 1/T$ and $S \propto T$. With this scaling we find that $Y_B \propto 1/T_N^2$ in regime **a** and $Y_B \propto 1/T_N$ in regime **b**. We note that as T_N increases the relative importance of $L_{\rm int}^B$ decreases, and we move from regime **b** to **a**.

[2]In two-Higgs doublet models CPV can originate from dim-4 operators, in which case the corresponding source would only scale quadratically with the vev.

7.3.4 Producing the universal baryon asymmetry with a tau source

Can CP violation in the lepton sector produce the observed baryon asymmetry? The asymmetry for the benchmark point in table 7.1 is fairly close to the observed value in eq. (5.1). The scale $\Lambda_\tau \sim 1\,\text{TeV}$ is fairly low, but not inconsistent with EDM and collider experiments. It could be even lowered somewhat to further increase Y_B but the EFT description becomes problematic for such low scales. As shown in the right panel of figure 7.1 the benchmark $v_w = 0.05$ is already close to optimal, and there is little room for improvement. Definite statements about the viability of the scenario are not easy to make, as the performed calculations still suffer from uncertainties, such as those related to the description of the phase transition, that are hard to quantify. We refer to e.g. Ref. [226] for a more general discussion of outstanding problems in calculations of EWBG. Nevertheless, our analysis indicates that CPV sources in the tau sector are viable despite the small Yukawa coupling and not yet significantly constrained by EDM experiments.

Our study of the dependence of Y_B on the value of y_τ can be directly used to study the cases of CP-violating electron and muon source terms. In such cases, the transport equations are identical after replacing the third-generation lepton number densities with the first- or second-generation densities and rescaling the $y_\tau \to y_{\mu,e}$. The left panel of figure 7.1 shows that for Yukawa couplings y_l larger than y_τ we are in regime **b** where Y_B grows linearly with y_l. For smaller Yukawa couplings however, we are in regime **a**, where Y_B decreases as y_l^2. For equal values of the scale of new physics $\Lambda_e = \Lambda_\mu = \Lambda_\tau$ the values of Y_B in the electron and muon scenarios are then suppressed by a factor $(y_e/y_\tau)^2 \simeq 8 \cdot 10^{-8}$ and $(y_\mu/y_\tau)^2 \simeq 4 \cdot 10^{-3}$, respectively. For the electron, EDM constraints require $\Lambda_e > 5.7$ TeV, which suppresses the baryon asymmetry even more. The resulting values of Y_B are far below the observed asymmetries and we conclude that electron and muon CPV sources do not lead to successful baryogenesis.

7.4 Baryogenesis with a quark source

In this section we discuss baryogenesis with a quark CPV source and at first neglect the additional lepton-quark interaction introduced in section 7.2.6. We start the discussion with a CPV source in the top-quark sector. This scenario has been discussed extensively in the literature, see for example Refs. [282, 306, 340] where the same dimension-six CPV operator has been considered. Since the source is proportional to the value of the Yukawa coupling squared $S_f \propto y_f^2$, the baryon asymmetry generated by a top source can be expected to be larger than for the corresponding source terms

Approximation	FR(q)	N(q,t,h)	N(q,t,h,u)	N(q,t,h,u,l)	A(q,t,h,u,l)
Y_B	1.6×10^{-12}	3.5×10^{-13}	3.4×10^{-13}	1.5×10^{-12}	1.1×10^{-12}

TABLE 7.3: Baryon asymmetry Y_B for a top source using different approximations discussed in the main text. We used the benchmark values for the bubble-wall profile given in section 7.2.1 and $\Lambda_t = 7.1$ TeV consistent with EDM experiments.

involving lighter fermions. But several factors that were identified in section 7.2.5 suppress the corresponding BAU. We therefore study how effective a top source actually is. In the process we investigate the role of SM bottom and tau Yukawa interactions that are typically neglected.

A CPV bottom source is suppressed by $(y_b/y_t)^2 \simeq 4 \times 10^{-4}$ with respect to a top source. Part of this suppression can be compensated as EDM experiments do not set as stringent constraints on the CPV bottom source. In addition, a smaller Yukawa coupling also implies less washout because $\Gamma_M^{(b)}$ is smaller and, as demonstrated for a tau source, it is not immediately clear how Y_B varies with the size of the Yukawa coupling, and thus how the top and bottom scenarios compare. While the bottom Yukawa coupling is still roughly a factor two larger than the tau Yukawa coupling, we nevertheless expect the asymmetry to be suppressed with respect to the tau source, because the bottom has strong sphaleron interactions and a smaller diffusion constant leading to less efficient generation of Y_B.

7.4.1 Top source

We calculate the baryon asymmetry arising from a top CPV source using various approximations:

1. The simplest approximation is to first neglect the small bottom and tau Yukawa couplings. Using eqs. (5.31) and (5.37) leaves us with three transport equations for the number densities q, t, and h. Finally, we apply the often-used fast-rate approximation which assumes that the top Yukawa and strong sphaleron transitions are fast and (nearly) in equilibrium [252, 311]. This leaves us with a single equation for q that can be solved analytically. We denote the solution by FR(q).

2. We neglect bottom and tau Yukawa couplings, but do not use the fast-rate approximation. Instead we numerically solve the set of three transport equations for q, t, and h and call the solution N(q,t,h).

3. Next we include the effects of the bottom Yukawa. We can no longer connect the b density to those of light quarks and the transport equation for u has to be included. The numerical solution of the four transport equations is called $\mathrm{N}(q, t, h, u)$.

4. We also include the tau Yukawa coupling and add the l transport equation. In principle, we should keep the right-handed lepton fields too, but, as discussed in the tau scenario, the approximation of local lepton number conservation, $D_l = D_\tau$, is reasonable and we can eliminate the right-handed leptons. The solution is called $\mathrm{N}(q, t, h, u, l)$.

5. We solve the same set of equations using the semi-analytical method [312], which neglects the variation of the rates over the bubble wall, and write this solution as $\mathrm{A}(q, t, h, u, l)$.

As before between brackets in $A(...)$ and $N(...)$ we list the transport equations that we solve explicitly. The obtained values for Y_B for our benchmark point with $\Lambda_t = 7.1$ TeV and bubble-wall velocity $v_w = 0.05$ in the various approximations are listed in table 7.3. To get the right sign for Y_B, the sign of the CPV operator in eq. (7.1) is set to $s_t = 1$.

The fast-rate approximation assumes thermal equilibrium for the strong sphaleron and top Yukawa rates, but this approximation is invalid close to the bubble wall in the symmetric phase and invalid everywhere in the broken phase where $\Gamma_M^{(t)}$ is instead the fastest rate. By comparing the solutions $\mathrm{FR}(q)$ and $\mathrm{N}(q, t, h)$ we see that the fast-rate approximation overestimates Y_B by roughly a factor five and is thus a poor approximation, in agreement with the findings of Ref. [312]. The fast-rate approximation should be avoided to calculate Y_B, especially since it does not represent a systematic expansion and as such the associated error cannot be systematically estimated.

By comparing $\mathrm{N}(q, t, h)$ and $\mathrm{N}(q, t, h, u)$ we see that including bottom Yukawa interactions only provides a few-percent correction. Considering the significant intrinsic uncertainties associated to EWBG calculations, neglecting the bottom Yukawa seems a good approximation. It might come as a surprise then that including the even smaller tau Yukawa interaction has a much greater impact. The baryon asymmetry associated to $\mathrm{N}(q, t, h, u, l)$ is roughly five times that of $\mathrm{N}(q, t, h, u)$. Where does this lepton-induced enhancement stem from?

As discussed in section 7.2.5, when the strong sphaleron interactions are (approximately) in thermal equilibrium, $\mu_{\mathrm{ss}} \simeq 0$, the total chiral asymmetry in quarks is highly suppressed. This is illustrated in the left panel of figure 7.2. The red line depicts the chiral asymmetry in just top quarks, $q(z)$, as a function of the distance to the bubble wall in the symmetric phase. This individual asymmetry is everywhere much larger than the total chiral asymmetry in the quark sector, $n_L^{(q)}(z) \equiv \sum_i q_i$, where

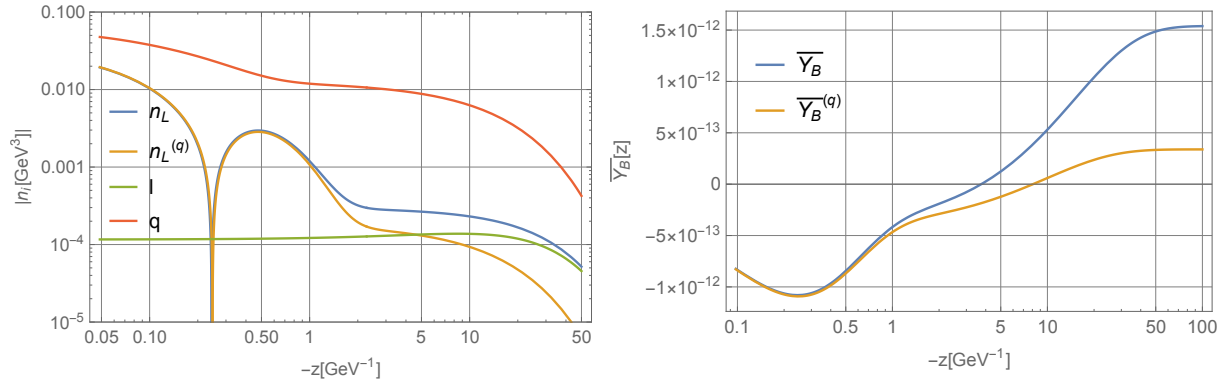

FIGURE 7.2: Left plot: absolute value of the number densities n_L, $n_L^{(q)}$, l, and q in the symmetric phase for a top source. The computation includes top, bottom and tau Yukawa interactions. Right plot: baryon asymmetry $\bar{Y}_B(z)$ and $\bar{Y}_B^{(q)}(z)$ as a function of the integration cut-off.

the sum runs over the three generations. $n_L^{(q)}(z)$ is plotted in orange and is itself larger than the chiral asymmetry in tau leptons, $l(z)$, depicted in green, up to $|z| \simeq 5\,\mathrm{GeV}^{-1}$. For larger distance $l(z)$ becomes larger and consequently dominates the total chiral asymmetry, $n_L(z) = n_L^{(q)}(z) + l(z)$, depicted in blue.

The distance from the bubble in the symmetric phase at which point the various densities start to drop can be understood qualitatively from the analytical solution for the lepton source discussed in the previous section. In analogy with the leptonic case there are three important length scales: the diffusion length $L^i_{\mathrm{diff}} \sim D_i/v_w$, the migration length set by strong sphaleron interactions $L_S^{(\mathrm{SS})} \sim \sqrt{k_q D_q/\Gamma_{\mathrm{ss}}} = \mathcal{O}(1)\,\mathrm{GeV}^{-1}$, and the migration length set by the top Yukawa interactions $L_S^{(y_t)} \sim \sqrt{k_q D_q/\Gamma_y^{(t)}} = \mathcal{O}(0.1)\,\mathrm{GeV}^{-1}$. The Yukawa interactions are strongest and provide the dominant source of washout near the bubble wall. This washout leads to the decrease of n_L for small values of z and the associated zero-crossing around $|z| = 0.2\,\mathrm{GeV}^{-1}$. At distances around $|z| \sim L_S^{(y_t)}$, the top Yukawa interactions are in equilibrium and the n_L would plateau to a constant value. However, this is not clear in figure 7.2 where n_L keeps decreasing because of washout from strong sphalerons which is active up to the larger distance $L_S^{(\mathrm{SS})}$. This washout, and the related decrease of n_L, ends for $|z| > L_S^{(\mathrm{SS})}$.

The individual particle densities migrate much further in the symmetric phase than the total quark chiral asymmetry, as their spread is only limited by diffusion. Indeed with both the top Yukawa and strong sphaleron interactions in equilibrium, the number densities of the left- and right-handed quarks and the Higgs are related (by the condition that the chemical potential vanishes). Physically what happens is that on the relevant time scales, quarks and Higgses are converted into each other

instantly, and they behave as a single degree of freedom that diffuses into the symmetric phase. Their diffusion length, which determines how far the densities extend, is dominated by the Higgs diffusion length which is large as the Higgs does not feel strong interactions. As such $L_{\rm diff} \sim D_h/v_w \simeq 20\,{\rm GeV}^{-1}$. A more precise estimate is obtained from the transport equation for the single degree of freedom, which gives (see eq. (77a) in Ref. [252]) $L_{\rm diff} \simeq 16\,{\rm GeV}^{-1}$.

Finally, the tau Yukawa interactions are out of equilibrium throughout. The lepton number density slightly increases away from the bubble wall as there is more time to convert Higgs quanta into leptons. The lepton asymmetry migrates over distances set by the lepton diffusion length $L_{\rm diff} \sim D_l/v_w \simeq 20\,{\rm GeV}^{-1}$. Because of the small tau Yukawa coupling the lepton density is always much smaller than the left-handed top density q. However, it is the chiral density that matters, and given the very efficient suppression of the chiral asymmetry in quarks, leptons actually start to dominate n_L for $|z| \gtrsim L_S^{(\rm SS)}$. This explains why the inclusion of leptons can give a sizeable correction to the final baryon asymmetry.

What is maybe surprising is that the leptons actually give the dominant contribution for our benchmark point. The reason for this is that $n_L^{(q)}$ crosses zero close to the bubble wall around $|z| = 0.25\,{\rm GeV}^{-1}$. In the right panel of figure 7.2 we show the contribution to the asymmetry from the wall up to a distance z. That is, we plot the function

$$\bar{Y}_B(z) = -\frac{3\Gamma_{\rm ws}}{2sD_q\alpha_+}\int_z^0 {\rm d}z'\, n_L(z'){\rm e}^{-\alpha_- z'}\,, \tag{7.24}$$

with $\alpha_\pm$ given in eq. (5.38). For our benchmark parameters, the chiral asymmetry close to the bubble wall $n_L \simeq n_L^{(q)}$ gives a negative contribution to the integral in eq. (5.38). However, past the zero-crossing the contribution becomes positive. Due to the sign change, the total asymmetry generated up to $z = 10\,{\rm GeV}^{-1}$ from just $n_L^{(q)}$ vanishes. Around this point, the chiral asymmetry in quarks is small and leptons dominate the chiral asymmetry. Integrating over larger distances, leptons then give the dominant contribution to Y_B. This sensitivity of Y_B to the tau Yukawa interactions is thus twofold: 1) even though small, they are the only mechanism via which the chiral asymmetry is transferred from the quark sector, where the CPV source is located, to the lepton sector, where they escape the efficient washout by strong sphalerons. 2) There is a cancellation of the contribution of $n_L^{(q)}$ to the baryon asymmetry.

We can now also understand why including bottom Yukawa interactions has less impact. These will transfer some of the top chiral asymmetry into a bottom chiral asymmetry, but the total is still

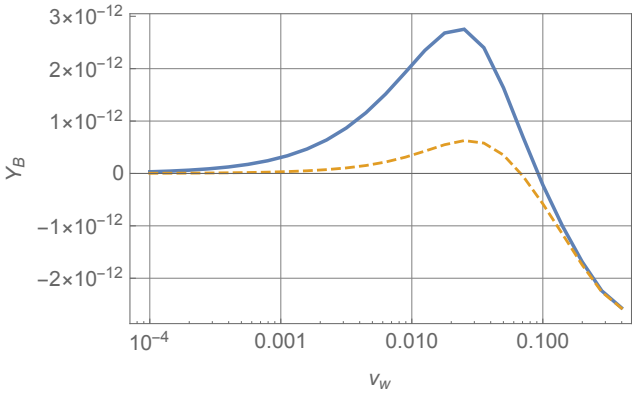

FIGURE 7.3: Y_B as a function of velocity v_w with (solid blue) and without (dashed orange) lepton interaction included.

washed out by strong sphaleron interactions. This transfer therefore does not lead to a significant change in Y_B.

An interesting question is now whether including tau leptons is generally important or whether it is a special feature of our benchmark parameters. To study this, we calculate Y_B associated to the $\mathrm{N}(q,t,h,u)$ and $\mathrm{N}(q,t,h,u,l)$ solutions for a wide range of bubble-wall velocities. The values of Y_B are plotted in figure 7.3. We conclude that the lepton contribution is important for a large range of velocities $v_w \sim 10^{-4} - 10^{-1}$, but becomes less relevant for larger velocities. For such large velocities the baryon asymmetry is dominated by the chiral asymmetry close to the bubble wall, where the leptons contribute little. In this case, the integral is cut off by the diffusion length $L_{\mathrm{diff}} \propto 1/v_w$, which becomes small.

7.4.2 Producing the universal baryon asymmetry with a top source

Let us finally answer whether a top source can produce the observed baryon asymmetry in eq. (5.1). For equal Wilson coefficients of the dimension-six CPV operators, $\Lambda_t = \Lambda_\tau$, the asymmetry induced by the top source is of the same order as for the tau source. However, for taus we can choose a fairly low scale $\Lambda_\tau \sim 1\,\mathrm{TeV}$, while EDM experiments constrain $\Lambda_t \geq 7.1$ TeV. As such, the asymmetry in our benchmark scenario is almost two orders of magnitude too small. As the asymmetry is rather sensitive to the Higgs vev at nucleation, this might be the easiest parameter to adjust to boost the asymmetry, but how much this is allowed depends on the details of the scalar sector that we have not specified. Our chosen bubble-wall velocity is already close to the optimal value as shown in figure 7.3. All things considered it seems unlikely that the dimension-six top Yukawa interaction can still lead to sufficient asymmetry.

Approximation	N(q,t,h,b)	N(q,t,h,b,l)	A(q,t,h,b)
Y_B	8.3×10^{-13}	8.4×10^{-13}	7.3×10^{-13}

TABLE 7.4: Baryon asymmetry Y_B for a bottom source with $\Lambda_b = 1\,\text{TeV}$ and $v_w = 0.05$ using different approximations discussed in the text.

It must be said, that the uncertainties in the calculation for a top CPV source are large. The vev-insertion approximation is dubious as the top Yukawa coupling is not small. We saw in section 5.3 that computing the top source in the semi-classical method of [266–268] leads to a source term that is about a factor 5 smaller. Another potentially large effect can be the inclusion of collective plasma effects, the so-called hole modes, in the calculation of the source term and interaction rates, see the discussion in Ref. [226]. Despite these caveats, it is fair to say that the observed baryon asymmetry is obtained more easily using a tau source, mainly due to the significant EDM constraints on the CPV top source. In section 7.5 we discuss ways of boosting the baryon asymmetry for top-source scenarios by adding additional BSM lepton-quark interactions. Other ways out could be by considering CP-violating interactions between top quarks and new scalar fields as such interactions are not directly constrained by EDMs if the new scalar field does not couple to electrons. Such a setup can appear in, for example, two-Higgs doublet models although several couplings have to be set to very small values by hand.

7.4.3 Bottom source

We now turn to the bottom source and investigate whether such a source can be as efficient as a tau source. To calculate the chiral asymmetry generated by a bottom source, one can use the same set of transport equations as for the top source. We calculate the asymmetry first by neglecting leptons and write this solution as $N(q,t,h,u)$. We then include tau Yukawa interactions and add the l-equation to the set of transport equations and obtain the solution $N(q,t,h,u,l)$. The corresponding semi-analytical solution is called A(q,t,h,u,l). The baryon asymmetry for our benchmark point with $\Lambda_b = 1\,\text{TeV}$ and bubble-wall velocity $v_w = 0.05$ is listed in table 7.4 (with $s_b = -1$ the sign of the dimension-six operator).

From the table it is clear that the asymmetry from a bottom source is almost two orders of magnitude smaller than the baryon asymmetry from a tau source for the same scale $\Lambda_b = \Lambda_\tau$. Just as for the top source, the chiral asymmetry in bottom quarks is effectively erased by the strong sphaleron interactions, which become important at $|z| \sim L_S^{(\text{SS})}$. Beyond this scale the leptons again give the dominant contribution to the chiral asymmetry, as can be seen in the left panel in figure 7.4.

However, unlike the top-source case, there is no zero-crossing, and thus no cancellation in Y_B. Now, the total baryon asymmetry is dominated by the contribution close to the bubble wall, where leptons are negligible, see the right panel in figure 7.4.

We conclude that the bottom source produces a value of Y_B that is about two orders of magnitude too small. What about sources involving even lighter quarks? In figure 7.5, the solid blue line depicts the value of Y_B as a function of the bottom Yukawa coupling y_b at the electroweak scale. The orange dashed line is a fit to a quadratic function of y_b. Effectively, for the SM value of y_b and smaller values we are in regime **a** discussed in section 7.3.3 where $Y_B \sim y_b^2$. Since the system of transport equations for an up, down, strange, or charm source is very similar to that of a bottom source, we expect that sources involving light quarks will be suppressed by $(y_q/y_b)^2$ compared to the numbers in table 7.4. Such sources will thus provide negligible contributions to Y_B. For $y_b \geq 0.04$ the asymmetry starts to scale linearly $Y_B \sim y_b$ (the system enters regime **b** discussed in section 7.3.3). The linear instead of quadratic scaling partially explains why a top source is not as effective compared to a bottom source as might be expected from just looking at the CPV source term.

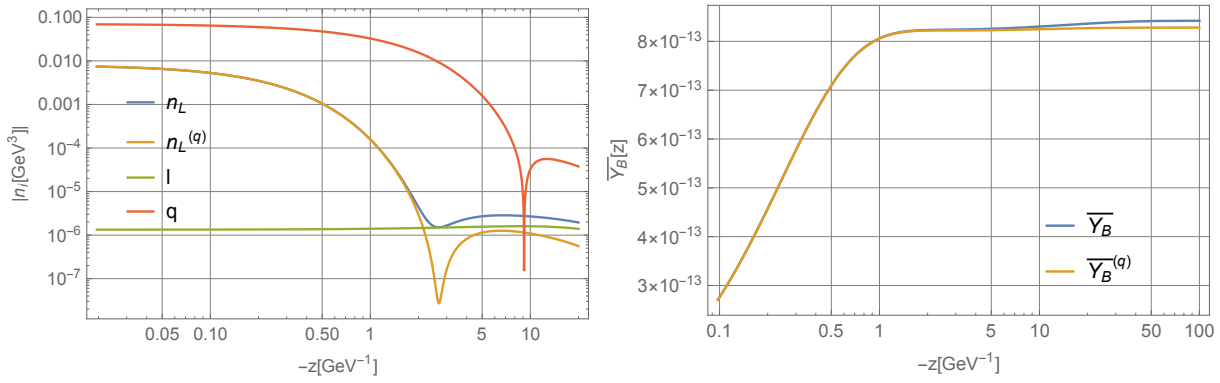

FIGURE 7.4: Left plot: absolute value of the number densities n_L, $n_L^{(q)}$, l and q in the symmetric phase for a bottom source. The computation includes top, bottom and tau Yukawa interactions. Right plot: baryon asymmetry $\bar{Y}_B(z)$ and $\bar{Y}_B^{(q)}$ as a function of the integration cut-off.

7.5 Consequences of additional quark-lepton interactions

In the previous sections we have argued that CP-violating leptonic sources are more effective than quark sources in generating a net baryon asymmetry. In this section, we analyze how we can modify the asymmetry by considering BSM interactions that transfer the chiral asymmetry from quarks into leptons (and vice versa). Such interactions can be induced in BSM models by the exchange of new particles such as additional scalar bosons or leptoquarks. In particular, we consider the

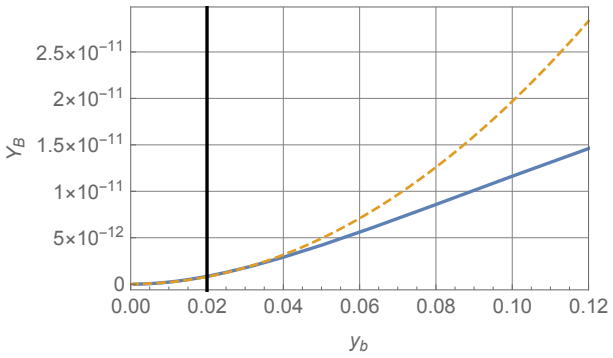

FIGURE 7.5: Baryon asymmetry for a bottom source as a function of the bottom Yukawa coupling y_b (solid blue line). The orange dashed line shows a quadratic fit and the black vertical line indicates the SM value of y_b at the electroweak scale.

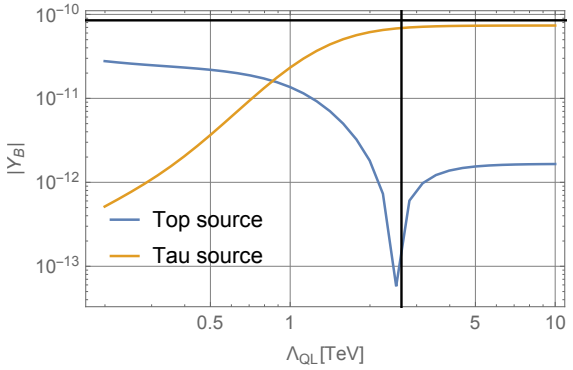

FIGURE 7.6: Y_B as function of $\Lambda_{\rm QL}$ for a top source with $\Lambda_t = 7.1 \times 10^3\,\text{GeV}$ (blue) and a lepton source with $\Lambda_\tau = 1 \times 10^3\,\text{GeV}$ (yellow). The vertical black line corresponds to the new interactions rate being equal to the lepton Yukawa interaction rate. The horizontal black line corresponds to the measured value of the baryon asymmetry.

effect of turning on a new top-tau coupling, which we parameterize by the dimension-six operator in eq. (7.13).

Intuitively, it is clear what to expect. For a top source, the chiral asymmetry in quarks is effectively washed out by the top Yukawa and especially by the strong sphaleron interactions. In such a scenario, any part of the chiral asymmetry that is transferred to the lepton sector survives this washout, and the more effectively this is done the larger the final baryon asymmetry. We thus expect an increase in Y_B for scales $\Lambda \lesssim 3\,\text{TeV}$ for which the new interaction rates becomes larger than the tau Yukawa interaction rate. For the lepton source scenario, we expect instead a decrease in the baryon asymmetry. The new interaction, if large, will transfer part of the chiral asymmetry from the lepton to the quark sector, where it is effectively washed out. This behavior is indeed borne out by our numerical simulations shown in figure 7.6, which shows the baryon asymmetry for a lepton (yellow line) and top-quark (blue line) source, for $\Lambda_\tau = 1\,\text{TeV}$ and $\Lambda_t = 7.1\,\text{TeV}$ consistent with experiment.

To obtain the observed baryon asymmetry eq. (5.1) with a top source requires a large top-lepton interaction, with a fairly low scale $\Lambda_{\rm QL} \lesssim 1\,\text{TeV}$ (as always, precise statements cannot be made due to significant theoretical uncertainties). To properly describe such a set-up probably requires going beyond the EFT description and adding the light degree of freedom that mediates the interaction. This might change the quantitative results, but we expect the results to be qualitatively the same. As the strength of the new coupling increases, the interactions approach equilibrium, and a further increase has limited effect; this explains the asymptotic flattening of Y_B for small cutoff $\Lambda_{\rm QL}$. The new coupling can boost the asymmetry by more than an order of magnitude. Naively one may have expected a $\mathcal{O}(10^2)$-increase, as the sphaleron washout reduces the chiral asymmetry in quarks by approximately this factor. However, even without the new interactions there is already transfer taking place via the SM Yukawa interactions. While the tau Yukawa is small, these effects already dominate the asymmetry for $\Lambda_{\rm QL} \to \infty$, as discussed in section 7.4.1.

While we considered here a top-tau interaction, the baryon asymmetry can also be boosted via additional interactions between top quarks and electrons or muons as the lepton flavor is irrelevant for the baryon asymmetry. The asymmetry can also be boosted by inclusion of BSM couplings between top and one of the lighter quarks. Such couplings, if sufficiently strong, would also avoid efficient washout by strong sphalerons, as discussed in section 7.2.6.

The effect of the dimension-six operator in eq. (7.13) in case of a lepton source is opposite as it now reduces the total asymmetry. As long as the new interactions are sufficiently suppressed $\Lambda_{\rm QL} \gtrsim 1\,\text{TeV}$, the chiral asymmetry stays mostly in the lepton sector and can be large enough to explain the observed value. However, for larger couplings the asymmetry can be suppressed by as much as two orders of magnitude. This effect can be seen in explicit models such as those studied in Refs. [326, 327] where a lepton CPV source is considered in the context of a two-Higgs doublet model. The source term, however, must be made rather large compared to the tau source discussed in section 7.3 (about a factor hundred larger) to generate a baryon asymmetry consistent with observations. The source originates from CPV Yukawa-interactions with heavier non-SM Higgs fields, which can be increased without running in conflict with experiments as long as the mixing angle between the heavier Higgs and the SM Higgs is sufficiently small. EDM bounds are also avoided by choosing couplings between the non-SM scalars and electrons and lighter quarks to be sufficiently small. The heavy scalars, however, lead to effective operators of the form of eq. (7.13) (although the actual lepton and quark flavor can vary) that, as shown in fig. 7.6, suppress the baryon asymmetry. As such, larger CPV sources are required. This example shows that the rather simple

framework considered here, based on effective operators can qualitatively describe the features of more complicated BSM models and can provide a useful guide in model building.

7.6 Discussion and conclusions

To satisfy the Sakharov conditions of CP-violation and out-of-equilibrium dynamics, many EWBG models have been proposed. In this chapter we do not commit to a specific model but instead apply EFT methods to describe the dynamics of EWBG. However, in chapter 6 we saw that EWBG cannot fully be embedded into the SM-EFT framework as a first-order phase transition requires additional light degrees of freedom that cannot be integrated out of the theory. In this chapter, we therefore describe the phase transition with a phenomenological ansatz and describe the required CPV with effective dimension-six operators containing SM fields only. Additional CPV operators involving the light degrees of freedom can certainly exist and be relevant, but as these are difficult to test experimentally, we leave them to future work.

We consider flavor-diagonal CPV dimension-six Yukawa operators of quarks and charged leptons with couplings that scale as y_f/Λ_f^2, where Λ_f is the scale where new physics appears and the EFT description breaks down. The resulting CPV source term that appears in the transport equation and drives the eventual generation of the baryon asymmetry scales as y_f^2/Λ_f^2. As such, for the same value of Λ_f it might be expected that the top quark would provide the largest baryon asymmetry. The recent electron EDM limit [297] sets a very strong constraint $\Lambda_t \geq 7.1$ TeV which ensures that a top CPV source as studied in this chapter cannot lead to the observed baryon asymmetry. For lighter fermions the CPV source term is suppressed by $(y_f/y_t)^2$, and even though the scale Λ_f is not as constrained, one might expect these light fermions to lead to even smaller asymmetries. We have investigated this in detail in this chapter and conclude that the naive scaling is not correct. Our main findings can be summarized as:

- Despite the Yukawa suppression, a CPV tau source leads to a baryon asymmetry of the same order of magnitude as induced by a top source for $\Lambda_\tau = \Lambda_t$. As EDM constraints on Λ_τ are much weaker, the tau source can produce the observed baryon asymmetry where a top source cannot. The relative effectiveness of the tau source with respect to the top source has several causes. While the top source is enhanced by $(y_t/y_\tau)^2$, the Yukawa and strong sphaleron rate effectively wash out a chiral asymmetry in top quarks. This washout is far less effective for tau leptons that have much smaller Yukawa couplings and do not participate in strong sphaleron

interactions. In addition, a chiral asymmetry in leptons diffuses much further into the plasma and electroweak sphaleron processes have more time to convert the chiral asymmetry into a baron asymmetry.

- We performed analytical and numerical calculations of varying sophistication of the baryon asymmetry in case of a tau CPV source. The analytical and numerical results are found to be in very good agreement. The analytical solutions provide insight into the dependence of the baryon asymmetry on parameters related to the phase transition, such as the bubble-wall velocity, and the size of the lepton Yukawa coupling. Depending on several parameters, we can identify regions where the baryon asymmetry scales as $\propto y_f^2$, as naively expected, but also as $\propto y_f$ showing explicit deviations from the naive scaling. As such, lighter fermions can be relatively effective in generating a baryon asymmetry.

- While tau leptons are more efficient than might be expected, our analytical solution shows that baryon asymmetries induced by muon or electron CPV dimension-six Yukawa interactions are suppressed by respectively $(y_\mu/y_\tau)^2$ and $(y_e/y_\tau)^2$. Such sources therefore lead to much too small baryon asymmetries and only the tau source is still phenomenologically relevant.

- Even in case of a top CPV source, leptons play an important role. The SM Yukawa interactions can convert a chiral asymmetry in quarks to a chiral asymmetry in leptons. This conversion is proportional to the tau Yukawa coupling and therefore often neglected. We find, however, that including tau leptons explicitly in the transport equations leads to a significant enhancement of the total baryon asymmetry up to an order of magnitude. This enhancement is a general feature over a wide range of bubble-wall velocities. We conclude that EWBG scenarios with CPV in the quark sector should explicitly include leptons in the transport equations. Despite this enhancement, the CPV top source from the dimension-six Yukawa interactions consistent with EDM experiments leads to a too small baryon asymmetry. This effectively rules out the minimal EWBG scenario of Ref. [278], although it must be stressed that the involved theoretical uncertainties are large.

- As a side result, we find that the fast-rate approximation which is often applied in studies of EWBG with CPV sources including top quarks, is not reliable. In our setup it significantly overestimates the total baryon asymmetry. This conclusion is in line with Ref. [312]. We recommend to avoid its use and to instead solve the complete set of transport equations.

- While the washout of the chiral asymmetry for a bottom CPV source is less effective than for a top CPV source, this does not compensate for the $(y_b/y_t)^2$ suppression of the CPV source.

We find that a CPV source from dimension-six bottom Yukawa interactions leads to a baryon asymmetry that is approximately two orders of magnitude smaller than a top CPV source for the same value $\Lambda_b = \Lambda_t$. For values of Λ_b consistent with EDM experiments this leads to a too small baryon asymmetry. For dimension-six Yukawa couplings for even lighter quarks the induced baryon asymmetries are even smaller.

- The total baryon asymmetry can be significantly altered in BSM models with more effective chiral-symmetry-breaking interactions between quarks and leptons than are present in the SM. In this chapter, we have modeled such interactions with effective dimension-six top-tau interactions that can be induced in explicit BSM models by the exchange of new particles. Such interactions can enhance, in case of a CPV quark source, or decrease, in case of a CPV lepton source, the baryon asymmetry by orders of magnitude. This mechanism can be useful to guide model building.

As a final remark, we would like to emphasize that although we looked at a specific implementation of CP violation via dimension-six Yukawa operators, our qualitative conclusions are more general. The importance of leptons and the related mechanism to boost the baryon asymmetry by transferring the chiral asymmetry from the quark to the lepton sector (or suppress it by doing the opposite), are independent of the details of our set-up.

Chapter 8

Summary and outlook

We have explored the phenomenology of the Higgs potential in the early universe. We have seen that a displacement from the zero-temperature vacuum expectation value $v_0 = 246\,\mathrm{GeV}$ has interesting consequences. We summarize our main findings in this chapter and give an outlook on possible directions for further research.

In chapter 3 we studied the possibility of a negative value of the Higgs self-coupling λ at large energy scales $\gtrsim 10^{11}\,\mathrm{GeV}$. A negative self-coupling results in a second minimum in the Higgs potential that is energetically more favorable than the electroweak minimum. Although a non-minimal coupling ξ between the Higgs field and the Ricci curvature scalar enhances electroweak stability during inflation, this non-minimal coupling leads to very efficient production of Higgs modes during preheating. The EW vacuum gets destabilized for $\xi \gtrsim 20$. For $\xi \lesssim 20$, particle production is less efficient and no vacuum-independent statements on the fate of the electroweak vacuum can be drawn.

It will be interesting to see whether production of other particles than the Higgs boson can have a stabilizing effect during preheating. So far, Higgs stability has not been been studied in a full multi-field context, in the sense that usually only the non-minimal coupling of the Higgs is taken into account. In a more general approach, the non-minimal couplings of the inflaton field as well as the Goldstone modes and possibly additional scalars should be included. For such an analysis, one can use the techniques of chapter 4.

In chapter 4 we assumed $\lambda > 0$ and studied the production of Higgs modes and gauge bosons after Higgs inflation. We found that gauge boson production is very efficient, but that perturbative decays of the gauge bosons shut off the resonance. Only for $\xi \gtrsim 1000$ is preheating into gauge bosons successful. The transfer of energy from the Higgs field to the gauge bosons completes within one oscillation. For $30 \lesssim \xi \lesssim 1000$ reheating proceeds through Higgs self-resonance, which completes approximately 3 e-folds after the end of inflation.

The non-minimal coupling to gravity introduces a UV-cutoff into the theory. Assuming very efficient thermalization, we find that the typical momentum in the thermal spectrum is above the unitarity scale for $\xi \gtrsim 300$. A more extensive study of the thermalization stage is needed to indicate more accurately for which values of ξ the unitarity scale is violated. To understand the behavior of the UV modes, it will be necessary to study preheating in a UV-complete model of Higgs inflation. Furthermore, a comparison to lattice simulations is needed to determine the regime of validity of our linearized analysis. This is work in progress.

It might seem that chapters 3 and 4 are mutually exclusive, since λ is negative in chapter 3 and positive in chapter 4 at the inflationary scale. In Ref. [341] it is argued that, when λ runs negative at some scale μ, it may become positive again at a larger energy scale, allowing for Higgs inflation with positive λ. It is shown in Ref. [341] that EW stability is maintained if the reheating temperature is large. It will be interesting to generalize these results in the full multi-field framework of chapter 4, including the non-trivial field-space metric.

In part II we studied electroweak baryogenesis. In chapter 6 we tested the applicability of EFT methods to study EWBG. We came to the conclusion that the requirement of a first-order electroweak phase transition introduces a low cut-off that results in a breakdown of the EFT. This implies that a new light degree of freedom should couple to the Higgs to allow for a first-order phase transition. This conclusion is somewhat disappointing, as we wanted to use the SM-EFT to study EWBG in a model-independent way. Nevertheless, we might learn about the nature of the light degree of freedom via collider experiments. Improved measurements of the Higgs cubic interaction could constrain the light degree of freedom. Another very exciting possibility to probe the first-order phase transition comes from gravitational wave experiments. The LISA experiment that is planned to be launched in the early 2030s can constrain the electroweak phase transition [342, 343].

In chapter 7 we found that the common practice of neglecting the Yukawa interactions of all fermions lighter than the top quarks in the computation of the baryon asymmetry leads to an underestimate of the value of the baryon asymmetry by approximately a factor 4. The enhancement of the asymmetry by the inclusion of lighter fermions is almost exclusively caused by the tau leptons. Furthermore, we showed that a CPV tau source can be more efficient in generating the baryon asymmetry than a top source. We also showed that including an effective lepton-quark interaction might enhance the baryon asymmetry in the case of a CPV top source, but decrease the asymmetry when the source is in the lepton sector. These are interesting considerations that can help model building.

Throughout part II we have commented several times on the (limited) accuracy of EWBG computations. A big source of uncertainty is the derivation of the relaxation rates and source terms. There are two different formalisms: the semi-classical approximation and the vev-insertion approximation that we have worked with. A thorough comparison of both methods is still lacking. Improvements in the accuracy of the computation of the baryon asymmetry are essential, especially when collider and gravitational wave experiments provide us with more information about the nature of the electroweak phase transition.

Appendix A

Rates and parameters for electroweak baryogenesis

In this appendix we list the values of various parameters for our benchmark scenario. For the values of the coupling constants at the electroweak scale $\mu = m_Z$ we use

$$g' = 0.36\,, \quad g = 0.65\,, \quad g_s = 1.23\,, \quad y_t = 1\,, \quad y_b = 0.02\,, \quad y_\tau = 0.01\,. \tag{A.1}$$

The diffusion constants are taken from Refs. [268, 325]

$$D_t \simeq \frac{6}{T}\,, \quad D_q \simeq \frac{6}{T}\,, \quad D_\tau \simeq \frac{100}{T}\,, \quad D_l \simeq \frac{380}{T}\,, \quad D_h \simeq \frac{100}{T}\,. \tag{A.2}$$

The SM thermal masses $\delta m_i^{\rm Re}$ are [273]

$$\begin{aligned}
(\delta m_Q^{\rm Re})^2 &= \left(\frac{1}{6}g_s^2 + \frac{3}{32}g^2 + \frac{1}{288}g'^2 + \frac{1}{16}y_t^2 + \frac{1}{16}y_b^2\right) T^2\,,\\
(\delta m_{t_R}^{\rm Re})^2 &= \left(\frac{1}{6}g_s^2 + \frac{1}{18}g'^2 + \frac{1}{8}y_t^2\right) T^2\,,\\
(\delta m_{b_R}^{\rm Re})^2 &= \left(\frac{1}{6}g_s^2 + \frac{1}{72}g'^2 + \frac{1}{8}y_b^2\right) T^2\,,\\
(\delta m_L^{\rm Re})^2 &= \left(\frac{3}{32}g^2 + \frac{1}{32}g'^2 + \frac{1}{16}y_\tau^2\right) T^2\,,\\
(\delta m_{\tau_R}^{\rm Re})^2 &= \left(\frac{1}{8}g'^2 + \frac{1}{8}y_\tau^2\right) T^2\,,\\
(\delta m_H^{\rm Re})^2 &= \left(\frac{3}{16}g^2 + \frac{1}{16}g'^2 + \frac{1}{4}y_t^2 + \frac{1}{4}\left(\frac{m_H^2}{v_0^2} - 3v_0^2\kappa\right) + 3\phi_0^2\kappa\right) T^2\,.
\end{aligned} \tag{A.3}$$

For the Higgs mass we included the contribution from the dimension six operator $\kappa(\varphi^\dagger\varphi)^3$. The result for the thermal masses can be derived from the effective potential in the high-temperature expansion (5.7).

	Broken phase	Symmetric phase
$\Gamma_{\rm ss}$	0.26	0.26
$\Gamma_M^{(t)}$	104	0
$\Gamma_Y^{(t)}$	2.7	2.7
$\Gamma_M^{(b)}$	$3.7 \cdot 10^{-2}$	0
$\Gamma_Y^{(b)}$	$1.1 \cdot 10^{-3}$	$1.1 \cdot 10^{-3}$
$\Gamma_M^{(l)}$	$4.6 \cdot 10^{-2}$	0
$\Gamma_Y^{(l)}$	$1.0 \cdot 10^{-4}$	$1.0 \cdot 10^{-4}$
$\Gamma_{\rm ws}$	0	$4.7 \cdot 10^{-4}$

TABLE A.1: Asymptotic values of the interaction rates in the broken and symmetric phase. All rates are in GeV. The relaxation rates $\Gamma_M^{(f)}$ are a function of the bounce solution ϕ_b and vary over the bubble wall.

The thermal widths $\Gamma_{t,i}$ are [227]

$$\Gamma_{t,Q} = 0.16T\,, \qquad \Gamma_{t,L} = 0.002T\,, \tag{A.4}$$

where $\Gamma_{t,Q}$ is for quarks and $\Gamma_{t,L}$ for leptons.

For the nucleation temperature we use

$$T_N = 88\,\text{GeV}\,. \tag{A.5}$$

This value was obtained by taking $\kappa = 2.0\,\text{TeV}^{-2}$ (corresponding to a scale of new physics $\Lambda \approx 0.71\,\text{TeV}$. The value of the Higgs field in the broken vacuum, the bubble-wall width and the bubble-wall speed are given by:

$$v_N = 152\,\text{GeV}\,, \quad L_w = 0.11\,\text{GeV}^{-1}\,, \quad v_w = 0.05\,. \tag{A.6}$$

The numerical values of the interaction rates are listed in table A.1.

Summary

This is a thesis about particle physics and cosmology. Particle physics is the science of the smallest constituents of matter that we know, and the interactions between them. We describe particle physics in terms of the Standard Model. Over the last decades, a large range of experiments has established its validity by carefully studying the reaction products of collisions in particle accelerators. The Standard Model of particle physics is a very successful theory; all the particles that it predicts have been found experimentally and so far no significant deviations of their properties have been observed.

Cosmology is the study of the evolution of the universe as a whole. General Relativity, the theory of gravity, describes the expansion of the universe. Unlike particle physics, we can not test cosmology in experiments, but only through observations of the cosmos. Observational data, such as the distribution of galaxies and the properties of the Cosmic Microwave Background, are very important for reconstructing the history of the universe.

On the surface, it might seem like particle physics and cosmology do not have much to do with each other. After all, we don't need elementary particle physics to describe the motion of the planets in the solar system. Particle interactions take place on tiny length scales, so why would they become relevant when we study the evolution of the universe as a whole? There are three main answers to this question:

- **The evolution of the universe depends on the particle content.** There are various contributions to the total energy of the universe, e.g. radiation, massive particles and dark energy. The dominant contribution determines the expansion rate of the universe. Understanding the history of the universe requires knowledge of the properties of all particles that are present at different stages of the cosmological evolution.

- **The history of the universe determines the present day particle content.** The masses of the elementary particles, as well as their interaction rates depend on the temperature of the universe. Initially, all interaction rates are very large and particles get converted into each other incessantly. When the temperature decreases, certain interactions become slow compared to

the expansion rate of the universe. As a consequence, some particles stop interacting and their amount remains fixed from that moment on. This process is called 'freeze-out'. The relic abundance of helium and the existence of a cosmic neutrino background are both results of freeze-out.

- **We can use cosmology to probe particle physics at very large energies.** There is strong evidence that the early universe goes through a period of cosmic 'inflation' during which it expands by at least a factor 10^{78}. During this enormous expansion, the tiny length scales relevant for particle physics get blown up to cosmologically observable scales. We can thus use telescopes to study traces of particle physics in the very early universe. This is extremely interesting, because we can not assess the large energy scale of the early universe in any experiment in the laboratory.

There is fairly strong consensus amongst cosmologists about the history of the universe. The standard picture is that the universe initially goes through a period of inflation and then follows 'Hot Big Bang' evolution: the evolution from a hot and dense particle soup to the universe of stars and galaxies that we live in today. In this cosmological framework, which is summarized in figure 1, one can correctly predict the relative amounts of light chemical elements (hydrogen, helium and lithium) and also the temperature and properties of the temperature fluctuations of the Cosmic Microwave Background radiation.

There are however clear signs that our understanding of cosmology and particle physics is not complete. Examples are the strong experimental evidence for the existence of dark matter and dark energy, and the asymmetry between matter and antimatter, which is the topic of the second part of this thesis. These observations might be explained by the existence of new particles or a modification of the theory of gravity. Modifying our existing theories is a very subtle task, because the Standard Model and General of Relativity have survived many experimental tests. Modifications of the theories should not affect these successful predictions.

The Higgs particle

The Higgs particle and the corresponding Higgs field play a very important role in this thesis. It is important to make a distinction between particles and fields. Fields are ubiquitous in physics. Examples are the gravitational field that determines how planets move around a star and the electric field that causes an electron to accelerate. We can associate a field to each particle of the Standard

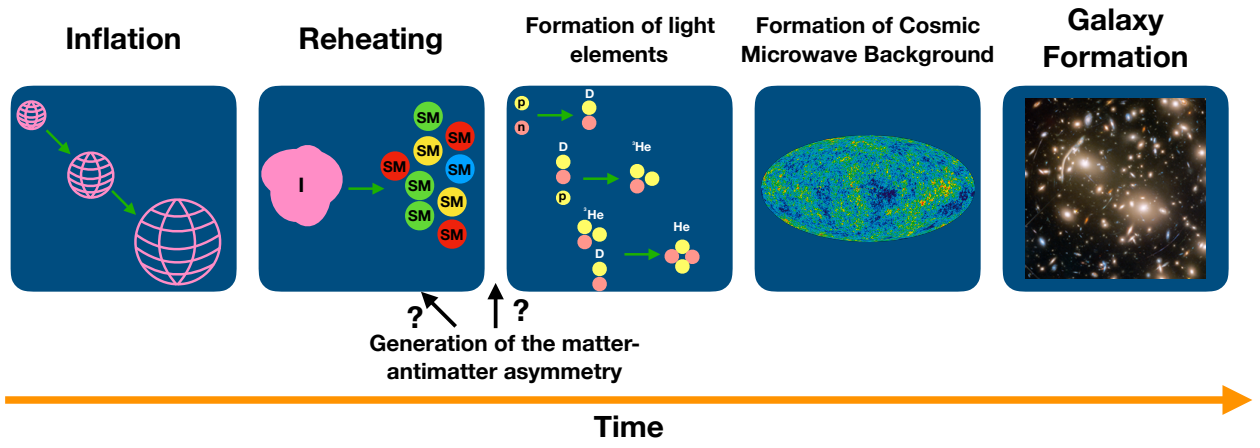

FIGURE 1: Timeline of the early universe. The picture merely shows the chronological order of the events, but time intervals are not to scale. The moment in which the asymmetry between matter and antimatter was formed is unknown. We know that this should have happened between inflation and the formation of light chemical elements.

Model. The particles, that can be detected in particle colliders, are excitations or 'ripples' of these fields. An example is the photon, which is an excitation of the electromagnetic field. Particles are localized in a small part of space, but the corresponding fields fill the entire space (although their values can be zero).

The values of the fields are determined by the corresponding potential energy function. We are all familiar with this concept through our experience with gravitational potential energy. This is the amount of energy that you need to climb a mountain, for example. Our experience also tells us that nature tends to minimize potential energy, this happens for example when a rock rolls down the slope of a mountain. The potential energy of all Standard Model fields is smallest when the fields are zero, except for the Higgs field. The potential of the Higgs field is shown in the left panel of figure 2. The black line displays the value of the potential energy as a function of the value of the field. The minimum is located at some non-zero value. The other particles of the Standard Model interact with the Higgs particle but also with the background value of the field. The interaction with the background value makes these particles massive.

The left panel of figure 2 shows the potential at low temperature. This picture is applicable today. In the early universe however, the large energy density during inflation and the high temperature after inflation modify the shape of the potential. In the research described in this thesis, the Higgs field is never at the low-temperature minimum. We will see that a displacement from this minimum leads to very interesting dynamics.

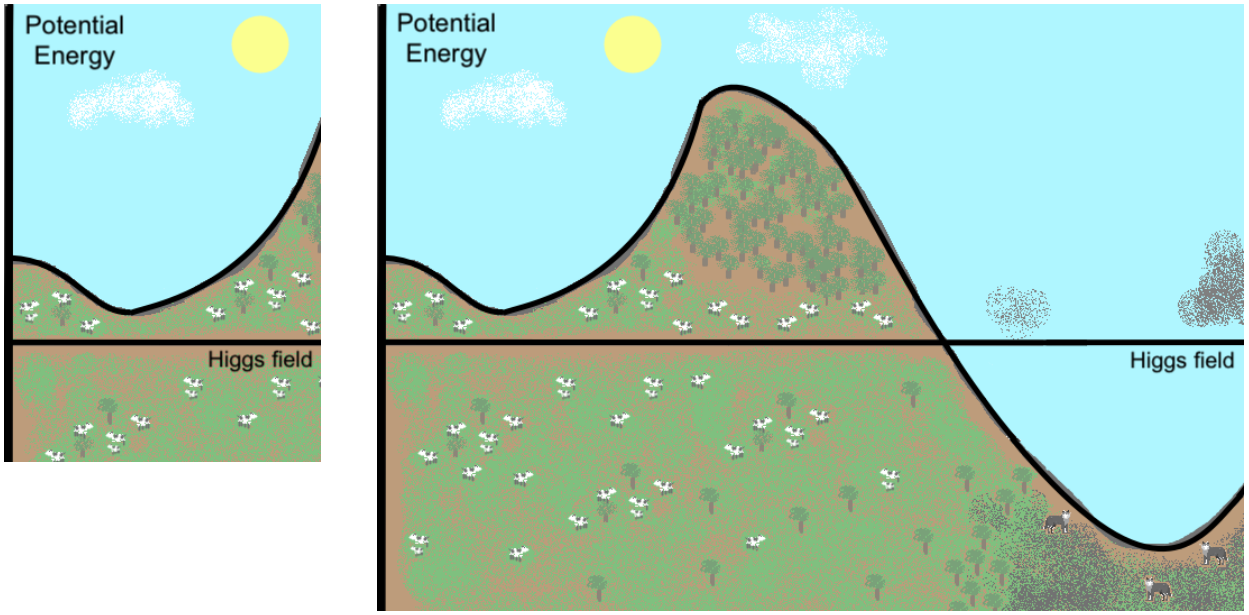

FIGURE 2:
Left: The Standard Model Higgs potential at low temperature. The Higgs field sits at the valley to minimize the potential energy.
Right: Measurements suggest that the Higgs potential might actually have a second minimum at a much larger field value.

Part I: Reheating the universe after inflation

In the standard picture of cosmology, the evolution of the universe starts with a period of inflation. During this period, the universe expands by an enormous factor. Inflation is driven by the inflaton field, which has a large amount of potential energy that dominates the entire universe. After a while, inflation ends. The inflaton then transfers its energy to the production of Standard Model particles. These particles form the hot and dense particle soup that evolves according to the standard Hot Big Bang model. The energy transfer from the inflaton to the Standard Model particles is called 'reheating'.

Higgs stability during reheating

The exact shape of the Higgs potential depends on the interactions of the Higgs field with other fields. Assuming that there are no new particles beyond the Standard Model, results from collider experiments indicate that the Higgs potential might look like the right panel of figure 2 instead of the left panel. There is a second, much deeper, minimum at a larger value of the Higgs field. We know that the Higgs field can not be situated in the deep minimum nowadays, since that would lead to a collapsing universe. In the present day universe, the bump that separates the minima prevents

a transition from the shallow minimum to the deep minimum. In the early universe, however, the Higgs field was displaced from the present day minimum, so we must try to understand why the Higgs field ended up in the shallow, safe minimum instead of the deep, dangerous minimum.

At first glance it seems that, during inflation, the energy in the universe is much larger than the energy required for the Higgs field to go over the bump; the Higgs field would thus end up in the deep minimum. Fortunately, an interaction between the Higgs field and gravity prevents this transition. This interaction raises the height of the barrier, such that the Higgs field can not pass it during inflation.

But unfortunately, the interaction between the Higgs field and gravity leads to problems during reheating, when the inflaton oscillates at the bottom of its potential causing the barrier to periodically appear and disappear. This leads to very efficient production of Higgs particles. In chapter 3 we show that the fate of the universe depends on the strength of the Higgs-gravity interaction. If the interaction is very strong, the efficient production of Higgs particles allows the Higgs field to transition to the dangerous deep vacuum. For a weaker Higgs-gravity interaction, we can not draw a conclusion, as our computational tools are not suitable to demonstrate that the Higgs stays in the safe area left from the barrier. The reason is that it is very difficult to correctly describe non-static processes.

So what should we conclude from this? Our mere presence proves that the universe did not collapse during reheating. Does this imply that the Higgs-gravity interaction is not so strong that the Higgs transitioned to the deep minimum during reheating? It might. It might also mean that the potential looks like the left panel of figure 2 after all, which could be the result of the presence of yet unknown particles.

Reheating after Higgs inflation

There are many different models for inflation. Typically, inflation is driven by a so-called scalar field. The Higgs field is the only scalar field that has been observed experimentally. It is therefore an interesting candidate for inflation. The Higgs field can only drive inflation if its potential becomes very flat (and positive) for very large field values. To satisfy this condition, we again need a Higgs-gravity interaction, which must be larger than the one of chapter 3.

Since the interactions between the Higgs field and the other Standard Model fields are known, we can predict how reheating proceeds in the Higgs inflation scenario. In chapter 4 we find that the

reheating process depends on the strength of the Higgs-gravity interaction. When the interaction is very strong, reheating is extremely fast, and the energy density in the Higgs field gets almost instantly transferred to the gauge bosons of the electroweak interaction. These gauge bosons will in turn decay into all the other particles of the Standard Model. When the Higgs-gravity interaction is weaker, reheating takes longer, and happens mostly through the production of Higgs particles. The Higgs particles will then also decay into other Standard Model particles.

Part II: Generating the matter-antimatter symmetry

According to the Standard Model, each particle has a corresponding antiparticle, that has the same mass, but opposite charge. If a particle and an antiparticle collide, they annihilate each other. All the matter that we see around us, on earth and in the universe, is actual matter, not antimatter. If particle physics were described by the Standard Model throughout the entire history of the universe, there would be no asymmetry between matter and antimatter. Apparently some unknown particle-physics process generated an excess of matter at some moment in the history of the universe. This process is referred to as 'baryogenesis'.

The Standard Model can not provide a process for baryogenesis for two reasons: it does not distinguish strongly enough between particles and antiparticles, and it does not give rise to any useful out-of-equilibrium process. Being out-of-equilibrium simply implies that the rate at which matter is created is not equal to the rate at which it is destroyed. If these rates always remain equal, an excess of matter can not be formed. Examples of out-of-equilibrium processes are the freeze-out of interaction rates and first-order phase transitions. To explain the excess of matter over antimatter, the Standard Model thus needs to be extended, for example by the addition of new particles that interact differently with matter and antimatter.

In part II of this thesis we study the possibility of generating the matter-antimatter asymmetry during the 'electroweak phase transition'. This process is sketched in figure 3. The existence of the electroweak phase transition is a consequence of the temperature dependence of the Higgs potential. At large temperature, the potential only has a minimum at zero field value. As the temperature lowers, the potential changes shape and the minimum at non-zero field, that we see in figure 2, appears. The electroweak phase transition is the moment when the Higgs field transitions from zero to the non-zero value. From that moment on, the other particles become massive. In the Standard Model, this is not a first-order phase transition, but a smooth, continuous process. Since the nature

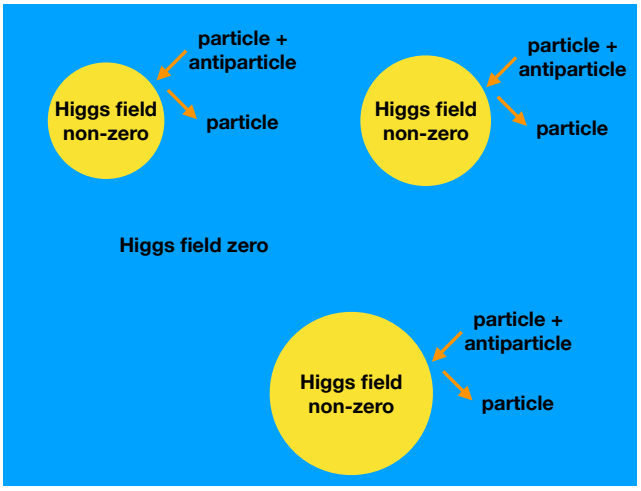

FIGURE 3: Sketch of electroweak baryogenesis. The first-order phase transition proceeds by the formation of bubbles in which the Higgs field has a non-zero value. The surrounding particles and antiparticles interact with the bubbles. In these interactions, an excess of matter is created. While swallowing the excess of matter, the bubbles expand until they fill the entire universe.

of the phase transition depends on the shape of the Higgs potential, we need to modify the potential by adding some new particle.

Model-independent description of baryogenesis during the electroweak phase transition

There are many different particles that one could add to fulfil the conditions for successful baryogenesis. Of course, the addition of these particles should be consistent with results from particle-physics experiments. In principle, for each different model of new physics, one should make a comparison to experimental results and compute the value of the matter-antimatter asymmetry.

In chapter 6 we attempt to study baryogenesis in a way that does not depend on the chosen model of new physics. As long as the newly added particles are sufficiently heavy, all models of new physics can be parameterized in a unified way: the Standard Model is extended by a set of so-called 'effective operators', which are new interactions between Standard Model particles. The conditions for the generation of the matter-antimatter asymmetry can now be fulfilled. One can compare the different effective operators to their experimental constraints and compute the value of the baryon asymmetry including these operators. In this way, all models with new heavy particles can be studied in one go.

In chapter 6 we focus on two effective operators in particular: a new interaction for the Higgs field and an interaction that distinguishes between top quarks and anti-top quarks. Unfortunately, we find that the method with effective operators is not completely feasible. The new particles that

need to be added to get a first-order phase transition need to be relatively light, which prohibits a parameterization in terms of effective operators. Our wish to study electroweak baryogenesis in a completely model-independent way can thus not be fulfilled.

The importance of leptons

The outcome of chapter 6 is not only disappointing because the approach with effective operators is not completely feasible, but also because the value of the matter-antimatter asymmetry is too small to explain the observed value. The strength of the interaction that distinguishes between particles and antiparticles is proportional to the mass of the particle. Since the top is the heaviest matter particle, the effects of other matter particles are often neglected in computations of the matter-antimatter asymmetry.

In chapter 7 we have shown that the tau lepton, a particle that is much lighter than the top quark, can play an important role during electroweak baryogenesis. Even if the new interaction that distinguishes between particles and antiparticles is only effective in the top-quark sector, including the tau leptons in the computation still enhances the asymmetry. The asymmetry becomes even larger when the distinction between particles and antiparticles is in the tau-lepton sector. The reason for this is the weaker experimental constraint on the new interaction involving the tau, but also the fact that the tau lepton can move more easily through the medium surrounding the bubbles, allowing more time for the matter excess to be formed. In this model, the observed value of the matter-antimatter asymmetry can be explained.

Outlook

The research described in this thesis does of course not end here. A possible direction of further research would be to reconcile the topics of chapters 3 and 4. It could be possible that the Higgs potential has a second, deep minimum but also supports inflation. What would happen during reheating in this case? To make really accurate predictions about reheating, one should use so-called lattice computations. Comparing lattice results to our results using the framework of chapter 4 is work in progress. Accurate predictions for reheating are essential for using the data from the Cosmic Microwave Background to determine the feasibility of different inflationary models.

On the electroweak baryogenesis side, the computational accuracy should be improved. There are different methods for computing the matter-antimatter asymmetry and the relation between these

methods should be better understood. Future collider and gravitational-wave experiments might shed light on the electroweak phase transition and, hopefully, help to understand how the matter-antimatter asymmetry was generated.

Samenvatting

Dit proefschrift gaat over deeltjesfysica en kosmologie. Deeltjesfysica is de wetenschap van de allerkleinste deeltjes waar materie uit is opgebouwd en de interacties tussen deze deeltjes. We beschrijven deeltjesfysica met behulp van het standaardmodel. In de afgelopen tientallen jaren heeft een groot aantal experimenten dit model bevestigd door zorgvuldig de reactieproducten van botsingen in deeltjesversnellers te bestuderen. Het standaardmodel van elementaire deeltjes is een zeer succesvolle theorie; alle deeltjes die de theorie voorspelt zijn daadwerkelijk gedetecteerd en er zijn vooralsnog geen significante afwijkingen gevonden in hun eigenschappen.

Kosmologie is de studie van het universum als geheel. De algemene relativiteitstheorie, de theorie van de zwaartekracht, beschrijft de uitdijing van het heelal. In tegenstelling tot deeltjesfysica, kunnen we kosmologie niet testen door middel van experimenten, maar alleen door de kosmos waar te nemen. Observationale gegevens, zoals de verdeling van sterrenstelsels en de eigenschappen van de kosmische achtergrondstraling, zijn heel belangrijk om de geschiedenis van het universum te reconstrueren.

Op het eerste gezicht lijken deeltjesfysica en kosmologie niet veel met elkaar te maken te hebben. We hebben per slot van rekening geen deeltjesfysica nodig om de beweging van de planeten in het zonnestelsel te beschrijven. Interacties tussen elementaire deeltjes vinden plaats op heel kleine afstanden, dus waarom zouden die belangrijk zijn wanneer we de globale evolutie van het heelal willen beschrijven? Er zijn drie antwoorden op deze vraag:

- **De evolutie van het universum wordt bepaald door de deeltjes die het bevat.** Er zijn verschillende bijdragen aan de totale energie in het universum. Voorbeelden zijn straling, massieve deeltjes en donkere energie. De grootste bijdrage aan de totale energie bepaalt de snelheid waarmee het heelal uitdijt. Om de geschiedenis van het heelal te begrijpen, moeten we dus de eigenschappen kennen van alle deeltjes die aanwezig waren in de verschillende fases van de kosmologische evolutie.

- **De geschiedenis van het universum bepaalt de huidige deeltjessamenstelling.** De massa's van de elementaire deeltjes en de sterkte van hun interacties hangen af van de temperatuur van het universum. In het begin zijn alle interacties heel sterk en worden alle deeltjes

steeds in elkaar omgezet. Wanneer de temperatuur daalt, worden bepaalde omzettingen trager dan de uitdijing van het heelal. Daardoor stoppen de reacties van bepaalde deeltjes en blijft hun hoeveelheid vanaf dat moment gelijk. Dit proces heet 'bevriezing'. De hoeveelheid helium in het heelal en het bestaan van een kosmische achtergrondstraling van neutrino's zijn het resultaat van bevriezing.

- **Kosmologie kan worden gebruikt om deeltjesfysica te bestuderen bij heel hoge energie.** Er zijn zeer sterke aanwijzingen dat het vroege universum een periode van kosmische 'inflatie' doormaakt, waarin het heelal met minstens een factor 10^{78} expandeert. Tijdens deze enorme uitdijing worden de minuscule lengteschalen waarop deeltjesfysica zich afspeelt opgeblazen tot kosmologische afstanden. Met behulp van telescopen kunnen we dus sporen bestuderen van deeltjesfysica in het heel vroege heelal. Dit is ontzettend interessant, omdat we de hoge energien van het vroege heelal in geen enkel experiment in het laboratorium kunnen bereiken.

Er is een behoorlijk sterke consensus onder kosmologen over de geschiedenis van het heelal. Het standaard beeld is dat het heelal eerst een periode van inflatie doormaakt en daarna 'Hete Oerknal'-evolutie volgt: de evolutie van een hete en dichte deeltjessoep tot het universum met sterren en sterrenstelsels waar we nu in leven. Met dit model, dat wordt samengevat in figuur 1, kunnen de relatieve hoeveelheden van de lichte chemische elementen (waterstof, helium en lithium), en de temperatuur en de eigenschappen van de temperatuurfluctuaties van de kosmische achtergrondstraling nauwkeurig worden voorspeld.

Toch lijkt het er sterk op dat ons begrip van kosmologie en deeltjesfysica niet compleet is. Voorbeelden hiervan zijn de vele experimentele aanwijzingen voor het bestaan van donkere materie en donkere energie, en de asymmetrie tussen materie en antimaterie, het onderwerp van het tweede deel van dit proefschrift. Deze observaties zouden verklaard kunnen worden door het bestaan van nieuwe deeltjes of een aanpassing van de theorie van de zwaartekracht. Het aanpassen van onze bestaande theorieën is geen makkelijke taak, aangezien het standaardmodel en de algemene relativiteitstheorie al veel experimentele tests hebben doorstaan. Aanpassingen van deze theorieën mogen deze correcte voorspellingen niet veranderen.

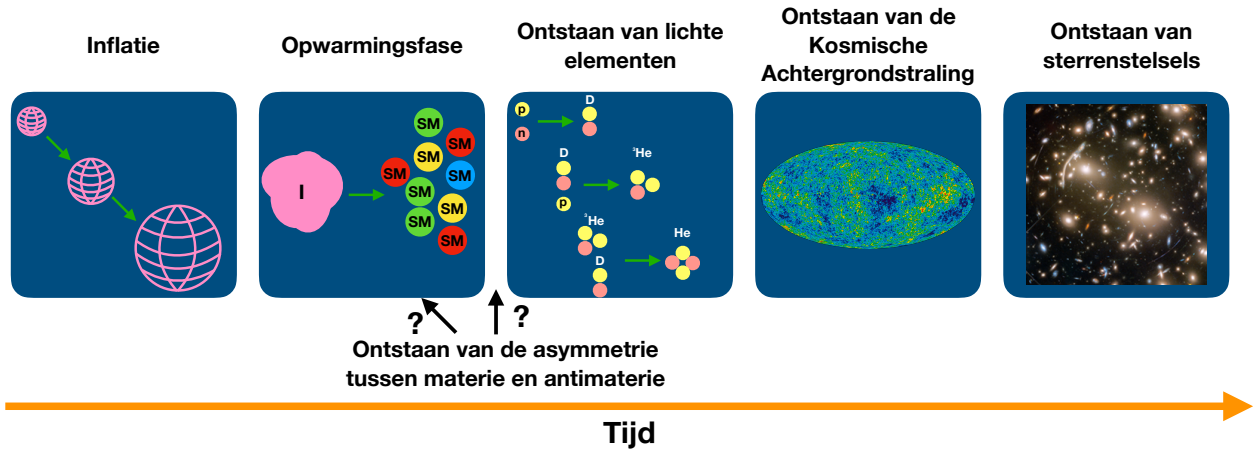

FIGUUR 1: Tijdlijn van het vroege universum. De illustratie laat voornamelijk de volgorde van de gebeurtenissen zien, maar de tijdsintervallen zijn niet op schaal. Het moment waarop de asymmetrie tussen materie en antimaterie is gevormd is niet bekend. We weten dat dit gebeurd moet zijn tussen inflatie en het ontstaan van de lichte chemische elementen.

Het Higgsdeeltje

Het Higgsdeeltje en het bijbehorende Higgsveld spelen een belangrijke rol in dit proefschrift. Het is belangrijk om onderscheid te maken tussen deeltjes en velden. Velden komen overal voor in de natuurkunde. Voorbeelden zijn het zwaartekrachtsveld, dat bepaalt hoe planeten bewegen rondom een ster, en het elektrische veld dat een elektron laat versnellen. We kunnen met elk deeltje van het standaardmodel een veld associeren. De deeltjes, die in deeltjesversnellers worden gedetecteerd, zijn excitaties of 'rimpelingen' in deze velden. Een voorbeeld is het foton, het deeltje dat hoort bij het elektromagnetische veld. Deeltjes zijn gelokaliseerd in een klein stukje ruimte, maar de bijbehorende velden vullen de gehele ruimte (al kan de waarde van de velden ook nul zijn).

De waardes van de velden worden bepaald door de bijbehorende potentiële-energiefunctie. Met potentiële energie zijn we allemaal bekend door onze ervaring met de potentiële energie die hoort bij de zwaartekracht: dit is de energie die je nodig hebt om een berg te beklimmen. Onze ervaring vertelt ons ook dat de natuur potentiële energie probeert te minimaliseren; dit gebeurt bijvoorbeeld wanneer een steen van de helling van een berg afrolt. De potentiële energie van de velden van het standaardmodel is het kleinst wanneer de waarde van de velden nul is, behalve bij het Higgsveld. De potentiaal van het Higgsveld is geschetst in het linker deel van figuur 2. De zwarte lijn geeft de waarde van de potentiële energie aan als een functie van de waarde van het veld. Het minimum bevindt zich op een waarde die niet nul is. De andere deeltjes van het standaardmodel wisselwerken met het Higgsdeeltje, maar ook met de waarde van het veld op de achtergrond. De wisselwerking met de achtergrondwaarde van het Higgsveld geeft die deeltjes massa.

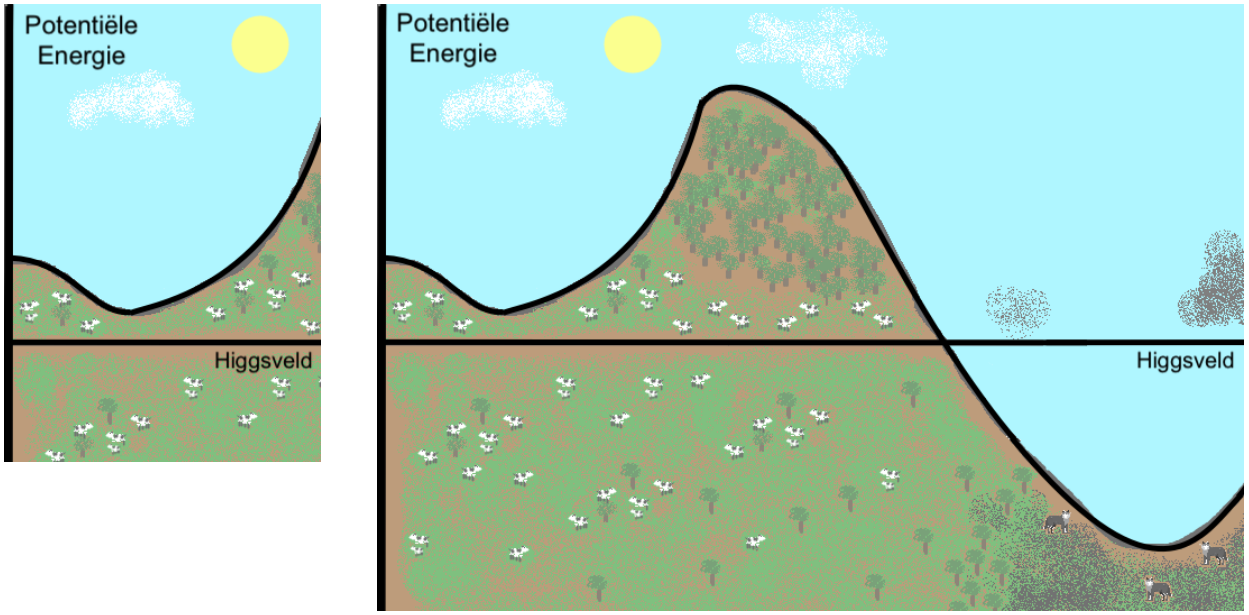

Figuur 2:
Links: De potentiaal van het Higgsveld bij lage temperatuur. Het Higgsveld bevindt zich in het dal om de potentiële energie te minimaliseren.
Rechts: Metingen suggereren dat de potentiaal van het Higgsveld een tweede minimum zou kunnen hebben voor een veel grotere waarde van het veld.

Het linker deel van figuur 2 laat de potentiaal zien bij lage temperatuur. Deze situatie is nu van toepassing, maar niet in het vroege heelal. De hoge energiedichtheid in het universum tijdens inflatie en de hoge temperatuur daarna veranderen de vorm van de potentiaal. In het onderzoek in dit proefschrift bevindt het Higgsveld zich nooit in het minimum waarin het zich nu bevindt. We zullen zien dat dit tot interessante dynamica leidt.

Deel I: Opwarming van het heelal na inflatie

In het standaard plaatje van kosmologie begint de evolutie van het universum met een periode van inflatie. Tijdens deze periode dijt het heelal enorm uit. Inflatie wordt aangedreven door het inflatonveld, dat een grote hoeveelheid potentiële energie heeft die het hele heelal domineert. Na een tijd komt inflatie tot een einde. Het inflatonveld draagt dan zijn energie over door deeltjes uit het standaardmodel te produceren. Deze deeltjes vormen de hete en dichte deeltjessoep die zich ontwikkelt volgens het standaard Hete Oerknalmodel. Het overbrengen van de energie van het inflatonveld naar de deeltjes van het standaardmodel heet de ‘opwarmingsfase’.

Stabiliteit van het Higgsveld tijdens de opwarmingsfase

De precieze vorm van de potentiaal van het Higgsveld hangt af van de interacties van het Higgsveld met de andere velden. Als we aannemen dat er geen andere deeltjes zijn dan die uit het standaardmodel, suggereren de resultaten van deeltjesversnellers dat de Higgspotentiaal er uitziet als het rechter deel van figuur 2, in plaats van het linker deel. Er is een tweede, veel dieper minimum voor een grotere waarde van het Higgsveld. We weten dat het Higgsveld zich nu niet in dat diepe minimum kan bevinden, want dat zou leiden tot een samenklappend heelal. In het huidige universum zorgt de barrière tussen de twee minima dat het Higgsveld zich niet verplaatst van het ondiepe naar het diepe minimum. Aangezien het Higgsveld zich niet in het huidige minimum bevindt in het vroege heelal, moeten we proberen te begrijpen hoe het in het ondiepe minimum terecht is gekomen.

Op het eerste gezicht lijkt het erop dat de energie in het universum tijdens inflatie veel groter is dan de energie die nodig is om over de barrière in de potentiaal te komen; het Higgsveld zou dus terecht komen in het diepe minimum. Gelukkig voorkomt een wisselwerking tussen het Higgsveld en de zwaartekracht dat het Higgsveld deze overgang maakt. Deze interactie vergroot de hoogte van de barrière, waardoor het Higgsveld er niet overheen kan tijdens inflatie.

Maar helaas leidt deze interactie tussen het Higgsveld en zwaartekracht tot problemen tijdens de opwarmingsfase, wanneer het inflaton oscilleert op de bodem van zijn potentiaal waardoor de barrière steeds verdwijnt en opnieuw verschijnt. Dit leidt tot een zeer efficiënte productie van Higgsdeeltjes. In hoofdstuk 3 laten we zien dat het lot van het universum afhangt van de sterkte van de Higgs-zwaartekrachtinteractie. Als deze interactie sterk is, zorgt de efficiënte productie van Higgsdeeltjes ervoor dat het Higgsveld in het gevaarlijke diepe minimum terecht komt. Als de interactie zwakker is, kunnen we niet vaststellen wat er gebeurt, doordat er geen geschikte methode is om aan te tonen dat het Higgsveld aan de veilige kant van de barrière blijft. De reden hiervoor is dat het erg moeilijk is om niet-statische processen correct te beschrijven.

Welke conclusie moeten we hieruit trekken? Ons bestaan bewijst dat het universum niet in elkaar is gestort tijdens de opwarmingsfase. Betekent dit dat de interactie tussen het Higgsveld en de zwaartekracht niet zo sterk is? Dat is een mogelijkheid. Het is ook mogelijk dat de potentiaal er toch uitziet zoals het linker deel van figuur 2, bijvoorbeeld door het bestaan van nog onbekende deeltjes.

Opwarming na Higgsinflatie

Er zijn veel verschillende modellen voor inflatie. In veel van die modellen wordt inflatie aangedreven door een zogenaamd scalair veld. Aangezien het Higgsveld het enige scalaire veld is dat experimenteel gedetecteerd is, is het een interessante kandidaat voor het inflatonveld. Het Higgsveld kan alleen inflatie veroorzaken als zijn potentiaal erg vlak (en positief) wordt voor heel grote waarden van het veld. Om dit te bewerkstelligen, hebben we weer een interactie nodig tussen het Higgsveld en de zwaartekracht, maar ditmaal nog sterker dan in hoofdstuk 3.

Aangezien de interacties tussen het Higgsveld en de andere velden van het standaardmodel bekend zijn, kunnen we voorspellen hoe de opwarmingsfase verloopt in het geval van Higgsinflatie. In hoofdstuk 4 vinden we dat het verloop van de opwarmingsfase afhangt van de sterkte van de Higgs-zwaartekrachtinteractie. Als die wisselwerking heel sterk is gaat de opwarming ontzettend snel en wordt de energie van het Higgsveld voornamelijk overgebracht naar de ijkbosonen van de electrozwakke interactie. Deze ijkbosonen vervallen op hun beurt in alle andere deeltjes van het standaardmodel. Als de Higgs-zwaartekrachtinteractie minder sterk is, duurt de opwarmingsfase langer. Er worden dan voornamelijk Higgsdeeltjes geproduceerd. De Higgsdeeltjes vervallen ook in de andere deeltjes van het standaardmodel.

Deel II: De asymmetrie tussen materie en antimaterie

Volgens het standaardmodel heeft elk deeltje een bijbehorend antideeltje, met dezelfde massa maar tegengestelde lading. Wanneer een deeltje en een antideeltje op elkaar botsen, annihileren ze elkaar. Alle materie die we om ons heen zien, zowel op aarde als in het universum, is gewone materie, geen antimaterie. Als deeltjesfysica beschreven zou worden door enkel het standaardmodel gedurende de gehele geschiedenis van het heelal, zou er geen asymmetrie zijn tussen materie en antimaterie. Blijkbaar heeft één of ander onbekend deeltje een overvloed aan materie veroorzaakt op een zeker moment in de geschiedenis van het universum. Dit proces heet ‘baryogenese’.

Er zijn twee redenen waarom het standaardmodel geen geschikt proces voor baryogenese kan beschrijven: het maakt geen sterk genoeg onderscheid tussen deeltjes en antideeltjes en het veroorzaakt geen processen die ‘uit evenwicht’ zijn. ‘Uit evenwicht’ betekent dat de snelheid waarmee materie wordt gemaakt niet gelijk is aan de snelheid waarmee materie wordt vernietigd. Als deze snelheden altijd gelijk aan elkaar zijn, kan er geen overschot aan materie ontstaan. Voorbeelden van processen uit evenwicht zijn het bevriezen van interacties, en eerste-orde faseovergangen. Om het overschot aan

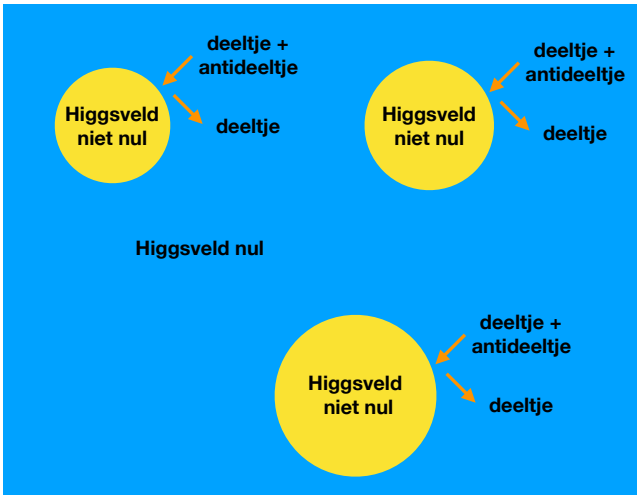

FIGUUR 3: Schets van electrozwakke baryogenese. De eerste-orde faseovergang vindt plaats door het vormen van bubbels waarin de waarde van het Higgsveld niet nul is. De deeltjes en antideeltjes in de omgeving reageren met de bubbels. In deze interacties wordt een overschot aan materie opgebouwd. De bubbels nemen dit overschot aan materie op terwijl ze uitdijen om uiteindelijk het gehele universum te vullen.

materie te verklaren, moeten we het standaardmodel dus uitbreiden, bijvoorbeeld door deeltjes toe te voegen die verschillend met materie en antimaterie wisselwerken.

In deel II van dit proefschrift bestuderen we de mogelijkheid om de asymmetrie tussen deeltjes en antideeltjes te maken tijdens de 'electrozwakke faseovergang'. Figuur 3 laat een schets zien van dit proces. De electrozwakke faseovergang is een gevolg van de temperatuurafhankelijkheid van de Higgspotentiaal. Bij hoge temperatuur heeft de potentiaal alleen een minimum wanneer het veld nul is. Wanneer de temperatuur omlaag gaat, verandert de potentiaal van vorm en verschijnt het minimum dat we zien in figuur 2. De electrozwakke faseovergang is het moment waarop het Higgsveld de overgang maakt van nul naar een waarde die niet nul is. Vanaf dat moment krijgen de andere deeltjes massa. In het standaardmodel is de faseovergang niet eerste orde, maar een geleidelijk, continu proces. Aangezien de aard van de faseovergang afhangt van de vorm van de Higgspotentiaal, moeten we de potentiaal veranderen door één of ander nieuw deeltje toe te voegen.

Modelonafhankelijke beschrijving van baryogenese tijdens de electrozwakke faseovergang

Er zijn veel verschillende deeltjes die je toe zou kunnen voegen om aan de voorwaarden voor baryogenese te voldoen. De toevoeging van deze deeltjes moet uiteraard consistent zijn met experimentele

resultaten. In principe moet je voor elk nieuw model een vergelijking maken met de bestaande metingen en de waarde van de asymmetrie tussen materie en antimaterie uitrekenen.

In hoofdstuk 6 proberen we baryogenese te bestuderen op een manier die niet afhangt van het model voor nieuwe deeltjesfysica. Zolang de nieuwe deeltjes zwaar genoeg zijn, kunnen alle modellen voor nieuwe natuurkunde op dezelfde manier worden geparameteriseerd: we breiden het standaardmodel uit met een set van zogenaamde 'effectieve operatoren'. Dit zijn nieuwe interacties tussen de deeltjes van het standaardmodel. Hiermee kan aan de voorwaarden voor baryogenese worden voldaan. Deze operatoren kunnen worden vergeleken met experimentele limieten, en hun effect kan worden meegenomen in de berekening van de asymmetrie tussen materie en antimaterie. Zo kunnen alle modellen met nieuwe zware deeltjes in één keer worden bestudeerd.

In hoofdstuk 6 richten we onze aandacht op twee specifieke operatoren: een nieuwe interactie voor het Higgsveld en een interactie die onderscheid maakt tussen topquarks en antitopquarks. Jammer genoeg blijkt dat de methode met effectieve operatoren niet helemaal werkt. Voor de eerste-orde faseovergang zijn relatief lichte deeltjes nodig, wat een parametrisatie met effectieve operatoren onmogelijk maakt. Onze hoop om electrozwakke baryogenese te bestuderen zonder een model te specificeren is daarmee vervlogen.

Het belang van leptonen

De uitkomst van hoofdstuk 6 is niet alleen teleurstellend omdat de aanpak met effectieve operatoren niet goed werkt, maar ook omdat de berekende waarde van de asymmetrie tussen materie en antimaterie veel kleiner is dan de gemeten waarde. De sterkte van de interactie die onderscheid maakt tussen deeltjes en antideeltjes is proportioneel aan de massa van het deeltje. Aangezien de topquark het zwaarste materiedeeltje is, worden de effecten van andere materiedeeltjes meestal verwaarloosd in berekeningen van de asymmetrie tussen materie en antimaterie.

In hoofdstuk 7 laten we zien dat het taulepton, een deeltje dat veel lichter is dan de topquark, een belangrijke rol kan spelen tijdens electrozwakke baryogenese. Zelfs wanneer de nieuwe interactie die onderscheid maakt tussen deeltjes en antideeltjes alleen actief is in de topquarksector, versterkt de bijdrage van tauleptonen nog altijd de asymmetrie. De asymmetrie wordt nog groter wanneer het onderscheid tussen deeltjes en antideeltjes wordt gemaakt in de tauleptonsector. De reden hiervoor is dat de experimentele limieten minder sterk zijn wanneer de nieuwe interactie het taulepton betreft, maar ook dat het taulepton zich makkelijker kan bewegen door het medium tussen de bubbels,

waardoor er meer tijd is om een overschot aan materie te maken. In dit model kan de gemeten waarde van de asymmetrie tussen materie en antimaterie wél worden verklaard.

Vooruitzichten

Het onderzoek uit dit proefschrift houdt hier natuurlijk niet op. Een mogelijke richting voor verder onderzoek is een combinatie van hoofdstuk 3 en 4. Het zou kunnen dat de Higgspotentiaal een tweede, diep minimum heeft, maar ook leidt tot inflatie. Wat zou er in dat geval gebeuren tijdens de opwarmingsfase? Om echt nauwkeurige voorspellingen te doen over de verhittingsfase, moet je eigenlijk zogenaamde roosterberekeningen gebruiken. Een vergelijking tussen resultaten van een rooster en onze resultaten met de methodes van hoofdstuk 4 is in de maak. Nauwkeurige voorspellingen voor de verhittingsfase zijn essentiëel wanneer men de data van de kosmische achtergrondstraling wil gebruiken om te bepalen welke modellen voor inflatie mogelijk zijn.

Ook de nauwkeurigheid van berekeningen aan electrozwakke baryogenese kan sterk worden verbeterd. Er zijn verschillende methodes om de asymmetrie tussen materie en antimaterie uit te rekenen, en de relatie tussen deze methodes wordt nog niet goed begrepen. In de toekomst zullen nieuwe deeltjesversnellers en detectoren van zwaartekrachtsgolven meer duidelijkheid geven over de electrozwakke faseovergang en zo, hopelijk, helpen te begrijpen hoe de asymmetrie tussen materie en antimaterie is ontstaan.

Dankwoord

Mijn eerste woord van dank gaat natuurlijk naar mijn PhD-begeleidster. Marieke, ik prijs mezelf zeer gelukkig dat ik mijn promotieonderzoek met jou heb mogen doen. Je kritische houding en de manier waarop jij een nieuw probleem te lijf gaat, bewonder ik zeer. Ik kon altijd met mijn vragen bij je terecht en ik heb ontzettend veel van je geleerd. Jan-Willem, hartelijk dank voor je optreden als mijn promotor. Ik waardeer je behulpzaamheid en je betrokkenheid bij mijn onderzoek.

I have enjoyed working in the Theory Group at Nikhef very much. I want to thank all the colleagues for the great atmosphere. In het bijzonder wil ik Eric bedanken, die me aangemoedigd heeft om twee maanden door te brengen in de Verenigde Staten, wat een fantastische ervaring was.

Of course I want to thank my collaborators, without whom the last few years would not have been so nice. Jordy, ik heb veel plezier beleefd aan onze ontdekkingstocht in het veld van de baryogenese. Ook dank aan jou, Corien en Tom voor de leuke tijd in Amherst. Evangelos, thank you for your encouragement and your contagious enthusiasm.

Lieve papa en mama, heel erg bedankt voor jullie steun, aanmoediging en betrokkenheid. En natuurlijk Joske, voor je gezelligheid en dat ik je altijd over mijn onderzoek kon vertellen.

Curriculum vitæ

I was born in Delft on December 30th, 1991. I graduated from Haags Montessori Lyceum in 2010. My final project (profielwerkstuk), about the use of the 'preasens historicum' in ancient Greek, was awarded by the Royal Netherlands Academy of Arts and Sciences (KNAW) with the 'Onderwijsprijs'.

In 2010, I enrolled in the bachelor in Physics at Leiden University. After my first year I was awarded the Young Talent Award by the Royal Holland Society of Sciences and Humanities (KHMW). I did my bachelor research on friction during ice skating, under supervision of Prof. Tjerk Oosterkamp and Prof. Joost Frenken.

I enrolled in the Casimir pre-PhD master program at Leiden University in 2013 and was awarded the Hendrik Casimir Prize in 2014. I did a short research project in the KM3NeT-group at Nikhef with Dr. Dorothea Samtleben and another short project in the Econophysics group of Dr. Diego Garlaschelli. For my master thesis I studied the motion of charged and spinning particles orbiting an electrically charged black hole, under supervision of Prof. Jan-Willem van Holten. I obtained my master's degree in 2015.

In that same year, I started my PhD research at Nikhef, under supervision of Dr. Marieke Postma. I presented my work at several international conferences and seminars, and in the last year of my PhD I spent two months at the University of Massachusetts in Amherst and the Massachusetts Institute of Technology.

In september 2019 I will start as Postdoc in the Particle Physics and Cosmology group at DESY in Hamburg, Germany.

Bibliography

[1] M. Postma and J. van de Vis, JCAP **1705**, 004 (2017), hep-ph/1702.07636.

[2] E. I. Sfakianakis and J. van de Vis, Phys. Rev. **D99**, 083519 (2019), hep-ph/1810.01304.

[3] J. de Vries, M. Postma, J. van de Vis, and G. White, JHEP **01**, 089 (2018), hep-ph/1710.04061.

[4] J. De Vries, M. Postma, and J. van de Vis, JHEP **04**, 024 (2019), hep-ph/1811.11104.

[5] G. d'Ambrosi, S. Satish Kumar, J. van de Vis, and J. W. van Holten, Phys. Rev. **D93**, 044051 (2016), gr-qc/1511.05454.

[6] A. I. Băbeanu, J. van de Vis, and D. Garlaschelli, New J. Phys. **20**, 103026 (2018), soc-ph/1712.05959.

[7] K. C. Freeman, Astrophys. J. **160**, 811 (1970).

[8] V. C. Rubin, W. K. Ford, Jr., and N. Thonnard, Astrophys. J. **225**, L107 (1978).

[9] A. Bosma, *The distribution and kinematics of neutral hydrogen in spiral galaxies of various morphological types*, PhD thesis, 1978.

[10] D. Clowe *et al.*, Astrophys. J. **648**, L109 (2006), astro-ph/0608407.

[11] Planck, P. A. R. Ade *et al.*, Astron. Astrophys. **594**, A13 (2016), astro-ph/1502.01589.

[12] M. Milgrom, Astrophys. J. **270**, 365 (1983).

[13] E. P. Verlinde, SciPost Phys. **2**, 016 (2017), hep-th/1611.02269.

[14] J. Lesgourgues and S. Pastor, Phys. Rept. **429**, 307 (2006), astro-ph/0603494.

[15] D. Griffiths, *Introduction to elementary particles* (Wiley-VCH Verlag GmbH & Co, Weinheim, Germany, 2008).

[16] M. Robinson, *Symmetry and the standard model: Mathematics and particle physics* (Springer, New York, USA, 2011).

[17] M. D. Schwartz, *Quantum Field Theory and the Standard Model* (Cambridge University Press, Cambridge, UK, 2014).

[18] S. Tomonaga, Prog. Theor. Phys. **1**, 27 (1946).

[19] H. A. Bethe, Phys. Rev. **72**, 339 (1947).

[20] J. S. Schwinger, Phys. Rev. **73**, 416 (1948).

[21] J. S. Schwinger, Phys. Rev. **74**, 1439 (1948).

[22] R. P. Feynman, Phys. Rev. **76**, 769 (1949).

[23] R. P. Feynman, Phys. Rev. **76**, 749 (1949).

[24] R. P. Feynman, Phys. Rev. **80**, 440 (1950).

[25] S. L. Glashow, Nucl. Phys. **22**, 579 (1961).

[26] S. Weinberg, Phys. Rev. Lett. **19**, 1264 (1967).

[27] A. Salam, Weak and Electromagnetic Interactions, in *8th Nobel Symposium Lerum, Sweden, May 19-25, 1968*, volume C680519, pp. 367–377, 1968.

[28] G. 't Hooft and M. J. G. Veltman, Nucl. Phys. **B44**, 189 (1972).

[29] T. P. Cheng and L. F. Li, *Gauge Theory of elementary particle physics* (Oxford University Press, Oxford, UK, 1984).

[30] P. W. Higgs, Phys. Rev. Lett. **13**, 508 (1964).

[31] ATLAS, G. Aad *et al.*, Phys. Lett. **B716**, 1 (2012), hep-ex/1207.7214.

[32] CMS, S. Chatrchyan *et al.*, Phys. Lett. **B716**, 30 (2012), hep-ex/1207.7235.

[33] F. Englert and R. Brout, Phys. Rev. Lett. **13**, 321 (1964).

[34] Planck, N. Aghanim *et al.*, (2018), astro-ph/1807.06209.

[35] S. Dodelson, *Modern Cosmology* (Academic Press, Amsterdam, the Netherlands, 2003).

[36] S. Weinberg, *Cosmology* (Oxford University Press, Oxford, UK, 2008).

[37] D. S. Gorbunov and V. A. Rubakov, *Introduction to the theory of the early universe: Cosmological perturbations and inflationary theory* (World Scientific Publishing Company, 2011).

[38] D. Baumann, Cosmology, part iii mathematical tripos.

[39] D. W. Hogg *et al.*, Astrophys. J. **624**, 54 (2005), astro-ph/0411197.

[40] Planck, P. A. R. Ade *et al.*, Astron. Astrophys. **561**, A97 (2014), astro-ph/1303.5090.

[41] P. Ntelis *et al.*, JCAP **1706**, 019 (2017), astro-ph/1702.02159.

[42] A. Friedmann, Z. Phys. **21**, 326 (1924).

[43] G. Lemaître, Ann. Soc. Sci. Brux. **47**, 49 (1927).

[44] H. P. Robertson, Rev. Mod. Phys. **5**, 62 (1933).

[45] A. G. Walker, Proc. Math. Soc, London, Ser. 2 **42**, 90 (1937).

[46] A. Einstein, Sitzungsberichte der Königlich Preußischen Akademie der Wissenschaften zu Berlin , 844 (1915).

[47] E. Hubble, Proc. Nat. Acad. Sci. **15**, 168 (1929).

[48] G. Lemaître, Nature **127**, 706 (1931).

[49] R. A. Alpher, H. Bethe, and G. Gamow, Phys. Rev. **73**, 803 (1948).

[50] A. Bazavov *et al.*, Phys. Rev. **D85**, 054503 (2012), hep-lat/1111.1710.

[51] R. V. Wagoner, W. A. Fowler, and F. Hoyle, Astrophys. J. **148**, 3 (1967).

[52] R. A. Alpher, H. Bethe, and G. Gamow, Phys. Rev. **73**, 803 (1948).

[53] G. Steigman, Ann. Rev. Nucl. Part. Sci. **57**, 463 (2007), astro-ph/0712.1100.

[54] B. D. Fields, P. Molaro, and S. Sarkar, Chin. Phys. **C38**, 339 (2014), astro-ph/1412.1408.

[55] R. H. Cyburt, B. D. Fields, K. A. Olive, and T.-H. Yeh, Rev. Mod. Phys. **88**, 015004 (2016), astro-ph/1505.01076.

[56] B. Fields and S. Sarkar, (2006), astro-ph/0601514.

[57] R. A. Alpher and R. C. Herman, Physical Review **74**, 1737 (1948).

[58] A. A. Penzias and R. W. Wilson, Astrophys. J. **142**, 419 (1965).

[59] WMAP, C. L. Bennett *et al.*, Astrophys. J. Suppl. **208**, 20 (2013), astro-ph/1212.5225.

[60] D. J. Fixsen *et al.*, Astrophys. J. **473**, 576 (1996), astro-ph/9605054.

[61] S. Sarkar, Measuring the baryon content of the universe, in *Proceedings, XIIIth Rencontres de Blois on Frontiers of the Universe*, pp. 53–63, 2004, astro-ph/0205116.

[62] G. Jungman, M. Kamionkowski, A. Kosowsky, and D. N. Spergel, Phys. Rev. **D54**, 1332 (1996), astro-ph/9512139.

[63] Planck, R. Adam *et al.*, Astron. Astrophys. **596**, A108 (2016), astro-ph/1605.03507.

[64] H. Mo, F. C. van den Bosch, and S. White, *Galaxy Formation and Evolution* (Cambridge University Press, Cambridge, UK, 2010).

[65] H. Bondi and T. Gold, Mon. Not. R. Astron. Soc. **108**, 252 (1948).

[66] F. Hoyle, Mon. Not. R. Astron. Soc. **108**, 372 (1948).

[67] C. W. Misner, Astrophys. J. **151**, 431 (1968).

[68] R. Dicke, Gravitation and the Universe, in *The Jayne Lectures for 1969*, p. 62, 1969.

[69] A. A. Starobinsky, JETP Lett. **30**, 682 (1979).

[70] A. H. Guth, Phys. Rev. **D23**, 347 (1981).

[71] A. D. Linde, Phys. Lett. **108B**, 389 (1982).

[72] W. H. Kinney, (2009), astro-ph/0902.1529.

[73] A. Riotto, Inflation and the Theory of Cosmological Perturbations, 2018.

[74] V. F. Mukhanov and G. V. Chibisov, JETP Lett. **33**, 532 (1981).

[75] V. F. Mukhanov, (2003), astro-ph/0303077.

[76] BICEP2, Keck Array, P. A. R. Ade *et al.*, Phys. Rev. Lett. **121**, 221301 (2018), astro-ph/1810.05216.

[77] Planck, Y. Akrami *et al.*, (2018), astro-ph/1807.06211.

[78] J. Martin, C. Ringeval, and V. Vennin, Phys. Dark Univ. **5-6**, 75 (2014), astro-ph/1303.3787.

[79] A. Albrecht, P. J. Steinhardt, M. S. Turner, and F. Wilczek, Phys. Rev. Lett. **48**, 1437 (1982).

[80] A. D. Dolgov and A. D. Linde, Phys. Lett. **116B**, 329 (1982).

[81] L. F. Abbott, E. Farhi, and M. B. Wise, Phys. Lett. **117B**, 29 (1982).

[82] A. D. Dolgov and D. P. Kirilova, Sov. J. Nucl. Phys. **51**, 172 (1990).

[83] J. H. Traschen and R. H. Brandenberger, Phys. Rev. **D42**, 2491 (1990).

[84] L. Kofman, A. D. Linde, and A. A. Starobinsky, Phys. Rev. Lett. **73**, 3195 (1994), hep-th/9405187.

[85] Y. Shtanov, J. H. Traschen, and R. H. Brandenberger, Phys. Rev. **D51**, 5438 (1995), hep-ph/9407247.

[86] D. Boyanovsky *et al.*, (1995), hep-ph/9505220.

[87] M. Yoshimura, Prog. Theor. Phys. **94**, 873 (1995), hep-th/9506176.

[88] D. I. Kaiser, Phys. Rev. **D53**, 1776 (1996), astro-ph/9507108.

[89] L. Kofman, A. D. Linde, and A. A. Starobinsky, Phys. Rev. **D56**, 3258 (1997), hep-ph/9704452.

[90] S. Hannestad, Phys. Rev. **D70**, 043506 (2004), astro-ph/0403291.

[91] P. F. de Salas *et al.*, Phys. Rev. **D92**, 123534 (2015), astro-ph/1511.00672.

[92] A. R. Liddle and S. M. Leach, Phys. Rev. **D68**, 103503 (2003), astro-ph/0305263.

[93] S. Dodelson and L. Hui, Phys. Rev. Lett. **91**, 131301 (2003), astro-ph/0305113.

[94] F. Bezrukov, M. Yu. Kalmykov, B. A. Kniehl, and M. Shaposhnikov, JHEP **10**, 140 (2012), hep-ph/1205.2893.

[95] G. Degrassi *et al.*, JHEP **08**, 098 (2012), hep-ph/1205.6497.

[96] V. Branchina and E. Messina, Phys. Rev. Lett. **111**, 241801 (2013), hep-ph/1307.5193.

[97] V. Branchina and E. Messina, EPL **117**, 61002 (2017), hep-ph/1507.08812.

[98] A. Kobakhidze and A. Spencer-Smith, (2014), hep-ph/1404.4709.

[99] A. Spencer-Smith, (2014), hep-ph/1405.1975.

[100] A. V. Bednyakov, B. A. Kniehl, A. F. Pikelner, and O. L. Veretin, Phys. Rev. Lett. **115**, 201802 (2015), hep-ph/1507.08833.

[101] J. R. Espinosa, G. F. Giudice, and A. Riotto, JCAP **0805**, 002 (2008), hep-ph/0710.2484.

[102] K. Enqvist, T. Meriniemi, and S. Nurmi, JCAP **1407**, 025 (2014), hep-ph/1404.3699.

[103] M. Fairbairn and R. Hogan, Phys. Rev. Lett. **112**, 201801 (2014), hep-ph/1403.6786.

[104] A. Kobakhidze and A. Spencer-Smith, Phys. Lett. **B722**, 130 (2013), hep-ph/1301.2846.

[105] A. Hook, J. Kearney, B. Shakya, and K. M. Zurek, JHEP **01**, 061 (2015), hep-ph/1404.5953.

[106] H. Georgi and S. L. Glashow, Phys. Rev. Lett. **32**, 438 (1974).

[107] P. Nath and P. Fileviez Perez, Phys. Rept. **441**, 191 (2007), hep-ph/0601023.

[108] E. W. Kolb, A. D. Linde, and A. Riotto, Phys. Rev. Lett. **77**, 4290 (1996), hep-ph/9606260.

[109] E. W. Kolb, A. Riotto, and I. I. Tkachev, Phys. Lett. **B423**, 348 (1998), hep-ph/9801306.

[110] J. Garcia-Bellido, D. Yu. Grigoriev, A. Kusenko, and M. E. Shaposhnikov, Phys. Rev. **D60**, 123504 (1999), hep-ph/9902449.

[111] A. Tranberg, J. Smit, and M. Hindmarsh, JHEP **01**, 034 (2007), hep-ph/0610096.

[112] D. J. H. Chung, E. W. Kolb, and A. Riotto, Phys. Rev. **D59**, 023501 (1999), hep-ph/9802238.

[113] V. Kuzmin and I. Tkachev, Phys. Rev. **D59**, 123006 (1999), hep-ph/9809547.

[114] P. Blasi, R. Dick, and E. W. Kolb, Astropart. Phys. **18**, 57 (2002), astro-ph/0105232.

[115] T. Markkanen and S. Nurmi, JCAP **1702**, 008 (2017), astro-ph/1512.07288.

[116] M. Fairbairn, K. Kainulainen, T. Markkanen, and S. Nurmi, (2018), astro-ph/1808.08236.

[117] K. Lozanov, Lectures on reheating after inflation, 2018.

[118] R. Allahverdi, R. Brandenberger, F.-Y. Cyr-Racine, and A. Mazumdar, Ann. Rev. Nucl. Part. Sci. **60**, 27 (2010), hep-th/1001.2600.

[119] M. A. Amin, M. P. Hertzberg, D. I. Kaiser, and J. Karouby, Int. J. Mod. Phys. **D24**, 1530003 (2014), hep-ph/1410.3808.

[120] M. E. Peskin and D. V. Schroeder, *An Introduction to quantum field theory* (Addison-Wesley, Reading, USA, 1995).

[121] E. Mathieu, J. Maths. Pures Appl. **13**, 137 (1868).

[122] N. McLachlan, *Theory and application of Mathieu functions* (Clarendon Press, Oxford, UK, 1947).

[123] G. N. Felder *et al.*, Phys. Rev. Lett. **87**, 011601 (2001), hep-ph/0012142.

[124] J. F. Dufaux, G. N. Felder, L. Kofman, M. Peloso, and D. Podolsky, JCAP **0607**, 006 (2006), hep-ph/0602144.

[125] S. Tsujikawa, K.-i. Maeda, and T. Torii, Phys. Rev. **D60**, 063515 (1999), hep-ph/9901306.

[126] B. A. Bassett and S. Liberati, Phys. Rev. **D58**, 021302 (1998), hep-ph/9709417.

[127] M. Herranen, T. Markkanen, S. Nurmi, and A. Rajantie, Phys. Rev. Lett. **113**, 211102 (2014), hep-ph/1407.3141.

[128] J. R. Espinosa *et al.*, JHEP **09**, 174 (2015), hep-ph/1505.04825.

[129] K. Kamada, Phys. Lett. **B742**, 126 (2015), hep-ph/1409.5078.

[130] M. Herranen, T. Markkanen, S. Nurmi, and A. Rajantie, Phys. Rev. Lett. **115**, 241301 (2015), hep-ph/1506.04065.

[131] Y. Ema, K. Mukaida, and K. Nakayama, JCAP **1610**, 043 (2016), hep-ph/1602.00483.

[132] K. Kohri and H. Matsui, Phys. Rev. **D94**, 103509 (2016), hep-ph/1602.02100.

[133] K. Kohri and H. Matsui, JCAP **1708**, 011 (2017), hep-ph/1607.08133.

[134] K. Enqvist, M. Karciauskas, O. Lebedev, S. Rusak, and M. Zatta, JCAP **1611**, 025 (2016), hep-ph/1608.08848.

[135] N. D. Birrell and P. C. W. Davies, *Quantum Fields in Curved Space* (Cambridge Univ. Press, Cambridge, UK, 1984).

[136] A. A. Starobinsky, Phys. Lett. **B91**, 99 (1980).

[137] B. Whitt, Phys. Lett. **145B**, 176 (1984).

[138] L. V. Keldysh, Zh. Eksp. Teor. Fiz. **47**, 1515 (1964).

[139] J. S. Schwinger, J. Math. Phys. **2**, 407 (1961).

[140] R. D. Jordan, Phys. Rev. **D33**, 444 (1986).

[141] E. Calzetta and B. L. Hu, Phys. Rev. **D35**, 495 (1987).

[142] E. Calzetta and B. L. Hu, Phys. Rev. **D37**, 2878 (1988).

[143] A. Ringwald, Z. Phys. **C34**, 481 (1987).

[144] A. Ringwald, Annals Phys. **177**, 129 (1987).

[145] J. Baacke, K. Heitmann, and C. Patzold, Phys. Rev. **D56**, 6556 (1997), hep-ph/9706274.

[146] J. Baacke, K. Heitmann, and C. Patzold, Phys. Rev. **D55**, 2320 (1997), hep-th/9608006.

[147] L. Parker and S. A. Fulling, Phys. Rev. **D9**, 341 (1974).

[148] S. A. Fulling, L. Parker, and B. L. Hu, Phys. Rev. **D10**, 3905 (1974).

[149] T. S. Bunch, J. Phys. **A13**, 1297 (1980).

[150] T. Markkanen and A. Tranberg, JCAP **1308**, 045 (2013), hep-ph/1303.0180.

[151] J. P. Paz and F. D. Mazzitelli, Phys. Rev. **D37**, 2170 (1988).

[152] V. Mukhanov and S. Winitzki, *Introduction to quantum effects in gravity* (Cambridge University Press, Cambridge, UK, 2007).

[153] S. R. Coleman and E. J. Weinberg, Phys. Rev. **D7**, 1888 (1973).

[154] I. G. Moss, (2015), hep-ph/1509.03554.

[155] F. L. Bezrukov and M. Shaposhnikov, Phys. Lett. **B659**, 703 (2008), hep-th/0710.3755.

[156] A. De Simone, M. P. Hertzberg, and F. Wilczek, Phys. Lett. **B678**, 1 (2009), hep-ph/0812.4946.

[157] F. L. Bezrukov, A. Magnin, and M. Shaposhnikov, Phys. Lett. **B675**, 88 (2009), hep-ph/0812.4950.

[158] F. Bezrukov and M. Shaposhnikov, JHEP **07**, 089 (2009), hep-ph/0904.1537.

[159] A. O. Barvinsky, A. Yu. Kamenshchik, C. Kiefer, A. A. Starobinsky, and C. Steinwachs, JCAP **0912**, 003 (2009), hep-ph/0904.1698.

[160] A. O. Barvinsky, A. Yu. Kamenshchik, C. Kiefer, A. A. Starobinsky, and C. F. Steinwachs, Eur. Phys. J. **C72**, 2219 (2012), hep-ph/0910.1041.

[161] K. Allison, JHEP **02**, 040 (2014), hep-ph/1306.6931.

[162] A. Salvio and A. Mazumdar, Phys. Lett. **B750**, 194 (2015), hep-ph/1506.07520.

[163] A. Salvio, Phys. Lett. **B780**, 111 (2018), hep-ph/1712.04477.

[164] D. I. Kaiser and E. I. Sfakianakis, Phys. Rev. Lett. **112**, 011302 (2014), astro-ph/1304.0363.

[165] R. Kallosh, A. Linde, and D. Roest, Phys. Rev. Lett. **112**, 011303 (2014), hep-th/1310.3950.

[166] R. Kallosh and A. Linde, JCAP **1312**, 006 (2013), hep-th/1309.2015.

[167] R. Kallosh, A. Linde, and D. Roest, JHEP **11**, 198 (2013), hep-th/1311.0472.

[168] M. Galante, R. Kallosh, A. Linde, and D. Roest, Phys. Rev. Lett. **114**, 141302 (2015), hep-th/1412.3797.

[169] R. Kallosh and A. Linde, Phys. Rev. **D91**, 083528 (2015), astro-ph/1502.07733.

[170] J. J. M. Carrasco, R. Kallosh, and A. Linde, Phys. Rev. **D92**, 063519 (2015), hep-th/1506.00936.

[171] J. Garcia-Bellido, D. G. Figueroa, and J. Rubio, Phys. Rev. **D79**, 063531 (2009), hep-ph/0812.4624.

[172] F. Bezrukov, D. Gorbunov, and M. Shaposhnikov, JCAP **0906**, 029 (2009), hep-ph/0812.3622.

[173] J. Repond and J. Rubio, JCAP **1607**, 043 (2016), astro-ph/1604.08238.

[174] M. P. DeCross, D. I. Kaiser, A. Prabhu, C. Prescod-Weinstein, and E. I. Sfakianakis, Phys. Rev. **D97**, 023526 (2018), astro-ph/1510.08553.

[175] M. P. DeCross, D. I. Kaiser, A. Prabhu, C. Prescod-Weinstein, and E. I. Sfakianakis, Phys. Rev. **D97**, 023527 (2018), astro-ph/1610.08868.

[176] M. P. DeCross, D. I. Kaiser, A. Prabhu, C. Prescod-Weinstein, and E. I. Sfakianakis, Phys. Rev. **D97**, 023528 (2018), astro-ph/1610.08916.

[177] Y. Ema, R. Jinno, K. Mukaida, and K. Nakayama, JCAP **1702**, 045 (2017), hep-ph/1609.05209.

[178] C. P. Burgess, H. M. Lee, and M. Trott, JHEP **09**, 103 (2009), hep-ph/0902.4465.

[179] C. P. Burgess, H. M. Lee, and M. Trott, JHEP **07**, 007 (2010), hep-ph/1002.2730.

[180] M. P. Hertzberg, JHEP **11**, 023 (2010), hep-ph/1002.2995.

[181] R. N. Lerner and J. McDonald, Phys. Rev. **D82**, 103525 (2010), hep-ph/1005.2978.

[182] S. Ferrara, R. Kallosh, A. Linde, A. Marrani, and A. Van Proeyen, Phys. Rev. **D83**, 025008 (2011), hep-th/1008.2942.

[183] F. Bezrukov, A. Magnin, M. Shaposhnikov, and S. Sibiryakov, JHEP **01**, 016 (2011), hep-ph/1008.5157.

[184] G. F. Giudice and H. M. Lee, Phys. Lett. **B694**, 294 (2011), hep-ph/1010.1417.

[185] F. Bezrukov, D. Gorbunov, and M. Shaposhnikov, JCAP **1110**, 001 (2011), hep-ph/1106.5019.

[186] R. N. Lerner and J. McDonald, JCAP **1211**, 019 (2012), hep-ph/1112.0954.

[187] D. A. Demir, (2012), hep-ph/1207.4584.

[188] M. Atkins and X. Calmet, Phys. Lett. **B697**, 37 (2011), hep-ph/1011.4179.

[189] X. Calmet and R. Casadio, Phys. Lett. **B734**, 17 (2014), hep-ph/1310.7410.

[190] F. Bezrukov, Class. Quant. Grav. **30**, 214001 (2013), hep-ph/1307.0708.

[191] J. Rubio, (2018), hep-ph/1807.02376.

[192] D. I. Kaiser, E. A. Mazenc, and E. I. Sfakianakis, Phys. Rev. **D87**, 064004 (2013), astro-ph/1210.7487.

[193] R. N. Greenwood, D. I. Kaiser, and E. I. Sfakianakis, Phys. Rev. **D87**, 064021 (2013), hep-ph/1210.8190.

[194] K. Schutz, E. I. Sfakianakis, and D. I. Kaiser, Phys. Rev. **D89**, 064044 (2014), astro-ph/1310.8285.

[195] V. F. Mukhanov, H. A. Feldman, and R. H. Brandenberger, Phys. Rept. **215**, 203 (1992).

[196] B. A. Bassett, S. Tsujikawa, and D. Wands, Rev. Mod. Phys. **78**, 537 (2006), astro-ph/0507632.

[197] K. A. Malik and D. Wands, Phys. Rept. **475**, 1 (2009), astro-ph/0809.4944.

[198] D. H. Lyth, JCAP **0712**, 016 (2007), astro-ph/0707.0361.

[199] F. Finelli and R. H. Brandenberger, Phys. Rev. Lett. **82**, 1362 (1999), hep-ph/9809490.

[200] B. A. Bassett, D. I. Kaiser, and R. Maartens, Phys. Lett. **B455**, 84 (1999), hep-ph/9808404.

[201] M. Parry and R. Easther, Phys. Rev. **D59**, 061301 (1999), hep-ph/9809574.

[202] B. A. Bassett, F. Tamburini, D. I. Kaiser, and R. Maartens, Nucl. Phys. **B561**, 188 (1999), hep-ph/9901319.

[203] B. A. Bassett, C. Gordon, R. Maartens, and D. I. Kaiser, Phys. Rev. **D61**, 061302 (2000), hep-ph/9909482.

[204] G. N. Felder, L. Kofman, and A. D. Linde, JHEP **02**, 027 (2000), hep-ph/9909508.

[205] R. Easther and M. Parry, Phys. Rev. **D62**, 103503 (2000), hep-ph/9910441.

[206] N. Afshordi and R. H. Brandenberger, Phys. Rev. **D63**, 123505 (2001), gr-qc/0011075.

[207] S. Tsujikawa and B. A. Bassett, Phys. Lett. **B536**, 9 (2002), astro-ph/0204031.

[208] P. Adshead, J. T. Giblin, T. R. Scully, and E. I. Sfakianakis, JCAP **1512**, 034 (2015), astro-ph/1502.06506.

[209] P. Adshead, J. T. Giblin, T. R. Scully, and E. I. Sfakianakis, JCAP **1610**, 039 (2016), astro-ph/1606.08474.

[210] R. Kallosh and A. Linde, JCAP **1310**, 033 (2013), hep-ph/1307.7938.

[211] F. Bezrukov and M. Shaposhnikov, Phys. Lett. **B734**, 249 (2014), hep-ph/1403.6078.

[212] Y. Hamada, H. Kawai, K.-Y. Oda, and S. C. Park, Phys. Rev. Lett. **112**, 241301 (2014), hep-ph/1403.5043.

[213] Y. Hamada, H. Kawai, K.-Y. Oda, and S. C. Park, Phys. Rev. **D91**, 053008 (2015), hep-ph/1408.4864.

[214] J. M. Ezquiaga, J. Garcia-Bellido, and E. Ruiz Morales, Phys. Lett. **B776**, 345 (2018), astro-ph/1705.04861.

[215] I. Masina, Phys. Rev. **D98**, 043536 (2018), hep-ph/1805.02160.

[216] F. Bezrukov, M. Pauly, and J. Rubio, JCAP **1802**, 040 (2018), hep-ph/1706.05007.

[217] S. Rasanen and P. Wahlman, JCAP **1711**, 047 (2017), astro-ph/1709.07853.

[218] V.-M. Enckell, K. Enqvist, S. Rasanen, and E. Tomberg, JCAP **1806**, 005 (2018), astro-ph/1802.09299.

[219] R. Cooke, M. Pettini, R. A. Jorgenson, M. T. Murphy, and C. C. Steidel, Astrophys. J. **781**, 31 (2014), astro-ph/1308.3240.

[220] A. D. Sakharov, Pis'ma Zh. Eksp. Teor. Fiz. **5**, 32 (1967).

[221] N. S. Manton, Phys. Rev. **D28**, 2019 (1983).

[222] F. R. Klinkhamer and N. S. Manton, Phys. Rev. **D30**, 2212 (1984).

[223] J. A. Harvey and M. S. Turner, Phys. Rev. **D42**, 3344 (1990).

[224] M. Trodden, Rev. Mod. Phys. **71**, 1463 (1999).

[225] J. M. Cline, Baryogenesis, in *Les Houches Summer School - Session 86: Particle Physics and Cosmology: The Fabric of Spacetime*, 2006, hep-ph/0609145.

[226] D. E. Morrissey and M. J. Ramsey-Musolf, New J. Phys. **14**, 125003 (2012), hep-ph/1206.2942.

[227] G. A. White, *A Pedagogical Introduction to Electroweak Baryogenesis* (Morgan & Claypool, San Rafael, USA).

[228] M. B. Gavela, P. Hernandez, J. Orloff, and O. Pene, Mod. Phys. Lett. **A9**, 795 (1994), hep-ph/9312215.

[229] P. Huet and E. Sather, Phys. Rev. **D51**, 379 (1995), hep-ph/9404302.

[230] M. B. Gavela, P. Hernandez, J. Orloff, O. Pene, and C. Quimbay, Nucl. Phys. **B430**, 382 (1994), hep-ph/9406289.

[231] K. Kajantie, M. Laine, K. Rummukainen, and M. E. Shaposhnikov, Nucl. Phys. B **466**, 189 (1996), hep-lat/9510020.

[232] M. Gurtler, E.-M. Ilgenfritz, and A. Schiller, Phys. Rev. **D56**, 3888 (1997), hep-lat/9704013.

[233] K. Rummukainen, M. Tsypin, K. Kajantie, M. Laine, and M. E. Shaposhnikov, Nucl. Phys. **B532**, 283 (1998), hep-lat/9805013.

[234] M. Laine and K. Rummukainen, Nucl. Phys. Proc. Suppl. **73**, 180 (1999), hep-lat/9809045.

[235] F. Csikor, Z. Fodor, and J. Heitger, Phys. Rev. Lett. **82**, 21 (1999), hep-ph/9809291.

[236] Y. Aoki, F. Csikor, Z. Fodor, and A. Ukawa, Phys. Rev. **D60**, 013001 (1999), hep-lat/9901021.

[237] M. Fukugita and T. Yanagida, Phys. Lett. **B174**, 45 (1986).

[238] T. Yanagida, Conf. Proc. **C7902131**, 95 (1979).

[239] M. Gell-Mann, P. Ramond, and R. Slansky, Conf. Proc. **C790927**, 315 (1979), hep-th/1306.4669.

[240] R. N. Mohapatra and G. Senjanović, Phys. Rev. Lett. **44**, 912 (1980).

[241] M. Trodden, Rev. Mod. Phys. **71**, 1463 (1999), hep-ph/9803479.

[242] C. Delaunay, C. Grojean, and J. D. Wells, JHEP **04**, 029 (2008), hep-ph/0711.2511.

[243] C. Grojean, G. Servant, and J. D. Wells, Phys. Rev. **D71**, 036001 (2005), hep-ph/0407019.

[244] M. Quiros, Finite temperature field theory and phase transitions, in *Proceedings, 1998 Summer School in High-energy physics and cosmology*, pp. 187–259, 1999, hep-ph/9901312.

[245] S. Coleman, Phys. Rev. D **15**, 2929 (1977).

[246] A. D. Linde, Nucl. Phys. **B216**, 421 (1983).

[247] J. Moreno, M. Quiros, and M. Seco, Nuclear Physics B **526**, 489 (1998).

[248] A. Masoumi, K. D. Olum, and B. Shlaer, JCAP **1701**, 051 (2017), gr-qc/1610.06594.

[249] H. H. Patel and M. J. Ramsey-Musolf, JHEP **07**, 029 (2011), hep-ph/1101.4665.

[250] K. Fuyuto and E. Senaha, Phys. Rev. **D90**, 015015 (2014), hep-ph/1406.0433.

[251] P. John, Phys. Lett. **B452**, 221 (1999), hep-ph/9810499.

[252] C. Lee, V. Cirigliano, and M. J. Ramsey-Musolf, Phys. Rev. D **71**, 075010 (2005), hep-ph/0412354.

[253] K. T. Mahanthappa, Phys. Rev. **126**, 329 (1962).

[254] P. M. Bakshi and K. T. Mahanthappa, Journal of Mathematical Physics **4**, 1 (1963).

[255] P. M. Bakshi and K. T. Mahanthappa, Journal of Mathematical Physics **4**, 12 (1963).

[256] K.-C. Chou, Z.-B. Su, B.-L. Hao, and L. Yu, Physics Reports **118**, 1 (1985).

[257] M. Carena, M. Quiros, M. Seco, and C. E. M. Wagner, Nucl. Phys. B **650**, 24 (2003), hep-ph/0208043.

[258] T. Konstandin, T. Prokopec, M. G. Schmidt, and M. Seco, Nucl. Phys. **B738**, 1 (2006), hep-ph/0505103.

[259] V. Cirigliano, C. Lee, M. J. Ramsey-Musolf, and S. Tulin, Phys. Rev. **D81**, 103503 (2010), hep-ph/0912.3523.

[260] V. Cirigliano, C. Lee, and S. Tulin, Phys. Rev. **D84**, 056006 (2011), hep-ph/1106.0747.

[261] K. Enqvist, A. Riotto, and I. Vilja, Phys. Lett. **B438**, 273 (1998), hep-ph/9710373.

[262] T. Liu, M. J. Ramsey-Musolf, and J. Shu, Phys. Rev. Lett. **108**, 221301 (2012), hep-ph/1109.4145.

[263] H. A. Weldon, Phys. Rev. **D40**, 2410 (1989).

[264] H. A. Weldon, Phys. Rev. **D61**, 036003 (2000), hep-ph/9908204.

[265] V. V. Klimov, Sov. J. Nucl. Phys. **33**, 934 (1981).

[266] J. M. Cline, Phil. Trans. Roy. Soc. Lond. **A376**, 20170116 (2018), hep-ph/1704.08911.

[267] M. Joyce, T. Prokopec, and N. Turok, Phys. Rev. Lett. **75**, 1695 (1995), hep-ph/9408339.

[268] J. M. Cline, M. Joyce, and K. Kainulainen, JHEP **07**, 018 (2000), hep-ph/0006119.

[269] V. Cirigliano, M. J. Ramsey-Musolf, S. Tulin, and C. Lee, Phys. Rev. D **73**, 115009 (2006), hep-ph/0603058.

[270] G. D. Moore and M. Tassler, JHEP **02**, 105 (2011), hep-ph/1011.1167.

[271] D. J. H. Chung, B. Garbrecht, M. J. Ramsey-Musolf, and S. Tulin, JHEP **2009**, 067 (2009), hep-ph/0908.2187.

[272] A. G. Cohen, D. B. Kaplan, and A. E. Nelson, Phys. Lett. **B336**, 41 (1994), hep-ph/9406345.

[273] D. J. H. Chung, B. Garbrecht, M. J. Ramsey-Musolf, and S. Tulin, Phys. Rev. D **81**, 063506 (2010), hep-ph/0905.4509.

[274] D. Bödeker, G. D. Moore, and K. Rummukainen, Phys. Rev. D **61**, 056003 (2000), hep-ph/9907545.

[275] G. D. Moore and K. Rummukainen, Phys. Rev. D **61**, 105008 (2000), hep-ph/9906259.

[276] G. D. Moore, Phys. Rev. D **62**, 085011 (2000), hep-ph/0001216.

[277] D. Bodeker, L. Fromme, S. J. Huber, and M. Seniuch, JHEP **02**, 026 (2005), hep-ph/0412366.

[278] S. J. Huber, M. Pospelov, and A. Ritz, Phys. Rev. **D75**, 036006 (2007), hep-ph/0610003.

[279] B. Grinstein and M. Trott, Phys. Rev. **D78**, 075022 (2008), hep-ph/0806.1971.

[280] P. H. Damgaard, A. Haarr, D. O'Connell, and A. Tranberg, JHEP **02**, 107 (2016), hep-ph/1512.01963.

[281] A. Kobakhidze, L. Wu, and J. Yue, JHEP **04**, 011 (2016), hep-ph/1512.08922.

[282] C. Balazs, G. White, and J. Yue, JHEP **03**, 030 (2017), hep-ph/1612.01270.

[283] H. Georgi, Ann. Rev. Nucl. Part. Sci. **43**, 209 (1993).

[284] D. B. Kaplan, Effective field theories, in *7th Summer School in Nuclear Physics Symmetries*, 1995, nucl-th/9506035.

[285] A. V. Manohar, Lect. Notes Phys. **479**, 311 (1997), hep-ph/9606222.

[286] C. P. Burgess, Ann. Rev. Nucl. Part. Sci. **57**, 329 (2007), hep-th/0701053.

[287] B. Henning, X. Lu, and H. Murayama, JHEP **01**, 023 (2016), hep-ph/1412.1837.

[288] J. Brod, U. Haisch, and J. Zupan, JHEP **11**, 180 (2013), hep-ph/1310.1385.

[289] Y. T. Chien, V. Cirigliano, W. Dekens, J. de Vries, and E. Mereghetti, JHEP **02**, 011 (2016), hep-ph/1510.00725.

[290] V. Cirigliano, W. Dekens, J. de Vries, and E. Mereghetti, Phys. Rev. **D94**, 016002 (2016), hep-ph/1603.03049.

[291] K. Fuyuto and M. Ramsey-Musolf, (2017), hep-ph/1706.08548.

[292] C. Arzt, Phys. Lett. **B342**, 189 (1995), hep-ph/9304230.

[293] W. Buchmüller and D. Wyler, Nucl. Phys. B **268**, 621 (1986).

[294] B. Grzadkowski, M. Iskrzynski, M. Misiak, and J. Rosiek, JHEP **10**, 085 (2010), hep-ph/1008.4884.

[295] S. Di Vita, C. Grojean, G. Panico, M. Riembau, and T. Vantalon, JHEP **09**, 069 (2017), hep-ph/1704.01953.

[296] C. W. Murphy, Phys. Rev. **D97**, 015007 (2018), hep-ph/1710.02008.

[297] ACME, V. Andreev *et al.*, Nature **562**, 355 (2018).

[298] ACME, J. Baron *et al.*, Science **343**, 269 (2014), physics.atom-ph/1310.7534.

[299] S. M. Barr and A. Zee, Phys. Rev. Lett. **65**, 21 (1990).

[300] J. Brod and E. Stamou, (2018), hep-ph/1810.12303.

[301] S. Weinberg, Phys. Rev. Lett. **63**, 2333 (1989).

[302] V. Cirigliano, W. Dekens, J. de Vries, and E. Mereghetti, Phys. Rev. **D94**, 034031 (2016), hep-ph/1605.04311.

[303] M. J. Dolan, P. Harris, M. Jankowiak, and M. Spannowsky, Phys. Rev. **D90**, 073008 (2014), hep-ph/1406.3322.

[304] A. Kobakhidze, N. Liu, L. Wu, and J. Yue, Phys. Rev. **D95**, 015016 (2017), hep-ph/1610.06676.

[305] B. Coleppa, M. Kumar, S. Kumar, and B. Mellado, Phys. Lett. **B770**, 335 (2017), hep-ph/1702.03426.

[306] F. P. Huang, P.-H. Gu, P.-F. Yin, Z.-H. Yu, and X. Zhang, Phys. Rev. **D93**, 103515 (2016), hep-ph/1511.03969.

[307] J. Kozaczuk, JHEP **10**, 135 (2015), hep-ph/1506.04741.

[308] D. Bodeker and G. D. Moore, JCAP **0905**, 009 (2009), hep-ph/0903.4099.

[309] D. Bodeker and G. D. Moore, JCAP **1705**, 025 (2017), hep-ph/1703.08215.

[310] G. C. Dorsch, S. J. Huber, and T. Konstandin, JCAP **1812**, 034 (2018), hep-ph/1809.04907.

[311] P. Huet and A. E. Nelson, Phys. Rev. D **53**, 4578 (1996), hep-ph/9506477.

[312] G. A. White, Phys. Rev. D **93**, 043504 (2016), hep-ph/1510.03901.

[313] D. Curtin, P. Meade, and H. Ramani, (2016), hep-ph/1612.00466.

[314] S. Tulin and P. Winslow, Phys. Rev. **D84**, 034013 (2011), hep-ph/1105.2848.

[315] D. J. H. Chung, B. Garbrecht, M. J. Ramsey-Musolf, and S. Tulin, Phys. Rev. Lett. **102**, 061301 (2009), hep-ph/0808.1144.

[316] J. R. Espinosa and M. Quiros, Phys. Lett. **B305**, 98 (1993), hep-ph/9301285.

[317] J. R. Espinosa and M. Quiros, Phys. Rev. **D76**, 076004 (2007), hep-ph/0701145.

[318] V. Barger, P. Langacker, M. McCaskey, M. J. Ramsey-Musolf, and G. Shaughnessy, Phys. Rev. **D77**, 035005 (2008), hep-ph/0706.4311.

[319] J. R. Espinosa, T. Konstandin, J. M. No, and M. Quiros, Phys. Rev. **D78**, 123528 (2008), hep-ph/0809.3215.

[320] J. R. Espinosa, T. Konstandin, and F. Riva, Nucl. Phys. **B854**, 592 (2012), hep-ph/1107.5441.

[321] J. M. Cline and K. Kainulainen, JCAP **1301**, 012 (2013), hep-ph/1210.4196.

[322] V. Vaskonen, Phys. Rev. **D95**, 123515 (2017), hep-ph/1611.02073.

[323] M. Joyce, T. Prokopec, and N. Turok, Phys. Lett. **B338**, 269 (1994), hep-ph/9401352.

[324] G. F. Giudice and M. E. Shaposhnikov, Phys. Lett. **B326**, 118 (1994), hep-ph/9311367.

[325] M. Joyce, T. Prokopec, and N. Turok, Phys. Rev. D **53**, 2930 (1996), hep-ph/9410281.

[326] C.-W. Chiang, K. Fuyuto, and E. Senaha, Phys. Lett. **B762**, 315 (2016), hep-ph/1607.07316.

[327] H.-K. Guo, Y.-Y. Li, T. Liu, M. Ramsey-Musolf, and J. Shu, Phys. Rev. **D96**, 115034 (2017), hep-ph/1609.09849.

[328] A. I. Bochkarev, S. V. Kuzmin, and M. E. Shaposhnikov, Phys. Lett. **B244**, 275 (1990).

[329] N. Turok and J. Zadrozny, Nucl. Phys. **B369**, 729 (1992).

[330] A. T. Davies, C. D. Froggatt, G. Jenkins, and R. G. Moorhouse, Phys. Lett. **B336**, 464 (1994).

[331] J. M. Cline and P.-A. Lemieux, Phys. Rev. **D55**, 3873 (1997), hep-ph/9609240.

[332] J. M. Cline, K. Kainulainen, and M. Trott, JHEP **11**, 089 (2011), hep-ph/1107.3559.

[333] G. C. Dorsch, S. J. Huber, T. Konstandin, and J. M. No, JCAP **1705**, 052 (2017), hep-ph/1611.05874.

[334] J. O. Andersen *et al.*, Phys. Rev. Lett. **121**, 191802 (2018), hep-ph/1711.09849.

[335] T. Gorda, A. Helset, L. Niemi, T. V. I. Tenkanen, and D. J. Weir, JHEP **02**, 081 (2019), hep-ph/1802.05056.

[336] Belle, K. Inami *et al.*, Phys. Lett. **B551**, 16 (2003), hep-ex/0210066.

[337] W. Altmannshofer, J. Brod, and M. Schmaltz, JHEP **05**, 125 (2015), hep-ph/1503.04830.

[338] J. Brod and D. Skodras, JHEP **01**, 233 (2019), hep-ph/1811.05480.

[339] ATLAS, M. Aaboud *et al.*, Submitted to: Phys. Rev. (2018), hep-ex/1811.08856.

[340] L. Fromme and S. J. Huber, JHEP **03**, 049 (2007), hep-ph/0604159.

[341] F. Bezrukov, J. Rubio, and M. Shaposhnikov, Phys. Rev. **D92**, 083512 (2015), hep-ph/1412.3811.

[342] M. Hindmarsh, S. J. Huber, K. Rummukainen, and D. J. Weir, Phys. Rev. Lett. **112**, 041301 (2014), hep-ph/1304.2433.

[343] D. G. Figueroa *et al.*, PoS **GRASS2018**, 036 (2018), astro-ph/1806.06463.